

TESIS DE LA UNIVERSIDAD  
DE ZARAGOZA

2022

120

Iulen Cabeza Gil

# A Numerical Exploration of the Crystalline Lens: from Presbyopia to Cataracts and Intraocular Lenses

Director/es

Calvo Calzada, Begoña

<http://zaguan.unizar.es/collection/Tesis>

ISSN 2254-7606



Prensas de la Universidad  
Universidad Zaragoza

© Universidad de Zaragoza  
Servicio de Publicaciones

ISSN 2254-7606



**Universidad**  
Zaragoza

Tesis Doctoral

A NUMERICAL EXPLORATION OF THE  
CRYSTALLINE LENS: FROM PRESBYOPIA TO  
CATARACTS AND INTRAOCULAR LENSES

Autor

Iulen Cabeza Gil

Director/es

Calvo Calzada, Begoña

**UNIVERSIDAD DE ZARAGOZA**  
**Escuela de Doctorado**

Programa de Doctorado en Ingeniería Mecánica

2022



UNIVERSITY OF ZARAGOZA

DOCTORAL THESIS

---

**A Numerical Exploration of the  
Crystalline Lens: from Presbyopia to  
Cataracts and Intraocular Lenses**

---

*Author: Iulen Cabeza Gil*

*Supervisor: Begoña Calvo Calzada*



**Universidad**  
Zaragoza

March 24, 2022



# Compendium of Publications

This Doctoral Thesis is a compendium of eight publications previously published in various international scientific journals and one in the process of publication in order to qualify for the title of Doctor by the University of Zaragoza, according to the agreement of June 26, 2020 of the Governing Council approving the Regulations on Doctoral Theses. The last study has been included since it closes the work developed in this thesis. According to this regulation, the first page of this document includes the compendium of publications together with the Journal Impact Factor (JIF) of each scientific journal.

1. Cabeza-Gil, I., Grasa, J. & Calvo, B. A validated finite element model to reproduce Helmholtz's theory of accommodation: a powerful tool to investigate presbyopia. *Ophthalmic and Physiological Optics* 41, 1241–1253 (2021) [1]. JIF (2020): 3.12 (Q2: 23/62 Ophthalmology).
2. Cabeza-Gil, I., Grasa, J. & Calvo, B. A numerical investigation of changes in lens shape during accommodation. *Scientific Reports* 11 (2021) [2]. JIF (2020): 4.38 (Q1: 17/72 Multidisciplinary Sciences).
3. Cabeza-Gil, I., Calvo, B., Rico, A., Reinhardt-Hervás, C. & Rodríguez, J. Mechanical characterisation of hydrophobic and hydrophilic acrylates used in intraocular lenses through depth sensing indentation. *Journal of the Mechanical Behavior of Biomedical Materials* 126, 104997 (2022) [3]. JIF (2020): 3.90 (Q2: 32/89 Biomedical Engineering).
4. Cabeza-Gil, I., Pérez-Gracia, J., Remón, L. & Calvo, B. Effect of haptic geometry in C-loop intraocular lenses on optical quality. *Journal of the Mechanical Behavior of Biomedical Materials* 114, 104165 (2021) [4]. JIF (2020): 3.90 (Q2: 32/89 Biomedical Engineering).
5. Cabeza-Gil, I., Ariza-Gracia, M. Á., Remón, L. & Calvo, B. Systematic Study on the Biomechanical Stability of C-Loop Intraocular Lenses: Approach to an Optimal Design of the Haptics. *Annals of Biomedical Engineering* 48, 1127–1136 (2019) [5]. JIF (2020): 3.93 (Q2: 31/89 Biomedical Engineering).
6. Remón, L., Cabeza-Gil, I., Calvo, B., Poyales, F. & Garzón, N. Biomechanical Stability of Three Intraocular Lenses With Different Haptic Designs: In Silico and In Vivo Evaluation. *Journal of Refractive Surgery* 36, 617–624 (2020) [6]. JIF (2020): 3.57 (Q1: 15/62 Ophthalmology).
7. Cabeza-Gil, I., Ríos-Ruiz, I. & Calvo, B. Customised Selection of the Haptic Design in C-Loop Intraocular Lenses Based on Deep Learning. *Annals of Biomedical Engineering* 48, 2988–3002 (2020) [7]. JIF (2020): 3.93 (Q2: 31/89 Biomedical Engineering).
8. Cabeza-Gil, I., Ríos-Ruiz, I. & Calvo, B. Experimental evaluation of the injection force exerted in intraocular lens delivery with syringe-type injectors. *Journal of the Mechanical Behavior of Biomedical Materials* 124, 104793 (2021) [8]. JIF (2020): 3.90 (Q2: 32/89 Biomedical Engineering).
9. UNDER REVIEW. Cabeza-Gil, I. & Calvo, B. Predicting the biomechanical stability of IOLs inside the post-cataract capsular bag with a finite element model.





## *Acknowledgements*

I can say without a doubt that during this period I have been happy. One reason is that I have felt fulfilled contributing my grain of sand in the field of ocular research and the other is because of the people with whom I have shared this time. Let these lines serve as a thank you.

I would like to thank my supervisor Begoña. I really do not know where I would be now if our paths had not come together. Your guidance and the trust you placed in me have made me the researcher I am now. I would also like to thank you for the opportunity to participate in so many congresses and to collaborate with different institutions.

I also would like to thank you Miguel Ángel for our long discussions, you have been like a second supervisor for me. Thank you Jorge for teaching me so much about software, helping me with any technical problem and for managing the cluster. Thank you Laura for being part of my beginnings. You were also important to start the Ph.D.

Thank you Carlos, Alex and Aitor for making the time in the lab always fantastic.

CoVid-19 has not allowed to take full advantage of it, but I would always remember to have shared this time with great people, Bea, José, Belén, Julio, Jara, María, Patri, Marco, Andrés, Quercus, Pau, Ortún, Alberto, Nico, Diego, and these last months, the 'post-CoVid' era Benedetta, Elena, Pedro, Ricardo, Raúl, Carlos, Álvaro, Ángela, Óscar. I really appreciate my time helping brilliant students with their thesis and viceversa, Santiago, Jorge, Mikel, María Pilar, Javier, Pablo.

Jesús, our collaboration was great. Thank you for printing some IOLs and making possible the collaboration with AJL. It was my pleasure to work with you, Álvaro, Carlos and Jesús.

I would like to express my gratitude to Adrian Glasser for the assistance to develop the finite element models of the accommodation process. The meetings with you considerably raised my research level.

No words for describing my great experience at Bascom Eye Palmer Institute. Marco, Fabrice, Jean-Marie, Rachele, Gabi, Leana, Joy, Noel, Noah, Bianca, Alex, Felipe, Valerie, you made me feel at home since the first day. Thank you Marco and Fabrice for letting me take part into your research. Normal people like you are the ones who move the research forward.

Finally, I would like to thank the Ph.D. for introducing me to you, Itziar. Everyone should know that all the work presented in this thesis takes your sign due to the extensive discussions and the careful reviews that you made. You put the sparkle in my life.



# Abstract

This thesis addresses three different case studies related to the crystalline lens. Firstly, the mechanical causes of the loss of accommodation amplitude with age, called presbyopia, were analysed through the finite element method. A high-fidelity simulation of the mechanism of accommodation including the contraction of the ciliary muscle was developed. This allowed us to analyse accommodation in depth, showing that although the lens capsule provides the force to accommodate, the stiffness ratio between the lens cortex and lens nucleus could have a higher effect on how the lens changes its shape. Secondly, the biomechanical stability of intraocular lenses (IOLs) was analysed. IOLs are essential for post-cataract patients as they substitute the functions of the crystalline lens. In this thesis, a wide variety of solutions were addressed: from the visco- and hyper-elasticity characterisation of IOL acrylic materials from depth sensing indentation and uniaxial tests to the simulation of the IOL biomechanical stability inside the capsular bag. We also performed a high-fidelity simulation of the IOL compression standards tests required by the IOLs to be commercialised and the results obtained were compared with clinical data. Lastly, we developed a patient-specific methodology to customise the IOL haptic design. Most of the numerical methodology developed is intended to be used in the IOL pre-design phase to avoid costs and time. Thirdly, the IOL delivery during cataract surgery was experimentally studied in order to avoid any possibility of IOL and eye damage. Apart from the injector size, the IOL material was the most influential parameter in the force exerted in IOL delivery.

## *Why is the crystalline lens of vital importance?*

The crystalline lens is the responsible for both the dynamic change of the refractive power of the eye through the mechanism of accommodation and the correction of cornea aberrations. The dynamic optical change is consequence of a geometrical change of the lens. However, as the lens ages over time, it decreases this dynamic optical change and becomes cloudy, what leads to the two most common lens-related pathologies, presbyopia and cataracts. For this reason, it is of utmost importance to study the lens mechanics and all issues related to the artificial intraocular lens that substitutes it during cataract surgery.



# Resumen

Esta tesis aborda, de forma numérica, la resolución de tres problemas relacionados con el cristalino. En primer lugar, se ha construido un modelo de elementos finitos del cristalino humano para abordar la simulación de la acomodación, gracias a la incorporación de la contracción muscular del músculo ciliar. El modelo se ha validado con resultados experimentales comparando con Ramasubramanian & Glasser, 2015. Con el mismo modelo, se ha estudiado como afecta el cambio de las propiedades mecánicas de los tejidos del cristalino en la pérdida de amplitud de la acomodación con la edad para entender si la rigidización de los tejidos juega un papel importante en la presbicia. La conclusión principal del estudio numérico ha sido que las propiedades mecánicas y tensiones iniciales de la cápsula del cristalino proporciona la fuerza necesaria para acomodar, es decir, cambiar su geometría para enfocar de cerca. Específicamente, el ratio de rigidez entre el núcleo y el cristalino gobierna cómo el cristalino cambia de forma. Con la edad, se produce una rigidización del núcleo, y el incremento de la relación entre ambas rigideces (núcleo y corteza) podría ser el principal responsable de la pérdida de la amplitud de acomodación con la edad.

En segundo lugar, se ha estudiado la estabilidad biomecánica de diferentes diseños de lentes intraoculares (IOL). Las IOLs sustituyen las funciones del cristalino en pacientes con cataratas, es por ello necesario garantizar su estabilidad en el interior del saco para garantizar una visión adecuada. Entre los aspectos estudiados destacar la caracterización mecánica de los materiales acrílicos con los que se fabrican las lentes. Para ello, se han combinado ensayos uniaxiales con ensayos de indentación. Éstos últimos se han utilizado para caracterizar la respuesta visco-elástica del material. El definir la respuesta del material mediante modelos visco-hiperelásticos es necesario para posteriormente analizar la estabilidad de la IOL mediante elementos finitos. Este análisis se ha definido a dos niveles, en un primer nivel se analiza la estabilidad de la IOL simulando el ensayo establecido en la norma ISO 11979-3:2012. Esta norma es de obligado cumplimiento para los fabricantes antes de introducir un nuevo diseño en el mercado. Se ha realizado un estudio estadístico para estudiar el efecto de la geometría de los hápticos tipo C-loop en la estabilidad mecánica de la IOL, obteniendo que el entronque, la unión entre el háptico y la lente, es el parámetro más influyente. Para validar la metodología numérica, se fabricaron varios diseños y se analizaron experimentalmente para comparar los resultados correspondientes al desplazamiento axial, rotación y la inclinación de la IOL.

En un segundo nivel, se ha simulado la respuesta de la IOL en el interior del saco capsular, estudiando la influencia de diferentes parámetros del paciente, como geometría y propiedades mecánicas del saco. También se ha analizado

la influencia de parámetros de la cirugía de la catarata, como es el diámetro y posición de la capsulorexis. En este último nivel, se ha estudiado tanto la respuesta instantánea, es decir, tras la cirugía, como a largo plazo, cuando sucede la huella de fusión (fusion footprint) entre la cápsula y la IOL.

Para que los modelos computacionales sean de ayuda a los cirujanos o puedan servir en tiempo real, se ha planteado una metodología basada en inteligencia artificial. En este caso la base de datos de partida corresponde a modelos numéricos altamente fiables y con ellos, se genera datos con los que se entrena la red neuronal. En esta tesis, se estudia la estabilidad de la lente en función del diámetro de compresión del paciente y la edad, que a su vez influye en las propiedades mecánicas del saco.

Por último, se ha evaluado experimentalmente la influencia del material de la IOL (hidrófobo o hidrofílico) y su geometría durante la inyección de la lente en el saco, registrando la fuerza de inyección que debe realizar el cirujano. De cara a evitar complicaciones durante la cirugía, es conveniente que la fuerza a ejercer sea baja. Se ha comprobado que su valor está fuertemente influenciado por el material de la lente.

### *¿Por qué el cristalino es de vital importancia?*

El cristalino es el responsable tanto del cambio dinámico de la potencia refractiva del ojo a través del mecanismo de acomodación como de la corrección de las aberraciones de la córnea. El cambio óptico dinámico es consecuencia de un cambio geométrico del cristalino. Sin embargo, a medida que el cristalino envejece, disminuye este cambio óptico dinámico y se opacifica, lo que da lugar a las dos patologías comúnmente asociadas al envejecimiento como es, la presbicia y las cataratas. Por este motivo, en esta tesis doctoral se ha profundizado en el estudio mecánico del cristalino y tras su sustitución mediante una lente intraocular artificial durante la cirugía de catarata. La metodología establecida pueden ayudar en un futuro tanto al diseño de nuevos implantes como a los oftalmólogos a seleccionar la IOL adecuada a cada paciente para mejora su calidad visual.

# Contents

<b>Compendium of Publications</b>	<b>iii</b>
<b>Acknowledgements</b>	<b>v</b>
<b>Abstract</b>	<b>vii</b>
<b>Resumen</b>	<b>ix</b>
<b>1 Introduction</b>	<b>1</b>
1.1 Physiological Anatomy of the Eye. Basic Concepts . . . . .	1
1.1.1 Anterior Segment . . . . .	1
1.1.2 Posterior Segment . . . . .	2
1.1.3 Optical System of the Human Eye . . . . .	3
1.2 Mechanism of Accommodation . . . . .	3
1.2.1 Alternative Approaches of the Mechanism of Accommodation . . . . .	5
1.2.2 Depth of Field and Measurements of Accommodation . . . . .	6
1.2.3 Anatomy of the accommodative system . . . . .	6
Ciliary Muscle . . . . .	6
Zonular Fibres . . . . .	8
Crystalline Lens . . . . .	10
Iris . . . . .	12
1.2.4 Presbyopia . . . . .	12
1.3 Cataracts . . . . .	13
1.3.1 Injectors - IOL delivery . . . . .	13
1.3.2 History of Cataract Surgery . . . . .	14
1.3.3 Causes and Types of Cataracts . . . . .	14
1.3.4 Ophthalmologic Solutions to Cataracts: IOLs . . . . .	15
Optical design . . . . .	16
Haptic design . . . . .	17
Minimum Requirements prior to be Commercialised . . . . .	18
1.3.5 Post-Cataract Surgery Complications . . . . .	19
1.4 Motivation . . . . .	20
1.4.1 Potential Tools for Understanding Presbyopia and Cataracts . . . . .	20
1.4.2 Open Questions . . . . .	21
1.4.3 Goals of this Thesis . . . . .	21
1.4.4 Justification of the Thematic Unit of the Thesis . . . . .	22
1.5 Structure . . . . .	23
<b>2 Biomechanical Analysis of the Mechanism of Accommodation</b>	<b>25</b>

2.1	Work 1: A validated finite element model to reproduce Helmholtz's theory of accommodation: a powerful tool to investigate presbyopia . . . . .	25
2.2	Work 2: A numerical investigation of changes in lens shape during accommodation . . . . .	39
<b>3</b>	<b>Numerical Methodology to test the Biomechanical Stability of IOLs</b>	<b>53</b>
3.1	Work 3: Mechanical characterisation of hydrophobic and hydrophilic acrylates used in intraocular lenses through depth sensing indentation . . . . .	54
3.2	Work 4: Effect of haptic geometry in C-loop in intraocular lenses on optical quality . . . . .	64
3.3	Work 5: Systematic Study on the Biomechanical Stability of C-loop Intraocular Lenses: Approach to an Optimal Design of the Haptics . . . . .	73
3.4	Work 6: Biomechanical Stability of Three Intraocular Lenses With Different Haptic Designs: In Silico and In Vivo Evaluation	84
3.5	Work 7: Customised Selection of the Haptic Design in C-Loop Intraocular Lenses Based on Deep Learning . . . . .	96
3.6	Work 8: Predicting the biomechanical stability of IOLs inside the post-cataract capsular bag with a finite element model. . .	112
<b>4</b>	<b>Evaluation of IOL delivery during Cataract Surgery</b>	<b>133</b>
4.1	Work 9: Experimental evaluation of the injection force exerted in intraocular lens delivery with syringe-type injectors . . . . .	133
<b>5</b>	<b>Discussion</b>	<b>143</b>
5.1	Achievements . . . . .	143
5.2	Conclusions . . . . .	145
5.3	Future Lines . . . . .	146
<b>6</b>	<b>Discusión</b>	<b>147</b>
6.1	Logros . . . . .	147
6.2	Conclusiones . . . . .	149
6.3	Líneas Futuras . . . . .	150
<b>7</b>	<b>Other Activities during the Ph.D. Period 2019-2022</b>	<b>151</b>
7.1	Diffusion of the Results . . . . .	151
7.1.1	Contributions by Iulen Cabeza Gil . . . . .	151
7.1.2	Contributions by Collaborators . . . . .	151
7.2	Stays in Research Institutions . . . . .	152
7.3	Previous Works related to this Thesis . . . . .	152
7.4	Projects with Multinational Corporations . . . . .	152
7.5	Supervisor of B.S. and M.Sc. Thesis . . . . .	153
7.6	Funding . . . . .	153
	<b>Bibliography</b>	<b>155</b>
	<b>A Metrics of the Scientific Journals</b>	<b>161</b>



## Chapter 1

# Introduction

### 1.1 Physiological Anatomy of the Eye. Basic Concepts.

The eyeball is formed by three concentric layers: the sclera and cornea that constitute the exterior layer; the uvea, the vascular layer in the middle, subdivided into the iris, ciliary body, and choroid; and the retina, which constitutes the innermost layer of the eye. In turn, the eye is divided into two cavities: the anterior segment, filled by the aqueous humour, and the posterior segment, filled by the vitreous humour, see Fig. 1.1.

#### 1.1.1 Anterior Segment

The anterior segment includes the cornea, iris, ciliary muscle, ciliary body, Zinn's zonules and crystalline lens and is filled by the aqueous humour, which bathes and nourishes the lens and maintains pressure within the eye. Since the lens and cornea have no blood supply, the aqueous humour performs the blood's job of carrying nutrients to those structures. The cornea and crystalline lens are the two lenses of the eye that refract light to be focused on the retina. The cornea is a clear membrane covering the front of the eye whilst the lens is located behind the pupil, suspended by the zonular fibres that are attached to the ciliary processes. The lens is the dynamic element responsible for adjusting the focus from far to near objects. The lens increases its refractive power changing its shape during accommodation.

The iris is a sphincter muscle (pupillary sphincter) that controls the amount of light that enters the eye making the pupil larger (dilated) or smaller (constricted). The ciliary muscle lies within the ciliary body and is the engine of accommodation. Its contraction produces the crystalline lens to change its shape by releasing the zonular tension. The ciliary body can be divided into two parts: the pars plicata (corona ciliaris) and the pars plana (orbicularis ciliaris). The pars plicata is the wider, anterior portion containing the ciliary processes, responsible for producing aqueous humour, whereas the pars plana is the flatter region of the ciliary body. It extends from the posterior of the pars plicata to the ora serrata, which is the transition between ciliary body and choroid. Lastly, the zonules connect the lens with the ciliary body, holding the lens in place. In the unaccommodated state, the zonules are stretched while most of them release their tension during accommodation [10].

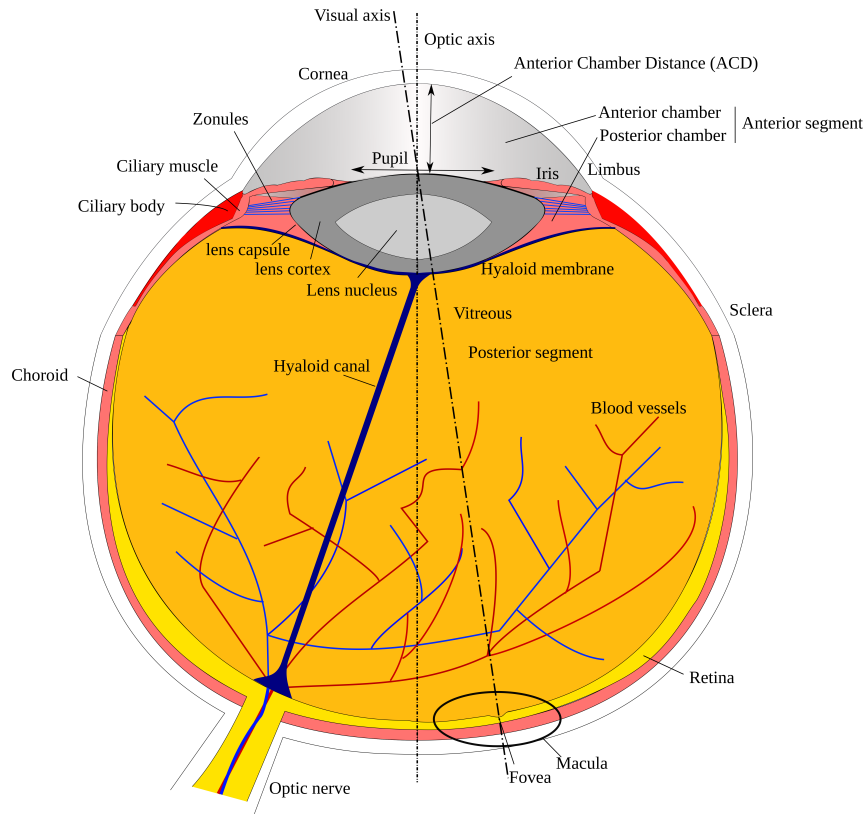


FIGURE 1.1: Overview of the main parts of the eyeball. The anterior segment is divided into anterior and posterior chamber. The anterior chamber is the front part of the eye between the cornea and the iris, with a mean depth of 3.00 mm [9], whilst the posterior chamber lies between the iris and the hyaloid membrane, including the crystalline lens. The hyaloid canal, placed at the posterior segment, has a key role in the fetus to supply blood to the developing lens. It appears to have no function in the adult eye.

### 1.1.2 Posterior Segment

The posterior segment is the back of the eye that includes the anterior hyaloid membrane and all of the optical structures behind it: the vitreous humour, retina, choroid, and optic nerve. Unlike the liquid aqueous humour, the vitreous humour is a gelatinous mass which does not regenerate. The choroid function is to supply oxygen and nutrients to the outer retina through blood vessels, light absorption (pigmented choroid), thermoregulation, and modulation of intraocular pressure. The retina serves a function analogous to that of the film or image sensor in a camera. The neural retina consists of several layers of neurons interconnected by synapses and is supported by an outer layer of pigmented epithelial cells. There are two main types of photoreceptor cells in the retina: rods that are sensitive to light level and provide black-and-white vision and cones that give color vision. A third type of light-sensing cell, the photosensitive ganglion cell, is important for entrainment of

circadian rhythms and reflexive responses such as the pupillary light reflex. Lastly, the function of the optic nerve is to transmit the visual information from the retina to the brain, specifically to the occipital lobe.

### 1.1.3 Optical System of the Human Eye

The optical system of the eye results from the combination of the two main refractive elements, cornea and lens, the iris diaphragm (pupil), and the retina, with their respective relative positions and orientations in the 3D space (axes).

There are two important axes of the eye, the optical axis and the visual axis, which form the angle kappa. This angle kappa has is an important clinical parameter, which has implications when it comes to refractive surgery, cataract surgery, strabismus, and even surgeries involving the retina and macula. The optical axis is the straight line passing through the geometrical centre of a lens and joining the two centres of curvature of its surfaces whereas the visual axis is the imaginary line passing from the midpoint of the visual field to the fovea, see Fig. 1.1.

The cornea is formed by two concave transparent curvatures and accounts for approximately two-thirds of the eye's total optical power ( $\simeq 43$  D). The remaining part is provided by the bi-convex crystalline lens. For a schematic paraxial model, the refractive power of the eye can be calculated with the Gullstrand's eye model formula as:

$$P_{eye} = P_{cornea} + P_{lens} - \frac{ACD}{n_a} P_{cornea} P_{lens} , \quad (1.1)$$

being  $P$  the corresponding refractive power,  $ACD$  the anterior chamber depth, and  $n_a$  the refractive index of the aqueous humour. The pupil has as crucial role in image and vision quality. It controls the amount of light coming into the retina by regulating the diameter of the pupil, which is also related with the aberrations of the eye.

## 1.2 Mechanism of Accommodation

Accommodation is a dynamic, optical increase in the dioptric power of the eye allowing the point of focus of the eye to be changed from distant to near objects. Following the most accepted theory of accommodation by Helmholtz [11], the accommodation process consists in increasing the refractive power of the lens by a contraction of the ciliary muscle [10]. The ciliary muscle contraction results in an inward movement of the apex of the ciliary processes towards the lens equator, that releases resting zonular tension and allows the lens to take a more curved shape, resulting in accommodation [12], see Fig. 1.2.

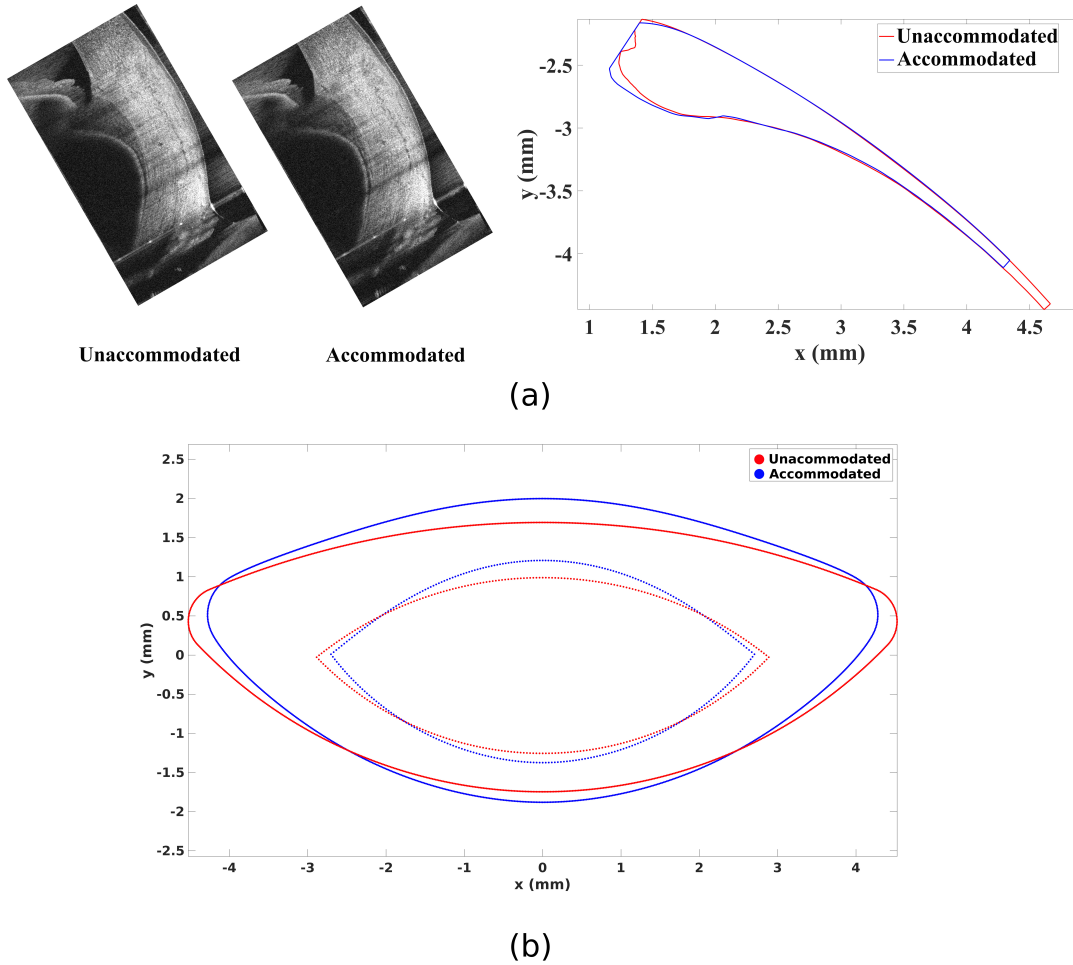


FIGURE 1.2: (a) Images from Spectral-Domain Optical Coherence Tomography (OCT) of the shape of the ciliary muscle unaccommodated and accommodated of a subject of 26 yo at the left. As the small accommodative change cannot be appreciated in the images, the undistorted geometries are shown at the right. (b) Accommodated and unaccommodated lens geometries for the simulation of a young subject [4]. Anterior and posterior radii of curvature become rounded.

When the eye is unaccommodated and focused for distance, the ciliary muscle is relaxed and the lens is stretched by the zonular fibres, see Fig 1.3. During accommodation, the ciliary muscle contracts, the zonular tension is released and the lens becomes rounded due to the force caused by the lens capsule [13, 14]. In other words, the lens capsule is stressed in the unaccommodated state and this pre-stress field makes the lens to become accommodated.

During accommodation, the human lens undergoes several changes: its diameter decreases, its thickness increases, the anterior and posterior surfaces of the lens move anteriorly and posteriorly, respectively, and the curvatures of the anterior and posterior surfaces of the lens increase [15]. Moreover, the change in lens thickness is mainly caused by the lens nucleus ( $\approx 80\%$ ) instead of the lens cortex ( $\approx 20\%$ ) [16].

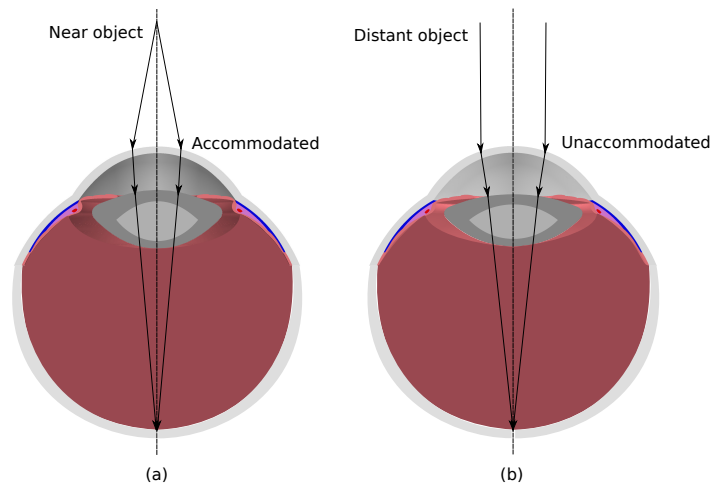


FIGURE 1.3: Accommodated (a) and unaccommodated (b) state of the eye. The ciliary muscle contracts and the lens becomes rounded during accommodation, increasing the refractive power of the eye.

### 1.2.1 Alternative Approaches of the Mechanism of Accommodation

Beyond the most important elements on accommodation, some studies suggest that other parts could also have an effect on accommodation. The hyaloid membrane bends posteriorly according to the accommodation amplitude [17] and there is also fluid flow that could result in a pressure differential [18]. Nevertheless, it is not known if they really have an effect on accommodation or are a consequence of the accommodative changes inside the eye. Accommodation still occurs after vitrectomy [19] and mechanical stretching studies of dissected eyes in which the vitreous is absent and no pressure differential can exist result in normal accommodative optical changes to the lens [13, 20]. Other studies also reported that the sclera could have an effect on accommodation [21, 22]. However, the results are in controversy as strict statistical analyses were not performed [23]. Conversely, other studies reported that the sclera does not deform during accommodation [24, 25].

Although accommodation is widely accepted to occur in accordance with the lenticular theory described by Helmholtz's (with small modifications) [11], other approaches emerged to explain accommodation: Coleman's theory [18] which stated that a continuous pressure difference makes the change of the lens shape; and Schachar's theory, which states that there is increased zonular tension during accommodation and this makes the lens change its shape [26, 27]. Some studies [17, 28] suggest that the vitreous could have an effect on accommodation as Coleman reported [18], however, their effect might be different to how Coleman initially explained. On the other hand, it has not proved that the zonules increase their tension during accommodation. To date, it is thought that the pre-stress field of the lens capsule in the unaccommodated state together with the release of the zonular tension makes the lens change its shape during accommodation.

### 1.2.2 Depth of Field and Measurements of Accommodation

The human being can also maintain an object on focus at various distances by modifying the depth of field (DOF). The DOF of the human eye is influenced by optical parameters (pupil size, optical aberrations, etc.), but is mainly affected by retinal, neural and more complex psychophysical factors [29]. In fact, during accommodation there is a combined action between the actual opto-mechanical changes of the lens and the DOF.

Objective accommodative measurements do not take into account the DOF effect. They are based on the lens refractive power or biometric lens measurements; whereas subjective measurements (taking into account DOF), the most common, require the patient to report when a near letter chart can no longer be maintained in clear, sharp focus. The effect of DOF makes believe that complete presbyopes can accommodate about 1 D, but this is not a true change in optical power of the eye and is therefore called pseudoaccommodation. Objective accommodation (accommodative response) is almost always lower than subjective accommodation (accommodative stimulus), see Fig. 1.4.

Some common instruments to measure the lens refractive power (objective) are autorefractors, which measure how light is changed as it enters a subject eye; and wavefront aberrometers, which offers detailed measurements of the movement of the light wavefront. For biometric measurements, some common techniques are: Scheimpflug Photography, which is a non-contact photographic technique with oblique viewing to obtain in-focus image of the anterior segment of the eye; and optical coherence tomography (OCT), which is based on low-coherence interferometry to capture 2D and 3D microresolution images, see an example in Fig. 1.2.a.

### 1.2.3 Anatomy of the accommodative system

#### Ciliary Muscle

The ciliary muscle is placed between the posterior sclera and surrounded by the ciliary body, see Fig. 1.1. Its origin is at the scleral spur, an annular protusion of the sclera into the anterior chamber. Anterior ciliary muscle tendons insert into the scleral spur and the trabecular meshwork, which serve as a fixed anterior anchor during its contraction [31]. The outer boundary of the ciliary muscle is surrounded by the ciliary body and the posterior attachment of the ciliary muscle is to the stroma of the choroid.

The ciliary muscle is a smooth muscle with both parasympathetic (dominant) and sympathetic innervation [32]. It is atypical for smooth muscles due to its speed of contraction, the large size of its motor neurons, the distance between the muscle and the motor neurons and the unusual ultrastructure of the ciliary muscle cells which in some ways resemble skeletal muscles (indeed, in birds it is a striated skeletal muscle) [10]. It also has a greater abundance of mitochondria than any other muscle in the body, indicating the extraordinary high energy demands and requirements of this muscle.

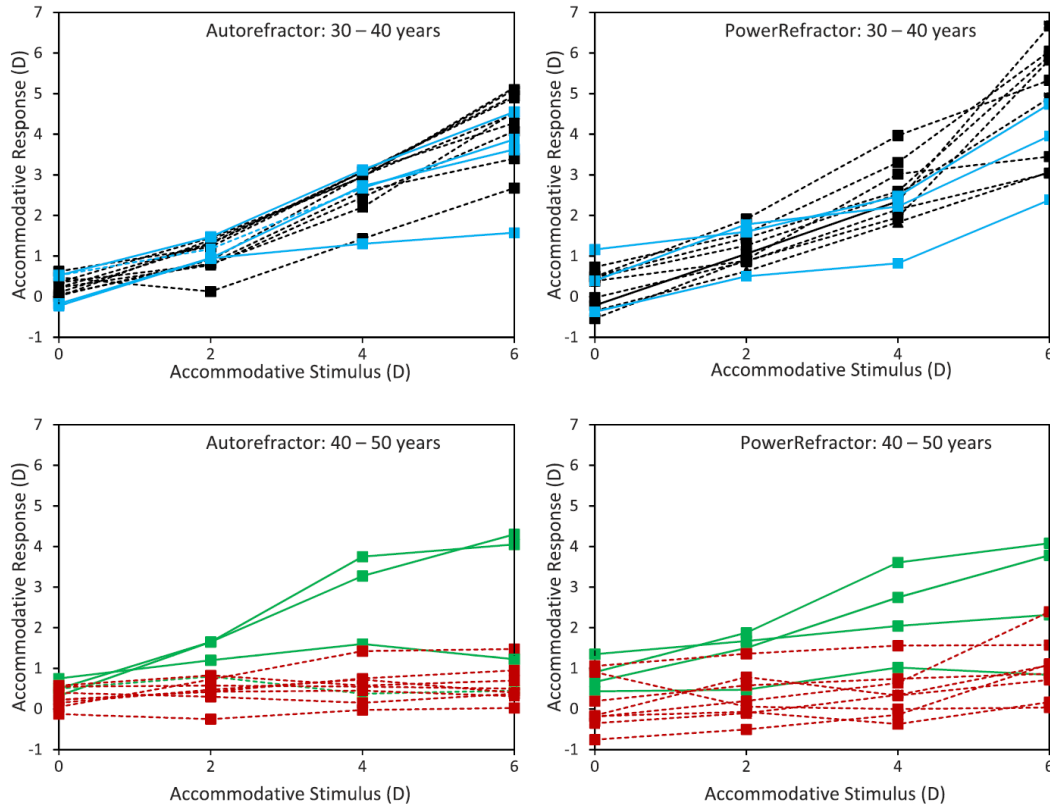


FIGURE 1.4: Accommodative response to 0-, 2-, 4-, and 6-D targets with the Auto-Refractor (left) and PowerRefractor (right). Black dashed lines: 30- < 35-year-old subjects; blue solid lines: 35- < 40-year-old subjects; green solid lines: 40- < 45-year-old subjects; red dashed lines 45- < 50-year-old subjects. Image taken from [30].

The ciliary muscle is composed of three families of fibres, see Fig. 1.5. The longitudinal fibres (or Brücke muscle) are the major group and are placed longitudinally between the scleral spur and the choroid adjacent to the posterior sclera. It is suggested that they are in charge of holding the muscle. Located inward to the longitudinal fibres are radial fibres, whose function is something intermediate between the longitudinal and the last family of fibres, the circular fibres (or Müller’s muscle) that act principally to pull the apex of the ciliary muscle toward the lens equator.

There is no mechanical characterisation of the activation of the ciliary muscle in the literature yet, and there are few measurements about the passive response. A young modulus of 0.12 MPa was given for the passive behaviour of 10% of elongation in a 46 yo subject [34].

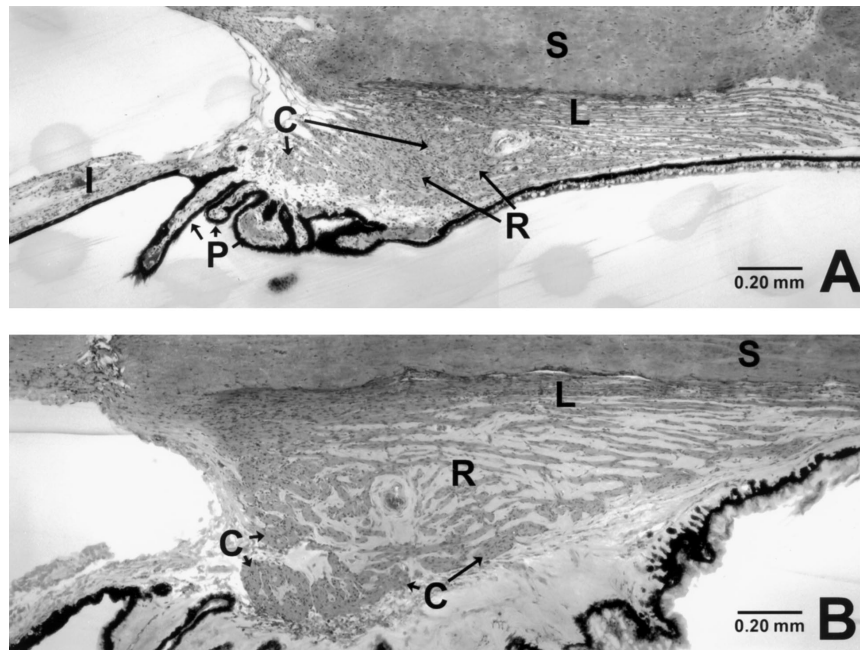


FIGURE 1.5: The ciliary muscles from a 1-day-old donor (A) and an 85-year-old donor (B) treated with pilocarpine. (A) In young eyes, the ciliary processes (P) are located far anterior to the ciliary body. The muscle fibres are packed tightly together with little connective tissue. The area of longitudinal (L) fibres is easily identifiable, however, the circular fibres (C) are intermixed with the radial fibres (R) making it difficult to locate specific areas of exclusively circular or radial fibres. (B) The amount of connective tissue in the ciliary muscle increases with age, which makes the three fiber types, circular (C), radial (R), and longitudinal (L), more clearly identifiable in the 85-year-old donor eyes. S, sclera; I, iris. Image taken from [33].

### Zonular Fibres

The zonular fibres are a complex meshwork of fibrils grouped into fiber bundles of 4 to 50 micrometers in diameter [35], see Fig. 1.6. The zonule is composed of the non-collagenous carbohydrate-protein mucopolysaccharide and glycoprotein complexes that are secreted by the ciliary epithelium. The zonular fibres are elastin-based elastic fibres and are thought to be much more elastic than the lens capsule with a reported young modulus of 0.27 in older subjects (ages 83-97) and 0.34 N/mm<sup>2</sup> in presbyopic ones (ages 47-60) [36]. Their primary function is to hold the lens in the physiological state and allow accommodation to occur.

One of the best schemes of the zonules architecture is provided by Bernal et al. [37], see Fig. 1.7 and the computed-animated model of Goldberg [38]. The attachment of the zonular fibres to the lens capsule is superficial with few fibres penetrating into the capsule to form a mechanical (possibly similar to Velcro) or chemical union [35].



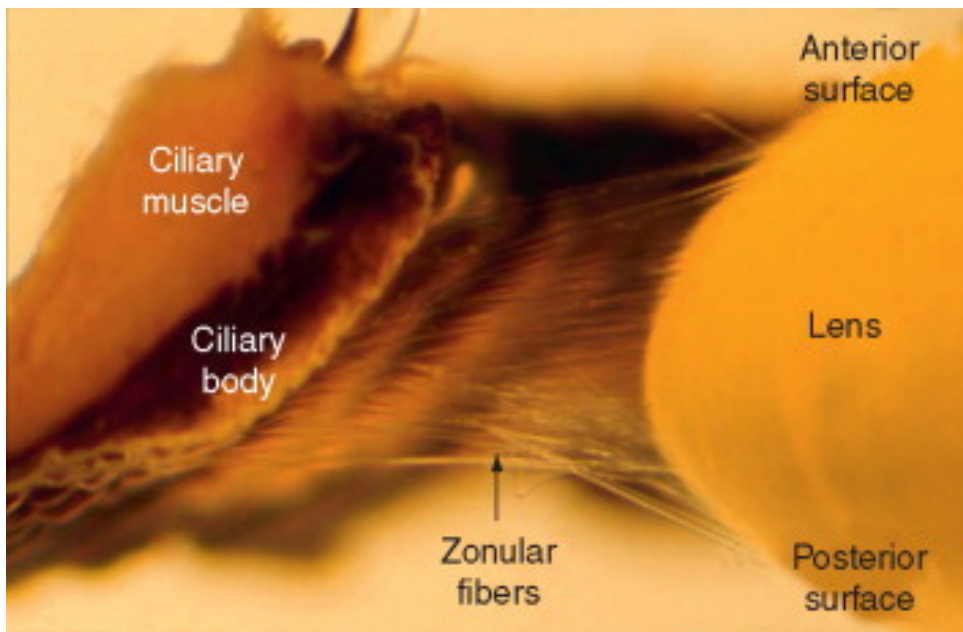


FIGURE 1.6: Photograph of a partially dissected human eye to show the accommodative structures. The cornea and sclera of the eye have been removed and the ciliary muscle and ciliary body have been cut through. The zonular fibres extend from all along the ciliary body across the circumferential space to insert into the capsule all around the lens equatorial region. Image taken from [13].

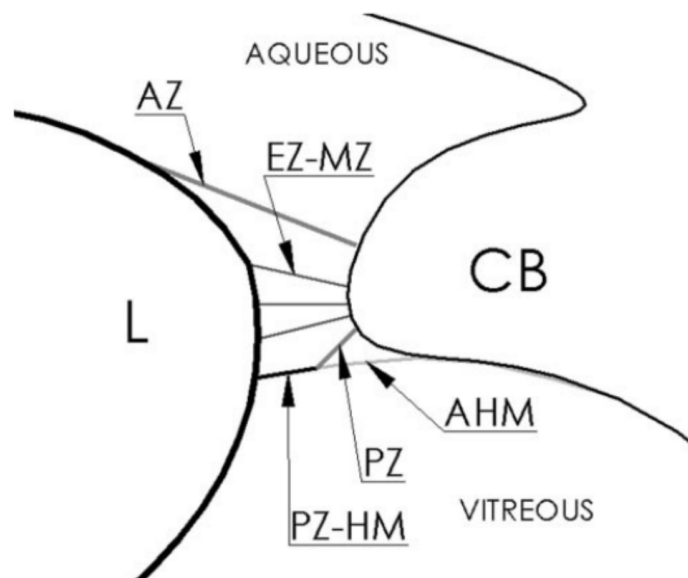


FIGURE 1.7: Proposed architecture of the accommodation apparatus. L, lens. CB, ciliary body. AZ, anterior zonule; EZ-MZ, equatorial and meridional zonule; PZ, posterior zonule; AHM, anterior hyaloid membrane; PZ-HM, posterior zonule embedded in the hyaloid membrane. Image taken from [37].

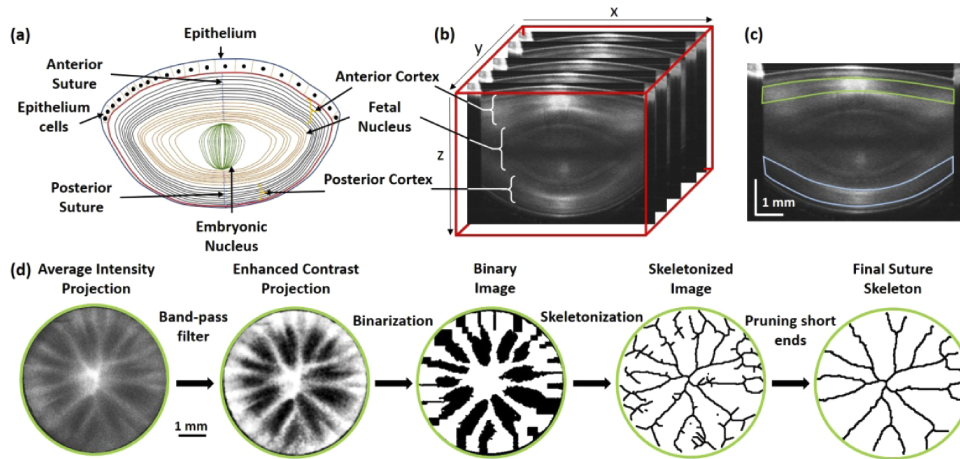


FIGURE 1.8: (a) Anatomy structure of the human crystalline lens. (b) OCT volumetric data of the crystalline lens of  $8 \times 8 \times 4$  mm<sup>3</sup>. (c) Segmented cortical layers of lens used to generate en-face projection images; green -anterior lens, blue -posterior lens. (d) Algorithm for image processing and extraction of suture pattern; averaged intensity en-face projection of anterior lens suture, image contrast enhancement with band pass filtering and CLAHE (contrast limited adaptive histogram equalization) contrast enhancement, image binarization, image skeletonization, pruning ends and false branches. Data presented here is anterior crystalline lens from the right eye of a 40-yo subject. Image taken from [41].

## Crystalline Lens

### Structure

The lens is composed of a clear membrane, the lens capsule, a subcapsular lens epithelium (only anteriorly), and lens fiber cells composing the lens nucleus and cortex, resulting in concentric layers that resemble the shape of an onion, see Fig. 1.8. The embryonic nucleus remains present at the center of the lens throughout life as the cortex grows progressively around it by the addition of an increasing number of layers of lens fiber cells generated from the lens epithelium [39].

The lens comprises approximately 65% water, 35% protein, and a few minerals such as potassium and ascorbic acid [39]. Metabolic activity is required for cellular replication and to maintain crystalline lens transparency [40]. The nutrients for the lens are obtained from the surrounding aqueous humor and vitreous humor as the capsule is permeable to water, ions, and proteins necessary for lens function and growth.

### Transparency

The main optical function of the lens is to transmit light, focusing it on the retina. Although the human lens is colorless at birth, there is a gradual increase in yellowish pigmentation with age. The lens transmits light with wavelengths up to 1200 nm efficiently, but transmits very little light below 390 nm [42]. The inability of cells to be replaced in the encapsulated lens combined with the inability of lens cell proteins to turn over in the non-nucleated fibre cells makes the lens particularly susceptible to damage with aging and

environmental perturbations such as UV light and other oxidative stresses. This results in a decrease in transmission of light and focusing even in the normal aged lens so that the intensity of light reaching the retina is reduced by about 10-fold by 80 years of age [43].

### Aging

The human lens is a living organism which continually grows throughout life. The lens becomes thicker and the curvature of the anterior and posterior surface increases with age [44]. A more curved shape would imply an increase in the refractive power. However, the lens refractive power decreases, what is known as the lens paradox. This phenomenon is explained by the associated change in the refractive index of the lens. The refractive index of the lens is not homogeneous [45, 46]. It is gradually distributed over the lens, with a higher refractive index in the lens center, and a lower refractive index towards the lens surface. This gradient refractive index (GRIN) changes with age, decreasing the equivalent refractive index of the lens [44, 47].

The mechanical properties of the lens also change with age, the lens nucleus stiffens from a very early-age, the cortex apparently keeps similar properties [48], see Fig. 1.9.a, and the stiffness of the lens capsule tends to increase [49, 50], Fig. 1.9.b. This change in mechanical properties is directly related to how the lens changes its shape. All this age-related factors influence the loss of accommodation amplitude and the developing of cataracts at an advanced age.

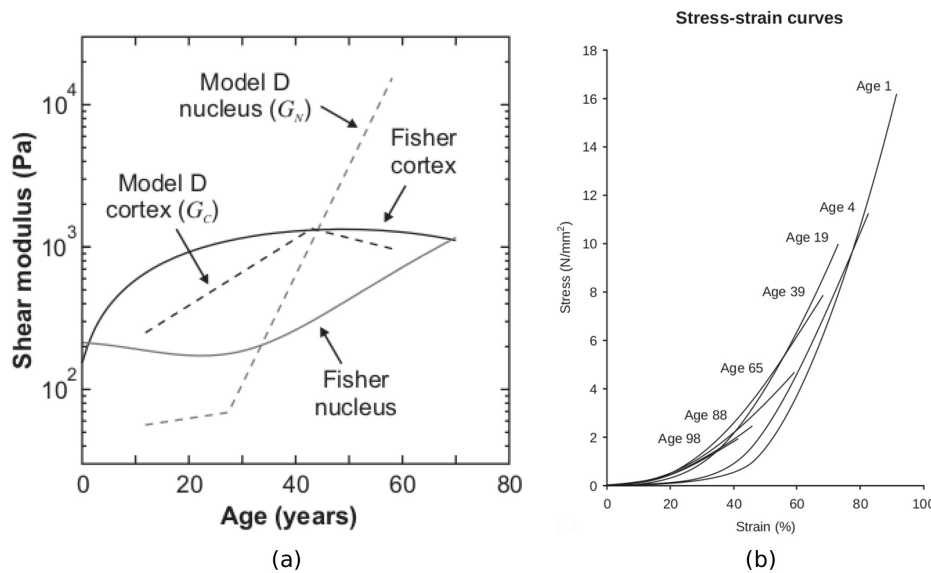


FIGURE 1.9: (a) Age-stiffness model for the nucleus and cortex reported by Fisher (1971) (solid lines) compared to the Model D age-stiffness model (dashed lines). The Fisher (1971) models have been translated from Young's modulus to shear modulus assuming incompressibility and plotted in log 10 -space. (b) Stress-strain curves for anterior lens capsules of different age. Stress values are calculated by normalizing load values to cross-sectional area of the test specimens. Strain values are calculated as deformation expressed in percent of the initial length of the test specimen. (a) and (b) Images taken from [48, 51].

## Iris

The iris also has a clear role on the accommodation reflex, which is an involuntary response to the accommodation stimulus. During accommodation, the iris constricts, what decreases the pupil diameter, resulting in an overall reduction in optical aberrations of the eye [52] and presumably in a DOF increase. Some subjects only constrict the iris to accommodate by reducing its optical aberrations and increasing its DOF. However, factors are not known yet. Even the company Allergo (Abbvie, US) has recently commercialised some drops that ‘increase’ your amplitude of accommodation during a short time. Those drops are intended to stimulate the iris constriction and allow accommodation to occur. Nevertheless, this is not accommodation, it is pseudoaccommodation since it is based on DOF increase.

### 1.2.4 Presbyopia

The term presbyopia derives from the greek meaning old-sight (presbys - opia). Nowadays, it is referred to the gradual age-related loss of accommodative amplitude which begins early in life and ultimately culminates in a complete loss of accommodation by about 50 years of age, see Fig. 1.10. Sometime after the age of 40, most people eventually develop presbyopia, usually signaled by a need for reading glasses or bifocal lenses. From the 50 years of age, some studies might suggest that human beings can accommodate about 1 diopters due to depth of field but the crystalline lens completely loses its ability to change its shape [53]. The aging of the lens (change in the GRIN, the geometry and the mechanical properties) is the main responsible for presbyopia [54].

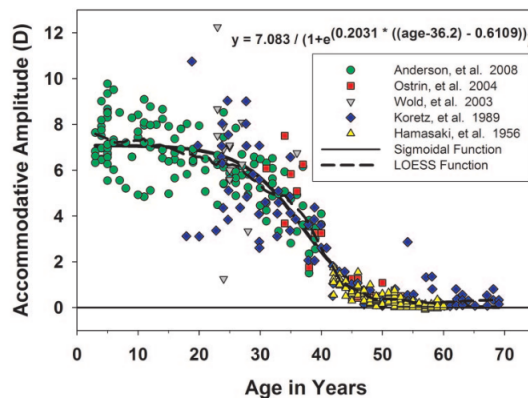


FIGURE 1.10: Maximum accommodative amplitudes for subjects pooled from the present study and four previous published studies [55–58]. Image taken from [53].

Around 1.8 billion of people are estimated to be affected by presbyopia [59]. Progressive lenses are a good option to correct presbyopia, since to date there are no surgical procedures that correct it. One of the most popular surgery approaches is the implantation of Accommodative Intraocular Lenses (AIOL) during cataract surgery. However, these solutions are not yet feasible mainly due to the lack of knowledge about the post-cataract state of accommodation.

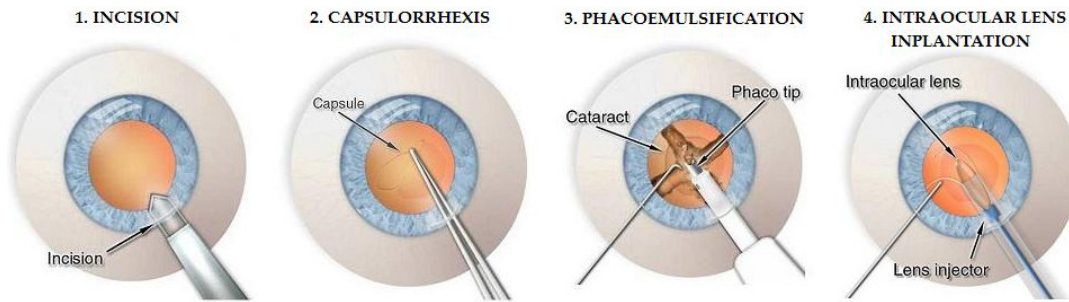


FIGURE 1.11: Cataract surgery using the phacoemulsification technique. Modified from: [www.vision-and-eye-health.com](http://www.vision-and-eye-health.com). Image taken from [60].

## 1.3 Cataracts

A cataract is the loss of lens transparency due to opacification of the lens. It is the leading cause of visual impairment and reversible blindness worldwide, being most prevalent in developing countries. Cataracts are treated by removing the opacified crystalline lens and replacing it with an intraocular lens (IOL), which is one of the most effective surgical procedures in any field of medicine. Inside cataract surgery, phacoemulsification is the gold standard procedure in developed countries while manual small incision is used frequently in developing countries. Phacoemulsification consists in emulsifying the lens with an ultrasonic handpiece and aspirating it from the eye. This aspiration is combined with irrigation of balanced salt solution to keep the intraocular pressure and maintain the anterior chamber of the eye stable.

Fig. 1.11 summarises the phases during cataract surgery. An incision of less than 2.2 mm is usually performed in the cornea. The capsulorhexis, a 5.5 mm diameter cut in the anterior lens capsule, is performed. Phacoemulsification is then applied to remove the lens. Finally, the IOL is implanted through an injector, whose main function is to deliver the IOL without any damage and without deforming the cornea.

### 1.3.1 Injectors - IOL delivery

The most common injector types are syringe and screw. The latter allows a constant insertion speed, avoiding abrupt alterations in the delivery. However, its mechanism requires the use of both hands. In contrast, syringe-type injectors can be operated using only one hand, allowing surgeons to use the other hand to secure and stabilize the eye. Their main limitation of these injectors is that the force applied needs to be manually controlled by the surgeon.

Injectors are constantly evolving to provide a better workflow to the surgeon and safely reduce the incision size. As a result, injectors with different technology are being marketed. Injectors are evaluated by measuring the force exerted in displacement tests and quantifying the final incision of the cornea after the IOL delivery [61]. Most injectors contains viscosurgical device (OVD) as a lubricating material to reduce the friction between the IOL and the cartridge of the injector.

### 1.3.2 History of Cataract Surgery

Until 1960s, the cataract (lens) was removed without a replacement, what restored the vision but resulted in a significant hyperopia caused by the absence of the lens power. To address this issue, Harold Ridley, a British ophthalmologist, had the idea of replacing the lens with an artificial lens after noticing the eye tolerance to polymethylmethacrylate (PMMA) in the eye injuries of Royal Air Force pilots.

The first IOLs were made of PMMA, a very stiff material that did not allow to manufacture foldable IOLs. Since then, IOLs have mainly evolved in design and material to perform smaller incisions in the cornea that reduce the probabilities of post-surgery complication [62]. PMMA has been widely replaced by softer materials such as hydrophilic and hydrophobic acrylates that allow to make incisions lower than 2.0 mm [62, 63].

Probably the greatest advantage of current IOLs is that in addition to restoring clarity, the refractive error (myopia, hypermyopia or astigmatism) of the patient can be corrected. The challenge remains in calculating the IOL power accurately to achieve emmetropes (no need of glasses) post-surgery. Due to the removal of the crystalline lens, the accommodative power of the lens is lost. Accommodative IOLs (AIOLs), which consists in an IOL which changes its shape during accommodation, and advanced techniques are emerging to correct also presbyopia in the cataract surgery, with no apparent result up to the moment.

### 1.3.3 Causes and Types of Cataracts

Aging is the most common cause of cataracts, however, other factors, including disease, trauma, UV radiation, chemical toxicity, genetic predisposition, etc., are also known to be associated with cataract formation [64].

There are three types of cataracts depending on the location of its opacification: nuclear, cortical, and posterior subcapsular cataracts (PSC), see Fig. 1.12, although most patients have more than one type of cataract[65].

Nuclear cataracts are the most common type and they begin with a gradual hardening and yellowing of the lens nucleus, called nuclear sclerosis [65]. Nuclear sclerosis might be caused by the agglutination of the proteins in the lens nucleus driven by age and exposure to UV light.

Cortical cataracts tends to occur more often in people with diabetes [66]. It begins in the peripheral lens in the outer cortical layers and then slowly moves inward in a spoking pattern.

Despite having spatially distinct damage phenotypes, it is thought that the failure of the lens microcirculation system to regulate cell volume in the lens cortex, or to deliver antioxidants to the lens nucleus, is a common underlying mechanism responsible for the light scattering observed in both types of cataract [67].

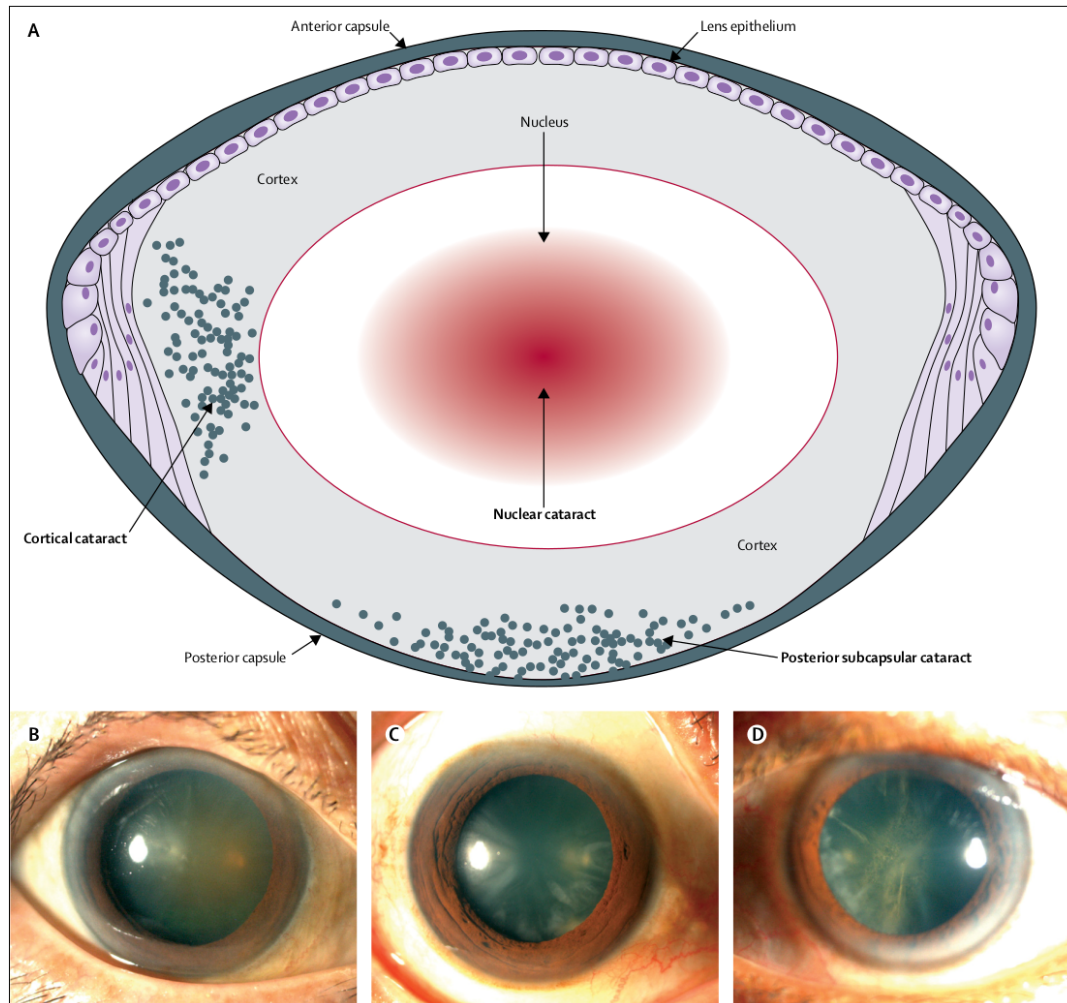


FIGURE 1.12: Characteristics of lens structures and different types of cataracts. (A) A schematic view of lens structures and corresponding types of cataracts. Slit lamp biomicroscopy photos showing (B) nuclear cataract, (C) wedge-shaped cortical cataract, and (D) subcapsular posterior cataract that has plaque opacity in the axial posterior cortical layer. Image taken from [65].

Lastly, PSC is plaque-like opacity develops in the axial posterior cortical layer. Significant symptoms may not occur until the cataract is well developed and these cataracts are commonly associated with corticosteroid use [64].

### 1.3.4 Ophthalmologic Solutions to Cataracts: IOLs

IOLs function as substitution of the crystalline lens and are housed in the capsular bag. They are formed by the haptics, which are responsible for the biomechanical stability of the IOL inside the capsular bag, and the optics, which substitute the refractive power of the crystalline lens.

## Optical design

One of the biggest benefits of IOLs is that they can correct refractive errors such as myopia, hipermyopia and astigmatism with the implated optics of the IOL, making emmetropes post-surgery (spherical equivalent  $\pm 0.5$  D and  $< 1.0$  D astigmatism are accepted values for which the blur allows independence from spectacles). There are different IOLs depending on its optical design:

- Monofocal IOLs present a fixed focus for one distance, which is usually for distance focus.
- Toric IOLs (T-IOLs) refer to astigmatism correcting IOLs [68]. These IOLs require a high-quality IOL biomechanical stability and a good placement by the surgeon.
- Multifocal IOLs (M-IOLs) achieve near and distance vision by having two (bifocal) or three (trifocal) focal points simultaneously [69]. Nevertheless, their use is under question due to the amount of patient dissatisfaction after cataract surgery (glare and halos). The concept is based on the principle that the pupil tends to constrict for near tasks, so the central portion of the lens is designed for near and the outer portion for distance.
- Extended Depth of Focus (EDOF) IOLs are an emerging alternative to multifocals IOLs. They work by creating a single elongated focal point to enhance the range of vision.

Both M- and EDOF-IOLs are considered to be pseudoaccommodative IOLs. The choice of one above the other depends on patient characteristics, i.e. dry eye, glaucoma, irregular cornea, etc.

Regardless of their optical design, there has been a wide range of IOL calculation formulas to predict IOL power [70]. However, none stands out above the rest. Different results have been obtained from different large-scale studies ( $> 10,000$  eyes): Melles et al. [71] reported a 80.8% of resulting emmetropes after cataract surgery in 18,501 eyes using Barret Universal II formula in two IOL models; Behndig et al. [72] and Lundstroem et al. [73] reported a 55% and 72.7% of emmetropes eyes in 17,056 eyes and 282,811 eyes with data taken from Swedish NCR and EUREQUO databases, respectively. Therefore, it seems that a more customisation approach using advanced optical systems should be developed in order to provide a more accurate IOL power calculation [74–78].

One of the main obstacles to accurately calculate IOL power is the post-operative effective lens position (ELP), that is the distance from the posterior cornea to the IOL. The short-term ELP depends mainly on the IOL biomechanical stability. IOL biomechanical stability depends on the shrinkage of the post-surgery cápsular bag (the cápsular bag diameter), the IOL design and the surgeon, who places the IOL inside the bag. Other factors such as the fusion footprint, associated with the connection between the anterior and posterior capsules days after cataract surgery, also influence the IOL biomechanical stability in the long-term.



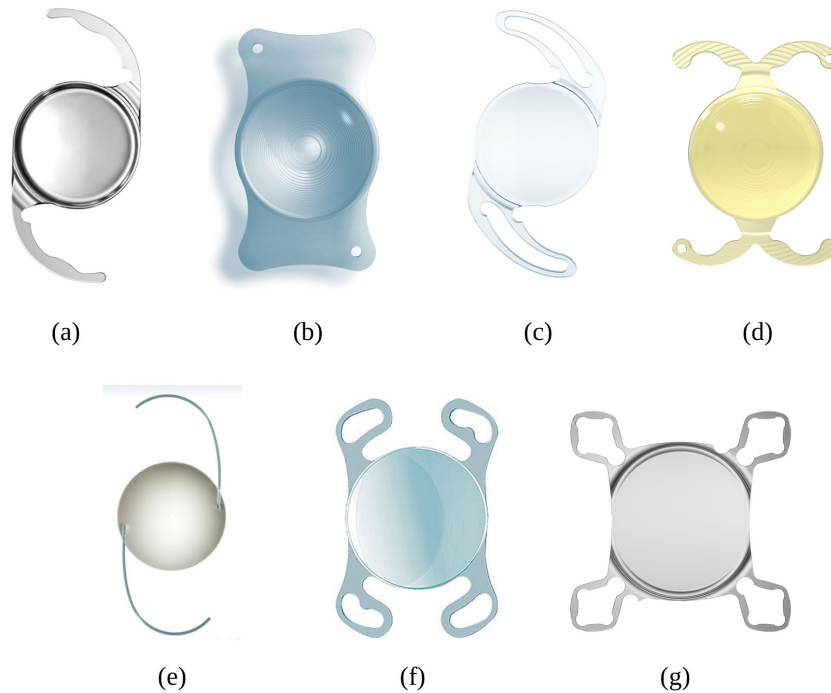


FIGURE 1.13: Different types of IOLs: (a) C-loop. (b) Plate. (c) J-loop. (d) Double C-loop. (e) C-loop with PMMA haptics. (f, g) specific plate-loop designs.

### Haptic design

The main function of haptics is to provide the proper positional stability to avoid tilt and decentration of IOL inside the capsular bag, which may affect the optical performance, particularly in multifocal [79] and toric IOL designs. There are a wide variety of IOLs depending on their haptic design, see Fig. 1.13, being the C-loop (or similar) and mono-plate designs the most common ones. It is considered that C-loop designs can provide less axial displacement due to their adaptable design to the capsular bag, whilst the mono-plate designs are robuster designs that provide lower rotation, ideal for toric IOLs [80, 81].

IOLs are usually made of hydrophobic and hydrophilic acrylic materials, that are also key factors to the mechanical stability of the IOL [82]. Hydrophobic acrylate used in IOLs is slightly stiffer than the hydrophilic material, what is considered for the IOL design.

Another factor when designing the haptic design is to assure the integrity of the IOL minimising the incision size during IOL delivery. IOLs fabricated with hydrophobic materials require a higher force and longer relaxation time injected to restore their desired shape. Both for this purpose and for testing the haptic design, numerical methods can help to avoid expensive experimental tests.

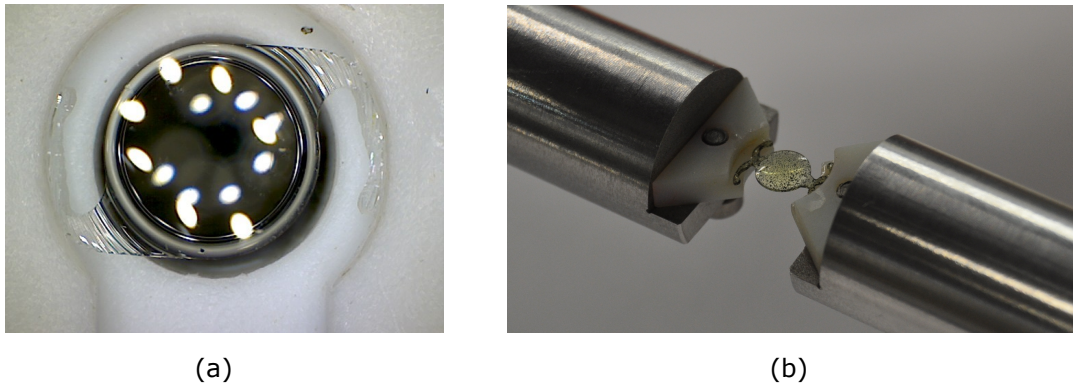


FIGURE 1.14: (a) C-loop IOL (AJL, Spain) design compressed in a well diameter of 10.00 mm. (b) POD F GF IOL design (PhysiOL, Beaver-Visitec International, USA) being compressed between two clamps. This methodology was developed in our laboratory to measure the mechanical response over a wide range of IOL compression diameters. The IOL mechanical biomarkers are measured through Digital Volume Correlation (DVC), a novel technique for full 3D strain and deformation measurements.

### Minimum Requirements prior to be Commercialised

In order to reliably predict the post-surgery optical performance, the IOLs must have strict quality and performance features. International Standard ISO 11979 defines the terms applicable to intraocular lenses and the methods to evaluate them. Inside the Standard, the two main important parts are Part 2 [83] (ISO 11979-2:2014. Optical properties and test methods) and Part 3 [84] (ISO 11979-3:2012. Mechanical properties and test methods).

ISO 11979-2:2014 [83] defines the requirements in terms of the optical performance (resolution efficiency or modulation transfer function) that the IOL must assure, whilst ISO 11979-3:2012 [84] defines the methods to test the mechanical stability of the IOL. This ISO 11979-3:2012 is mainly focused on the compression of the IOL in a well with a diameter of 10.00 mm, see Fig. 1.14. In this deformed configuration, the mechanical biomarkers that are related to the IOL optical performance (axial displacement, tilt, rotation and decentration of the IOL optics) are measured. The optics of the post-cataract eye depends on the refractive power of the cornea and the IOL. Therefore, the ELP, the axial displacement, the tilt of the IOL and the rotation directly influence the visual performance of the subject.

Some limitations of the ISO 11979-3 [84] are that rigid clamps are considered, while the capsular bag is elastic, and that only one compression diameter is required to be tested. The post-cataract capsular diameter is disperse (approximately between 9.00 and 11.00 mm) [85] and therefore the IOLs should be tested for a wider range or specific IOLs should be designed for determined ranges of compression diameters. The fatigue durability of the IOL haptics is also measured in this part. However, there has not been reports about the failure of the IOL haptic design in the long-term. Lastly, another limitation of the ISO 11979-3 [84] is that numerical methods could be considered as an additional constraint to check the feasibility of the IOL.

### 1.3.5 Post-Cataract Surgery Complications

The main difference between the two most widely used types of acrylate polymers, hydrophobic and hydrophilic, is their ability to absorb and retain water [63]. This implies that these two acrylates behave differently when implanted within the eye, leading to different post-surgery complications. Hydrophobic acrylates are associated with glistening and dysphotopsias due to their high refractive index, while the main complication related to hydrophilic acrylates are the early onset of posterior capsule opacification (PCO) [63].

PCO is the most common complication of cataract surgery and is the proliferation of lens epithelial cells (LECs) in the posterior capsular bag. It is easily treated with Nd:YAG laser capsulotomy, that consists in breaking the posterior capsule where LECs have migrated. PCO prevention is highly important as the potential post-complications of removing the posterior capsular bag are huge. IOL design and material, together with pharmacological interventions, are suggested to be the most important factors regarding the appearance of PCO [86]. A sharp square edge design is thought to reduce risk of PCO compared with round optic edge [87]. Other relatively uncommon post-cataract complications include uveitis, glaucoma, endophthalmitis, and posterior vitreous detachment (PVD).

Another possible post-surgery complication is the biomechanical stability of the IOL. The IOL can present axial displacement, tilt or rotation in the capsular bag due to a bad alignment of the surgeon or because post-cataract capsular bag diameter is too small for the IOL haptic design. These problems usually occur hours or few days after the surgery and a new intervention is needed to place the IOL properly. The biomechanical stability of the IOL can worsen with time because of the shrinkage of the capsular bag [88] or by the fusion footprint associated with connection between the anterior and posterior capsules days after cataract surgery [85]. Small geometrical changes can hugely affect the visual performance of the subject.

There are several methods to measure IOL axial displacement, decentration and tilt once the IOL is implanted inside the pseudophakic eyes. These include slit lamp assessment [89], Scheimpflug imaging [90], optical coherence tomography [91], and measurements using Purkinje reflections [92].

## 1.4 Motivation

Presbyopia and cataracts are the two most common crystalline lens diseases. Presbyopia is the gradual loss of the accommodation amplitude of the eye, i.e., the ability to focus on near objects, and is caused by the aging of the crystalline lens. Although the amplitude of accommodation decreases with age from a very early age [53], it begins to affect near visual tasks around 40 years until around 55 years, when there is little to no accommodative ability [55]. In 2015, the global prevalence of presbyopia was estimated to be around 1.09-1.8 billion [59, 93]. Presbyopia affects to 100% of the people, although the prevalence slightly differs depending on the age and population [94].

On the other hand, cataracts is the clouding or the loss of transparency of the lens that leads to a decrease in vision. Cataracts is estimated to affect 95 million people worldwide [65], being the most frequently performed surgical procedure in many economically developed countries. Moreover, the number of cataract blind people will reach 40 million in 2025 according to the World Health Organization (WHO) [95], remaining the leading cause of blindness in developing countries. Even the number of people who develop cataracts is expected to become even bigger as life expectancy increases and people live longer. The only way to treat cataracts is by surgery, which consists in substituting the opacified crystalline lens by an intraocular lens (IOL).

### 1.4.1 Potential Tools for Understanding Presbyopia and Cataracts

Numerical methods give us the possibility to create high-fidelity simulations. These simulations have the ability to predict events or give us certain information that we cannot physically know, helping us to deepen in diverse phenomena. One of the leading numerical methods for complex problems is the Finite Element Method (FEM), which consists in solving partial differential equations (PDEs) in discrete domains, which are discretised by means of elements (hence its name). These PDEs capture the physics of the problem on which the simulation is based.

FEM was initially used to calculate structural problems. However, due to its potential to model endless different engineering problems, its use has been widespread throughout the biomedical field, from explaining orbit blast injury mechanisms [96] up to evaluation of the cornea biomechanics after intrastromal ring surgery [97] and explaining lens mechanics [98, 99].

One of the disadvantages of FEM is the excessive computational time in complex problems (non-linear geometry, behaviour or contact between solids), which makes it inadequate for clinical practice. One of the alternatives is the use of Artificial Intelligence (AI), which allows to comprise and calculate complex information in real-time [100, 101].

For these reasons, this thesis has used the potential of the FEM and AI both to explore and further understand presbyopia and cataracts and to bring numerical methods closer to the clinical practice.

### 1.4.2 Open Questions

This thesis attempts to answer the following six questions where numerical methods are indispensable as they could not be addressed experimentally due to either economical reasons or actual feasibility with current methods.

- Could a numerical model be developed to reproduce the mechanism of accommodation proposed by Helmholtz? This model could be used to definitively understand the accommodation process and serve as a role model for possible advanced ophthalmic solutions in presbyopia and cataracts.
- There are several FE models trying to simulate ex-vivo stretching tests of the lens. However, there is an overall lack of understanding about the lens mechanics due to the complexity of the problem. It is common to establish simplifying hypotheses or make wrong physiological assumptions that lead to no conclusions. Therefore, it is important to address this problem to conclude the governing factors (mechanical properties, zonular arrangement, lens geometry, etc.) on how the lens changes its shape to further understand presbyopia.
- IOLs need to follow some standards [83, 84] prior to be market commercialised. There is a numerical trend to add numerical models to support certain regulations. These standards could be numerically performed, saving costs and time in the pre-design phase.
- How does the haptic design affect the IOL biomechanical stability? Is a haptic design customisation needed?
- There is not a predictive study about the biomechanical stability of IOLs inside the capsular bag. Some numerical methodologies could help customise IOL haptic design according to patient characteristics (capsular bag shrinkage, material properties), significantly improving patient satisfaction after cataract surgery.
- Incision size is directly related to the success of cataract surgery. How small can an incision be made in the eye, or rather, how much can an IOL be folded without compromising its structure?

### 1.4.3 Goals of this Thesis

The thesis is divided into three main goals: I) the numerical study of the mechanism of accommodation; II) the analysis of the biomechanical stability of intraocular lenses (IOLs); and III) the evaluation of IOL delivery during cataract surgery. In turn, There are some specific goals in each objective.

The specific goals in the study of the mechanism of accommodation are:

- To develop a high-fidelity simulation of the mechanism of accommodation.
- To analyse the lens mechanics based on the lens geometry, lens mechanical properties, lens capsule thickness and stiffness gradient.
- To study the mechanical causes of presbyopia.

The specific goals in the methodology to test IOL haptic design are:

- To test and numerically evaluate the haptic design in intraocular lenses following the compression standard tests ISO 11979-3:2012 [84].
- To propose a methodology to create patient-specific haptic design solutions based on neural networks.
- To develop a high-fidelity simulation that predicts the IOL position inside the capsular bag in the short-and long-term.

The specific goals in the evaluation of the force exerted in IOL delivery are to experimentally evaluate the following factors:

- IOL haptic design, IOL thickest area and IOL material.

#### 1.4.4 Justification of the Thematic Unit of the Thesis

Given the worldwide importance of these two lens-diseases, presbyopia and cataracts, this thesis is focused on further understanding presbyopia and developing novel methodologies for testing intraocular lenses. Fig. 1.15 summarises the investigations performed during this thesis all-related with the crystalline lens.

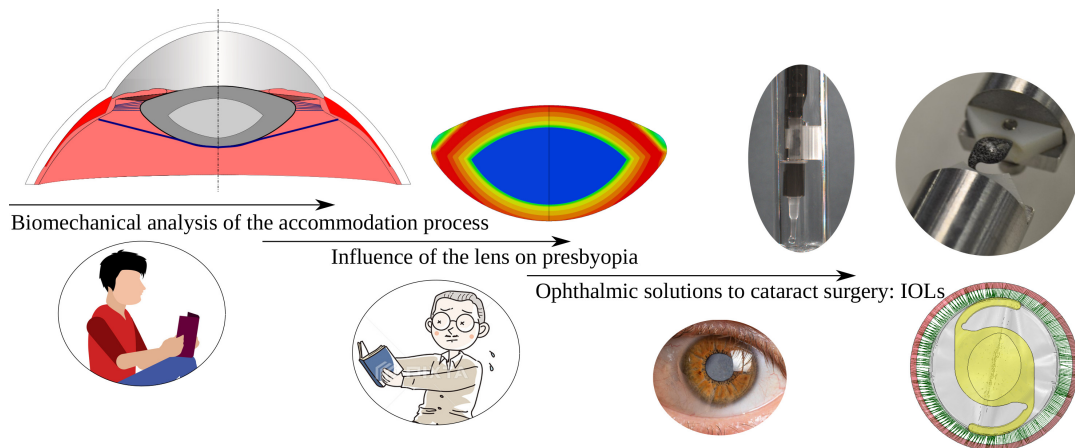


FIGURE 1.15: The first part of this thesis focuses on developing high-fidelity simulations of the mechanism of accommodation and analysing the influence of the crystalline lens on presbyopia comparing the lens mechanical properties with age. Then, a numerical and experimental methodology to test the biomechanical stability of IOLs and the force exerted in IOL delivery is presented in this thesis.

## 1.5 Structure

This thesis is presented as a compendium of nine research articles, which have been grouped in three chapters. The thesis is organised by chapters as follows:

- **Chapter 1: Introduction** initially gives a state of the art about the relevant topics of this thesis: the mechanism of accommodation, presbyopia, cataracts and its ophthalmic solutions, IOLs. Then, the motivation, open questions and goals of this thesis are presented.
- **Chapter 2: Biomechanical analysis of the Mechanism of Accommodation** explores the lens mechanics and the ciliary muscle movement through high-fidelity simulations of the accommodation process and ex-vivo stretching tests.
  1. Cabeza-Gil et al. A validated finite element model to reproduce Helmholtz's theory of accommodation: a powerful tool to investigate presbyopia [1].
  2. Cabeza-Gil et al. A numerical investigation of changes in lens shape during accommodation [2].
- **Chapter 3: Numerical Methodology to test the Biomechanical Stability of IOLs** provides an extensive methodology to test the haptic design of IOLs. It includes the mechanical characterisation of acrylates used in IOLs needed to perform the simulations, the validation of the FE model of the compression standards tests, the correlation between the mechanical biomarkers of IOLs and the visual performance, the in-vivo evaluation of three IOLs, a patient-specific methodology for the customisation of the haptic design and a high-fidelity simulation of the IOL position inside the post-cataract capsular bag.
  1. Cabeza-Gil et al. Mechanical characterisation of hydrophobic and hydrophilic acrylates used in intraocular lenses through depth sensing indentation [3].
  2. Cabeza-Gil et al. Effect of haptic geometry in C-loop in intraocular lenses on optical quality [4].
  3. Cabeza-Gil et al. Systematic Study on the Biomechanical Stability of C-loop Intraocular Lenses: Approach to an Optimal Design of the Haptics [5].
  4. Remon et al. Biomechanical Stability of Three Intraocular Lenses With Different Haptic Designs: In Silico and In Vivo Evaluation [6].
  5. Cabeza-Gil et al. Customised Selection of the Haptic Design in C-loop Intraocular Lenses Based on Deep Learning [7].
  6. Cabeza-Gil, I. & Calvo, B. Predicting the biomechanical stability of IOLs inside the post-cataract capsular bag with a finite element model.
- **Chapter 4: Evaluation of IOL delivery** evaluates through one study the force exerted by different kind of IOLs for different injection sizes.
  1. Cabeza-Gil et al. Experimental evaluation of the injection force exerted in intraocular lens delivery with syringe-type injectors [8].
- **Chapter 5: Discussion** gives a summary of achievements and conclusions of this thesis, and gives an outlook on possible future work.
- **Chapter 6: Other Activities during the Ph.D. Period 2019-2022** gives a summary of the congresses, research stays, previous works and funding of this thesis.





## Chapter 2

# Biomechanical Analysis of the Mechanism of Accommodation

Two different numerical studies address the study of accommodation and the lens mechanics with age, achieving similar conclusions.

1. **Work 1 (W1). Cabeza-Gil et al. [1]** provides a high-fidelity simulation of the mechanism of accommodation and analyses the ciliary muscle movement as well as the influence of each part of the crystalline lens with age.
2. **W2. Cabeza-Gil et al. [2]** analyses the change in lens shape for different mechanical properties of the nucleus, cortex and capsule through ex-vivo lens stretching tests.

### 2.1 Work 1: A validated finite element model to reproduce Helmholtz's theory of accommodation: a powerful tool to investigate presbyopia



Cabeza-Gil I., Grasa J. and Calvo B.  
 Ophthalmic & Physiological Optics  
 JIF (2020) = 3.12 (Q2: 23/62 Ophthalmology)  
 SJR (2020) = 1.15 (Q1: 26/120 Ophthalmology)

# A validated finite element model to reproduce Helmholtz's theory of accommodation: a powerful tool to investigate presbyopia

Iulen Cabeza-Gil<sup>1</sup>  | Jorge Grasa<sup>1,2</sup> | Begoña Calvo<sup>1,2</sup>

<sup>1</sup>Aragón Institute of Engineering Research (i3A), University of Zaragoza, Zaragoza, Spain

<sup>2</sup>Bioengineering, Biomaterials and Nanomedicine Networking Biomedical Research Centre (CIBER-BBN), Zaragoza, Spain

## Correspondence

Iulen Cabeza-Gil, Aragón Institute of Engineering Research (i3A), University of Zaragoza, Zaragoza, Spain.  
Email: iulen@unizar.es

## Funding information

Ministerio de Ciencia, Innovación y Universidades, Grant/Award Number: DPI2017-84047-R

## Abstract

**Purpose:** To reproduce human in vivo accommodation numerically. For that purpose, a finite element model specific for a 29-year-old subject was designed. Once the proposed numerical model was validated, the decrease in accommodative amplitude with age was simulated according to data available in the literature.

**Methods:** In contrast with previous studies, the non-accommodated eye condition was the reference configuration. Consequently, two aspects were specifically highlighted: contraction of the ciliary muscle, which was simulated by a continuum electro-mechanical model and incorporation of initial lens capsule stresses, which allowed the lens to become accommodated after releasing the resting zonular tension.

**Results:** The morphological changes and contraction of the ciliary muscle were calibrated accurately according to the experimental data from the literature. All dynamic optical and biometric lens measurements validated the model. With the proposed numerical model, presbyopia was successfully simulated.

**Conclusions:** The most widespread theory of accommodation, proposed by Helmholtz, was simulated accurately. Assuming the same initial stresses in the lens capsule over time, stiffening of the lens nucleus is the main cause of presbyopia.

## KEYWORDS

accommodative change, finite element method, human eye accommodation, lens shape, presbyopia

## INTRODUCTION

Accommodation is a dynamic change in the dioptric power of the eye that allows a change in focus from distant to near objects. This process is achieved by changing the shape of the lens, following contraction of the ciliary muscle, thereby releasing the zonular tension around the lens equator, according to the widely accepted accommodation theory of

Helmholtz.<sup>1</sup> Numerous authors have confirmed this theory over time, including Fincham,<sup>2</sup> who demonstrated the ability of the elastic lens to round up after the release of zonular tension, and Glasser and Kaufmann,<sup>3</sup> who showed relaxation of the zonules due to ciliary muscle contraction along with other investigators.<sup>4</sup>

The ciliary muscle is the engine that drives the accommodation process. It consists of three groups of muscle fibres (i.e., longitudinal, radial and circular), although their

This is an open access article under the terms of the Creative Commons Attribution License, which permits use, distribution and reproduction in any medium, provided the original work is properly cited.

© 2021 The Authors. *Ophthalmic and Physiological Optics* published by John Wiley & Sons Ltd on behalf of College of Optometrists.

division is somewhat arbitrary. There is a gradual transition from the outermost longitudinal muscle fibres through the radial fibres to the innermost circular muscle fibres, with some intermingling of the different fibre types.<sup>4-6</sup> Contraction of the entire ciliary muscle as a whole pulls the anterior choroid forward, moving the apex of the ciliary processes towards the lens equator, and serves the primary function of releasing resting zonular tension at the lens equator to allow accommodation.<sup>4,5</sup> During contraction of the ciliary muscle, the circular portion of the ciliary muscle tends to increase in thickness, whilst the radial and longitudinal portions decrease in thickness.

The crystalline lens is the ocular element that alters the focal length of the eye. During accommodation, the human lens undergoes several changes: its diameter decreases, its thickness increases, the anterior and posterior surfaces of the lens move anteriorly and posteriorly, respectively and the curvatures of the anterior and posterior surfaces of the lens increase. Moreover, the thickness of the lens nucleus increases, but without a significant change in thickness of the cortex.<sup>4,7</sup> Several authors have designed finite element (FE) models to explain and understand accommodation.<sup>8-15</sup> However, most of these biomechanical models are based on accommodated geometry, and reproduced the accommodation process in reverse by applying the forces exerted by the relaxation of the ciliary muscle to reach the non-accommodated state. These FE models are a powerful tool to understand the opto-mechanical crystalline lens changes. However, *in vivo* accommodation cannot be reproduced faithfully through these tests, and thus some key aspects of accommodation which involves other tissues (ciliary muscle, sclera) cannot be analysed properly. In contrast to these previous studies, the reference configuration of our FE model is the non-accommodated state, which is the resting state of the physiological system.

We propose a 3-dimensional FE model that incorporates contraction of the ciliary muscle to reproduce *in vivo* human accommodation. This FE model is standardised for a 29-year-old subject as there is sufficient comparative and physiological data in the literature to develop the model and evaluate it with experimental data. Ciliary muscle contraction is simulated with an electro-chemical-mechanical continuum model.<sup>16,17</sup> Moreover, to allow the lens to change its shape after release of zonular tension, the initial stresses of the lens capsule are included in the model.

The proposed FE model was validated by comparison with the experimental optical and main biometric changes during human *in vivo* accommodation provided by Ramasubramanian and Glasser.<sup>18,19</sup> To achieve this aim, the ciliary muscle contraction was calibrated by comparing the morphological changes with the recent work of Wagner *et al.*,<sup>20</sup> who evaluated ciliary muscle thickness (CMT) profiles derived from optical coherence tomography (OCT) images during *in vivo* human accommodation.

With the proposed FE model, the physiological decrease in accommodation amplitude with age was evaluated and compared with experimental data.<sup>21-23</sup> A sensitivity

### Key Points

- A novel finite element model that reproduces ocular accommodation is presented. The decrease in accommodative amplitude with age was reproduced using the proposed model.
- The main cause of presbyopia is the stiffening of the lens nucleus with age.
- The numerical model can help to understand human accommodation.

analysis of the mechanical properties of the crystalline lens as a function of age was performed to observe the most influential mechanical factors in the development of presbyopia.<sup>24-26</sup>

Justification of the geometry and the 3-dimensional FE model are presented in the Method section, followed by a description of the constitutive laws of all materials involved, including the formulation of the active behaviour of the ciliary muscle and the mechanical properties used to analyse the decrease in accommodation amplitude with age. Methodology is provided to analyse the optical and biometric changes during accommodation. The results of these changes are presented together with some calibration parameters of the muscle activation. Once the ciliary muscle is engaged, it is coupled with the accommodation system to simulate the change in shape of the lens, and thus the refractive power change. An analysis of the decrease in accommodation amplitude with age is shown.

## MATERIALS & METHODS

### Finite element model

To obtain the most realistic representation possible, this model of the accommodation system comprises the most relevant components in the accommodation process: the shell of the eye composed of the cornea and sclera; iris; lens nucleus, cortex and capsule; zonules of Zinn divided into anterior and equatorial zonules and the ciliary body, which is composed of the ciliary muscle and processes.

Figure 1 shows the dimensions of the different components of the FE model in the non-accommodated state standardised for a 29-year-old subject. Lens dimensions were obtained from the OCT study of Chang *et al.*,<sup>27</sup> with a radius of curvature of the anterior ( $r_a$ ) and posterior ( $r_p$ ) lens surfaces of 11.00 and 6.10 mm, respectively, sagittal thickness of the lens ( $T_L$ ) of 3.44 mm and an anterior chamber depth (ACD) of 3.03 mm. As the lens equatorial diameter cannot be obtained by OCT, it was extracted from the MRI work of Kasthurirangan *et al.*<sup>29</sup> with the value of 9.04 mm being obtained. The anterior and posterior thickness of the lens cortex were 0.80 mm and 0.50 mm, respectively, with

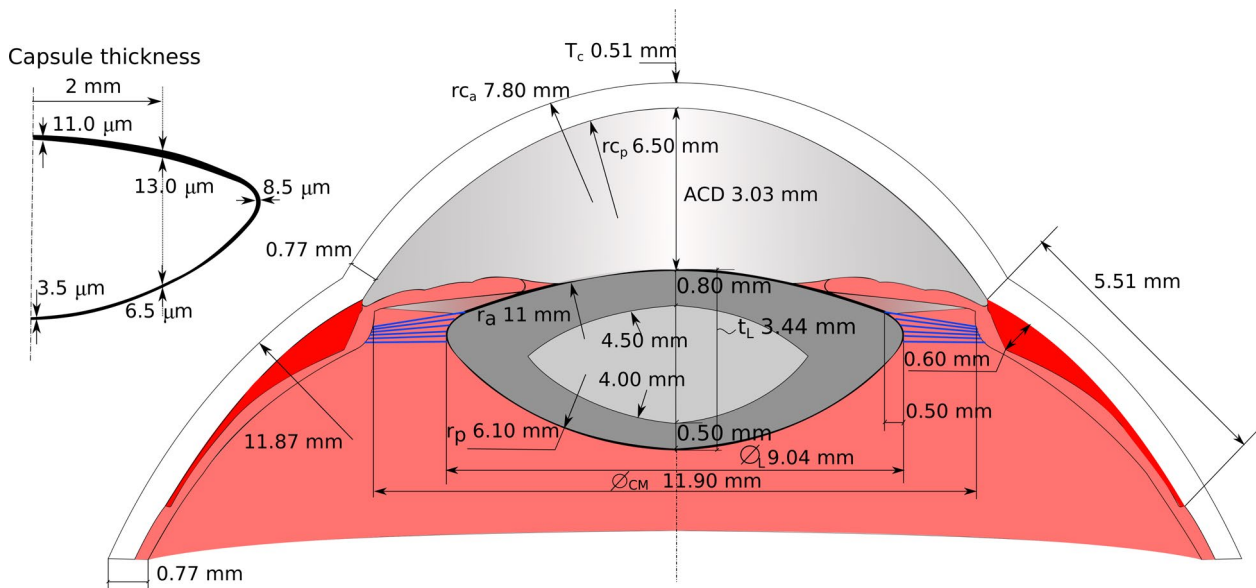


**FIGURE 1** Dimensions of the finite element (FE) model. It includes the lens, the zonules of Zinn (blue), the ciliary muscle (red), the iris and ciliary processes (light pink) as well as the sclera and cornea (white). A detailed view reflecting capsule thickness is shown on the left. Due to the lack of available data in the literature, the thickness distribution of the lens capsule used was taken from a 36-year-old subject<sup>28</sup>

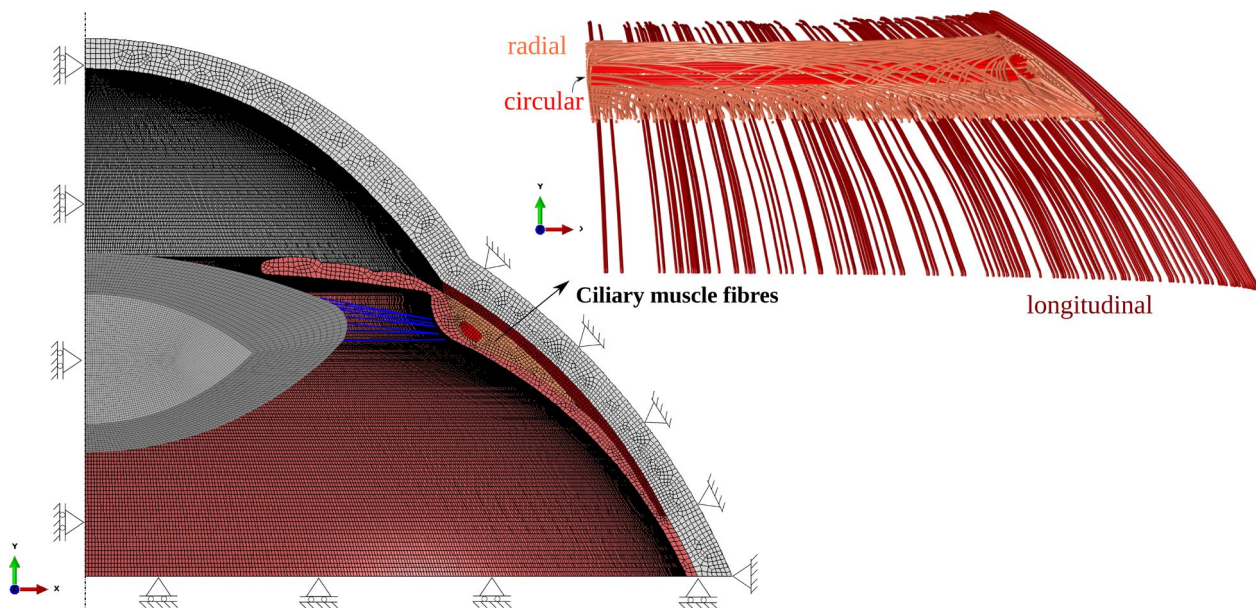


**FIGURE 2** 3D finite element (FE) model of the accommodative system: lens, zonules, ciliary muscle, iris, sclera and cornea. The arrangement and orientation of the ciliary muscle fibres, longitudinal (yellow), radial (orange) and circumferential (red), is shown on the right. The FE model contained 402,373 elements

an anterior and posterior surface radius of curvature of 4.50 and 4.00 mm, respectively.<sup>30,31</sup> Zonules were anchored 0.50 mm in the anterior capsule based on Bernal *et al.*,<sup>32</sup> and the ciliary body ring diameter was 11.90 mm.

The averaged ciliary muscle geometry of emmetropic eyes reported by Wagner *et al.*<sup>20</sup> was used in our model. In their study, the geometry was provided by a CMT profile, which was obtained from OCT images following the methodology of Straßer *et al.*<sup>33</sup> Therefore, an in-house code in

MATLAB 2020b (MathWorks, mathworks.com) with the inverse methodology<sup>33</sup> was created and implemented to obtain the geometry from the CMT profile.

The ciliary muscle was arranged into three families of muscle fibres, i.e., circular, radial and longitudinal, according to the distribution reported by Pardue and Sivak.<sup>6</sup> The volume percentage of the circular, radial and longitudinal muscle fibres is 12%, 33% and 55% respectively, and their distribution is shown in Figure 2.

Considering that the material model allows only one preferential direction, the orientation of the radial fibres was defined as a transition from the circular to the longitudinal fibres; see *Figure 2*.

Regarding the iris, a trabecular-iris angle of  $40^\circ$  and a thickness at  $750\ \mu\text{m}$  from the scleral spur of  $0.40\ \text{mm}$  were considered for visual effects since its contraction was not considered.<sup>34,35</sup> Finally, the shell of the eye was designed according to the Le Grand<sup>36</sup> model. The thickness of the sclera and cornea were readjusted for a 29 year old subject<sup>37</sup>; see *Figure 1*.

Considering all the above-mentioned factors regarding the geometry, a 3-dimensional FE mesh of the anterior half of the ocular globe was designed. Due to the symmetry, only a quarter of the geometry was considered, ensuring the corresponding symmetry boundary conditions. Axial displacements were restrained at the bottom scleral surface. Moreover, the exterior surfaces of the sclera were fixed by the extraocular muscles. The general-purpose finite element code Abaqus FEA version 14.1 (Simulia, 3ds.com) was used to build the FE model. A mesh sensitivity analysis was performed in order to establish the final mesh size; see *Figure 2*. The lens nucleus and cortex were considered solid bodies and were meshed with 96,640 hybrid linear hexahedral (C3D8H) elements; the capsule was meshed with 5290 4-node membrane (M4) elements; 546 zonules were modelled using Abaqus connector elements, whose nonlinear behaviour is explained below; the ciliary muscle was meshed with 94,809 linear hexahedral (C3D8) elements and the ciliary body was meshed with 201,110 C3D8 elements and 3978 linear wedge (C3D6) elements.

The fluids filling the eye, namely the aqueous and vitreous humours, were not included in the model as we considered that there is a homogeneous pressure inside the eye during accommodation. Due to the boundary conditions applied in the sclera, the eyeball structure is stable.

## Material behaviour

### Ciliary muscle

The process of smooth muscle contraction can be initiated by mechanical, electrical or chemical stimuli. The contractile mechanism involves several signal transduction pathways, all of which converge to increase the intracellular calcium concentration, resulting in phosphorylation of myosin.<sup>38</sup> Regarding the ciliary muscle, the action of the neurotransmitter acetylcholine on post-synaptic muscarinic receptors controls muscle activation. This system forms part of the parasympathetic branch of the autonomic nervous system. On the other hand, an inhibitory effect is driven by the sympathetic system, which is mediated principally by the action of the neurotransmitter noradrenaline on  $\beta_2$  receptors.<sup>39</sup>

In this work, the passive and active finite strain response of the ciliary muscle was simulated within the framework of continuum mechanics using a common methodology based on postulating the existence of a strain energy density function (SEF).<sup>16,17</sup> This function depends on a series of state variables related to the deformation of the active and passive elements, the contraction level and the muscle fibre arrangement:

$$\Psi = \Psi(\mathbf{C}, \mathbf{C}_e, \lambda_a, \mathbf{N}). \quad (1)$$

$\mathbf{C} = \mathbf{F}^T \mathbf{F}$  is the right Cauchy–Green deformation tensor with  $\mathbf{F}$  the deformation gradient.  $\mathbf{C}_e$  is an equivalent deformation tensor associated with the deformation of the elastic components in the muscle, and it arises from a two-step formulation of the contraction process.<sup>16</sup> From this formulation, a decomposition of the strain deformation gradient is proposed as  $\mathbf{F} = \mathbf{F}_e \mathbf{F}_a$ . Therefore, the elastic deformation gradient can be defined as  $\mathbf{C}_e = \mathbf{F}_e^T \mathbf{F}_e$ .  $\lambda_a$  is the contraction or stretch of the active component of the muscle fibres that forms the active strain deformation gradient  $\mathbf{F}_a$  assuming

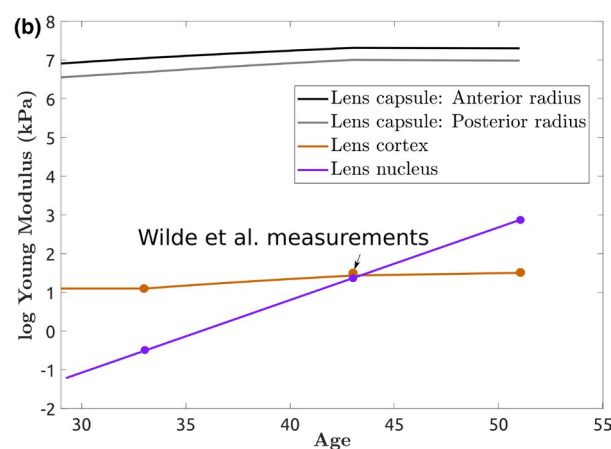
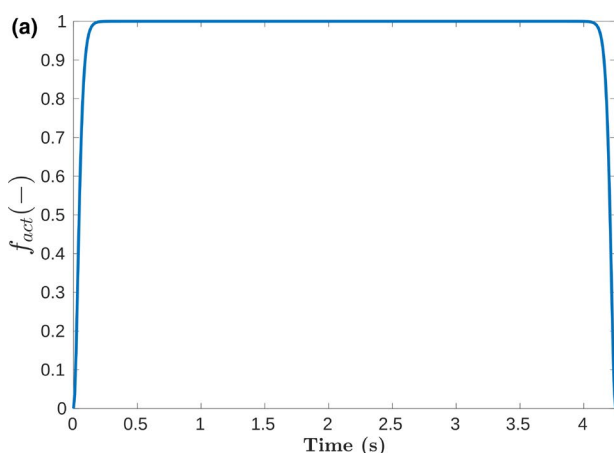


**FIGURE 3** (a) Activation function of the ciliary muscle and (b) mechanical properties of the crystalline lens used in this study. There is a circle in the lens nucleus and cortex plot indicating the values reported by Wilde *et al.*<sup>26</sup> The mechanical properties of the lens capsule were characterised by Krag and Andreassen<sup>41,42</sup>

incompressibility.<sup>16</sup> The structural tensor  $\mathbf{N} = \mathbf{n}_0 \otimes \mathbf{n}_0$  defines the anisotropy of the muscle due to the direction of muscular fibres  $\mathbf{n}_0$ .

The SEF is decoupled into volume-changing and volume-preserving parts in order to handle the quasi-incompressibility constraint. Furthermore, the deviatoric part is divided into a passive contribution due to the collagen and elastin,  $\bar{\Psi}_p$ , and an active contribution associated with the muscular fibres,  $\bar{\Psi}_a$ . Thus, the total strain energy function  $\Psi$  can be expressed as follows:

$$\Psi = \Psi_{vol}(J) + \bar{\Psi}_p(\bar{\mathbf{C}}, \mathbf{N}) + \bar{\Psi}_a(\bar{\mathbf{C}}_e, \bar{\lambda}_a, \mathbf{N}), \quad (2)$$

where the relations  $\bar{\mathbf{C}} = J^{-2/3}\mathbf{C}$ ,  $\bar{\mathbf{C}}_e = J^{-2/3}\mathbf{C}_e$  and  $\bar{\lambda}_a = J^{-1/3}\lambda_a$  have been applied with  $J = \det(\mathbf{F})$  being the Jacobian of the transformation. Equation 2 can be particularised for the behaviour of the ciliary muscle and formulated in a more proper way for computational purposes as:

$$\Psi = \Psi_{vol}(J) + \bar{\Psi}_p(\bar{I}_1, \bar{I}_2, \bar{I}_4) + f_\lambda f_{act} \bar{\Psi}'_a(\bar{J}_4). \quad (3)$$

where  $f_\lambda$  is the force-stretch relationship that account for the actin and myosin overlap,  $f_{act}$  is the activation function and  $\bar{\Psi}_a$  is the active SEF. The passive SEF,  $\bar{\Psi}_p$ , is defined as a function of the invariants of the isochoric right Cauchy-Green tensor:

$$\bar{I}_1 = \text{tr}\bar{\mathbf{C}}, \quad \bar{I}_2 = \frac{1}{2}((\text{tr}\bar{\mathbf{C}})^2 - \text{tr}\bar{\mathbf{C}}^2), \quad \bar{I}_4 = \mathbf{n}_0 \cdot \bar{\mathbf{C}}\mathbf{n}_0 = \bar{\lambda}^2, \quad (4)$$

where  $\bar{I}_1$  and  $\bar{I}_2$  are the first and second modified strain invariants and  $\bar{I}_4$  is the invariant related to the anisotropy of the passive response. According to the SEF proposed by Calvo *et al.*,<sup>40</sup> the passive response  $\bar{\Psi}_p$  can be written:

$$\bar{\Psi}_p = c_1(\bar{I}_1 - 3) + \frac{c_3}{c_4}(e^{c_4(\bar{I}_4 - \bar{I}_{40})} - c_4(\bar{I}_4 - \bar{I}_{40}) - 1). \quad (5)$$

The active SEF,  $\bar{\Psi}_a$ , associated with the active response, and consequently with the actin-myosin interaction, is expressed as the product of two functions that scale the energy stored due to contraction in the elastic element  $\bar{\Psi}'_a$ .<sup>16</sup> The influence of filament overlap on the active response of the muscle  $f_\lambda$  is formulated in terms of the muscle fibre stretch  $\lambda_a$ , the optimum stretch  $\lambda_{opt}$  and the coefficient  $\xi$ :

$$f_\lambda = e^{-\frac{(\lambda_a - \lambda_{opt})^2}{2\xi^2}}. \quad (6)$$

The activation function  $f_{act}$  is assumed to represent the excitation input signal that triggers the contraction independently of its origin. In this work, the product of two squared hyperbolic tangents has been selected as:

$$f_{act} = (\tanh^2(s_1(t - t_i))\tanh^2(s_2(t - (t_i + t_s)))), \quad (7)$$

where  $s_1$  and  $s_2$  regulate the initial and final slope of the function, respectively,  $t$  is the time variable, and  $t_i$  and  $t_s$  define the

start of the activation and the stimulus duration, respectively. *Figure 3a* shows the activation function used in the study. The energy stored in the cross-bridges is expressed in terms of the invariant associated to  $\bar{\mathbf{C}}_e$  in the direction of the muscle fibres  $\mathbf{n}_0$ :

$$\bar{\Psi}'_a = \frac{1}{2}P_0(\bar{J}_4 - 1)^2, \quad \bar{J}_4 = \mathbf{n}_0 \cdot \bar{\mathbf{C}}_e\mathbf{n}_0 = \bar{\lambda}_e^2. \quad (8)$$

where  $P_0$  is a proportionality factor related to the maximum active stress due to muscle contraction.<sup>16</sup>

Due to the non-recoverable deformation that occurs in the active part of the muscle fibres (its initial shape is only recovered with the help of the elastic components), the model incorporates a dissipation energy rate associated with active stresses and strains.<sup>16</sup> Using the second law of thermodynamics in the shape of the Clausius-Planck inequality and neglecting the thermal dissipation rate, some of the power produced internally is stored while another portion is dissipated.<sup>16</sup> From this expression, two constitutive relationships can be derived. The first one is used to obtain the classical relation between the derivative of the so-called strain energy density function with respect to the elastic strain tensor and the second the Piola-Kirchhoff stress tensor. The second relationship allows establishment of the evolution of the contraction velocity  $\dot{\lambda}_a$  as a function of the same strain energy and stresses<sup>16</sup>:

$$P_a - \frac{\partial \bar{\Psi}}{\partial \lambda_a} + \left( 2\bar{\mathbf{C}}_e \frac{\partial \bar{\Psi}}{\partial \bar{\mathbf{C}}_e} \mathbf{F}_a^{-T} \right) : \frac{\partial \bar{\mathbf{F}}_a}{\partial \lambda_a} = C \dot{\lambda}_a, \quad (9)$$

where  $P_a = -\tilde{\nu}P_0f_\lambda f_{act}$  is the active stress, with  $\tilde{\nu}$  being a friction parameter that considers the relative sliding speed between actin and myosin. The parameter  $C$  is defined as:

$$C = \frac{1}{v_0}P_0f_\lambda f_{act}, \quad (10)$$

where  $v_0$  is associated with the initial contraction velocity. A set of preliminary analyses, explained in the Results section, was performed to obtain the parameters  $P_0$  and  $v_0$  of the active behaviour of the ciliary muscle; see *Tables 1* and *2*.

## Constitutive laws of the remaining tissues

The whole lens was modelled with an elastic behaviour. The lens capsule was modelled via membrane elements, assuming pure traction behaviour. In turn, the lens capsule was divided into anterior and posterior regions, characterising their mechanical properties differently based on the work of Krag and Andreassen,<sup>41,42</sup> see *Table 3*.

In contrast with those of the lens capsule, the mechanical properties of the lens nucleus and cortex are unclear and somewhat controversial. Burd *et al.*<sup>43</sup> reported that Fisher's<sup>24</sup> spinning lens measurements might not be

TABLE 1 Parameters of the active behaviour of the continuum model adapted for the smooth ciliary muscle

Active behaviour								
$\lambda_{opt} (-)$	$\xi (-)$	$t_s$	$t_i$	$s_q$	$s_2$	$P_0 (MPa)$	$\nu_0 (-)$	$\bar{\nu} (-)$
1.00	0.16	4.25	0.00	20.00	20.00	1.50	0.90	0.59

TABLE 2 Parameters of the passive behaviour of the ciliary muscle

Passive behaviour			
$c_1 (kPa)$	$c_3 (kPa)$	$c_4 (-)$	$I_0 (-)$
8.37	9.87	2.23	1.25

TABLE 3 Mechanical properties of the different tissues of the FE model for the subject of 29 years old

	$E (kPa)$	$\nu (-)$	$C_1 (kPa)$	$D_1 (kPa^{-1})$	References
Nucleus	0.30	0.49	-	-	25,26
Cortex	3.00	0.49	-	-	25,26
Anterior capsule	1000	0.49	-	-	41,42
Posterior capsule	700	0.49	-	-	41,42
Sclera	-	-	102.73	89.71	46
Cornea	-	-	222.64	194.13	47
Ciliary processes	-	-	0.80	0.70	48

Note: The lens was modelled through an elastic behaviour (Young modulus), whilst the remaining parts of the accommodative system were modelled with a neo-Hookean hyperelastic model.

reliable, and relatively few subsequent studies regarding the mechanical properties of the internal lens have been performed,<sup>25,26,44</sup> with slight differences being observed between them. We determined the values reported by Wilde *et al.*,<sup>26</sup> taking into account the stress-strain relationship  $E = 3G$ , with  $G$  being the shear modulus, can be considered for isotropic elastic linear and incompressible materials. Due to the lack of data, we extrapolated values from a 33-years-old lens to a 29-years-old one; see Figure 3b.

The cornea, sclera and ciliary processes were modelled through an isotropic, quasi-incompressible Neo-Hookean hyperelastic model. The material properties for the 29-year-old subject were chosen from the data available in the literature, as displayed in Table 3.

The zonules were modelled with linear connector elements as Helmholtz's accommodation theory postulates,<sup>1,2</sup> i.e., they are stretched in the non-accommodated state, which is the reference configuration. This was considered as an initial force value  $F_0$  in the force-displacement equation that defines their behaviour:

$$F(u) = F_0 + ku, \quad (11)$$

with  $F_0 = 50$  mN,  $k = 100$  mN mm<sup>-1</sup> and  $u$  being the displacement in the direction of the zonule (element).<sup>45</sup> No compression was considered.

## Analysis procedure

The most common theory of accommodation, proposed by Helmholtz,<sup>1</sup> was considered, and the contraction and relaxation of the ciliary muscle were reproduced in order to simulate the distant (non-accommodated) and near vision (accommodated) states.

The reference configuration of the FE model corresponds to the non-accommodated geometry, where the lens capsule and the Zinn zonules are not stress free. The decapsulated lens substance assumes a maximally unaccommodated form after removing the capsule, and thus the decapsulated lens was initially stress free.<sup>49</sup> The initial stress distribution ( $\sigma_{ij}^0$ ) was obtained with an extra analysis, stretching the lens from the accommodated to the non-accommodated state; see Figure 4a. The stress results at the integration points were mapped to the new lens capsule geometry.

All dynamic optical and biometric lens measurements of the accommodation mechanism were evaluated for each increment of the evolution process modelled in the simulation. For that purpose, displacement of the lens nodes and nucleus contour were registered by an URDFIL Abaqus subroutine and post-processed with MATLAB R2020b.

To measure the actual accommodative change (difference between the non-accommodated and corresponding accommodated states), the central optical power of the eye ( $COP_{Eye}$ ) was evaluated throughout the simulation using Gullstrand's eye formula:

$$COP_{Eye} = COP_c + COP_L - \frac{ACD}{n_a} COP_c COP_L, \quad (12)$$

with the central optical powers of the lens ( $COP_L$ ) and the cornea ( $COP_c$ ):<sup>8</sup>

$$COP_L = \frac{n_L - n_a}{r_a} + \frac{n_L - n_a}{r_p} - \frac{T_L(n_L - n_a)^2}{r_p r_a n_L}, \quad (13)$$

$$COP_c = \frac{n_c - n_{air}}{r_{c_a}} + \frac{n_a - n_c}{r_{c_p}} - \frac{(n_c - n_{air})(n_a - n_c)T_c}{n_c r_{c_a} r_{c_p}}, \quad (14)$$

where  $n_a = 1.336$  is the refractive index of the aqueous humour,  $n_L = 1.42$  is the estimated overall refractive index of the lens,  $n_c = 1.376$  is the refractive index of the cornea and  $n_{air} = 1.00$  is the refractive index of air. The remaining biometric terms,  $r_a$ ,  $r_p$ ,  $T_L$ ,  $ACD$ ,  $r_{c_a}$ ,  $r_{c_p}$  and  $T_c$ , defined in Figure 1, vary throughout the simulation. The power of the cornea was

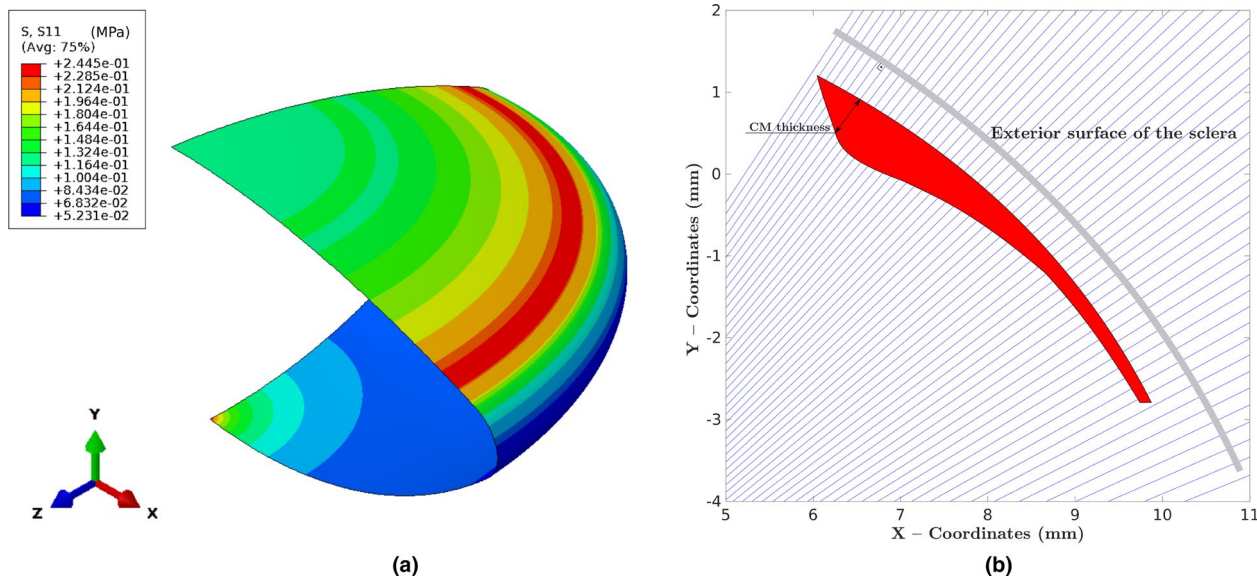


**FIGURE 4** (a) Stress distribution ( $\sigma_x^0$ ) of the lens capsule in the non-accommodated state. This stress distribution makes the lens accommodate after the zonular tension is released.  $\sigma_x^0 \approx \sigma_y^0$ , with  $\sigma_z^0 = 0$  due to the state of plane stress considered. (b) optical coherence tomography (OCT) measurement technique used to evaluate ciliary muscle thickness (CMT) profiles during accommodation<sup>33</sup>

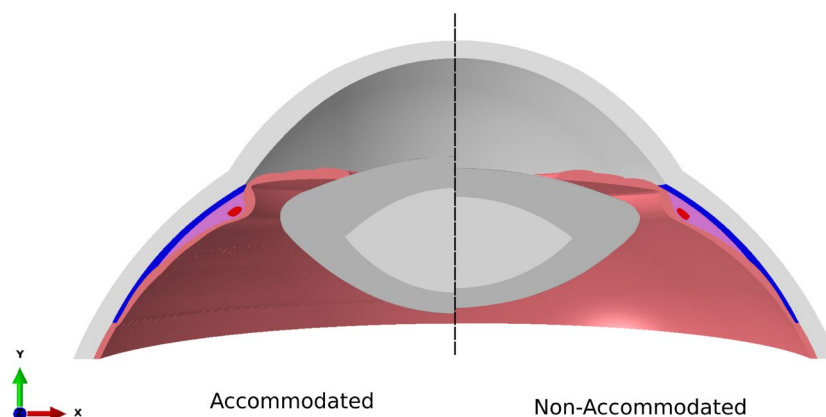


**FIGURE 5** Numerical solution of the accommodated state (left) and non-accommodated state (right). The accommodated state and the reference configuration provide 63.82 D and 58.00 D, respectively

kept constant throughout the simulation. The radii of curvature were calculated throughout the stretching process through an equation for a conic section having an apex at the origin and tangent to the y axis.

$$y^2 - 2rx + (K + 1)x^2 = 0. \tag{15}$$

To obtain the corresponding radius of curvature ( $r$ ) and the conic constant ( $K$ ), a non-linear system of equations formed by the coordinates of the nodes ( $x, y$ ) was solved. The goodness of the fit was  $R^2 > 99\%$ . The standardised design of the eye had 58 dioptres (D) in the far-vision state.

Lastly, the deformed geometry of the ciliary muscle was also measured during accommodation for each increment of the evolution process modelled in the simulation.

Straßer's<sup>33</sup> methodology was used to measure the CMT profile along the overall length of the muscle, which consists of measuring the distance between the sclera and the outer boundary of the ciliary muscle from perpendicular rays originating in the exterior surface of the sclera; see Figure 4b.

## RESULTS

During ciliary body contraction, the zonules release tension to allow the lens to round up to its accommodated state, see Figure 5. The FE solution, corresponding to an actual accommodation amplitude of 5.82 D, is shown on the left whilst the reference configuration, the non-accommodated state is depicted on the right to show



the geometrical changes, mainly in the ciliary muscle and lens.

To evaluate the accuracy of the proposed FE model of accommodation, we compared the dynamic changes produced in the ciliary muscle and lens during accommodation with experimental values collected from the literature.

## Ciliary muscle contraction

Figure 6 shows the morphological comparison between the numerical and experimental ciliary muscle contraction.<sup>20</sup> The experimental ciliary muscle contraction corresponds to an accommodation stimulus of 4 D.<sup>20</sup> The actual accommodative response is lower than the accommodation stimulus.<sup>50,51</sup> Figure 6a presents the contour of both the non-deformed and deformed geometries, while Figure 6b depicts comparison between the numerical and experimental CMT profiles.<sup>20</sup>

Once the numerical and experimental contractions of the ciliary muscle were compared, we calibrated the main parameters of active behaviour of the ciliary muscle, maximum active stress ( $P_0$ ) and the initial contraction velocity ( $v_0$ ) in order to reproduce the contraction and relaxation of the ciliary muscle. The maximum active stress is related to the maximum change in the ciliary muscle ring diameter ( $\phi_{CM}$ ), whereas the initial contraction velocity ( $v_0$ ) is related to the temporal performance of the muscle contraction. Due to the lack of data in the literature, we calibrated the muscle properties based on a virtual case.<sup>52</sup> Glasser *et al.*<sup>52</sup> provided electrical innervation to quantify the changes in lens diameter in rhesus monkeys. The virtual case attempted to replicate this situation but by quantifying the change in the ciliary body ring diameter. An accommodation square wave was implemented for 4 s by simulating electrical innervation. For the maximum electrical innervation, a maximum change in  $\Delta\phi_{CM}$  of 0.70 mm was presumably obtained. The methodology proposed would be the same for an actual case.

These properties were calibrated by means of a sensitivity analysis observing  $\Delta\phi_{CM}$ . First, the maximum active stress ( $P_0$ ) was obtained at the maximum response amplitude, 0.70 mm.<sup>52</sup> To do so,  $P_0$  ranged from 0.50 to 2.00 MPa, with  $v_0 = 3.00$  based on a previous study.<sup>17</sup> Figure 7a shows that a  $\Delta\phi_{CM}$  of 0.70 mm is obtained for  $P_0 = 1.50$  MPa. Once the maximum active stress was achieved, sensitivity analysis of the initial contraction velocity,  $v_0$ , was performed to calibrate the temporal performance (activation and deactivation) of the ciliary muscle; see Figure 7b.

## Coupling of the ciliary muscle and lens

Before analysing the dynamic biometric and optical measurements of the lens, we will describe the joint performance of the ciliary muscle and lens. Figure 8 presents three conditions of the ciliary muscle and lens based upon different accommodated states, namely, at 0.00, 0.75 and 1.50 s, which correspond to different ciliary body ring diameters ( $\Delta\phi_{CM}$ ). The numerical FE model presented a maximum accommodation of 5.82 D.

The accommodative response followed a linear relationship with the  $\Delta\phi_{CM}$  with an increase of 5.82 D and an increase in lens thickness of 0.44 mm for a reduction of 0.66 mm in  $\Delta\phi_{CM}$  or 67.54  $\mu\text{m}$  in  $\Delta\text{CMT}_{max}$ . Due to the way in which the CMT profiles are obtained with the perpendicular rays from the sclera, the changes observed in the CMT profiles are of lower magnitude.

## Dynamic optical and biometric lens measurements

The experimental *in vivo* results in humans obtained by Ramasubramanian and Glasser<sup>18,19</sup> were used for comparison with the numerical dynamic optical and biometric lens measurements. Figure 9a shows the changes in the anterior

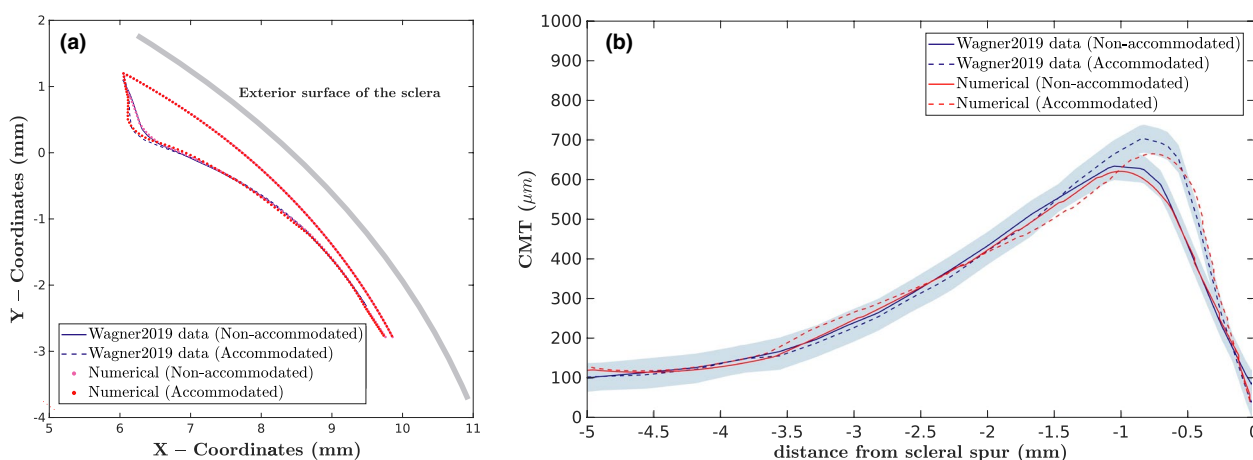


**FIGURE 6** Comparison between the morphological changes in ciliary muscle contraction. (a) In blue: the experimental ciliary muscle contour before and after contraction; in red: the numerical result. (b) Comparison between the experimental and numerical CMT profiles during far and near (4D) accommodation

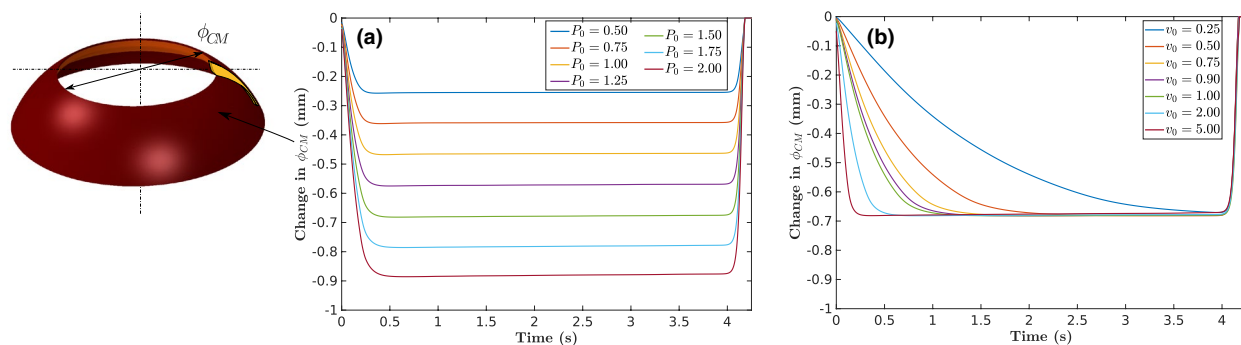


**FIGURE 7** Calibration of the ciliary muscle properties by means of a sensitivity analysis of: (a) the maximum active isometric stress ( $P_0$ ) and (b) the initial velocity ( $v_0$ )

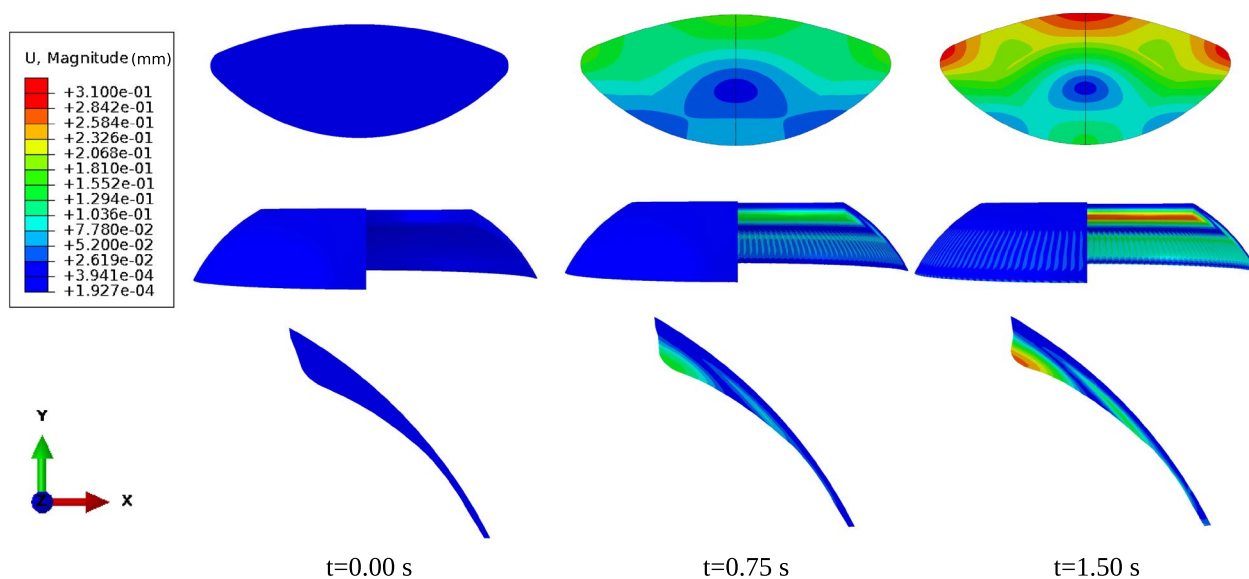


**FIGURE 8** Morphological shape of the ciliary muscle and the lens in different moments of the accommodation process

and posterior lens radius of curvature against the actual accommodative change of the eye. This graph shows where the optical change is happening. Both surface curvatures fit perfectly according to the experimental data. However, the anterior radius of curvature does not fit as well at the end of accommodation. This result may be due to a slight inconsistency in the definition of the initial stresses of the lens capsule compared with the physiological values.

Figure 9b shows the changes in lens thickness ( $\Delta T_L$ ) and ACD as a function of the accommodative change. There is a  $\Delta T_L$  of 0.44 mm and  $\Delta ACD$  of 0.31 mm for an accommodative change of 5.82 D. The orange line shows the change in the numerical nucleus thickness, which influences approximately 80% of the lens thickness, as previously reported.<sup>7,31</sup>

As a consequence of the increase in lens thickness, the lens moves anteriorly and posteriorly; see Figure 9c. The anterior lens movement is notably higher, approaching 0.31 mm anteriorly and 0.13 mm posteriorly for an accommodative change of 5.82 D.

Lens diameter (see Figure 9d) was compared with *ex vivo* experimental tests due to the difficulty of measuring the lens diameter *in vivo*. Data for a 29-year-old individual were obtained by interpolation from human groups aged 14 to 39.5 years as reported by Manns *et al.*<sup>53</sup> The numerical data fit perfectly with the interpolated data for a 29-year-old. All optical and biometric eye measurements were within the deviation reported by Ramasubramanian and Glasser.<sup>18,19</sup>

### Analysing the influence of lens mechanical properties in presbyopia

The mechanical properties of the lens are fundamentally related to how it changes its shape,<sup>8,10,26</sup> above other factors such as the lens geometry.<sup>15</sup> Therefore, we analysed the decrease in accommodation amplitude by varying the mechanical properties, i.e., the lens capsule, nucleus and cortex, while we kept the remaining tissues of the FE model proposed for the 29-year-old subject constant. Thus, in this

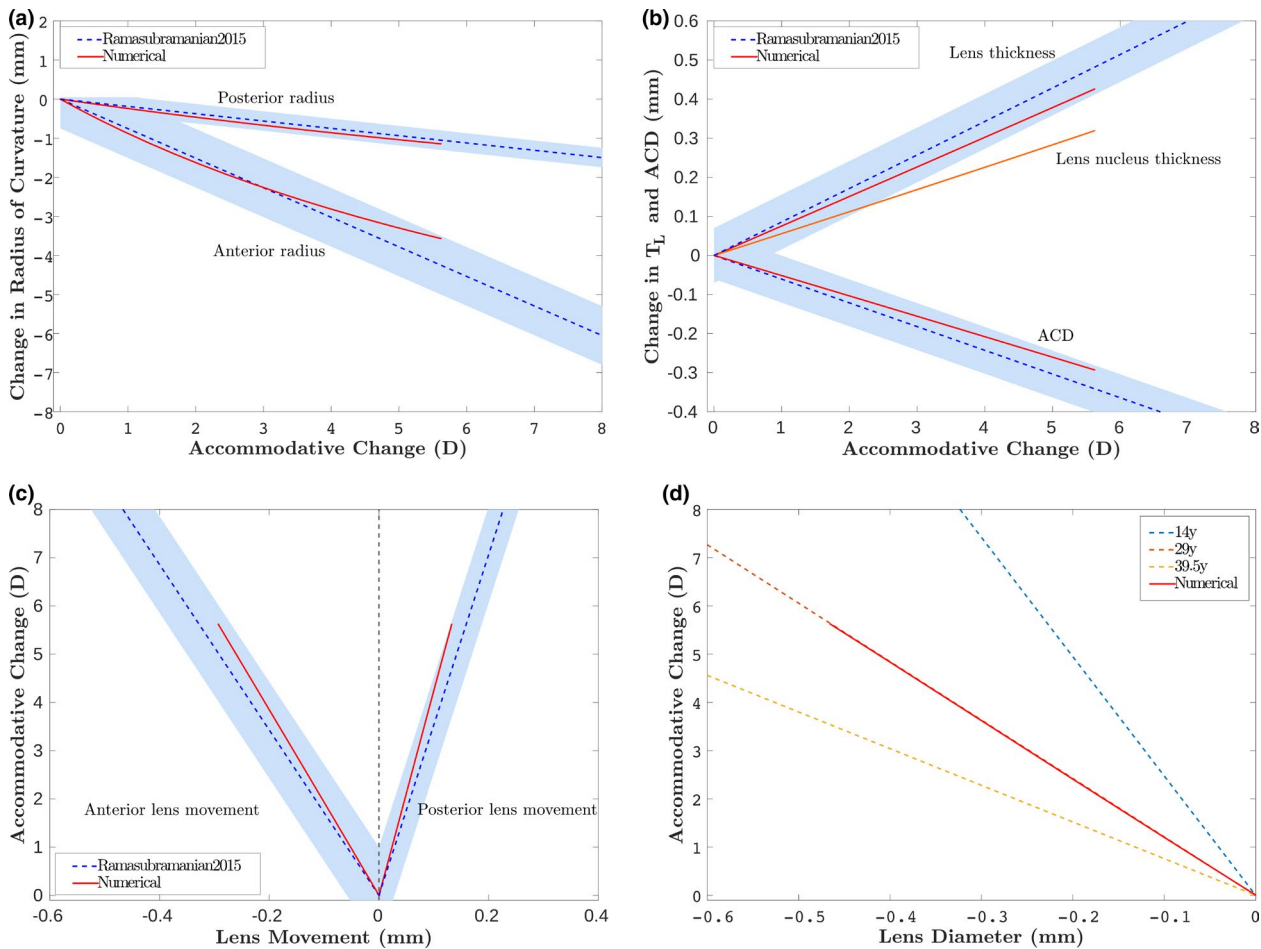


**FIGURE 9** (a) Change in the anterior ( $r_a$ ) and posterior ( $r_p$ ) lens radius of curvature, (b) lens thickness ( $T_L$ ) and anterior chamber distance (ACD), (c) anterior and posterior lens movement and (d) lens diameter, as functions of the change in accommodation

hypothetical case, we kept the same lens geometry and the initial stresses of the lens capsule calculated for the validated FE model, as reflected in *Figure 4a*.

We analysed three different cases: Case A, corresponding to all mechanical properties being fixed for a 29-year-old subject, except for the mechanical properties of the lens nucleus and cortex; Case B is the same as A, but with the change in the anterior and posterior lens capsule and Case C is a combination of Cases A and B. Both the mechanical properties of the lens capsule, nucleus and cortex were modified according to aging experimental data,<sup>25,26</sup> see *Figure 3b*.

*Figure 10* shows the accommodation amplitude data as a function of age for three different numerical cases against the experimental data.<sup>21-23</sup> Case B, changing the mechanical properties of the lens capsule, presents a small decrease in accommodation amplitude, from 5.82 D for a 29-year-old subject to 4.24 D for a 51-year-old. By contrast, Cases A and C, where the mechanical properties of the lens nucleus and cortex change with age, present decreasing amplitudes similar to the experimental data.<sup>21-23</sup>

## DISCUSSION

The main goal of this study was to develop an FE model that reproduced the *in vivo* accommodation process in humans. The proposed model reproduced Helmholtz's theory of accommodation and compared successfully with quality experimental data.<sup>18-20</sup> We accomplished this goal by quantifying contraction of the ciliary muscle and the optical and biometric measurements of accommodation, see *Figures 6 and 9*.

The resulting movement of the ciliary muscle comes from simultaneous contraction of the circular, radial and longitudinal muscle fibres. We faithfully reproduced the morphological changes in the ciliary muscle contraction of an emmetropic eye<sup>20</sup> by means of a computational eye model, which includes continuum and structural mechanics.<sup>16,17</sup> The morphological changes in the numerical and experimental ciliary muscle were similar, contracting towards the lens equator to release the resting tension on the zonular fibres, see *Figure 6*. This action was produced mainly by the circular muscle fibres, which governed ciliary muscle contraction. The numerical ciliary muscle became

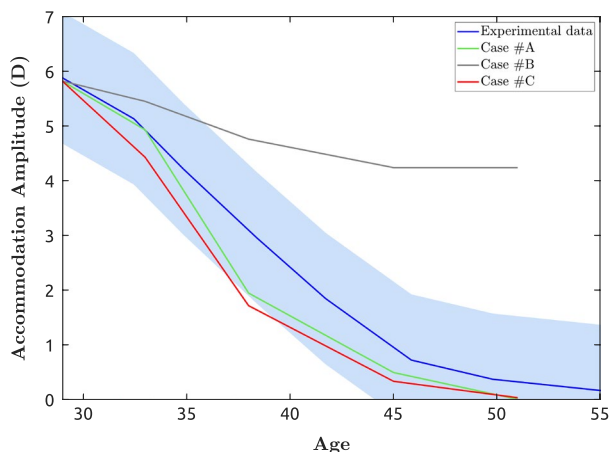


**FIGURE 10** Decrease in accommodative amplitude with age. Experimental<sup>21-23</sup> and numerical data are compared

slightly thinner below the apex of the ciliary muscle, in contrast with the experimental values.<sup>20</sup> However, detecting small changes is highly difficult experimentally because the OCT measurement technique depends upon the patient's sclera radius of curvature and on the operator.<sup>33</sup>

The longitudinal muscle fibres appear to have little influence on ciliary muscle contraction. It is true that there is a slight decrease in the length of the ciliary muscle as a result of pulling the posterior part of the ciliary muscle forward to the scleral spur. However, the circular fibres contract slightly upwards intrinsically due to the geometry of the muscle itself, and not due to the contraction of the longitudinal fibres. This might be due to the boundary condition applied in the sclera, which made the interaction between the ciliary muscle and the sclera too stiff. On the other hand, Glasser reported<sup>4</sup> that the longitudinal fibres seem to brace the system rapidly so that the contraction of the inner portion is most effective; this is consistent with the numerical results obtained in the present study.

One weakness of the FE model is that we modelled the radial muscle fibres as a mixture of circular and longitudinal muscle fibres due to limitations in numerically designing the radial fibres. The radial muscle fibres are supposed to perform a combined effect of the circular and longitudinal fibres.<sup>4</sup> Another weakness is that the iris constriction, which increases the depth of focus of the eye, was not simulated because it is not relevant from a mechanical point of view.

Two of the limitations of the FE model arose from a lack of data in the literature. First, we considered that all muscular fibres were activated equally, although the force exerted, which depends on the force-stretch relationship ( $f_\lambda$ ), was higher for the circular fibres. Second, the muscle properties were calibrated according to a virtual case based on the electrical innervation provided to rhesus monkeys by Glasser *et al.*<sup>52</sup> Nevertheless, the ciliary muscle could be updated according to new investigations with the proposed methodology.

The joint performance of the ciliary muscle and lens with respect to accommodation was analysed numerically. We obtained a linear response with an increase in accommodation of 5.82 D and an increase in  $T_L$  of 0.44 mm for a reduction of 0.66 mm in the ciliary muscle ring diameter ( $\Delta\phi_{CM}$ ), or 67.54  $\mu\text{m}$  in the maximum ciliary muscle thickness ( $\Delta CMT_{max}$ ). These values were within the range reported in the literature. Strenk *et al.*<sup>54</sup> reported  $\Delta\phi_{CM}$  values ranging from 0.50 to 1.00 mm for an 8 D accommodative stimulus. Ruggeri *et al.*<sup>55</sup> reported  $\Delta T_L$  and  $\Delta CMT_{max}$  values of 0.20 mm and 72.0  $\mu\text{m}$ , respectively, for an accommodation stimulus of 4 D in a 22-year-old subject. Additionally, Richdale *et al.*<sup>51</sup> reported a  $\Delta T_L$  of 0.38 mm and  $\Delta CMT_{max}$  of 98.41  $\mu\text{m}$  for a 5.85 D accommodative response in a 29-year-old subject (taken from their fitted regression line). Although these values are within the range of the numerical values reported, it is difficult to compare the  $\Delta CMT_{max}$  values because the experimental measurements depend upon the technique applied and the image quality.

Human accommodation is similar to that of other hominids. However, depending on the species and age, accommodation occurs in slightly different ways; for example, lens thickness and diameter change in humans is reduced compared with rhesus monkeys for the same accommodation amplitude.<sup>3,19,53,56</sup> For this reason, validating the main optical and biometric lens measurements was complicated and meaningful.

In this study, we present a numerical approach standardised for a 29-year-old individual, accurately reproducing human accommodation. The optical and biometric measurements of the lens were compared with *in vivo* accommodation dynamic measurements by Ramasubramanian and Glasser,<sup>18,19</sup> and all the numerical data presented were within the range of the experimental measurements. To achieve this aim, we previously reported that the mechanical properties of the crystalline lens are key to how the lens shape changes.<sup>15</sup> The presented model indicates that several factors such as lens mechanical properties, the zonular arrangement and capsule thickness distribution must be included to simulate the accommodation of humans.

We hypothesise that the stresses in the non-accommodated lens capsule should vary little over time for two reasons. Were they to increase, then accommodation would become higher over time while if they were to decrease, then the stiffness added with age would cause an earlier appearance of presbyopia. With this hypothesis, we determined that stiffening of the lens nucleus was mainly responsible for the decrease in accommodation amplitude (see Figure 10), rather than the increased stiffness in the lens capsule with increasing age. This conclusion is supported by our previous work,<sup>15</sup> where we observed that the stiffness ratio between the lens nucleus and cortex is key to how the lens changes its shape. In contrast to Wilkes *et al.*,<sup>12</sup> our FE model can explain some causes of presbyopia over a wider age range. Additional studies considering more factors involved in accommodation as well as mechanical data regarding the internal properties of the lens are needed to understand presbyopia further.

In contrast to other FE models that stretched the lens, simulating *ex vivo* conditions,<sup>8-14</sup> we designed our reference configuration using non-accommodated geometry. Designing the 3D FE model in this way allowed us to take lens movement into consideration, which is essential because changes in lens curvature do not reflect all significant accommodative changes.<sup>57</sup> In the numerical validation, 0.97 D (16%) of the 5.82 D of the accommodation amplitude was produced by lens movement. Furthermore, this model could be compared with novel research from the literature<sup>18-20</sup> and provides the necessary background to analyse and evaluate fundamental aspects of accommodation, as well as the detailed geometry of a 29-year-old individual for other research studies.

## ACKNOWLEDGEMENTS

We would like to thank Adrian Glasser for the helpful and comprehensive discussions on this project. The authors also gratefully acknowledge research support from the Spanish Ministerio de Ciencia, Innovación y Universidades (Grant DPI2017-84047-R) and the Department of Industry and Innovation (Government of Aragon) through the research group Grant T24-20R (cofinanciado con Feder 2014-2020: Construyendo Europa desde Aragon). Part of the work was performed by the ICTS "NANBIOSIS" specifically by the High Performance Computing Unit (U27), of the CIBER in Bioengineering, Biomaterials & Nanomedicine (CIBER-BBN at the University of Zaragoza). I. Cabeza-Gil was supported by PRE2018-084021.

## CONFLICT OF INTEREST

The authors report no conflicts of interest and have no proprietary interest in any of the materials mentioned in this article.

## AUTHOR CONTRIBUTIONS

**Iulen Cabeza-Gil:** Conceptualization (equal); Methodology (equal); Software (equal); Writing-original draft (equal). **Jorge Grasa:** Resources (equal); Software (equal); Supervision (equal); Writing-review & editing (equal). **Begoña Calvo:** Conceptualization (equal); Project administration (equal); Supervision (equal); Writing-review & editing (equal).

## ORCID

Iulen Cabeza-Gil  <https://orcid.org/0000-0001-8219-2365>

## REFERENCES

- Helmholtz H. Ueber die accommodation des auges. *Albrecht von Graefes Arch Klin Expl Ophthalmol*. 1855;2:1-74.
- Fincham F. The changes in the form of the crystalline lens in accommodation. *Trans Opt Soc*. 1925;26:239-269.
- Glasser A, Kaufman PL. The mechanism of accommodation in primates. *Ophthalmology*. 1999;106:863-872.
- Levin LA, Nilsson SFE, Ver Hoeve J, Wu S, Kaufman PL, Alm A (Eds.). *Adler's Physiology of the Eye*. Chapter 3 (A. Glasser): Accommodation. Edingburg: Elsevier Health Sciences; 2011.
- Tamm S, Tamm E, Rohen JW. Age-related changes of the human ciliary muscle. A quantitative morphometric study. *Mech Ageing Dev*. 1992;62:209-221.
- Pardue MT, Sivak JG. Age-related changes in human ciliary muscle. *Optom Vis Sci*. 2000;77:204-210.
- Brown N. The change in shape and internal form of the lens of the eye on accommodation. *Exp Eye Res*. 1973;15:441-459.
- Burd HJ, Judge SJ, Cross JA. Numerical modelling of the accommodating lens. *Vis Res*. 2002;42:2235-2251.
- Hermans EA, Dubbelman M, van der Heijde GL, Heethaar RM. Estimating the external force acting on the human eye lens during accommodation by finite element modelling. *Vis Res*. 2006;46:3642-3650.
- Van de Sompel D, Kunkel GJ, Hersh PS, Smits AJ. Model of accommodation: contributions of lens geometry and mechanical properties to the development of presbyopia. *J Cataract Refract Surg*. 2010;36:1960-1971.
- Lanchares E, Navarro R, Calvo B. Hyperelastic modelling of the crystalline lens: accommodation and presbyopia. *J Optom*. 2012;5:110-120.
- Wilkes RP, Reilly MA. A pre-tensioned finite element model of ocular accommodation and presbyopia. *Int J Adv Eng Sci Appl Math*. 2015;8:25-38.
- Wang K, Venetsanos D, Wang J, Pierscionek BK. Gradient moduli lens models: how material properties and application of forces can affect deformation and distributions of stress. *Sci Rep*. 2016;6:31171. <https://doi.org/10.1038/srep31171>
- Wang K, Venetsanos DT, Hoshino M, Uesugi K, Yagi N, Pierscionek BK. A modeling approach for investigating opto-mechanical relationships in the human eye lens. *IEEE Trans Biomed Eng*. 2020;67:999-1006.
- Cabeza-Gil I, Grasa J, Calvo B. A numerical investigation of changes in lens shape during accommodation. *Sci Rep*. 2021;11:9639. <https://doi.org/10.1038/s41598-021-89145-z>
- Hernández-Gascón B, Grasa J, Calvo B, Rodríguez JF. A 3D electro-mechanical continuum model for simulating skeletal muscle contraction. *J Theor Biol*. 2013;335:108-118.
- Grasa J, Sierra M, Lauzeral N, Muñoz MJ, Miana-Mena FJ, Calvo B. Active behavior of abdominal wall muscles: experimental results and numerical model formulation. *J Mech Behav Biomed Mater*. 2016;61:444-454.
- Ramasubramanian V, Glasser A. Can ultrasound biomicroscopy be used to predict accommodation accurately? *J Refract Surg*. 2015;31:266-273.
- Ramasubramanian V, Glasser A. Objective measurement of accommodative biometric changes using ultrasound biomicroscopy. *J Cataract Refract Surg*. 2015;41:511-526.
- Wagner S, Zrenner E, Straßer T. Emmetropes and myopes differ little in their accommodation dynamics but strongly in their ciliary muscle morphology. *Vis Res*. 2019;163:42-51.
- Koretz JF, Kaufman PL, Neider MW, Goeckner PA. Accommodation and presbyopia in the human eye-aging of the anterior segment. *Vis Res*. 1989;29:1685-1692.
- Ostrin LA, Glasser A. Accommodation measurements in a pre-presbyopic and presbyopic population. *J Cataract Refract Surg*. 2010;36:1960-71.
- Anderson HA, Hentz G, Glasser A, Stuebing KK, Manny RE. Minus-lens-stimulated accommodative amplitude decreases sigmoidally with age: a study of objectively measured accommodative amplitudes from age 3. *Invest Ophthalmol Vis Sci*. 2008;49:2919-2926.
- Fisher RF. Elastic constants of the human lens capsule. *J Physiol*. 1969;201:1-19.
- Weeber HA, Eckert G, Pechhold W, Heijde RGL. Stiffness gradient in the crystalline lens. *Graefes Arch Clin Exp Ophthalmol*. 2007;45:1357-1366.
- Wilde GS, Burd HJ, Judge SJ. Shear modulus data for the human lens determined from a spinning lens test. *Exp Eye Res*. 2012;97:36-48.
- Chang Y-C, Mesquita GM, Williams S, et al. In vivo measurement of the human crystalline lens equivalent refractive index using extended-depth OCT. *Biomed Opt Express*. 2019;10:411-422.
- Barraquer RI, Michael R, Abreu R, Lamarca J, Tresserra F. Human lens capsule thickness as a function of age and location along the sagittal lens perimeter. *Invest Ophthalmol Vis Sci*. 2006;47:2053-2060.

29. Kasthurirangan S, Markwell EL, Atchison DA, Pope JM. MRI study of the changes in crystalline lens shape with accommodation and aging in humans. *J Vis.* 2011;11:19,1–16.
30. Dubbelman M, Heijde GL, Van WHA, Vrensen GFJM. Changes in the internal structure of the human crystalline lens with age and accommodation. *Vis Res.* 2003;43:2363–2375.
31. Hermans E, Dubbelman M, Heijde R, Heethaar R. The shape of the human lens nucleus with accommodation. *J Vis.* 2007;7:16. <https://doi.org/10.1167/7.10.16>
32. Bernal A, Jean-Marie P, Manns F. Evidence for posterior zonular fiber attachment on the anterior hyaloid membrane. *Invest Ophthalmol Vis Sci.* 2006;47:4708–4713.
33. Straßer T, Wagner S, Zrenner E. Review of the application of the open-source software CIOCT for semi-automatic segmentation and analysis of the ciliary muscle in OCT images. *PLoS One.* 2020;15:e0234330.
34. Lee RY, Huang G, Porco TC, Chen Y, He M, Lin SC. Differences in iris thickness among African Americans, Caucasian Americans, Hispanic Americans, Chinese Americans, and Filipino-Americans. *J Glaucoma.* 2013;22:673–678.
35. Fernández-Vigo JI, García-Feijóo J, Martínez-de-la-Casa JM, et al. Fourier domain optical coherence tomography to assess the iridocorneal angle and correlation study in a large Caucasian population. *BMC Ophthalmol.* 2016;16:42. <https://doi.org/10.1186/s12886-016-0219-z>
36. Le-Grand Y, El-Hage SG. *Physiological Optics. (Translation and update of Le Grand Y, La dioptrique de l'oeil et sa correction), vol. 1. Heidelberg: Springer-Verlag. 1968; p. 57–69.*
37. Siu A, Herse P. The effect of age on human corneal thickness. *Acta Ophthalmol.* 2009;71:51–56.
38. Stålhand J, Klarbring A, Holzapfel GA. A mechanochemical 3D continuum model for smooth muscle contraction under finite strains. *J Theor Biol.* 2011;268:120–130.
39. Mallen EA, Gilmartin B, Wolffsohn JS. Sympathetic innervation of ciliary muscle and oculomotor function in emmetropic and myopic young adults. *Vis Res.* 2005;45:1641–1651.
40. Calvo B, Sierra M, Grasa J, Muñoz MJ, Peña E. Determination of passive viscoelastic response of the abdominal muscle and related constitutive modeling: stress-relaxation behavior. *J Mech Behav Biomed Mater.* 2014;36:47–58.
41. Krag S, Andreassen TT. Mechanical properties of the human lens capsule. *Prog Retin Eye Res.* 2003;22:749–767.
42. Krag S, Andreassen TT. Mechanical properties of the human posterior lens capsule. *Invest Ophthalmol Vis Sci.* 2003;44:691–696.
43. Burd HJ, Wilde GS, Judge SJ. Can reliable values of Young's modulus be deduced from Fisher's (1971) spinning lens measurements? *Vis Res.* 2006;46:1346–1360.
44. Heys KR, Cram SL, Truscott RJW. Massive increase in the stiffness of the human lens nucleus with age: the basis for presbyopia? *Mol Vis.* 2004;10:956–963.
45. Michael R, Mikielewicz M, Gordillo C, et al. Elastic properties of human lens zonules as a function of age in presbyopes. *Invest Ophthalmol Vis Sci.* 2012;53:6109–6114.
46. Friberg TR, Lacey JW. A comparison of the elastic properties of human choroid and sclera. *Exp Eye Res.* 1988;47:429–436.
47. Li C, Guan G, Huang Z, Johnstone M, Wang RK. Noncontact all-optical measurement of corneal elasticity. *Opt Lett.* 2012;37:1625. <https://doi.org/10.1364/OL.37.001625>
48. Alphen G, Graebel WP. Elasticity of tissues involved in accommodation. *Vis Res.* 1991;31:1417–1438.
49. Glasser A, Campbell MCW. Biometric, optical and physical changes in the isolated human crystalline lens with age in relation to presbyopia. *Vis Res.* 1999;39:1991–2015.
50. Schmid KL, Strang NC. Differences in the accommodation stimulus response curves of adult myopes and emmetropes: a summary and update. *Ophthalmic Physiol Opt.* 2015;35:613–621.
51. Richdale K, Sinnott LT, Bullimore MA, et al. Quantification of age-related and per diopter accommodative changes of the lens and ciliary muscle in the emmetropic human eye. *Invest Ophthalmol Vis Sci.* 2013;54:1095–1105.
52. Glasser A, Wendt M, Ostrin L. Accommodative changes in lens diameter in rhesus monkeys. *Investig Ophthalmol Vis Sci.* 2006;47:ARVO E-Abstract 278.
53. Manns F, Parel J-M, Denham D, et al. Optomechanical response of human and monkey lenses in a lens stretcher. *Invest Ophthalmol Vis Sci.* 2007;48:3260–3268.
54. Strenk SA, Semmlow JL, Strenk LM, et al. Age-related changes in human ciliary muscle and lens: a magnetic resonance imaging study. *Invest Ophthalmol Vis Sci.* 1999;40:1162–1169.
55. Ruggeri M, de Freitas C, Williams S, et al. Quantification of the ciliary muscle and crystalline lens interaction during accommodation with synchronous OCT imaging. *Biomed Opt Express.* 2016;7:1351–1364.
56. Vilupuru AS, Glasser A. The relationship between refractive and biometric changes during Edinger-Westphal stimulated accommodation in rhesus monkeys. *Exp Eye Res.* 2005;80:349–360.
57. Croft MA, Heatley G, McDonald JP, Katz A, Kaufman PL. Accommodative movements of the lens/capsule and the strand that extends between the posterior vitreous zonule insertion zone and the lens equator, in relation to the vitreous face and aging. *Ophthalmic Physiol Opt.* 2015;36:21–32.

**How to cite this article:** Cabeza-Gil I, Grasa J, Calvo B. A validated finite element model to reproduce Helmholtz's theory of accommodation: a powerful tool to investigate presbyopia. *Ophthalmic Physiol Opt.* 2021;41:1241–1253. <https://doi.org/10.1111/opo.12876>

## 2.2 Work 2: A numerical investigation of changes in lens shape during accommodation



Cabeza-Gil I., Grasa J. and Calvo B.  
Scientific Reports  
JIF (2020) = 4.38 (Q1: 17/72 Multidisciplinary Sciences)  
SJR (2020) = 1.24 (Q1: 10/135 Multidisciplinary)



OPEN

# A numerical investigation of changes in lens shape during accommodation

I. Cabeza-Gil<sup>1</sup>✉, J. Grasa<sup>1,2</sup> & B. Calvo<sup>1,2</sup>

The purpose of this study was to investigate how the mechanical properties and geometry of the lens influence the changes in lens shape during accommodation. To do so, *ex vivo* stretching tests of the isolated lens were simulated via finite element analysis. In these tests, the lens is stretched from the accommodated state to the non-accommodated state. Several key characteristics of the lens were studied: the stiffness gradient of the lens material, the distribution of the capsule thickness, the mechanical properties of the capsule and the material comprising the lens, nucleus and cortex, and the influence of two different age-related lens geometries (17 and 29 y/o subjects). To determine the effects on the changes in lens shape during accommodation, changes in the anterior and posterior radius, the lens and nucleus thicknesses and the equatorial lens diameter were analysed. The results suggest that multiple factors exert statistically significant influences on how the lens changes its shape, but two factors predominate over the rest: the stiffness ratio between the nucleus and cortex and the stiffness of the capsule, specifically the posterior surface.

The restoration of dynamic accommodation in presbyopic eyes and in the context of cataracts has not yet been successfully achieved<sup>1</sup>. So far, the most widespread solution has been the use of accommodating intraocular lenses; however, their development remains in progress as the restoration of dynamic accommodation is not yet fully achieved<sup>2,3</sup>. One of the main difficulties in the development of novel ophthalmologic solutions to restore dynamic accommodation is the absence of quality explanations of the biomechanical process of accommodation. On this basis, we hypothesise that numerical methods could help the research community and manufacturers to find better solutions by providing fundamental knowledge of this phenomena.

To the best of our knowledge, several authors have designed finite element (FE) models to explain and understand some aspects of the accommodation process following Helmholtz's accommodation theory. Burd et al.<sup>4</sup> designed an axisymmetric model for different ages in an attempt to observe some of the features of presbyopia. Other authors followed the same criteria, using 3D modelling to measure the forces applied by the zonules and the focal changes of the lens<sup>5-7</sup>. Lanchares et al.<sup>8</sup> reproduced the compliance of the materials by a hyperelastic model, and recently, Wang et al.<sup>9-11</sup> studied both the focal changes of the lens for different age-related properties and the effects of zonular union.

In more detail, those FE models tried to replicate isolated *ex vivo* stretching tests of the crystalline lens<sup>12-16</sup>. These experimental protocol tests were performed on post-mortem human and monkey lenses and reported the dynamic optical and biometric changes of the lenses.

The dynamic changes in the anterior and posterior radii of curvature, lens thickness and lens diameter vary slightly upon accommodation depending on the type of hominid and the age of the subject<sup>13,14,17,18</sup>. Therefore, our hypothesis is that the main dynamic biometric changes in hominids depend on lens material properties and geometry, both of which in turn depend on age.

For this reason, to achieve a better understanding of the focal change of the lens during accommodation, the purpose of this study is to shed light on how the lens changes its shape depending on the lens mechanical properties and lens geometry for young subjects using finite element analysis (FEA). To do so, the effects of the mechanical properties of the capsule and the material comprising the lens, nucleus and cortex, on the changes in lens shape were evaluated together with two age-related geometries. Contrary to other FE studies, we attempted to completely describe the changes in lens shape by measuring the changes in anterior and posterior radii, lens and nucleus thicknesses and the equatorial lens diameter.

<sup>1</sup>Aragón Institute of Engineering Research (i3A), University of Zaragoza, Mariano Esquillor s/n, Zaragoza 50018, Spain. <sup>2</sup>Centro de Investigación Biomédica en Red en Bioingeniería, Biomateriales y Nanomedicina (CIBER-BBN), Zaragoza, Spain. ✉email: iulen@unizar.es



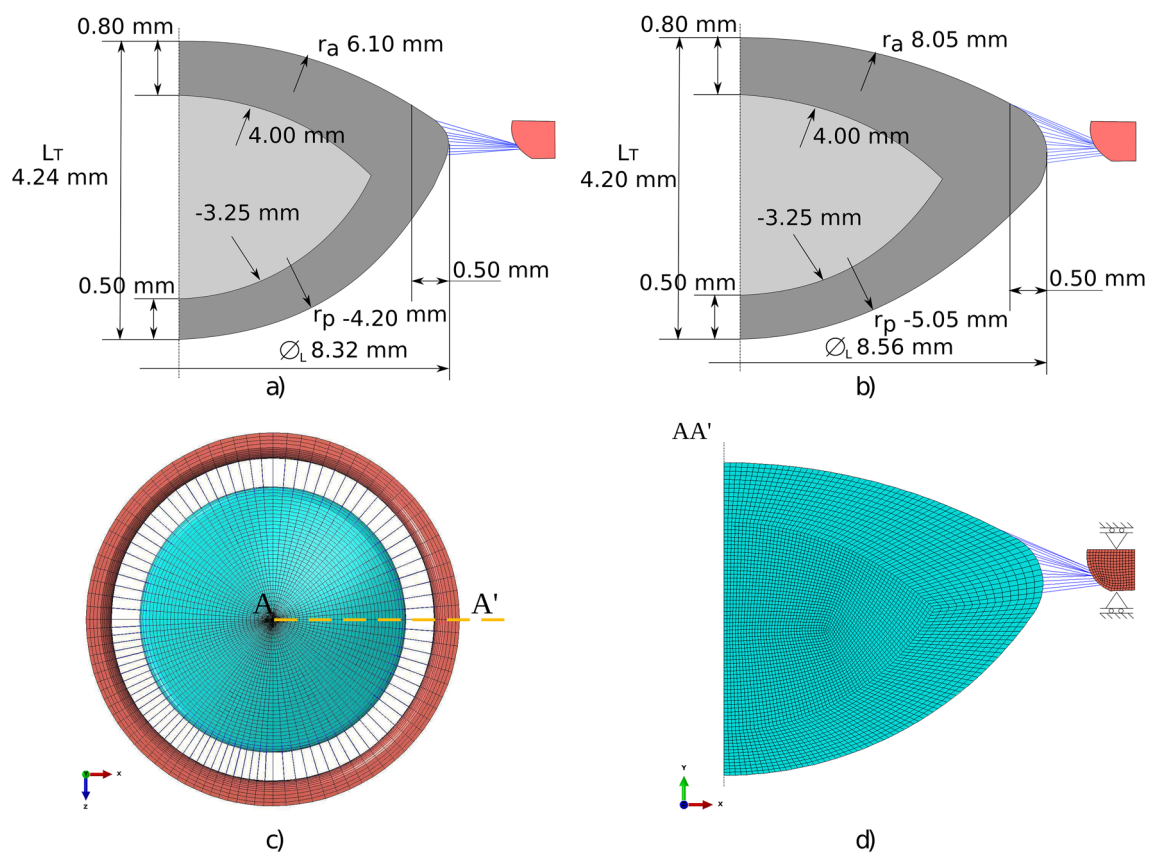


**Figure 1.** The dimensions of the 17-year-old (a) and 29-year-old (b) lens geometry. The nucleus is depicted in light grey, whilst the cortex is in dark grey. A plane (c) and profile (d) view of the FE model for the 29 y/o subject is presented. Zonules and part of the ciliary body ring are depicted in blue and red, respectively.

Due to its complexity, this study also helps to identify the lens material properties in order to determine them experimentally. Burd et al.<sup>19</sup> reported that the spinning lens measurements of Fischer<sup>20</sup> might not be reliable, and since then, few studies pertaining to the internal lens mechanical properties have been performed without individually characterising the mechanical properties of the lens nucleus and cortex<sup>21,22,23</sup>.

To provide a more accurate approach, the effects of two key lens mechanical aspects on accommodation were previously studied. On the one hand, the lens stiffness gradient was analysed because there is an evidence that the morphological shape of the lens forms a gradient of refractive index (GRIN) and stiffness<sup>22–25</sup>. On the other hand, the distribution of the capsule thickness was studied as the lens capsule thickness varies along the lens location<sup>26,27</sup>.

The paper is organised as follows. First, the FE model, together the stretching test, is described in “Methods”; then, the case studies analysed in this research are explained. After that, the results are presented sequentially as in “Case studies” section to be finally discussed in the last section.

## Methods

The lens geometries of 17 and 29 y/o subjects, the material approach for each tissue and the mesh structure are described in “FE model” section. Then, the lens stretching test simulated in this study is presented in “Analysis procedure” section. Lastly, the case studies are described, which includes the influences of the lens stiffness gradient and the distribution of the capsule thickness on the ability of the lens to change its shape. Both studies were initially performed for the 29 y/o lens geometry. Once both effects were numerically analysed, the lens mechanical properties for two different geometries corresponding to two different ages (17 and 29 y/o) were analysed following the design of experiments (DoE) methodology with a full factorial design<sup>28</sup>.

**FE model.** The lens geometries were generated according to various studies for isolated lenses as a function of age. The anterior and posterior curvature radii were extracted from Borja et al.<sup>29</sup>, whilst the lens thickness and diameter were based on the study by Martinez-Enriquez et al.<sup>30</sup> For both geometries, the anterior and posterior thickness values of the cortex were 0.80 mm and 0.50 mm, respectively, assuming that hardly any change in the cortex thickness occurs upon accommodation<sup>31,32</sup>. Radii of curvature of the anterior and posterior surfaces of 4.00 and 3.25 mm, respectively, were considered<sup>32,33</sup>. Zonules were anchored 0.50 mm in the anterior capsule and in the lens equatorial diameter according to the study by Bernal et al.<sup>34</sup>. The zonules emerged from the apex area of the ciliary body. Figure 1a,b summarises the lens dimensions for both 17 and 29 y/o subjects.

Abaqus v.14.1 was chosen as the software suite for the FEA. An axisymmetric FE model was designed to perform the lens stretching tests. A mesh sensitivity analysis was previously performed in order to establish the final mesh size; see Fig. 1c,d. The lens nucleus and cortex were considered solid bodies and were meshed with 4672 4-node bilinear axisymmetric quadrilateral hybrid elements (CAX4H); the capsule was meshed with 203 2-node linear axisymmetric membrane elements (MAX1); 10 zonules were modelled using Abaqus connector elements; and the ciliary body was meshed with 231 CAX4H elements. The lens material was modelled with an incompressible linear elastic behaviour ( $E=f(r, z)$ ,  $\nu = 0.5$ ). The lens capsule was modelled via membrane elements, assuming a state of tensile stress without allowing any bending or transverse shear stiffness. In turn, the mechanical properties of the anterior and posterior lens capsule were modelled individually according to the study of Krag and Andreassen<sup>35,36</sup>, who reported different mechanical properties for both surfaces.

The zonules were modelled with linear connector elements. These elements were characterised by means of a force-displacement equation:

$$F(u) = ku, \quad (1)$$

with  $k = 100$  mN/mm and  $u$  representing the displacement in the direction of the zonule (element)<sup>37</sup>. No compression was considered.

**Analysis procedure.** The experimental lens stretching tests<sup>13,14</sup> were simulated via FEA. These tests attempt to reproduce the relaxation of the ciliary muscle, adjusting the focal length from the near to the far vision state. Therefore, the reference configuration of our FE model corresponds to the accommodated geometry (near state vision), where a stress-free state of both zonules and lens can be considered. To simulate the relaxation of the ciliary muscle, in all cases of the study, a radial displacement of 0.50 mm in the whole ciliary body ring was imposed, isolating the effect of the stretching process in the lens; see Fig. 1d.

During the simulation, all dynamic optical and biometric lens measurements were evaluated in each time increment. For that purpose, the displacements of the nodes of the lens contour were registered by an URDFIL Abaqus subroutine and post-processed with MATLAB R2020b. To measure the lens power, the thick lens formula was used:

$$L_P = (n_L - n_a) \left[ \frac{1}{r_a} - \frac{1}{r_p} + \frac{L_T(n_L - n_a)}{r_p r_a n_L} \right], \quad (2)$$

where  $n_a = 1.336$  represents the refractive index of the aqueous humour and  $n_L = 1.42$  is the estimated equivalent refractive index of the lens<sup>25</sup>. The remaining biometric terms,  $r_a$ ,  $r_p$  and  $L_T$ , defined in Fig. 1a,b, vary throughout the simulation. The radii of curvature throughout the stretching process were calculated through an equation for a conic section with apex at the origin and tangent to the y-axis.

$$y^2 - 2rx + (k + 1)x^2 = 0. \quad (3)$$

To obtain the corresponding radius ( $r$ ) and the conic constant ( $K$ ), a nonlinear system of equations formed by the coordinates of the nodes ( $x, y$ ) was solved. The goodness of the fit was confirmed, with  $R^2 > 99\%$ . Note that the change in the lens power ( $\Delta L_P$ ) obtained is negative because the lens power decreases with this stretching process.

**Case studies.** *Evaluation of the lens stiffness gradient.* The lens nucleus and cortex are widely modelled in the literature with homogeneous material behaviour<sup>4,7,8</sup>. However, it has been reported that the stiffness varies within the lens according to its morphological shape<sup>21,22</sup>. Weeber et al.<sup>22</sup> reported that the lens shear modulus ( $G$ ) varies with location, showing a maximum value at a distance of 2.5–3.0 mm from the centre of the lens in young eyes. Weeber et al.<sup>6</sup> modelled three different cases of age-related lenses with stiffness gradients; however, the mechanical influence of having or not having a stiffness gradient was not analysed. Thus, to evaluate whether the stiffness gradient ( $\nabla E(r, z)$ , with  $E(r, z)$  representing the elastic modulus) has a significant mechanical influence on the ability of the lens to change its shape, an exhaustive analysis with multiple scenarios of the stiffness gradient in the lens was performed.

To do so, we designed a stiffness gradient ( $E = f(FV)$ ) as a function of the location, creating a field variable  $FV$  to attempt to reproduce the actual lens layered structure<sup>38</sup>; see Fig. 2a.  $FV$  measures the perpendicular absolute distance (mm) between a point in the lens and the anterior or posterior radius of the lens nucleus according to the region in which the point is located (anterior or posterior, separated by the lens equator). As observed in Fig. 2a,b,  $FV$  is 0.00 mm in the anterior and posterior radii of the lens nucleus and reaches its maximum of 1.40 mm in the equatorial lens diameter and in the centre of the lens.

Based on the studies by Weeber et al.<sup>22</sup> and Wilde et al.<sup>23</sup>, and considering that the stress–strain relationship  $E = 3G$ ,  $G_{cortex} = 3.00$  kPa and  $E_{nucleus} = 0.30$  kPa were calculated as a reference scenario<sup>23</sup>; see case #HC in Fig. 2,  $E = f(FV)$ . The first gradient (#A) was derived from Weeber's<sup>22</sup> measurements for a 30 y/o subject (scaled to fit scenario #HC); see Fig. 2,  $E = 3.00$ ,<sup>22</sup>,  $FV > 1.10$ ,<sup>20,31,2</sup>,

In all analyses, the elastic modulus of the anterior capsule was  $E = 1.00$  MPa, and that of the posterior capsule was  $E = 0.70$  MPa. The distribution of capsule thickness reported by Fincham<sup>26</sup> is shown by the black line in Fig. 3, where the 29 y/o lens geometry was considered.

*Evaluation of the distribution of the lens capsule thickness.* Fincham<sup>26</sup> and Barraquer et al.<sup>27</sup> reported five different distributions of the capsule thickness. However, the mechanical influence of this factor has not yet been numerically evaluated. For this reason, five experimental distributions of the capsule thickness were analysed:

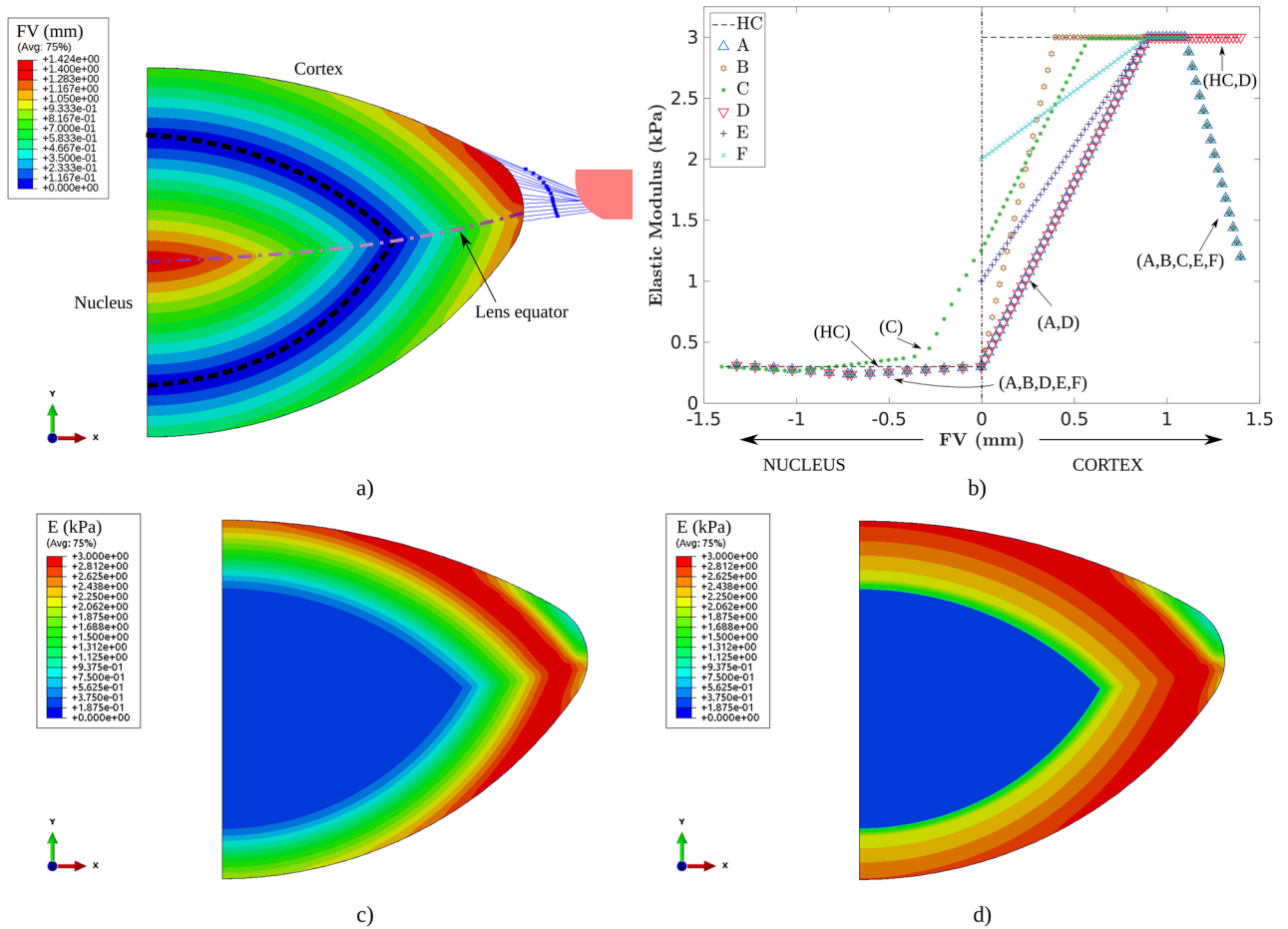


**Figure 2.** (a) FV variable which measures the absolute perpendicular distance from a point in the lens to the anterior or posterior radius of the lens nucleus. (b)  $E = f(FV)$  for the seven different scenarios analysed. The values of elastic modulus  $E$  within the lens for scenarios #A and #F are depicted in (c) and (d), respectively.

two of them are reported by Fincham<sup>26</sup> and indicated by the black and grey dashed lines in Fig. 3, and three different distributions according to different ages of 36, 65 and 92 years are reported by Barraquer et al.<sup>27</sup>. For this study, the elastic modulus of the anterior capsule was 1.00 MPa, and that of the posterior capsule was 0.70 MPa. The nucleus and cortex were considered homogeneous, with  $E_{cortex} = 3.00$  kPa and  $E_{nucleus} = 0.30$  kPa. All analyses were calculated for the 29 y/o lens geometry.

Moreover, to help extract and isolate the effects of the lens capsule on the focal changes of the lens, three different uniform thicknesses of 7, 13 and 20  $\mu\text{m}$ , with the same elastic modulus for the entire lens capsule,  $E = 1.00$  MPa, were analysed and compared.

*Evaluation of the lens mechanical properties and geometry.* Considering the elastic modulus values of the lens tissues (nucleus, cortex and capsule) to be homogeneous, a full factorial design was performed to analyse the effect of its magnitude on the ability of the lens to change its shape, i.e., the change in lens power ( $\Delta L_P$  – dioptres (D)), the change in lens thickness due to the nucleus ( $\frac{\Delta L_T}{\Delta L_P}$  – %), the anterior and posterior radii of curvature ( $\frac{\Delta r_a}{\Delta L_P}$  and  $\frac{\Delta r_p}{\Delta L_P}$  – mm/D) and the lens thickness and diameter ( $\frac{\Delta L_T}{\Delta L_P}$  and  $\frac{\Delta \varnothing_L}{\Delta L_P}$  – mm/D). To do so, following the DoE methodology used in our previous work analysing the design of intraocular lenses (IOLs)<sup>28,39</sup>, a full factorial design with four factors (the elastic modulus values of the nucleus, cortex and anterior and posterior capsule) and five levels, i.e.,  $4^5 = 625$ , was performed. The minimum and maximum level for the mechanical properties of the lens capsule and lens nucleus and cortex were obtained from literature<sup>20–22,35,36</sup>. Table 1 presents the elastic modulus levels of the factors analysed.

Furthermore, to observe the influence of the geometry, the analysis was performed for two lens geometries depending on age (17 and 29 y/o<sup>29,30</sup>), resulting in  $625 \cdot 2 = 1250$  simulations. For these analyses, the distribution of the capsule thickness reported by Fincham<sup>26</sup>, indicated by the black line in Fig. 3, was considered.

## Results

In this section, the influences of the lens stiffness gradient is explained first. Then, the distribution of the capsule thickness on the ability of the lens to change its shape is analysed. Once both effects are numerically analysed, the lens mechanical properties for two different geometries corresponding to two different ages (17 and 29 y/o)

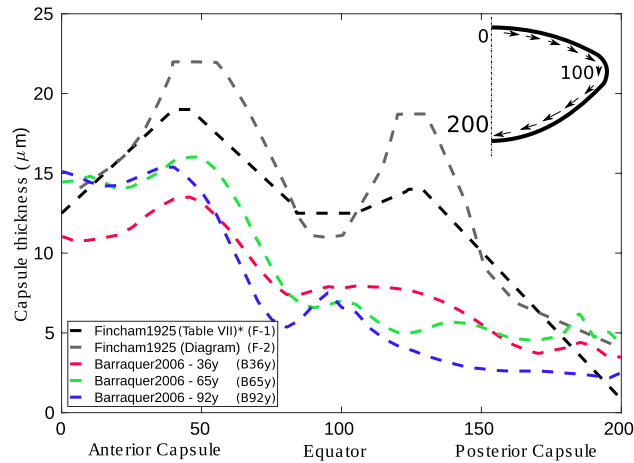


**Figure 3.** Five different cases of capsule thickness distribution ( $\mu\text{m}$ ) as a function of the standardised capsule perimeter. An outline for understanding standardisation is attached. \*The mean values were obtained with the first and third row data from Table VII—thickness of lens capsule from Fincham<sup>26</sup>. The second row data of this table were discarded due to notable differences with the other data.

Factors	Elastic modulus (kPa)				
	L1	L2	L3	L4	L5
Anterior capsule	100	300	500	700	1000
Posterior capsule	100	300	500	700	900
Cortex	0.75	1.50	2.25	3.00	3.75
Nucleus	0.10	0.20	0.30	0.40	0.50

**Table 1.** Material properties for the different levels (L) of the DoE. Four factors and five levels were considered for two different geometries according to age (17 and 29 y/o).

are analysed following the design of experiments (DoE) methodology with a full factorial design<sup>28</sup>. To evaluate the ability of the lens to change its shape, the results are presented as a ratio between the variation of each biometric term and the change in lens power, i.e., the following ratios:  $\frac{\Delta r_a}{\Delta L_p}$ ,  $\frac{\Delta r_p}{\Delta L_p}$ ,  $\frac{\Delta L_T}{\Delta L_p}$  and  $\frac{\Delta \varnothing_L}{\Delta L_p}$ . This was possible to perform because all analyses followed a linear response. Additionally, the maximum change in lens power ( $\Delta L_p$ ) and the percentage of variation in the lens thickness due to the nucleus ( $\frac{\Delta L_N}{\Delta L_T}$ ) were registered. All ratios and the maximum change in lens power are presented in absolute values. Therefore, a higher ratio between the anterior and posterior radius values ( $\frac{\Delta r_a}{\Delta L_p}$ ,  $\frac{\Delta r_p}{\Delta L_p}$ ) indicates a greater effect of the corresponding parameter on the focal change of the lens. Note that the ratios  $\frac{\Delta r_a}{\Delta L_p}$  and  $\frac{\Delta r_p}{\Delta L_p}$  can not be compared faithfully between them as their initial value is different and thus their absolute change affects differently in Eq. (2).

**Influence of the lens stiffness gradient.** Figure 4a,b show the influence of the stiffness gradient on the dynamic optical and biometric lens measurements for the 29 y/o lens geometry. There is a notable difference between the homogeneous materials (nucleus and cortex) scenario #HC and scenario #A, especially in terms of the  $\Delta L_p$ , 2.26 against 1.95 D, an increase of 16%. This is mainly produced by the  $\Delta r_p$ , which is 0.17 mm in scenario #HC against 0.03 mm for scenario #A, implying a disaccommodation amplitude of 0.42 D more for scenario #HC in the posterior surface term of Eq. (2). Although the change in the anterior surface is the main factor accountable for lens accommodation,  $\Delta r_a$  was similar for both scenarios, 1.71 and 1.83 mm for scenarios #HC and #A, respectively, which implied a disaccommodation amplitude of only 0.11 D more for scenario #A.

This difference in  $\Delta L_p$  could be explained by an underestimation of the stiffness gradient. After all, the cortex and nucleus were not differentiated in the experimental study by Weeber et al.<sup>22</sup>. Thus, we designed four lens stiffness gradient scenarios with two different approaches (#B, #C, #E and #F). For all four scenarios, the results were similar to the homogeneous scenario (#HC) with uniform stiffness in the nucleus and cortex. Surprisingly, when the stiffness gradient starts in the nucleus (#C), the results are almost identical to those of the scenario with uniform stiffness (#HC).

Last, there was hardly any difference between scenarios #A and #D, which indicated the lower influence of the elastic modulus on the equatorial lens diameter. All analyses are summarised in Table 2.

**Influence of the lens capsule thickness.** The influence of the distribution of the capsule thickness for the five cases analysed is shown in Fig. 4c,d. There is a statistically significant difference ( $p_{value} < 0.05$ ) between

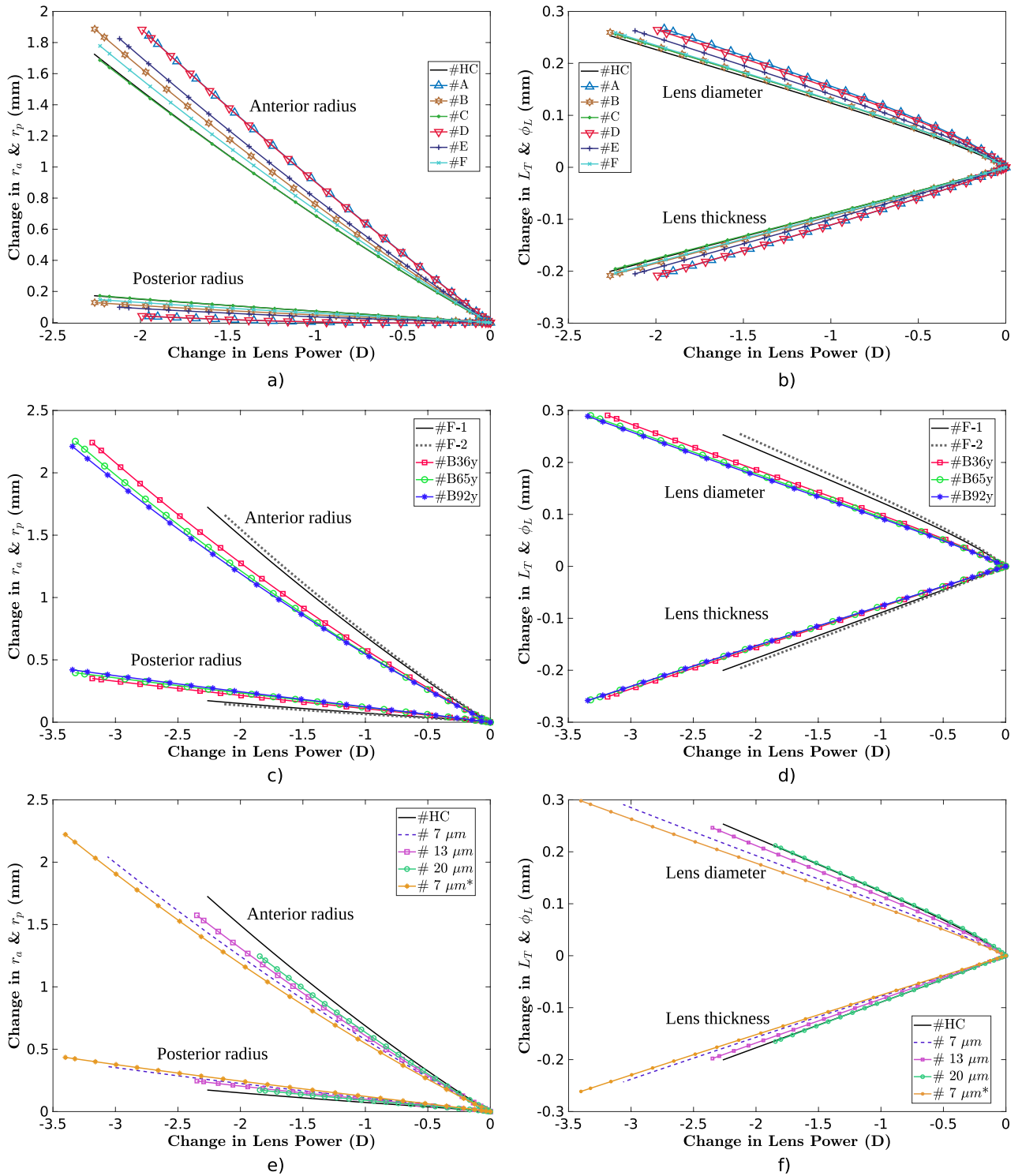


**Figure 4.** Change in the main biometric parameters of the lens for different case studies according to the focal change of the lens: anterior and posterior radius (a,c,e) and lens thickness and diameter (b,d,f). (a) and (b) depict the results for all stiffness gradient scenarios described in “Evaluation of the lens stiffness gradient” section; (c) and (d), the results for the five experimental distributions of the lens capsule thickness shown in Fig. 3; (e) and (f), the results for different uniform lens capsule thickness together with the reference scenario (#HC). All calculations were performed for the 29 y/o lens geometry and summarised in Table 2.

Scenario (section)	Factors					Change in the lens shape					
	CT	AC (MPa)	PC (MPa)	LC (kPa)	LN (kPa)	$\Delta L_P$ (D)	$\frac{\Delta L_N}{\Delta L_T}$ (%)	$\frac{\Delta r_a}{\Delta L_P}$ (mm/D)	$\frac{\Delta r_p}{\Delta L_P}$ (mm/D) $10^{-2}$	$\frac{\Delta L_T}{\Delta L_P}$ (mm/D) $10^{-2}$	$\frac{\Delta \varnothing_L}{\Delta L_P}$ (mm/D) $10^{-2}$
#HC, F-1 (G,T,TH)	F1	1.00	0.70	3.00	0.30	2.26	75.84	0.76	7.62	11.19	8.85
#A (G)	F1	1.00	0.70	E(FV)	E(FV)	1.95	71.45	0.94	2.04	13.63	10.50
#B (G)	F1	1.00	0.70	E(FV)	E(FV)	2.26	73.45	0.83	5.67	11.48	9.21
#C (G)	F1	1.00	0.70	E(FV)	E(FV)	2.23	74.99	0.75	7.73	11.48	8.75
#D (G)	F1	1.00	0.70	E(FV)	E(FV)	1.99	71.83	0.94	2.12	13.28	10.46
#E (G)	F1	1.00	0.70	E(FV)	E(FV)	2.11	73.65	0.86	4.63	12.39	9.67
#F (G)	F1	1.00	0.70	E(FV)	E(FV)	2.23	74.56	0.79	6.60	11.60	9.11
#F-2 (T)		1.00	0.70	3.00	0.30	2.13	75.81	0.78	6.80	11.98	9.21
#B-36y (T)		1.00	0.70	3.00	0.30	3.18	78.42	0.70	11.01	9.11	7.87
#B-65y (T)		1.00	0.70	3.00	0.30	3.32	80.25	0.67	11.94	8.73	7.73
#B-92y (T)		1.00	0.70	3.00	0.30	3.34	81.76	0.66	12.55	8.63	7.71
#7 μm (UT)		1.00	1.00	3.00	0.30	3.06	78.17	0.66	11.80	9.50	7.93
#10 μm (UT)		1.00	1.00	3.00	0.30	2.34	78.55	0.67	10.42	10.48	8.42
#20 μm (UT)		1.00	1.00	3.00	0.30	1.84	79.32	0.67	9.34	11.49	8.95
#7 μm* (UT)		1.00	0.70	3.00	0.30	3.40	78.84	0.65	12.77	8.76	7.68

**Table 2.** The results for the corresponding scenario, together with the corresponding section to which it belongs, gradient (G), thickness (T) or uniform thickness (UT), is described. The corresponding factor for each scenario is described: the distribution of the capsule thickness (CT) for the gradient section. In turn, the section thickness describes itself, as do the Young’s modulus values of the anterior capsule (AC), posterior capsule (PC), lens cortex (LC) and lens nucleus (LN). Furthermore, the registered lens biometric measurements are presented: the maximum change in lens power ( $\Delta L_P$ ), the variation in the lens thickness of the nucleus ( $\frac{\Delta L_N}{\Delta L_T}$ ) and the following ratios:  $\frac{\Delta r_a}{\Delta L_P}$ ,  $\frac{\Delta r_p}{\Delta L_P}$ ,  $\frac{\Delta L_T}{\Delta L_P}$ , and  $\frac{\Delta \varnothing_L}{\Delta L_P}$ .

the ratios obtained for all biometric terms with respect to the simulations performed with the distributions of the capsule thickness reported by Fincham<sup>26</sup> and Barraquer et al.<sup>27</sup>.

The results obtained with the capsule thickness distribution reported by Barraquer et al.<sup>27</sup> (referred to as Barraquer’s group hereinafter) presented a larger average change in lens power, 3.27 D against 2.18 D. For Barraquer’s<sup>27</sup> group, a higher ratio in the posterior radius of curvature was presented, with an average value ( $\frac{\Delta r_p}{\Delta L_P}$ ) of  $11.80 \cdot 10^{-2}$  against  $7.24 \cdot 10^{-2}$  mm/D for those obtained with the capsule thickness distribution reported by Fincham<sup>26</sup> (referred to as Fincham’s group hereinafter). As a consequence, a lower ratio in the anterior radius was obtained, with an average value ( $\frac{\Delta r_a}{\Delta L_P}$ ) of 0.68 against 0.77 mm/D.

The results for Barraquer’s<sup>27</sup> group presented a lower ratio of lens thickness and diameter, with average values ( $\frac{\Delta L_T}{\Delta L_P}$ ,  $\frac{\Delta \varnothing_L}{\Delta L_P}$ ) of  $7.78 \cdot 10^{-2}$  and  $8.82 \cdot 10^{-2}$  mm/D, whereas for Fincham’s group, average values ( $\frac{\Delta L_T}{\Delta L_P}$ ,  $\frac{\Delta \varnothing_L}{\Delta L_P}$ ) of  $9.05 \cdot 10^{-2}$  and  $11.53 \cdot 10^{-2}$  mm/D were obtained, respectively. Moreover, the variation in lens nucleus with the change in lens thickness ( $\frac{\Delta L_N}{\Delta L_T}$ ) was 80.14% as determined by Barraquer’s group, in comparison with 75.82% for Fincham’s<sup>26</sup>.

Regarding the case of a uniform capsule thickness, when the thickness is lower, the posterior radius of curvature exerts greater influence on the focal change of the lens, as displayed in Fig. 4e. The thinnest thickness (#7 μm) of the lens capsule presented the highest lens focal change of 3.06 D, in comparison with 1.84 D for the thickest thickness (#20 μm). Regarding the changes in lens thickness and diameter, as shown in Fig. 4f, the lower the uniform thickness is, the lower the ratio of the lens thickness and diameter. For the thinnest thickness (#7 μm),  $\frac{\Delta L_T}{\Delta L_P}$  and  $\frac{\Delta \varnothing_L}{\Delta L_P}$  of  $9.50 \cdot 10^{-2}$  and  $7.93 \cdot 10^{-2}$  mm/D were obtained, respectively, whilst for the thickest thickness (#20 μm),  $\frac{\Delta L_T}{\Delta L_P}$  and  $\frac{\Delta \varnothing_L}{\Delta L_P}$  of  $11.49 \cdot 10^{-2}$  and  $8.95 \cdot 10^{-2}$  mm/D were obtained, respectively. A similar case as the thinnest thickness (#7 μm), but with an elastic modulus for the posterior capsule of 0.70 MPa, was also calculated (#7 μm\*), presenting a maximum change in lens power of 3.40 D. Interestingly, all cases present similar  $\frac{\Delta L_N}{\Delta L_T}$  ratios of approximately 78%. All analyses are summarised in Table 2.

**Influence of the mechanical properties and age-related lens geometry on accommodation.** After the 1, 250 simulations, a screening analysis was performed to remove data in which the change of the lens power increases. These cases corresponded to the lowest level of the elastic modulus of the cortex ( $E = 0.75$  kPa) and the highest levels of the nucleus ( $E = 0.50$  kPa) and the posterior capsule ( $E = 0.90$  MPa). This will be explained in the evaluation of the DoE. In total, 115 simulations were removed.

For the remaining simulations, 1, 135, a regression model with  $R^2 > 99\%$  was designed for each response ( $\Delta L_P$ ,  $\frac{\Delta L_N}{\Delta L_T}$ ,  $\frac{\Delta r_a}{\Delta L_P}$ ,  $\frac{\Delta r_p}{\Delta L_P}$ ,  $\frac{\Delta L_T}{\Delta L_P}$ , and  $\frac{\Delta \varnothing_L}{\Delta L_P}$ ) to evaluate the biomechanical effects of the factors of the DoE performed (anterior capsule stiffness (AC), posterior capsule stiffness (PC), lens cortex stiffness (LC), lens nucleus stiffness (LN), and lens geometry depending on age (Age)). The statistical model used to describe the results included up to second order terms.

The influence of each factor on the responses analysed was evaluated by means of a Pareto analysis. The change in lens power ( $\Delta L_P$ ) is mostly influenced by the stiffness of the posterior capsule (PC, 42.59%), the lens nucleus

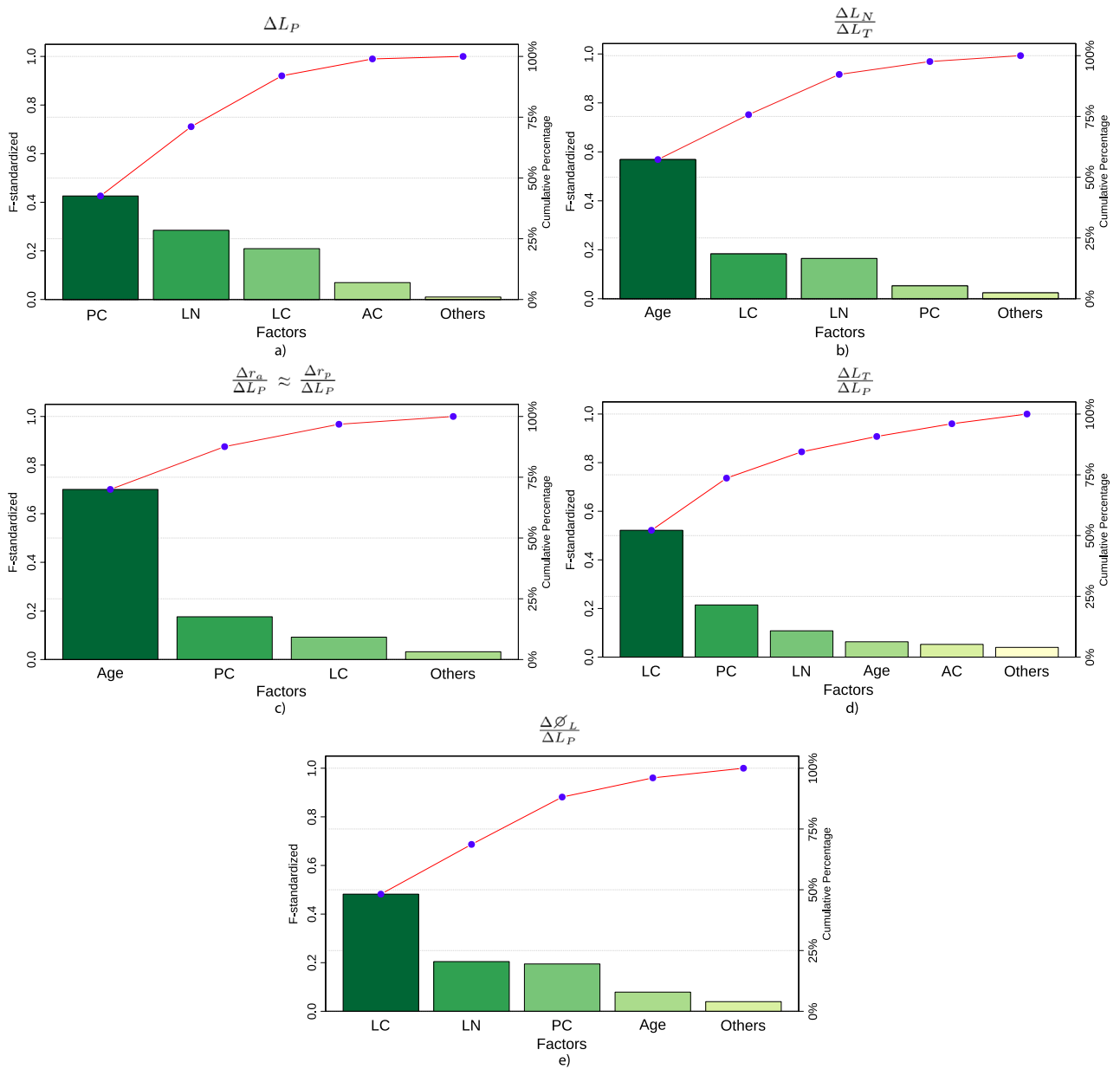


**Figure 5.** Pareto chart of the standardised effects on the six responses analysed:  $\Delta L_P$  (a),  $\frac{\Delta L_N}{\Delta L_T}$  (b),  $\frac{\Delta r_a}{\Delta L_P} \approx \frac{\Delta r_p}{\Delta L_P}$  (c),  $\frac{\Delta L_T}{\Delta L_P}$  (d), and  $\frac{\Delta \emptyset_L}{\Delta L_P}$  (e). As the results for the anterior and posterior radius were similar, a Pareto chart is used for both factors. Factors: the stiffness of the anterior capsule (AC), the posterior capsule (PC), lens cortex (LC) and lens nucleus (LN), and the age-related lens geometry (Age). Terms in the statistical model up to second order were included.

(LN, 28.49%) and the lens cortex (LC, 20.92%); see Fig. 5a. Other responses with respect to the age-related lens geometry were statistically significant, but their influences were lower than the stiffness of the PC, LN and LC.

The age-related lens geometry was the most influential factor (Age, 58.86%) on lens nucleus variation in the total change in lens thickness ( $\frac{\Delta L_N}{\Delta L_T}$ ), as displayed in Fig. 5b, followed by the internal properties of the lens (LC, 18.95% and LN, 16.44%). The lens geometry depending on age (Age, 69.98%) was also the most relevant factor to the ratios  $\frac{\Delta r_a}{\Delta L_P}$  and  $\frac{\Delta r_p}{\Delta L_P}$ ; see Fig. 5c. As the initial anterior and posterior radii in the 17 y/o lens are lower, their variation produces a greater change in lens power; see Eq. (2). This explains the relevance of the age-related lens geometry to the ratios  $\frac{\Delta r_a}{\Delta L_P}$  and  $\frac{\Delta r_p}{\Delta L_P}$ .

A similar trend occurs in the ratios  $\frac{\Delta L_T}{\Delta L_P}$  and  $\frac{\Delta \emptyset_L}{\Delta L_P}$ ; see Fig. 5d,e. The stiffness of the lens cortex is the most influential factor for both responses. To a lesser extent, the posterior capsule and lens nucleus also exert relevant influences on both responses. Further analysis based on the Pearson correlation matrix (see Fig. 6) supports these findings.

A stiffer lens cortex produced a greater change in the lens power ( $\Delta L_P$ ); see Fig. 6. Moreover, the posterior capsule and the lens cortex were confirmed to be strongly inversely correlated with the change in lens power. Surprisingly,  $\frac{\Delta r_a}{\Delta L_P}$  and  $\frac{\Delta r_p}{\Delta L_P}$  presented a high correlation with the posterior capsule, but not with the anterior

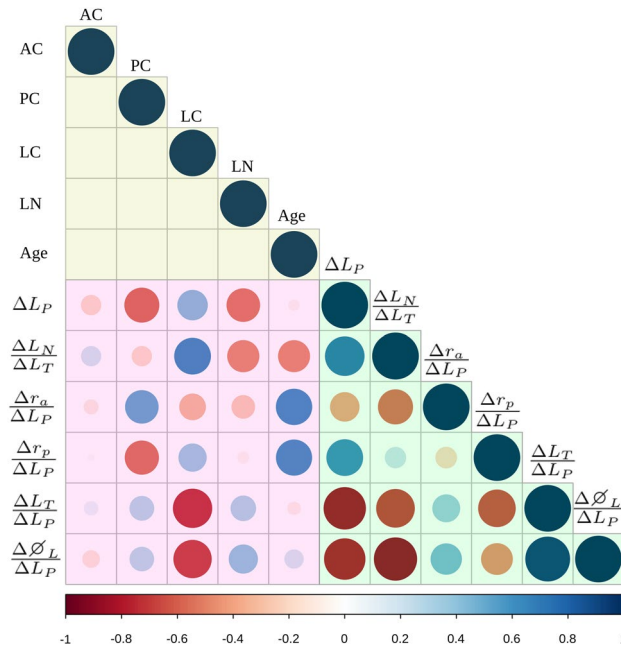


**Figure 6.** Pearson correlation matrix (full-level factorial design,  $2 \cdot 5^4 = 1250$ ). Factors: stiffness of the anterior capsule (AC), posterior capsule (PC), lens cortex (LC) and lens nucleus (LN), and the lens geometry depending on age (Age). Level - 1 corresponds to 17 y/o and level 1 to 29 y/o). Biometric lens measurements:  $\Delta L_p$ ,  $\frac{\Delta L_N}{\Delta L_T}$ ,  $\frac{\Delta r_a}{\Delta L_p}$ ,  $\frac{\Delta r_p}{\Delta L_p}$ ,  $\frac{\Delta L_T}{\Delta L_p}$ , and  $\frac{\Delta \phi_L}{\Delta L_p}$ . The color of each circle depicts whether the linear correlation is direct (positive) or inverse (negative) (blueish palette, direct; reddish palette, inverse). The larger the circle diameter, the higher the correlation.

capsule, which confirms that the posterior capsule governs the change in lens power. Regarding the change in lens thickness due to the nucleus ( $\frac{\Delta L_N}{\Delta L_T}$ ), the greater the difference in stiffness between the nucleus and cortex, the larger the change in  $\frac{\Delta L_N}{\Delta L_T}$  is. For the younger geometry, the  $\frac{\Delta L_N}{\Delta L_T}$  was higher.

A stiffer posterior capsule produced a higher ratio  $\frac{\Delta r_a}{\Delta L_p}$  and a lower ratio  $\frac{\Delta r_p}{\Delta L_p}$ . As mentioned, the 29 y/o lens (value 1 in Fig. 6) requires a greater change in the anterior and posterior radii to produce the same change in lens power (strong direct correlation with  $\frac{\Delta r_a}{\Delta L_p}$  and  $\frac{\Delta r_p}{\Delta L_p}$ ).

The stiffness of the lens cortex was strongly inversely correlated with the ratios  $\frac{\Delta L_T}{\Delta L_p}$  and  $\frac{\Delta \phi_L}{\Delta L_p}$ , which indicates that a stiffer lens cortex produces a lower change in the ratios  $\frac{\Delta L_T}{\Delta L_p}$  and  $\frac{\Delta \phi_L}{\Delta L_p}$ . The posterior capsule and lens nucleus exhibited direct correlation with  $\frac{\Delta L_T}{\Delta L_p}$  and  $\frac{\Delta \phi_L}{\Delta L_p}$ . The  $\frac{\Delta L_T}{\Delta L_p}$  ratio presented a slight direct correlation with the anterior capsule and a slight inverse correlation with the age-related lens geometry. Contrary to this, the  $\frac{\Delta \phi_L}{\Delta L_p}$  ratio presented the opposite behaviour as described for the  $\frac{\Delta L_T}{\Delta L_p}$ .

Regarding the correlation between the lens biometric terms, there was a strong direct correlation between the change in lens power ( $\Delta L_p$ ) and the  $\frac{\Delta r_p}{\Delta L_p}$  ratio, whereas there was a strong inverse correlation between  $\frac{\Delta L_T}{\Delta L_p}$ ,  $\frac{\Delta \phi_L}{\Delta L_p}$  and the change in lens power ( $\Delta L_p$ ).

There was an inverse correlation between the  $\frac{\Delta r_a}{\Delta L_p}$  and  $\frac{\Delta r_p}{\Delta L_p}$  ratios, a strong inverse correlation between  $\frac{\Delta r_p}{\Delta L_p}$  and  $\frac{\Delta L_T}{\Delta L_p}$  and a strong direct correlation between  $\frac{\Delta L_T}{\Delta L_p}$  and  $\frac{\Delta \phi_L}{\Delta L_p}$ . Main effect and interaction plots were analysed to confirm the consistency of the correlation analysis.

### Discussion

The results in this study provide essential data regarding how the crystalline lens changes its shape depending on different lens factors such as the stiffness gradient of the lens<sup>21,22</sup>, the distribution of the capsule thickness<sup>26,27</sup>, the mechanical properties of the lens nucleus, cortex and anterior and posterior capsules in young subjects<sup>35,36</sup>, and the influence of two different lens geometries depending on age (17 and 29 y/o)<sup>29</sup>.

The stiffness gradient of the lens was evaluated using different possible scenarios for a young adult subject based on experimental data<sup>22</sup>. There was a significant difference in the posterior radius response between scenario #A, with a stiffness gradient (see Fig. 4a,b and Table 2), and a scenario with homogeneous materials (scenario #HC). Nevertheless, it is true that the stiffness gradient might be understudied, as the mechanical properties of the nucleus and cortex were not individually characterised due to the high complexity of taking these measurements. When smoothing the stiffness gradient, there was similarity between the results presented (see scenarios #B, #C, #E and #F in Figs. 3a, 4b and Table 2). As observed in the study, the difference in stiffness between the nucleus and cortex is crucial to how the lens changes its shape. The greater the difference is, the more significant the effect of the posterior and anterior surface, and thus the higher the change in lens power, as presented throughout the study. Based on this statement, the ideal case is the scenario with homogeneous materials (#HC), where the difference between the stiffness of the nucleus and cortex is the greatest and most abrupt. Thus, the



closer the gradient is to the homogeneous case, the greater the focal change of the lens. Therefore, we consider that the assumption of modelling the nucleus and cortex with homogeneous behaviour is appropriate for a theoretical approach.

Regarding the capsule thickness distribution, five different distributions, divided into Fincham<sup>26</sup> and Barraquer et al.<sup>27</sup> groups, and four different uniform thicknesses were evaluated. The main difference was that for Barraquer's<sup>27</sup> group, there is a decrease in thickness in the posterior capsule, as shown in Fig. 3. This decrease entails a higher lens focus and diminished changes in lens thickness and diameter, mainly produced by the increased changes in the posterior radius and lens nucleus. The trend was confirmed by the homogeneous scenarios; see Table 2. A thinner capsule thickness produces a similar effect to that of a capsule with a lower elastic modulus.

The use of numerical models along with advanced statistical tools (i.e., full factorial analysis) allows the study of the impacts of lens factors (material behaviour of the anterior capsule, posterior capsule, lens cortex and nucleus, and the age-related lens geometry) on the ability of the lens to change its shape (change in lens power ( $\Delta L_p$ ), percentage of the lens nucleus in the change in the lens thickness ( $\frac{\Delta L_N}{\Delta L_T}$ ), and the following ratios which reproduce how the shape of the lens changes:  $\frac{\Delta r_a}{\Delta L_p}$ ,  $\frac{\Delta r_p}{\Delta L_p}$ ,  $\frac{\Delta L_T}{\Delta L_p}$ , and  $\frac{\Delta \varnothing_L}{\Delta L_p}$ ). Based on the presented results, the mechanical properties of the posterior capsule, lens cortex and lens nucleus are the most important factors affecting the ability of the lens to change its shape. The age-related lens geometry and the stiffness of the anterior capsule were also statistically significant, but their influences were lower.

Individually, the analysed factors differently influenced the ability of the lens to change its shape; see Fig. 6. A greater stiffness in the anterior capsule produced a lower change in lens power. It also presented a weak direct correlation with the lens thickness and a weak inverse correlation with the lens diameter. The posterior capsule presented a strong inverse correlation with the change in lens power and the posterior radius. A stiffer lens cortex implied a greater change in lens power and a higher ratio with respect to the posterior radius. The stiffness of the cortex was strongly inversely correlated with the thickness and diameter ratios. The stiffness of the lens nucleus presented the opposite behaviour as that of the cortex, which confirmed the strong influence of the difference in stiffness between both observations in the elastic gradient section. Furthermore, the screening analysis performed in the DoE where 115 simulations were removed showed that the lens would lose its accommodative properties if the stiffness ratio between the nucleus and cortex would be close to 1.00, which could explain some causes of presbyopia. The stiffness of the lens nucleus might have presented a weaker correlation than the cortex due to the lower variation in the levels of the DoE performed.

Finally, the 17 y/o lens geometry presented a higher change in lens power. The change in the lens geometry was strongly and directly correlated with the anterior and posterior radius ratios because the changes in the anterior and posterior radii differ depending on the initial values in the accommodated state. A variation in the anterior radius from 6.00 to 8.00 mm does not influence the same focal change as the variation from 8.00 to 10.00 mm; see Eq. (2). Furthermore, the lens thickness ratio was lower in the 29 y/o lens geometry, whilst the lens diameter ratio was larger.

One of the limitations of this study is that contrary to the works of Manns et al.<sup>13</sup> and Augusteyn et al.<sup>14</sup>, the force exerted to stretch the lens could not be compared with experimental data. This result was due to two factors: first, it would have involved the characterisation of all relevant tissues (ciliary body and sclera), and second, the exact geometry involved in these experimental tests. Nevertheless, with the essential data provided in this study, any change in lens shape for any hominid species, including humans, could be reproduced, which validates the model. One weakness is that the study was focused on healthy crystalline lenses (17–29 y/o). It would be interesting to broaden the scope of this research to include pathological eyes, with cataracts or presbyopia, of older adults.

To ease the understanding of the objective of the study, the thick lens formula has been used, see Eq. (2), instead of a GRIN optical model. The authors have checked that the pattern results of the study is the same with a four-surface shell model<sup>40</sup> and the use of Eq. (2) with an equivalent refractive index. The authors also have checked the consistency of the study observing the change in curvature of the posterior and anterior radius nucleus. Moreover, Van Sompel et al.<sup>7</sup> also showed for the 29 y/o subject that the relative lens accommodative amplitude appears to be unaltered using a uniform or GRIN optical model. The group will focus on validating a GRIN optical model for the crystalline lens in future investigations.

Unlike other numerical papers that modelled the zonules with few “wires”, we have modelled them in order to provide continuity in the displacement field of the lens. Their design was set according to experimental images<sup>34</sup>. Contrary to other studies, we evaluated the main biometric lens parameters which explain its change in shape ( $\frac{\Delta r_a}{\Delta L_p}$ ,  $\frac{\Delta r_p}{\Delta L_p}$ ,  $\frac{\Delta L_T}{\Delta L_p}$ ,  $\frac{\Delta \varnothing_L}{\Delta L_p}$  and  $\frac{\Delta L_N}{\Delta L_T}$ ), and interestingly, most simulations prove that the  $\frac{\Delta L_N}{\Delta L_T}$  ratio was approximately 80%, as Brown<sup>31</sup> experimentally reported. Like Van Sompel et al.<sup>7</sup>, we observed that the lens geometry has an important role with respect to the change in lens focus. However, the change in lens focus is overly complex since it depends on so many factors, including capsule thickness, mechanical properties of all parts of the lens, geometry, etc., that it is difficult to highlight one over the others. The situation becomes even more complicated in accommodation, which is produced not only by focal changes of the lens but also by lens movement. This study provides compelling evidence that the stiffness values of the posterior capsule, lens cortex and nucleus are the most influential factors with respect to the ability of the lens to change its shape.

This work has been made possible by the emergence of new quality experimental studies, which enables the design of more complex and realistic numerical models. This study has demonstrated how lens focus is influenced by the main lens mechanical properties, allowing for a slightly improved understanding of the accommodation process. We hope to illuminate the mechanisms of the accommodation field, helping manufacturers and researchers find better solutions for dysfunctional lens conditions such as presbyopia and cataracts. Furthermore, our group will be focused on how presbyopia progresses according to the mechanical properties of age-related lens.

Received: 8 February 2021; Accepted: 22 April 2021  
Published online: 05 May 2021

## References

1. Glasser, A. Restoration of accommodation: Surgical options for correction of presbyopia. *Clin. Exp. Optom.* **91**, 279–295. <https://doi.org/10.1111/j.1444-0938.2008.00260.x> (2008).
2. Alió, J. L., del Barrio, J. L. A. & Vega-Estrada, A. Accommodative intraocular lenses: Where are we and where we are going. *Eye Vis.* **4**, 1–12. <https://doi.org/10.1186/s40662-017-0077-7> (2017).
3. de la Hoz, A. *et al.* Design and ex situ performance of a shape-changing accommodating intraocular lens. *Optica* **6**, 1050. <https://doi.org/10.1364/optica.6.001050> (2019).
4. Burd, H., Judge, S. & Cross, J. Numerical modelling of the accommodating lens. *Vis. Res.* **42**, 2235–2251. [https://doi.org/10.1016/S0042-6989\(02\)00094-9](https://doi.org/10.1016/S0042-6989(02)00094-9) (2002).
5. Hermans, E., Dubbelman, M., van der Heijde, G. & Heethaar, R. Estimating the external force acting on the human eye lens during accommodation by finite element modelling. *Vis. Res.* **46**, 3642–3650. <https://doi.org/10.1016/j.visres.2006.04.012> (2006).
6. Weeber, H. A. & van der Heijde, R. G. On the relationship between lens stiffness and accommodative amplitude. *Exp. Eye Res.* **85**, 602–607. <https://doi.org/10.1016/j.exer.2007.07.012> (2007).
7. Sompel, D. V., Kunkel, G. J., Hersh, P. S. & Smits, A. J. Model of accommodation: Contributions of lens geometry and mechanical properties to the development of presbyopia. *J. Cataract Refract. Surg.* **36**, 1960–1971. <https://doi.org/10.1016/j.jcrs.2010.09.001> (2010).
8. Lanchares, E., Navarro, R. & Calvo, B. Hyperelastic modelling of the crystalline lens: Accommodation and presbyopia. *J. Optom.* **5**, 110–120. <https://doi.org/10.1016/j.optom.2012.05.006> (2012).
9. Wang, K., Venetsanos, D., Wang, J. & Pierscionek, B. K. Gradient moduli lens models: How material properties and application of forces can affect deformation and distributions of stress. *Sci. Rep.* **6**, 1–10 (2016).
10. Wang, K., Venetsanos, D. T., Wang, J., Augousti, A. T. & Pierscionek, B. K. The importance of parameter choice in modelling dynamics of the eye lens. *Sci. Rep.* **7**, 1–12. <https://doi.org/10.1038/s41598-017-16854-9> (2017).
11. Wang, K. *et al.* A modeling approach for investigating opto-mechanical relationships in the human eye lens. *IEEE Trans. Biomed. Eng.* **67**, 999–1006. <https://doi.org/10.1109/tbme.2019.2927390> (2020).
12. Glasser, A. & Campbell, M. C. Biometric, optical and physical changes in the isolated human crystalline lens with age in relation to presbyopia. *Vis. Res.* **39**, 1991–2015. [https://doi.org/10.1016/S0042-6989\(98\)00283-1](https://doi.org/10.1016/S0042-6989(98)00283-1) (1999).
13. Manns, F. *et al.* Optomechanical response of human and monkey lenses in a lens stretcher. *Investig. Ophthalmol. Vis. Sci.* **48**, 3260. <https://doi.org/10.1167/iovs.06-1376> (2007).
14. Augusteyn, R. C. *et al.* Age-dependence of the optomechanical responses of ex vivo human lenses from India and the USA, and the force required to produce these in a lens stretcher: The similarity to in vivo disaccommodation. *Vis. Res.* **51**, 1667–1678. <https://doi.org/10.1016/j.visres.2011.05.009> (2011).
15. Nankivil, D. *et al.* The zonules selectively alter the shape of the lens during accommodation based on the location of their anchorage points. *Investig. Ophthalmol. Vis. Sci.* **56**, 1751–1760. <https://doi.org/10.1167/iovs.14-16082> (2015).
16. Michael, R. *et al.* Deformations and ruptures in human lenses with cortical cataract subjected to ex vivo simulated accommodation. *Investig. Ophthalmol. Vis. Sci.* **62**, 12. <https://doi.org/10.1167/iovs.62.1.12> (2021).
17. Glasser, A., Wendt, M. & Ostrin, L. Accommodative changes in lens diameter in rhesus monkeys. *Investig. Ophthalmol. Vis. Sci.* **47**, 278. <https://doi.org/10.1167/iovs.05-0890> (2006).
18. Ramasubramanian, V. & Glasser, A. Objective measurement of accommodative biometric changes using ultrasound biomicroscopy. *J. Cataract Refract. Surg.* **41**, 511–526. <https://doi.org/10.1016/j.jcrs.2014.08.033> (2015).
19. Burd, H., Wilde, G. & Judge, S. Can reliable values of Young's modulus be deduced from Fisher's (1971) spinning lens measurements?. *Vis. Res.* **46**, 1346–1360. <https://doi.org/10.1016/j.visres.2005.07.012> (2006).
20. Fisher, R. F. Elastic constants of the human lens capsule. *J. Physiol.* **201**, 1–19. <https://doi.org/10.1113/jphysiol.1969.sp008739> (1969).
21. Heys, K. R., Cram, S. L. & Truscott, R. J. W. Massive increase in the stiffness of the human lens nucleus with age: The basis for presbyopia?. *Mol. Vis.* **10**, 956–963 (2004).
22. Weeber, H. A., Eckert, G., Pechhold, W. & van der Heijde, R. G. L. Stiffness gradient in the crystalline lens. *Graefes Arch. Clin. Exp. Ophthalmol.* **245**, 1357–1366. <https://doi.org/10.1007/s00417-007-0537-1> (2007).
23. Wilde, G. S., Burd, H. J. & Judge, S. J. Shear modulus data for the human lens determined from a spinning lens test. *Exp. Eye Res.* **97**(1), 36–48 (2012).
24. Maceo, B. M. *et al.* Contribution of the crystalline lens gradient refractive index to the accommodation amplitude in non-human primates: In vitro studies. *J. Vis.* **11**, 23–23. <https://doi.org/10.1167/11.13.23> (2011).
25. Birkenfeld, J., de Castro, A., Ortiz, S., Pascual, D. & Marcos, S. Contribution of the gradient refractive index and shape to the crystalline lens spherical aberration and astigmatism. *Vis. Res.* **86**, 27–34. <https://doi.org/10.1016/j.visres.2013.04.004> (2013).
26. Fincham, E. F. The changes in the form of the crystalline lens in accommodation. *Trans. Opt. Soc.* **26**, 239–269. <https://doi.org/10.1088/1475-4878/26/5/301> (1925).
27. Barraquer, R. I., Michael, R., Abreu, R., Lamarca, J. & Tresserra, F. Human lens capsule thickness as a function of age and location along the sagittal lens perimeter. *Investig. Ophthalmol. Vis. Sci.* **47**, 2053. <https://doi.org/10.1167/iovs.05-1002> (2006).
28. Montgomery, D. *Design & Analysis of Experiments* 5th edn. (Wiley, 2001).
29. Borja, D. *et al.* Optical power of the isolated human crystalline lens. *Investig. Ophthalmol. Vis. Sci.* **49**, 2541. <https://doi.org/10.1167/iovs.07-1385> (2008).
30. Martinez-Enriquez, E. *et al.* Age-related changes to the three-dimensional full shape of the isolated human crystalline lens. *Investig. Ophthalmol. Vis. Sci.* **61**, 11. <https://doi.org/10.1167/iovs.61.4.11> (2020).
31. Brown, N. The change in shape and internal form of the lens of the eye on accommodation. *Exp. Eye Res.* **15**, 441–459. [https://doi.org/10.1016/0014-4835\(73\)90136-x](https://doi.org/10.1016/0014-4835(73)90136-x) (1973).
32. Dubbelman, M., der Heijde, G. V., Weeber, H. & Vrensen, G. Changes in the internal structure of the human crystalline lens with age and accommodation. *Vis. Res.* **43**, 2363–2375. [https://doi.org/10.1016/S0042-6989\(03\)00428-0](https://doi.org/10.1016/S0042-6989(03)00428-0) (2003).
33. Hermans, E., Dubbelman, M., van der Heijde, R. & Heethaar, R. The shape of the human lens nucleus with accommodation. *J. Vis.* **7**, 16. <https://doi.org/10.1167/7.10.16> (2007).
34. Bernal, A., Parel, J.-M. & Manns, F. Evidence for posterior zonular fiber attachment on the anterior hyaloid membrane. *Investig. Ophthalmol. Vis. Sci.* **47**, 4708. <https://doi.org/10.1167/iovs.06-0441> (2006).
35. Krag, S. & Andreassen, T. T. Mechanical properties of the human lens capsule. *Prog. Retinal Eye Res.* **22**, 749–767. [https://doi.org/10.1016/S1350-9462\(03\)00063-6](https://doi.org/10.1016/S1350-9462(03)00063-6) (2003).
36. Krag, S. & Andreassen, T. T. Mechanical properties of the human posterior lens capsule. *Investig. Ophthalmol. Vis. Sci.* **44**, 691. <https://doi.org/10.1167/iovs.02-0096> (2003).
37. Michael, R. *et al.* Elastic properties of human lens zonules as a function of age in presbyopes. *Investig. Ophthalmol. Vis. Sci.* **53**, 6109. <https://doi.org/10.1167/iovs.11-8702> (2012).

38. Hovee, J. V., Nilsson, S. F. E., Wu, S., Kaufman, P. L. & Alm, A. *Adler's Physiology of the Eye* (Elsevier - Health Sciences Division, 2011).
39. Cabeza-Gil, I., Ariza-Gracia, M. Á., Remón, L. & Calvo, B. Systematic study on the biomechanical stability of c-loop intraocular lenses: Approach to an optimal design of the haptics. *Ann. Biomed. Eng.* <https://doi.org/10.1007/s10439-019-02432-9> (2019).
40. Navarro, R. & López-Gil, N. Impact of internal curvature gradient on the power and accommodation of the crystalline lens. *Optica* 4, 334–340. <https://doi.org/10.1364/OPTICA.4.000334> (2017).

## Acknowledgements

We would like to thank Adrian Glasser for the helpful and comprehensive discussions on this project. The authors gratefully acknowledge research support from the Spanish Ministerio de ciencia, innovacion y universidades (Grant DPI2017-84047-R ) and the Department of Industry and Innovation (Government of Aragon) through the research group Grant T24-20R (cofinanciado con Feder 2014-2020: Construyendo Europa desde Aragon). Part of the work was performed by the ICTS "NANBIOSIS" specifically by the High Performance Computing Unit (U27), of the CIBER in Bioengineering, Biomaterials & Nanomedicine (CIBER-BBN at the University of Zaragoza). I. Cabeza-Gil was supported by PRE2018-084021.

## Author contributions

I.C.G. and B. C. conceived the research. I.C.G. performed and analysed the simulations. J.G and B.C. supervised the results. All authors reviewed the manuscript.

## Competing interests

The authors declare no competing interests.

## Additional information

**Correspondence** and requests for materials should be addressed to I.C.-G.

**Reprints and permissions information** is available at [www.nature.com/reprints](http://www.nature.com/reprints).

**Publisher's note** Springer Nature remains neutral with regard to jurisdictional claims in published maps and institutional affiliations.



**Open Access** This article is licensed under a Creative Commons Attribution 4.0 International License, which permits use, sharing, adaptation, distribution and reproduction in any medium or format, as long as you give appropriate credit to the original author(s) and the source, provide a link to the Creative Commons licence, and indicate if changes were made. The images or other third party material in this article are included in the article's Creative Commons licence, unless indicated otherwise in a credit line to the material. If material is not included in the article's Creative Commons licence and your intended use is not permitted by statutory regulation or exceeds the permitted use, you will need to obtain permission directly from the copyright holder. To view a copy of this licence, visit <http://creativecommons.org/licenses/by/4.0/>.

© The Author(s) 2021



## Chapter 3

# Numerical Methodology to test the Biomechanical Stability of IOLs

A comprehensive methodology to test the IOL haptic design is presented through six research works.

1. **W3. Cabeza-Gil et al.** [3], where we obtained the visco-elastic properties of the hydrophobic and hydrophilic acrylates used in IOLs through microindentation tests and the finite element method.
2. **W4. Cabeza-Gil et al.** [4] compares in-vitro and in-silico values of the mechanical biomarkers of IOLs in compression standard tests ISO 11979-2[84] and relates these biomarkers of the compressed IOL to the optical performance[83].
3. **W5. Cabeza-Gil et al.** [5] analyses through a full factorial design the influence of several parameters of C-loop haptic design.
4. **W6. Remon et al.** [6] clinically evaluates the performance of three different IOLs and relate the results with the results provided in the numerical tests of the standard ISO [84].
5. **W7. Cabeza-Gil et al.** [7] proposes a methodology to customise the haptic design of the IOL depending on the patient characteristics.
6. **W8. Cabeza-Gil, I. & Calvo, B.** reproduces a high-fidelity simulation of the IOL inside the capsular bag after cataract surgery. This simulation would allow manufacturers to anticipate post-surgical results.

### 3.1 Work 3: Mechanical characterisation of hydrophobic and hydrophilic acrylates used in intraocular lenses through depth sensing indentation



Cabeza-Gil I., Calvo B., Rico. A, Reinhards-Hervás C., Rodríguez. J.  
Journal of the Mechanical Behavior of Biomedical Materials  
JIF (2020) = 3.90 (Q2: 32/89 Biomedical Engineering)  
SJR (2020) = 0.86 (Q2: 69/232 Biomedical Engineering)



# Mechanical characterisation of hydrophobic and hydrophilic acrylates used in intraocular lenses through depth sensing indentation

I. Cabeza-Gil<sup>a</sup>, B. Calvo<sup>a,b</sup>, A. Rico<sup>c</sup>, C. Reinhardt-Hervás<sup>c</sup>, J. Rodríguez<sup>c,\*</sup>

<sup>a</sup> Aragon Institute of Engineering Research (i3A), University of Zaragoza, Spain

<sup>b</sup> Centro de Investigación Biomédica en Red en Bioingeniería, Biomateriales y Nanomedicina (CIBER-BBN), Spain

<sup>c</sup> Durability and Mechanical Integrity of Structural Materials, Rey Juan Carlos University, Spain

## ARTICLE INFO

### Keywords:

Intraocular lenses  
Acrylates  
Depth sensing indentation  
Visco-hyperelasticity  
Cataract surgery

## ABSTRACT

In this work, the mechanical behaviour of hydrophilic and hydrophobic acrylates has been characterised by depth sensing indentation. Time-dependent behaviour has been studied using load-relaxation tests. Experiments have been simulated with a finite element software using a visco-hyperelastic material model. The parameters of this model have been determined using deep learning techniques. The developed material models have been used to mechanically simulate a standard compression test of a prototype intraocular lens.

## 1. Introduction

The earliest intraocular lenses (IOLs), in 1949, were made of a fairly rigid material, the polymethylmethacrylate (PMMA) (Ridley, 1952). Since then, other material alternatives have gradually emerged: hydrophilic acrylate-based hydrogels with a glass transition temperature,  $T_g$ , clearly above the operating temperature; hydrophobic acrylates with  $T_g$ s below the working temperature; and, finally, a family of silicone-based materials, although they have been overtaken by soft acrylates due to the risk of tearing when placing the IOL and their tendency to become opalescent (Argal, 2013). The use of foldable materials such as hydrophobic and hydrophilic acrylate polymers in IOLs have increased greatly since 1970s with the introduction of phacoemulsification and the ability to remove the cataract with smaller incisions (Amzallag and Pynson, 2007; Zvorničanin and Zvorničanin, 2018).

The excellence biocompatibility and optical clarity of acrylates, along with the ease of manufacture and implantation have made them the leading edge of IOLs to date (Kirchhof et al., 2015; Bhamra and Tighe, 2017). Even these acrylates have contributed to other ophthalmic solutions such as contact lenses (Pérez-Vives, 2018). The main difference between the two most widely used types of acrylate polymers, hydrophobic and hydrophilic, is the ability to absorb and retain water (Zvorničanin and Zvorničanin, 2018). This implies that these two acrylates behave differently when implanted within the eye, leading to different postoperative complications. Hydrophobic acrylate is associated with glistening and dysphotopsias due to its high refractive index

while the main complication related to hydrophilic acrylate is the early onset of posterior capsule opacification (PCO) (Zvorničanin and Zvorničanin, 2018; Pérez-Vives, 2018).

There are few studies that intrinsically analyse the raw properties of acrylic materials. Kamata et al. (2015) (Kamata et al., 2015) evaluated the importance of swelling control on the subsequent mechanical behaviour in hydrogels. A group from Birmingham analysed the mechanical and surface properties of different hydrophilic monomers, typical of contact lenses (Kamata et al., 2015; Barnes et al., 1988; Bhamra et al., 2018). Finally, we proposed a hyperelastic model to reproduce the mechanical behaviour of IOL hydrophobic acrylate through macroscopic experimental tests under hydrated conditions (Cabeza-Gil et al., 2020, 2021a). However, in our tests we also observed a significant viscoelastic influence as reported by Bayat et al. (2020) (Bayat et al., 2020) in hydrogels, which could be key in the post-surgical biomechanical behaviour of the IOL within the capsular bag.

To our knowledge, the time-dependent mechanical behaviour of hydrophobic and hydrophilic IOL acrylates has not been characterised under dry and hydrated conditions, beyond the aforementioned studies and certain mechanical characteristics that may appear in manufacturer's catalogues (Benz Research & Development). Therefore, the objective of this study is twofold: to characterise the mechanical behaviour in dry and hydrated states of the hydrophobic and hydrophilic acrylates used in IOLs and to describe the time-dependent response. To do this, both materials were tested using spherical micro-indentation, as recent studies have shown the ability to reliably and

\* Corresponding author.

E-mail address: [jesus.rodriguez.perez@urjc.es](mailto:jesus.rodriguez.perez@urjc.es) (J. Rodríguez).

<https://doi.org/10.1016/j.jmbbm.2021.104997>

Received 24 September 2021; Received in revised form 8 November 2021; Accepted 23 November 2021

Available online 25 November 2021

1751-6161/© 2021 The Authors.

Published by Elsevier Ltd.

This is an open access article under the CC BY-NC-ND license

(<http://creativecommons.org/licenses/by-nc-nd/4.0/>).

consistently probe the mechanical properties of materials at the micro-scale (Shan et al., 2007; Patel and Kalidindi, 2016; Pathak and Kalidindi, 2015; MacManus et al., 2017). A visco-hyperelastic model whose parameters has been extracted by an iterative inverse finite element algorithm (hereinafter iFEM) was used to describe the mechanical behaviour of the IOL acrylates under investigation. With this increasingly popular methodology, it is possible to bypass the manufacturing stage and numerically analyse a larger number of samples.

Due to the importance of the patient's visual quality in the post-cataract surgery period (appearance of post-operative cataract complications and the biomechanical stability of the IOL), the biomedical performance of IOL acrylates is of enormous relevance. There are several investigations looking at post-cataract complications related to IOL materials, such as in-vivo PCO (Findl et al., 2010; Chang and Kugelberg, 2016) and glistenings (Pagnouille et al., 2012; Tetz and Jorgensen, 2015). A combination of both materials, hydrophobic and hydrophilic acrylate, has even been made using interpenetrating photopolymers to avoid such complications (Shaik et al., 2016). To introduce a new IOL to the market, mechanical stability must be analysed, following the standard compression test ISO 11979-3 (Cabeza-Gil et al., 2020; Cabeza-Gil et al., 2021a; BS EN ISO 11979-3:2012, 2012). This test is usually carried out experimentally, however, it is also possible to carry it out numerically, with the advantage of reducing both time and costs (Cabeza-Gil et al., 2020; Bozukova Dand Werner et al., 2015; Remón et al., 2018). To obtain accurate results, it is essential to have a proper characterisation of the behaviour of the IOL material. Therefore, in addition to characterising the hydrophobic and hydrophilic material used in IOLs, the standard IOL compression test (BS EN ISO 11979-3:2012, 2012) was simulated with the proposed material models to show a possible application of the analyses performed here.

## 2. Materials & methods

### 2.1. Materials

Two different materials have been selected: hydrophobic acrylic material Benz HF-1.2 Universal Blank (Benz Research and Development, USA) and hydrophilic acrylic material Benz IOL 25 (Benz Research & Development, USA) (Benz Research & Development). Hydrophilic acrylate has a greater tendency to hydrate (30 wt%) compared to hydrophobic acrylate (<5 wt%). Both materials have been characterised in two different conditions: hydrated to equilibrium and dry. Dry cylindrical specimens of 2.56 mm and 2.19 mm in height, and 15.22 mm and 12.75 mm in diameter have been used for hydrophilic and hydrophobic acrylate, respectively. To achieve hydration, specimens were immersed in 0.9% Vitulia physiological serum for a period of 48 h to guarantee the balance of the systems. This time is much longer than that required to achieve maximum hydration, which has been experimentally determined at 20 min for hydrophobic acrylate and at 24 h for hydrophilic acrylate.

### 2.2. Spherical indentations

Load-relaxation microindentation tests were carried out using an Agilent G200 nanoindenter equipped with a Keysight XP indentation head and a 500 mN load cell. All the tests were performed at a controlled temperature of 20 °C using an 800 µm ruby spherical tip. Three batches of load-relaxation tests have been completed maintaining the penetration distance for a holding time of 1500 s for each material. The hydrated samples have been tested in a sample holder that allows them to be kept submerged in 0.9% physiological saline during the tests. In this way, constant hydration conditions are guaranteed. Table 1 shows the most important parameters used to perform the tests.

**Table 1**  
Tests parameters.

Material	Condition	Holding Penetration Distance	Holding Time	Loading Rate	Drift Rate		
(-)	(-)	(µm)	(s)	(s <sup>-1</sup> )	(nm/s)		
Hydrophilic acrylate	Dry	2.5	>1500	0.006	<0.05		
		5					
	Hydrated	7.5		0.004			
		10		0.033			
Hydrophobic acrylate	Dry	15	0.011	0.011	<0.05		
		20					
		10					
	Hydrated	15				0.011	<1
		20					
25							

### 2.3. Computational finite element model

The microindentation experiments were simulated by developing a 2D axisymmetric finite element (FE) model using the Abaqus software, see Fig. 1. Large strain and non-linear features were adopted in this dynamic simulation. It is assumed that a spherical indenter tip is pressed into a cylinder of material that should be representative of a homogeneous infinite half space. The diamond spherical indenter tip was modelled as a rigid material and its loading was prescribed as an applied displacement coincident with that of the experiments. The specimen is assumed to be a deformable solid and is characterised by an incompressible visco-hyperelastic Neo-Hookean material model, which is described in Eq. (1):

$$\psi(\mathbf{C}, t) = C_{10}^R(t) (I_1 - 3) \quad (1)$$

Being  $\psi(\mathbf{C}, t)$  the strain energy density function,  $C_{10}^R(t)$  the hyperelastic Neo-Hookean constant and  $I_1$  the first invariant of the right Cauchy-Green deformation tensor,  $\mathbf{C}$ . The time dependence of  $C_{10}^R(t)$  is defined by a two term ( $N = 2$ ) Prony series:

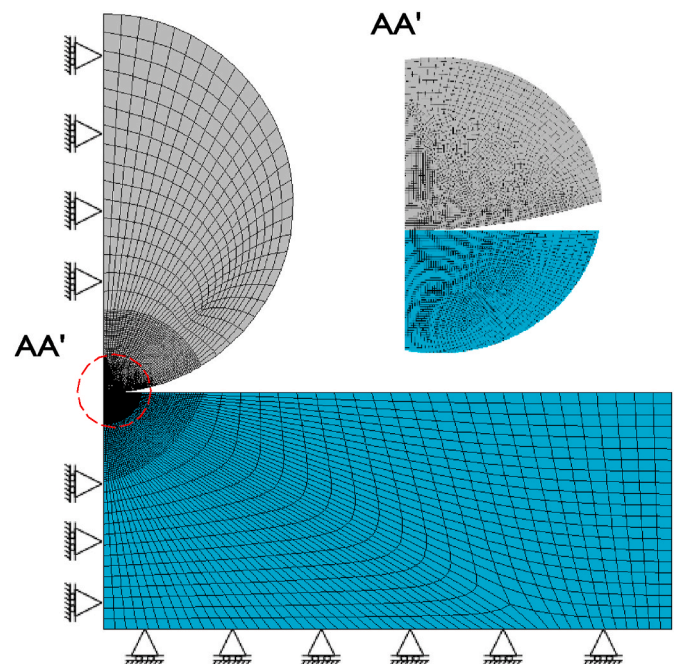


**Fig. 1.** FE model used to simulate the microindentation experiments. The material specimen (blue) was meshed with 4563 CAX4H elements whilst the spherical indenter (grey) was meshed with 3333 CAX4 elements.



$$C_{10}^R(t) = C_{10}^0 \left( 1 - \sum_{i=1}^N g_i \left( 1 - e^{-\frac{t}{\tau_i}} \right) \right) \quad (2)$$

$$C_{10}^\infty = C_{10}^0 \left( 1 - \sum_{i=1}^N g_i \right) \quad (3)$$

Being  $C_{10}^0$ , the instantaneous modulus and  $C_{10}^\infty$ , the long-term modulus, defined in Eq. (2) and (3). The Prony series parameters are defined by the pre-exponential factors  $g_i$  and the relaxation times  $\tau_i$ .

For consistency with linear elasticity in small deformations, the incompressible Neo-Hookean model can be converted to a linear elastic model with the following relationship:

$$\mu = 2C_{10}, \quad E = 3\mu \quad (4)$$

Being  $\mu$  the first Lamé parameter, and  $E$ , the Young' modulus.

A four-node quadrilateral hybrid element (CAX4H) was used to mesh the indenter and the specimen using a finer mesh in the region where the two bodies are expected to be in contact. The size of the elements is  $4 \mu\text{m}$  for the indenter and the specimen in the area of interest, see Fig. 1. Surface-to-surface contact definition was used to avoid any accumulation of concentrated force on the individual nodes at the initial point of contact, and the 'hard' contact approach, that uses the direct method as constraint contact method, was considered to minimise penetration between the slave and master surfaces. The direct method strictly enforces a given pressure-overclosure behaviour for each constraint, without approximation or use of augmentation iterations.

### 2.4. iFEM optimisation

To adjust the visco-hyperelastic response of the materials analysed, a two-step inverse methodology was proposed. First, the long-term modulus of the hyperelastic contribution of the material was obtained. For this, it is assumed that the load at the end of each experimental test ( $t = 1500 \text{ s}$ ) only had a hyperelastic contribution, that is, the viscoelastic relaxation has previously occurred. As a result, we had the load relaxation curves associated with the three experimental tests performed at

three different holding penetration distances. To compare the experimental and numerical results, the error considered was the normalized mean absolute error (nMSE). To find the optimal hyperelastic parameter ( $C_{10}^\infty$ ) of the Neo-Hookean model proposed, a batch of 20 simulations was initially performed. The hyperelastic parameter ( $C_{10}^\infty$ ) of this batch of simulations was calculated based on a theoretical approach (Cabeza-Gil et al., 2020; Syngellakis et al., 2017). Then, the inverse finite element iterative algorithm (iFEM) sought the optimal parameter that minimised the error (nMSE) through a process of optimisation of the simulation database. If no case was deemed suitable ( $error > Tol_{max}$ ), a deep neural network (DNN) fed by the database, calculated the optimal material parameter which minimised the error. A new simulation was submitted with this calculated material coefficient and added to the database. This process was repeated until the imposed tolerance was accomplished, see Fig. 2. The implemented DNN was based on the work of Papazafeiropoulos et al. (2017) (Papazafeiropoulos et al., 2017) to calculate the optimal cohesive and friction coefficients. The time required by iFEM to fit material properties was highly dependent on the first batch of simulations submitted.

Second, the same procedure was followed to fit the Prony series parameters. In this case, a dynamic simulation was performed that exactly replicates the experimental test conditions. The database was generated from 300 simulations for each loading displacement in each material, resulting in 900 simulations. Contrary to the fitting of the hyperelastic material properties, the use of DNN is key in this procedure due to the high non-linearity related to the four adjusted Prony parameters ( $g_1, g_2, \tau_1$  and  $\tau_2$ ). In this case, six points were experimentally and numerically compared: for each holding penetration distance, the maximum load applied by the indenter ( $t = 90 \text{ s}$  for hydrophobic materials) and the load applied at  $t = 140 \text{ s}$ . The implemented methodology is summarised in Fig. 2.

### 3. Results and discussion

The resulting displacement obtained from the microindentation experiments is shown in Fig. 3, as proof of the adequate execution of the tests with excellent indenter control. After an initial ramp with the strain

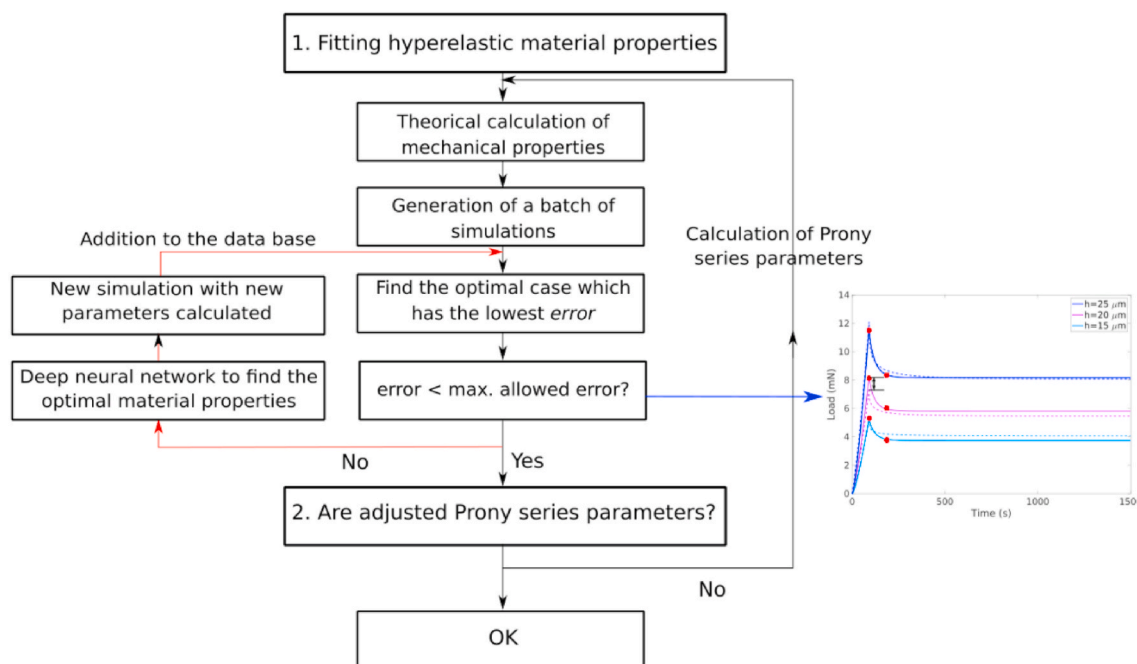


Fig. 2. Outline of the inverse methodology to find the optimal Prony series parameters. An example of the six points used to calculate the error and fit the DNN is shown on the right (red points). Each individual error was calculated as the absolute difference between the experimental and numerical data. The error used to fit the DNN was calculated as the average normalized mean of the six points compared.

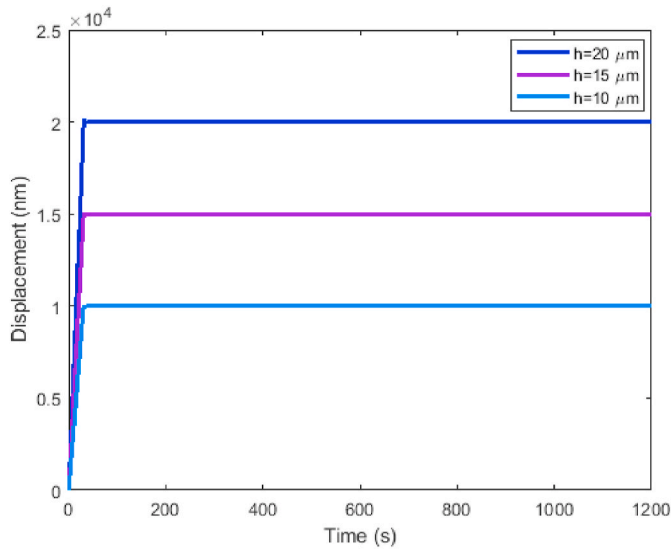


Fig. 3. Example of displacement control for experimental relaxation corresponding to the hydrophilic material tested, at hydrated conditions.

rate prescribed in Table 1, a holding penetration distance was kept during more than 1500 s.

### 3.1. Calibration of the visco-hyperelastic material model

Fig. 4 shows the experimental and numerical data of the tests performed for the three holding penetration distances, see Table 1, on each acrylate material in both states, hydrated and dry. The visco-hyperelastic coefficients obtained after performing the iFEM optimisation are presented in Table 2. All numerical values were within the deviation measured in the experimental tests, and the average nMAE of the three holding penetration distances was always below 0.02. The

response surface methodology is the one commonly used in parameter fitting problems. On the contrary, in this case the iFEM optimisation has been used to adjust the visco-hyperelastic coefficients (Papazafeiropoulos et al., 2017), which allowed reducing computational costs. The presented methodology could be more useful in highly non-linear approaches.

It should be noted that the load response presents a time-dependence for all materials regardless their degree of hydration. It can be seen that the time-dependent trends seem to find a horizontal asymptote within the test time. There is also, as expected, a perfect correlation between greater penetration distances and higher loads. In all the samples tested, lower loads are observed when they are in the hydrated condition compared to the dry samples of the same material. This decrease in stiffness is a consequence of introducing serum inside, an obviously more pronounced behaviour in hydrophilic acrylate due to its much higher water absorption capacity.

The results and the parameters obtained show the different behaviour between the hydrophobic and hydrophilic acrylate. While the mechanical properties of the hydrophobic acrylate change slightly in the state of hydration, the properties of the hydrophilic change completely according to its state. This is due to its  $T_g$ , which is several tens above the working temperature.

An estimation of the long-term Young' modulus was performed considering the consistency with linear elasticity of Neo-Hookean hyperelastic model of an incompressible material, see Eq. (4). The values obtained, see Table 2, are consistent with the values reported in literature (Bhamra et al., 2018; Cabeza-Gil et al., 2020) and with the manufacturer's catalogs (Benz Research & Development). The numerical fitting showed that the hydrated hydrophilic acrylate is the most flexible material, followed by the hydrated and dry hydrophobic acrylate. The dry hydrophilic acrylate is significantly stiffer than the materials mentioned above. For the same holding penetration distance of 15  $\mu\text{m}$ , the hydrated hydrophilic acrylate presented a maximum load of  $3.76 \pm 0.26$  mN while the hydrated and dry hydrophobic acrylate presented a maximum load of  $5.06 \pm 0.14$  mN and  $8.21 \pm 0.33$  mN,

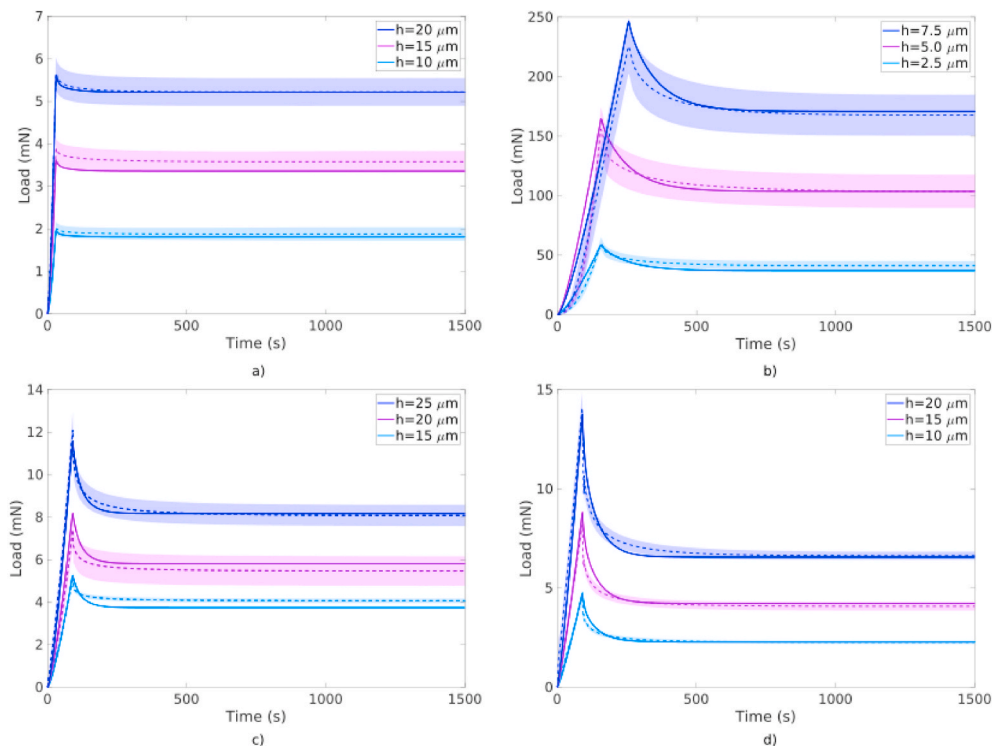


Fig. 4. Experimental (mean (dashed line) and standard deviation) and numerical (continuous line) loads vs. time. a) Hydrophilic tested at hydrated conditions. b) Hydrophilic tested at dry conditions. c) Hydrophobic tested at hydrated conditions. d) Hydrophobic tested at dry conditions.

**Table 2**  
Viscohyperelastic parameters for the materials adjusted in the spherical indentation tests.

Acrylate	State	Hyperelastic contribution		Viscohyperelastic contribution			
		$C_{10}^0$ (MPa)	$E$ (MPa) (Eq. (4))	$g_1$ (-)	$g_2$ (-)	$\tau_1$ (s)	$\tau_2$ (s)
Hydrophilic	hydrated	0.18	1.08	0.11	0.04	11.30	57.25
Hydrophilic	Dry	33.88	203.30	0.39	0.20	88.01	10.00
Hydrophobic	hydrated	0.21	1.26	0.30	0.26	15.04	39.12
Hydrophobic	Dry	0.24	1.44	0.64	0.21	5.16	48.80

respectively. The same trend was obtained analysing the experimental force exerted in IOL delivery (Cabeza-Gil et al., 2021b). This additional stiffness in the dry material could involve some risk factors such as damaging in IOL delivery. Considering the importance of using soft materials in delivery and placement, IOLs should always be in their hydrated state prior to be injected in the eye (Cabeza-Gil et al., 2021b).

### 3.2. Theoretical calculation of linear modulus

In a linear elastic material, a spherical indentation is described by the following relationship between the applied load,  $P$ , and the depth of penetration,  $h$ :

$$P = \frac{4}{3} R^{1/2} h^{3/2} \frac{E}{1 - \nu^2} \quad (5)$$

where  $R$  is the indenter radius,  $E$  the elastic modulus and  $\nu$  the Poisson's ratio. Zhang et al. (2014) (Zhang et al., 2014) extended this expression to non-linear elastic behaviour, introducing correction terms calculated from finite element simulations. In the case of a Neo-Hookean model, Eq. (5) is modified by a factor that depends on the relative penetration:

$$P = \frac{4}{3} R^{1/2} h^{3/2} \frac{E}{1 - \nu^2} \left( 1 - 0.15 \frac{h}{R} \right) \quad (6)$$

For small penetration depths, the correction included in Eq. (6) is negligible. In the case of a viscoelastic material, the elastic modulus is substituted by the relaxation function  $E(t)$ . Poisson's ratio is usually assumed to be constant, for the sake of simplicity. Fig. 5 shows the value of  $E(t)$  for the hydrophobic and hydrophilic acrylates both in dry and hydrated conditions.

As can be seen, hydrophilic acrylate hardly shows relaxation when it acts in hydration, being a very good approximation to consider it as an eminently elastic material. The response in dry conditions is very different showing a strong viscoelastic character. However, this matter is of no practical interest since the material is not used under these conditions. Regarding to hydrophobic acrylate, the material shows a marked relaxation close to 20% and although, as already mentioned, it presents stiffness values similar to those of hydrophilic, the response to relaxation constitutes an important difference between both materials. The elastic modulus calculated with the theoretical approach were similar to those calculated numerically with the finite element method, see Table 2.

### 3.3. Linear time-dependent behaviour

The time-dependent response can be characterised assuming a linear viscoelastic behaviour. The relaxation function can be written as a Prony

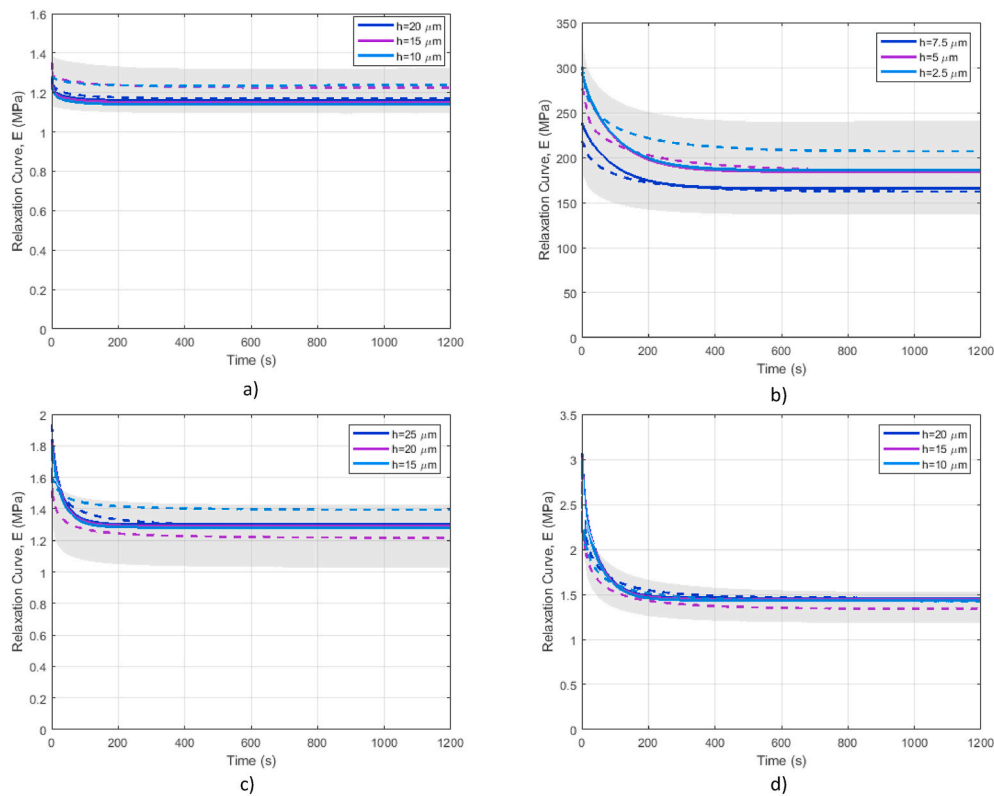


**Fig. 5.** Experimental (solid lines) and numerical (dashed lines) relaxation curves. a) Hydrophilic tested at hydrated conditions. b) Hydrophilic tested at dry conditions. c) Hydrophobic tested at hydrated conditions. d) Hydrophobic tested at dry conditions. Grey zone includes the experimental absolute error.

series by Eq. (7).

$$E(t) = E_\infty + (E_0 - E_\infty) \left( \sum_{i=1}^n A_i e^{-t/\tau_i} \right) \quad (7)$$

where  $E_0$  and  $E_\infty$  are the instantaneous and long-term value of the relaxation function,  $\tau_i$  the relaxation time of the  $i$ -term of the Prony series with the pre-exponential factor  $A_i$ . The experimental loads in the spherical indentation tests can be normalized by using Eq. (8).

$$\frac{P(t) - P_\infty}{P_0 - P_\infty} = \frac{E(t) - E_\infty}{E_0 - E_\infty} = \left( \sum_{i=1}^n A_i e^{-t/\tau_i} \right) \quad (8)$$

Using the above equation allows you to cancel out differences in stiffness and focus on relaxation in relative terms. In a primarily viscoelastic material, the indentation curves corresponding to different penetration depths should collapse in a single curve. As it can be observed in Fig. 6, this is precisely the case for the materials under investigation, despite the experimental uncertainty. Especially in the hydrophobic material that responds perfectly to what a viscoelastic material should do (experimental curves at different penetrations merge into a single curve in a practically ideal way). Fig. 5 and 6 together give us an idea of the behaviour of the materials used in IOLs, always in hydrated conditions. The results indicate that the stiffness of the hydrophobic and hydrophilic materials is similar, but hydrophobic acrylate appears to have a more marked time-dependent behaviour, with clearly greater absolute relaxation. The clinical importance of this aspect should be analysed but it is outside the scope of this work. In any case, the experimental results are consistent with the use of viscoelastic models to describe these materials. This is the main result of this work, in which the hydrophobic and hydrophilic acrylates have been adjusted to a hyperelastic-linear viscoelastic FE model, which reasonably describes the experiments as indicated in Fig. 5. The specific values of the parameters after the simulation optimisation process have been included in Table 2.

### 3.4. Discussion about the contact model in terms of adhesion

As was previously stated, experimental curves have been mainly interpreted in terms of a Hertz - type contact model, although hyperelastic and viscoelastic modifications have been introduced in both the theoretical and numerical models. It is worthy to note that several hypothesis are linked to this model. Particularly, adhesion between material and indenter should be carefully treated, because Hertz theory framework does not take into account this type of interaction. Note that in soft and sticky materials, adhesion could be a relevant phenomenon that has to be considered if adhesion level is high enough to show relative importance on the experimental forces that are measured during the relaxation experiments.

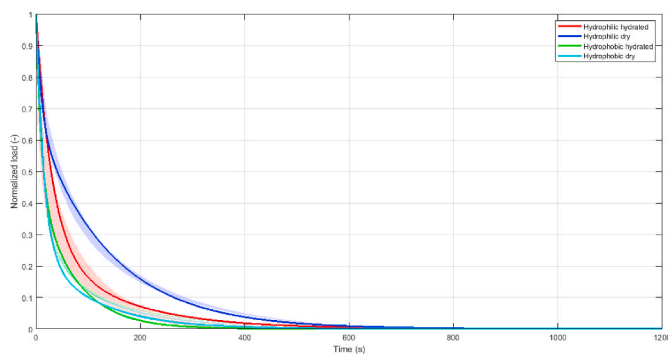


Fig. 6. Time-dependent response: normalized load vs. time. Shaded zones correspond to experimental variability and solid lines are the numerical outputs.

Several models have been developed to include the adhesion in contact mechanics (Popov et al., 2019; Borodich, 2014). The applicability of these models is determined by the so - called Tabor parameter, which scales the extension of the adhesion area between indenter and sample. Several authors have claimed (Ciavarella et al., 2019) that a normalized load can be included to determine exactly the adhesion regime describing a particular indenter/sample system. Moreover, indenter radius and contact radius established between sample and indenter also play a role in determining the adhesion regime that characterises a particular experimental situation. An adhesion map (Ciavarella et al., 2019) can be consulted in terms of the normalized load and the Tabor parameter. The normalized load is computed as:

$$\hat{P} = \frac{P}{\pi R \omega} \quad (9)$$

where  $\omega$  is the work of adhesion per unit area,  $P$  is the load imposed during the experiment and  $R$  is the indenter radius. To obtain the value of the normalized load it is necessary to know  $\omega$ , that can be computed from the initial stage of the loading branch of the indentation tests. In Fig. 7, loading curves from hydrated hydrophilic and hydrophobic acrylates are shown. A detail of the starting part of the loading trend is also

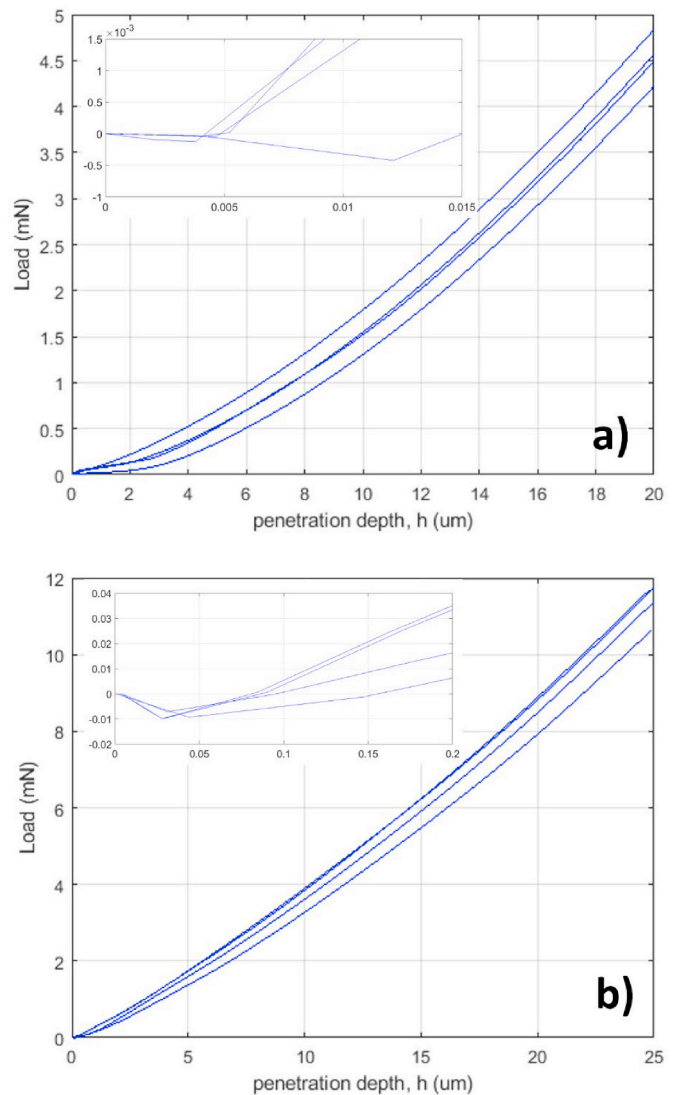


Fig. 7. Load vs. displacement curve. Detail of the initial part of the loading curve are included as an inserts in figures. a) Hydrophilic acrylate. b) Hydrophobic acrylate.

depicted.

Negative values of the compression force, i.e., tension values, are observed for the low penetration depth regime. This a sign of adhesion between sample and indenter. The maximum force in the adhesion loop,  $F_c$ , can be used to estimate the adhesion work per unit area. Following the Johnson – Kendal – Roberts adhesion theory and taking into account that the tests are performed under displacement control,  $\omega$  can be computed as:

$$\omega = \frac{6 F_c}{5 \pi R} \tag{10}$$

In Table 3 maximum adhesion forces,  $F_c$ , and work of adhesion derived using Eq. (10) are collected for both materials under hydrated conditions for all experimental tests. The work of adhesion is much lower for hydrophilic material than for hydrophobic acrylate and, although adhesion should be measured for the particular system between materials in contact, these values are in the same order of magnitude than others previously measured in similar materials (Lombardo et al., 2009). Using Eq. (9), the normalized load can be determined for the maximum load reached for each sample during the relaxation test (5 mN and 12 mN for hydrophilic and hydrophobic materials, respectively, see Fig. 4). The normalized load reaches values of 6600 and 720 for hydrophilic and hydrophobic materials, respectively. If these values are translated to the adhesion map in (Ciavarella et al., 2019), it is clear that only two models for the mechanics of this particular contact are valid. For low or intermediate values of Tabor parameter, Hertz model describes the particular contact under the experimental conditions. However, if Tabor parameter is relatively high, Johnson – Kendal – Roberts adhesion theory becomes a better description of the contact mechanics for this situation (Johnson et al., 1971). This justifies the use of Eq. (10) for calculating the work of adhesion.

When non-adhesive indentation experiments are performed, the effective elastic modulus  $E^*$  (or the indentation relaxation function for viscoelastic materials) is usually estimated using the contact stiffness,  $S$ , which is the slope the  $P - h$  curve at the unloading branch. Using Hertz model, contact stiffness can be calculated taking the derivative of the load over the displacement in Eq. (5), resulting in:

$$S = \frac{dP}{dh} = 2E^* a \tag{11}$$

where  $a$  is the contact radius (equal to  $\sqrt{Rh}$ ). However, due to adhesive effects Eq. (11) should be modified using a JKR approach:

$$S = 2E^* a f \tag{12}$$

where  $f$  is a correction factor depending on the work of adhesion per unit area, the effective modulus and the contact radius, following Borodich et al. (2021) (Borodich et al., 2021):

**Table 3**  
Experimental adhesion load and adhesion work for hydrophilic and hydrophobic acrylates tests.

Material	Radius	Max Penetration	Adhesion Load	Adhesion work
(-)	( $\mu\text{m}$ )	( $\mu\text{m}$ )	(mN)	(J/m <sup>2</sup> )
Hydrophilic Acrylate	800	20	-0,00042	0,00020
			-0,00005	0,00002
			-0,00004	0,00002
			-0,00010	0,00005
			<b>Average</b>	<b>-0,00015</b>
		<b>Std. Desv.</b>	<b>0,00005</b>	<b>0,00002</b>
Hydrophobic Acrylate	25	25	-0,010	0,0048
			-0,009	0,0045
			-0,010	0,0047
			-0,007	0,0034
			<b>Average</b>	<b>-0,009</b>
		<b>Std. Desv.</b>	<b>0,001</b>	<b>0001</b>

$$f = \frac{1 - 3\sqrt{\frac{\pi R^2 \omega}{8E^* a^3}}}{1 - \sqrt{\frac{\pi R^2 \omega}{8E^* a^3}}} \tag{13}$$

The  $f$  factor can be used as a criterion to establish if Hertz – type models are suitable for use. If the factor  $f$  is close to one (for example if work of adhesion is low in relation to the material stiffness) then, it is not necessary to take adhesion into account for calculations and Eq. (11) can be used by committing a low error. Note that  $f$  factor needs the modulus and contact radius to be determined in advance. The contact radius can be obtained using the JKR expression relating contact radius and penetration depth in Eq. (14):

$$h = \frac{a^2}{R} - \sqrt{\frac{2\pi a \omega}{E^*}} \tag{14}$$

Penetration depth is continuously measured during the loading branch of the relaxation test, and it is set at a constant value in the relaxation part of the experiment (see Fig. 3). If effective modulus is known, by solving Eq. (14), contact radius can be determined for the entire experimental test.

However, due to the viscous nature of the materials involved,  $f$  factor could change during the relaxation of the sample, leading to an evolution of the adhesion effect during the test. As the work of adhesion has been measured for hydrated materials,  $f$  factor can be computed for different values of the effective modulus. Fig. 8, shows the variation of the  $f$  factor with the penetration depth for hydrophilic and hydrophobic materials. Shaded areas corresponds to  $f$  factor computed for effective moduli ranging from 0.5 MPa (dashed lines) to 3 MPa (solid lines), covering the values that have been reported for relaxation functions in previous sections for both materials. The  $f$  factor is higher than 0.92 in the worst experimental conditions, corresponding to the hydrophobic material tested at the lower penetration depth (15  $\mu\text{m}$ ). The hydrophilic material shows an  $f$  factor higher than 0.95 for all cases due to the low work of adhesion that has been measured for this material.

According to these values, adhesion had a minor importance during the relaxation tests performed in this work. The use of an indenter of high radius (800  $\mu\text{m}$ ) and the range of experimental penetration depths, in addition to the low values of the work of adhesion measured, lead to contact conditions in which the Hertz – type models are reasonably applicable. Last, note that highest errors that have been computed are lower than the intrinsic experimental dispersion presented as shaded areas in Fig. 5.

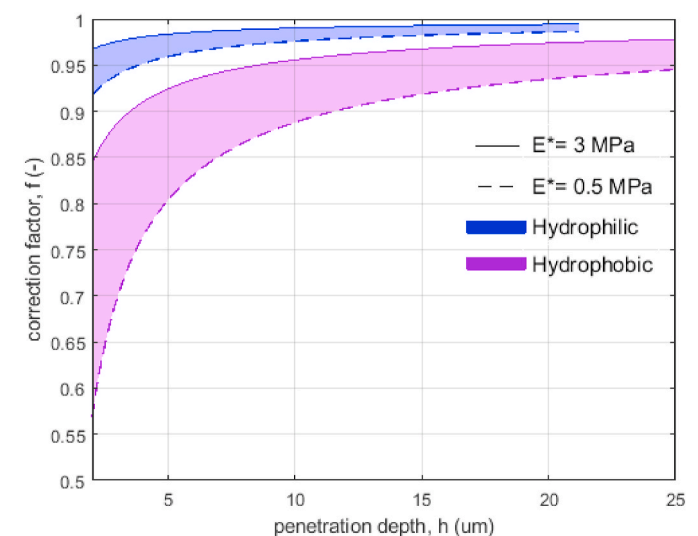


Fig. 8.  $f$  factor variation in terms on the penetration depth.

### 3.5. IOL compression standard test

To illustrate a case of application of the proposed material models, an IOL prototype (model #C in Cabeza -Gil et al. (2021) (Cabeza-Gil et al., 2021a)) was tested following the Standard ISO 11979-3:2012 (BS EN ISO 11979-3:2012, 2012). The IOL was compressed between two clamps from a compression diameter of 13 mm up to 10 mm in 90 s and kept the strain applied during 1500 s, see Fig. 9 (for graphical purposes the graph is only up to 600 s). To simulate the working condition, the IOL was modelled using the parameters determined for the hydrophobic and hydrophilic acrylates in hydrated condition.

The compression force was registered as the average of the two clamps, considered as rigid solids, throughout the dynamic simulation. The hydrophobic and hydrophilic IOL showed a relaxation similar to that of the microindentation tests, 35.03%, and 5.00%, respectively. Both models of IOL material presented adequate biomechanical stability (without axial displacement, tilt or rotation) in a compression diameter of 10 mm as seen in Remón et al. (2018) (Remón et al., 2018), providing quality optical performance in a hypothetical implantation.

## 4. Conclusions

In this work, the time-dependent mechanical behaviour of two acrylates used in the manufacture of IOLs (hydrophobic acrylic material, Benz HF-1.2 Universal Blank, Benz Research and Development USA; and hydrophilic acrylic material, Benz IOL 25, Benz Research and Development, USA) has been described through a numerical model fitted using spherical indentation relaxation tests carried out on dry and hydrated materials. The following conclusions can be drawn:

- A hyperelastic-viscoelastic model has been used to describe the behaviour of the material. The hyperelastic part captures the material non-linearity while the linear viscoelastic contribution accounts for the time-dependence of the elastic constants. The proposed material models describe relaxation tests within the experimental variability and can be used, as shown in Fig. 9, in the IOL design stage.
- The fitting procedure in the numerical model followed an optimisation process based on deep learning techniques, which represents a saving of computational time compared to other methodologies such as the response surface methodology, in addition to ensuring good agreement with the experimental results.
- Under hydrated conditions, where IOLs materials really work, the stiffnesses of hydrophobic and hydrophilic acrylates are quite similar, although the hydrophobic material is 17% stiffer. However, if the hydrophobic material is implanted in dry conditions, there is an increase in its stiffness (33% compared to the hydrated hydrophilic) that could discourage its use in clinical practice. The elastic constants corresponding to dry hydrophilic acrylate are much higher than the rest, but this is not significant due to its inappropriate use under these conditions.
- Hydrophobic acrylate shows a more pronounced time-dependent behaviour than hydrophilic one, having a higher degree of relaxation in absolute terms. Furthermore, the time dependence of the mechanical properties of the hydrophobic acrylate studied in this work is adequately described with a linear viscoelastic model. Interestingly, the normalized load versus time curve follows the same path regardless of whether the material is hydrated or dry. This is a substantial difference from the hydrophilic acrylate.
- Although adhesion effects may become important in this type of materials, it has been found that the relative influence in the experiments carried out in this work is low as a consequence of a combination of favorable experimental conditions, which justifies the use of Hertzian contact models.

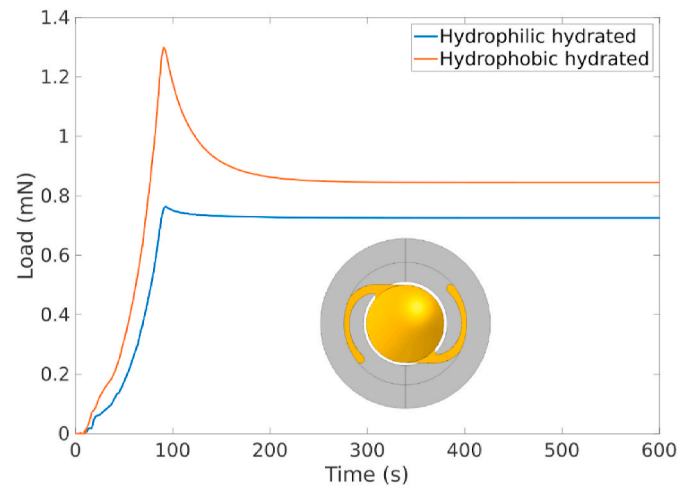


Fig. 9. Compression force of the hydrophobic and hydrophilic model #C in the standards compression tests. The FE model of the standard test can be seen in Remón et al. (2018) (Remón et al., 2018).

## CRediT authorship contribution statement

**I. Cabeza-Gil:** Writing – original draft, Methodology, Investigation, Conceptualization. **B. Calvo:** Writing – review & editing, Conceptualization, Funding acquisition, Methodology. **A. Rico:** Conceptualization, Formal analysis, Methodology, Writing – review & editing. **C. Reinhardt-Hervás:** Writing – original draft, Methodology, Investigation, Conceptualization. **J. Rodríguez:** Writing – review & editing, Methodology, Funding acquisition, Conceptualization.

## Declaration of competing interest

The authors declare that they have no known competing financial interests or personal relationships that could have appeared to influence the work reported in this paper.

## Acknowledgements

The authors gratefully acknowledge research support from the Spanish Ministerio de Ciencia, Innovación y Universidades (Grant number PID 2019-108968RB-I00 and Grant DPI 2017-84047-R) and the Department of Industry and Innovation (Government of Aragon) through the research group Grant T24-20R (cofinanciado con Feder 2014–2020: Construyendo Europa desde Aragon). Part of the work was performed by the ICTS “NANBIOSIS” specifically by the Tissue & Scaffold Characterisation Unit (U13) and High Performance Computing Unit (U27), of the CIBER in Bioengineering, Biomaterials & Nanomedicine (CIBER-BBN at the University of Zaragoza). I. Cabeza-Gil was supported by PRE 2018-084021.

## References

- Amzallag, T., Pynson, J., 2007. *J. Fr. Ophthalmol.* 30, 757–767.
- Argal, S., 2013. *J. Clin. Ophthalmol. Res.* 1, 113.
- Barnes, A., Corkhill, P.H., Tighe, B.J., 1988. *Polymer* 29, 2191–2202.
- Bayat, M.R., Wang, K., Baghani, M., 2020. *Int. J. Eng. Sci.* 152, 103294. Benz Research & Development, (n.d.).
- Bhamra, T.S., Tighe, B.J., 2017. *Contact Lens Anterior Eye* 40, 70–81.
- Bhamra, T.S., Tighe, B.J., Li, J., 2018. *J. Biomed. Mater. Res. B Appl. Biomater.* 107, 1645–1653.
- Borodich, F.M., 2014. *Adv. Appl. Mech.* 47, 225–366.
- Borodich, F.M., Galanov, B.A., Keer, L.M., Suarez-Alvarez, M.M., 2021. *Phil. Trans. Math. Phys. Eng. Sci.* 379, 20200289.
- Bozokova Dand Werner, L., Mamalis, N., Gobin, L., Pagnouille, C., Floyd, A., Liu, E., Stallings, S., Morris, C., 2015. *J. Cataract Refract. Surg.* 41, 1490–1502.
- BS EN ISO 11979-3:2012, 2012. *Ophthalmic Implants. Intraocular Lenses. Mechanical Properties and Test Methods.* BSI Standards Limited.

- Cabeza-Gil, I., Ariza-Gracia, M.Á., Remón, L., Calvo, B., 2020. *Ann. Biomed. Eng.* 48.
- Cabeza-Gil, I., Pérez-Gracia, J., Remón, L., Calvo, B., 2021a. *J. Mech. Behav. Biomed. Mater.* 114, 104165.
- Cabeza-Gil, I., Ríos-Ruiz, I., Calvo, B., 2021b. *J. Mech. Behav. Biomed. Mater.* 124.
- Chang, A., Kugelberg, M., 2016. *Eur. J. Ophthalmol.* 27, 164–168.
- Ciavarella, M., Joe, J., Papangelo, A., Barber, J.R., 2019. *J. R. Soc. Interface* 16, 20180738.
- Findl, O., Buehl, W., Bauer, P., Sycha, T., 2010. *Cochrane Database of Systematic Reviews*.
- Johnson, K.L., Kendall, K., Roberts, A.D., 1971. *Proc. Roy. Soc. Lond. Math. Phys. Sci.* 324, 301–313.
- Kamata, H., Li, X., Chung, U., Sakai, T., 2015. *Adv. Healthc. Mater.* 4, 2360–2374.
- Kirchhof, S., Goepferich, A.M., Brandl, F.P., 2015. *Eur. J. Pharm. Biopharm.* 95, 227–238.
- Lombardo, M., Carbone, G., Lombardo, G., De Santo, M.P., Barberi, R., 2009. *J. Cataract Refract. Surg.* 35, 1266–1272.
- MacManus, D.B., Pierrat, B., Murphy, J.G., Gilchrist, M.D., 2017. *Acta Biomater.* 48.
- Pagnoulle, C., Bozukova, D., Gobin, L., Bertrand, V., Pauw, M.-C.G.-D., 2012. *J. Cataract Refract. Surg.* 38, 1271–1277.
- Papazafeiropoulos, G., Muñiz-Calvente, M., Martínez-Pañeda, E., 2017. *Adv. Eng. Software* 105, 9–16.
- Patel, D.K., Kalidindi, S.R., 2016. *Acta Mater.* 112, 295–302.
- Pathak, S., Kalidindi, S.R., 2015. *Mater. Sci. Eng. R Rep.* 91, 1–36.
- Pérez-Vives, C., 2018, 2018 *J. Ophthalmol.* 1–17.
- Popov, V.L., Heß, M., Willert, E., 2019. **Springer, Berlin, ISBN 978-3-662-58708-9.** <https://doi.org/10.1007/978-3-662-58709-6>.
- Remón, L., Siedlecki, D., Cabeza-Gil, I., Calvo, B., 2018. *J. Biomed. Opt.* 23, 1.
- Ridley, H., 1952. *Br. J. Ophthalmol.* 36, 113–122.
- Shaik, S.H., Donempudi, S., Tammishetti, S., Garikapati, K.R., Bhadra, M.P., 2016. *J. Appl. Polym. Sci.* 134.
- Shan, Z.W., Mishra, R.K., Asif, S.A.S., Warren, O.L., Minor, A.M., 2007. *Nat. Mater.* 7, 115–119.
- Syngellakis, S., Habbab, H., Mellor, B.G., 2017. *Int. J. Comput. Methods. Exp. Meas.* 6, 749–763.
- Tetz, M., Jorgensen, M.R., 2015. *Curr. Eye Res.* 40, 969–981.
- Zhang, M.G., Cao, Y.P., Li, G.Y., Feng, X.Q., 2014. *Biomech. Model. Mechanobiol.* 13.
- Zvorničanin, J., Zvorničanin, E., 2018. *J. Curr. Ophthalmol.* 30, 287–296.

### 3.2 Work 4: Effect of haptic geometry in C-loop in intraocular lenses on optical quality



Cabeza-Gil I., Pérez-Gracia J., Remón L., Calvo B.  
Journal of the Mechanical Behavior of Biomedical Materials  
JIF (2020) = 3.90 (Q2: 32/89 Biomedical Engineering)  
SJR (2020) = 0.86 (Q2: 69/232 Biomedical Engineering)





Contents lists available at ScienceDirect

## Journal of the Mechanical Behavior of Biomedical Materials

journal homepage: [www.elsevier.com/locate/jmbbm](http://www.elsevier.com/locate/jmbbm)

Research paper



## Effect of haptic geometry in C-loop intraocular lenses on optical quality

I. Cabeza-Gil <sup>a,\*</sup>, J. Pérez-Gracia <sup>b</sup>, L. Remón <sup>b</sup>, B. Calvo <sup>a,c</sup><sup>a</sup> Aragón Institute of Engineering Research (I3A), University of Zaragoza, Spain<sup>b</sup> Departamento de Física Aplicada, University of Zaragoza, Spain<sup>c</sup> Centro de Investigación Biomédica en Red en Bioingeniería, Biomateriales y Nanomedicina (CIBER-BBN), Spain

## ARTICLE INFO

## Keywords:

Biomechanical stability  
IOLs  
Finite element  
Optical performance  
Haptic design  
Hydrophobic acrylate

## ABSTRACT

The biomechanical stability of intraocular lenses (IOLs) must achieve high-quality optical performance and clinical outcomes after cataract surgery. For this reason, the quality and performance features of the IOLs should be previously analysed following the Standard ISO 11979-2 and ISO 11979-3. The ISO 11979-3 tries to reproduce the behaviour of the IOL in the capsular bag by compressing the lens between two clamps. With this test, it has been demonstrated that the haptic design is a crucial factor to obtain biomechanical stability. Hence, the main goal of this study was to design an aberration-free aspheric IOL and to study the influence of haptic geometry on the optical quality. For that purpose, 5 hydrophobic IOLs with different haptic design were manufactured and their biomechanical stability was compared experimentally and numerically. The IOLs were classified as stiff and flexible designs depending on their haptic geometry. The biomechanical response was measured by means of the compression force, the axial displacement, the angle of contact or contact area, the decentration, the tilt and the strain energy. The results suggest that *in vitro* and *in silico* compression tests present similar responses for the IOLs analysed. Furthermore, the flexible IOL designs presented better biomechanical stability than stiff designs. These results were correlated with the optical performance, where the optical quality decreases with worst biomechanical stability. This numerical methodology provides an indisputable advance regarding IOL designs, leading to reduce costs by exploring a feasible space of solutions during the product design process and prior to manufacturing.

## 1. Introduction

The mechanical stability of intraocular lenses (IOLs) inside the capsular bag is a critical factor that affects the optical performance and clinical outcomes after cataract surgery. The biomechanical response is essential in IOLs which demand a fixed optic position, as for example, premium IOLs such as multifocal, toric, and aspheric designs (Alió et al., 2013; Pérez-Merino and Marcos, 2018; Zvorničanin and Zvorničanin, 2018). IOL axial displacement, rotation, decentration and tilt can result in residual refractive errors and other complications, requiring explantation or repositioning of the IOL in certain cases (Chan et al., 2010).

Intraocular lens stability depends on some factors such as: capsulorhexis size (Nagy et al., 2011), IOL diameters versus capsular bag diameter (Vounotrypidis et al., 2018), IOL material properties (Chua et al., 2012; Bozukova et al., 2013), and above all, haptic design (Wirtitsch et al., 2004; Crnej et al., 2011; Choi et al., 2018). The main function of the haptics is to offer proper positional stability, avoiding tilt, decentration, or rotation of the optic (Garzón et al., 2015; Miháľtz et al., 2018). There are different haptics designs which depend on the

shape such as plate and open-loop style (Chang, 2008; Prinz et al., 2011; Bozukova et al., 2015). However, the effectiveness of one against the other has not yet been proved, being the open-loop style the most common design. Furthermore, the shape of the haptics can be planar (0-degree angle); step-vaulted (having an offset from the optical plane); and angulated (forming an angle relative to the optic plane). Several clinical studies have evaluated mechanical stability with each of these designs (Schmidbauer et al., 2002; Vock et al., 2007).

In order to reliably predict the postoperative optical performance and the mechanical behaviour of the intraocular implant, the IOLs must have strict quality and performance features. IOL designs must fulfil the strict requirements in terms of the optical performance (resolution efficiency or modulation transfer function) following the requirements set out by the International Standards ISO (11979-2:2014), and in terms of mechanical properties (compression force, dimension tolerance, and dynamic fatigue durability), following the guidelines specifies in the International Standards ISO (11979-3:2012). Several studies have experimentally and numerically evaluated the biomechanical properties

\* Correspondence to: Calle María de Luna, 50018, Edificio Betancourt, University of Zaragoza, Spain.  
E-mail address: [iulen@unizar.es](mailto:iulen@unizar.es) (I. Cabeza-Gil).

<https://doi.org/10.1016/j.jmbbm.2020.104165>

Received 31 December 2019; Received in revised form 11 August 2020; Accepted 23 October 2020

Available online 27 October 2020

1751-6161/© 2020 Elsevier Ltd. All rights reserved.

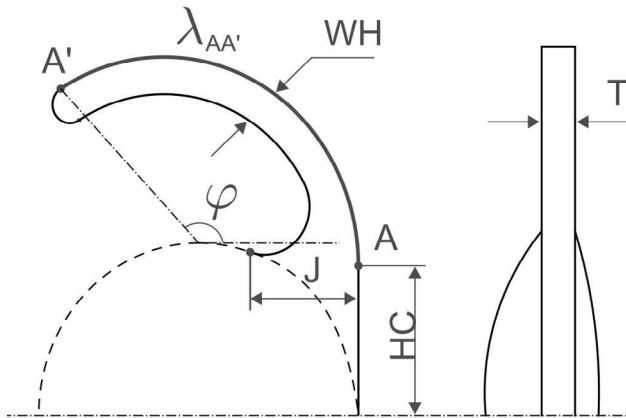


Fig. 1. Geometry of the IOLs under investigation.

of different IOLs (Lane et al., 2004; Bozukova et al., 2015; Remón et al., 2018; Lane et al., 2019).

In our previous study (Cabeza-Gil et al., 2019), we performed a numerical study through finite element method (FEM) to determine the effect on the biomechanical stability of haptic geometry in C-loop IOLs, based on the methodology of design of experiments (Montgomery, 2001). We suggested that stiffer designs provide a worse response within the capsular bag, according to the procedure described by ISO (11979-3:2012). Hence, we designed five IOLs with the same optic, classified in two patterns, stiff and flexible, which depend mainly on the haptic-optic junction, see Fig. 1. The aim of the present work was to confirm experimentally the same tendency of the numerical results. For that purpose, five IOLs were manufactured and tested on a commercial device MFC-1385-IOL (AMCC, France). The experimental and numerical results were correlated, analysing the following mechanical biomarkers: compression force, axial displacement, angle of contact, decentration and tilt. Moreover, from the *in vitro* results, the optical properties were evaluated using a PMTF (Lambda-X, Belgium) system according to the procedure described by ISO (11979-2:2014). The effect of IOL misalignment, tilt and axial displacement on the imaging quality was evaluated.

The results obtained in this study could be a milestone in the design of intraocular lenses. The numerical model could help manufacturers during the design phase and increase the predictability of cataract surgery. In this way, a major advance in time and cost savings could be added using the proposed methodology.

## 2. Materials and methods

### 2.1. Intraocular lenses

Five 1-piece C-loop IOLs with different haptic design were manufactured according to the results obtained in our previous work (Cabeza-Gil et al., 2019). The geometry of the haptics was parametrised by six factors: the length ( $\lambda_{AA'}$ ), the width (WH), the thickness (T) and the opening angle ( $\varphi$ ) of the haptic, the start of the curvature haptic (HC), and the haptic-optic junction (J), see Fig. 1 and Table 1. Based on the haptic-optic junction (J), the models A, C, and E were classified as flexible models while the models B and D as stiff ones. All models presented an overall diameter of 13.00 mm, except for Model E, which had 11.50 mm. The optic body diameter was 6.00 mm.

All the IOLs were designed with an aberration-free aspheric optic design at the anterior lens surface. IOLs were manufactured in hydrophobic acrylic material Benz HF-1.2 Universal Blank (Benz Research and Development, USA), with a dioptric power of 20.00 dioptres (D). The refractive index is  $n = 1.485$  at the design wavelength  $\lambda_0 = 546$  nm. The radii of curvature for the front and back surfaces were 11.49 mm

Table 1  
Values of the geometrical parameters of the IOLs under investigation.

IOLs	Geometrical parameters					
	$\lambda_{AA'}$ [mm]	WH [mm]	$\varphi$ [°]	J [mm]	HC [mm]	T [mm]
#A	8.80	0.40	115	0.60	2.30	0.40
#B	8.80	0.40	115	1.80	2.30	0.40
#C	8.80	0.65	115	0.60	2.30	0.40
#D	8.80	0.65	115	1.80	2.30	0.40
#E	8.80	0.40	135	0.60	2.50	0.40

and  $-21.00$  mm, respectively. To design the aspheric IOL, a numerical model of a pseudophakic eye was implemented in an optical analysis software OSLO EDU (Lambda Research Corporation, USA). The model eye was based on the Navarro et al. (1985) schematic eye where the crystalline lens was replaced by the IOL. The aberration free design was intended to avoid adding fourth-order Zernike spherical aberration (Z04).

The IOLs were manufactured by a lathe-milling process without polishing step, see Fig. 2. Differences between the theoretical design and the manufactured IOL geometrical parameters were lower than 0.3 mm as measured with a Leica S6D LED microscope (Leica Camera AG, Germany). The haptic design is the differentiating factor between these five models.

### 2.2. Material characterisation

In order to evaluate the mechanical response of the hydrophobic acrylate material of the IOLs, uniaxial tensile and compression tests were conducted under displacement control on an INSTRON 5548 Electroplus microtester with a 150.00 N full scale load cell. Three dogbone flat samples with a gauge length of 7.50 mm, a width of 1.00 mm and an overall length of 15.00 mm were used for the tensile test. Whereas three disks of 3.00 mm thickness and 15.00 mm of diameter were used for the compression test. Before the experiments, all samples were submerged for 72 h in a saline bath at 35 °C.

Samples were subjected to four loading/unloading cycles up to 20% deformation in compression and to 10% in tensile stress, since its breaking point was close to this value. The velocity rate of the clamps for all samples was  $v = 1$  mm/min, assuming a quasi-static situation. Samples were kept submerged during the entire experiment. With the data recorded during the test, the stretch was calculated as  $\lambda = \frac{L_0 + \Delta L}{L_0}$ , where  $L_0$  is the initial length between clamps and  $\Delta L$  is the clamp displacement. Finally, the nominal stress or first Piola-Kirchhoff stress was obtained as  $P = \frac{N}{CSA}$ , where N is the applied load and CSA is the cross-section of the sample.

### 2.3. In silico compression test

Numerical simulations of the mechanical stability of the IOL during a compression test were performed using Abaqus 6.14 (Dassault Systèmes, France) according to ISO 11979-3. The biomechanical stability was evaluated through five main responses: *compression force* –mN–, *axial displacement* –mm–, *tilt* –degrees, °–, *contact angle* –degrees, °– and *decentration* –mm–. Moreover, thanks to the finite element (FE) model, the actual *contact area* –mm<sup>2</sup>–, a more accurate measurement than the contact angle, and the *strain energy*, –μJ–, could be measured.

In this compression test, the IOL is placed between two clamps (with a curvature radius of 5.00 mm) and compressed to measure its mechanical stability. The FE model is shown in Fig. 3a. A ‘hard’ contact relationship was used to minimise penetration between the contact surfaces and a friction coefficient of  $\mu = 0.2$  was considered due to the high cohesiveness of the material seen in the experimental tests. A node-to-surface contact was used to ease convergence. The material considered for the lens was assumed to be hyperelastic and isotropic while the clamps were considered as rigid solids. The clamps

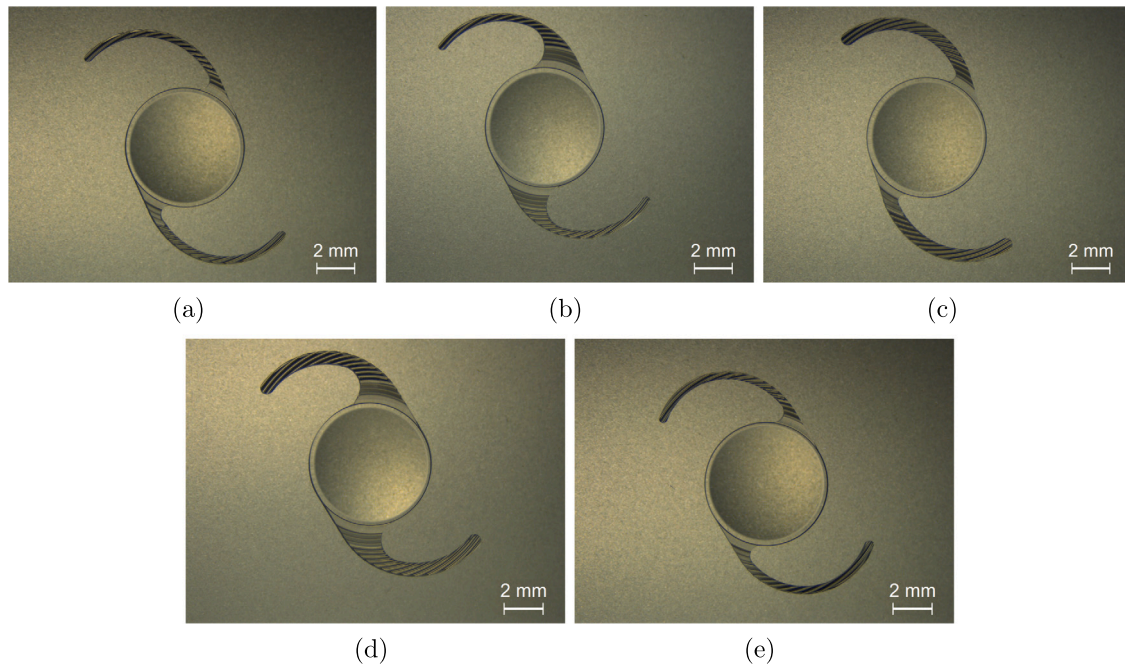


Fig. 2. Images of the manufactured lenses taken with Leica S6D LED. (a) Model A. (b) Model B. (c) Model C. (d) Model D. (e) Model E. An anti-stick profile was included in the haptic design to provide better unfolding when inserting the lenses.

are initially separated a distance greater to the overall dimension of the IOL to allow its gentle positioning without introducing pretension (see Fig. 3(a)). Then, the right clamp is displaced until a compression diameter of 9.00 mm while the left clamp remains fixed (see Fig. 3b–c). The biomechanical response was evaluated over its entire range. The standard ISO 11979-3 establishes that five key points must be recorded in order to determine the stability of the IOL (see Fig. 3b–c).

#### 2.4. *In vitro* compression test

*In vitro* tests were performed using the MFC-1385-IOL device (AMCC, France), see Fig. 4. The IOLs under investigation were compressed at a diameter of 10.00 mm following the standard ISO 11979-3 specifications for the intended use in the capsular bag. The clamps of the device are made of High-Density Polyethylene (HDPE) and the IOLs compressed in clamps were submerged in a saline solution at  $35 \pm 2$  °C, simulating *in vivo* conditions. The device provides directly the compression force at a  $10.00 \pm 0.10$  mm haptic compression. A USB camera was used to capture the images before and after the compression test. From these images the axial displacement, tilt and contact angle were measured with AutoCAD software (Autodesk, USA). All measurements were performed under identical conditions. Five IOLs of each group were tested sequentially.

#### 2.5. *In vitro* optical performance

To study the effect of misalignment (decentration), tilt and axial displacement on the imaging quality, the optical properties were evaluated experimentally using the optical bench PMTF (Lambda-X S.A., Belgium). This device follows the requirements of ISO standard 11979-2. The equipment disposes of two model corneas with different values of spherical aberrations (SA): The ISO1 model cornea with zero spherical aberration and the ISO2 model cornea with  $+0.280$   $\mu\text{m}$  SA for 5.00 mm pupil aperture. In this study, ISO2 was used as a cornea. The *in vitro* results of the mechanical biomarkers at 10.00 mm were introduced as input parameters to evaluate the optical performance. To do this, IOLs were first tilted, then decentered and finally, the CCD camera was moved axially to simulate the axial displacement of the

IOL. In this situation, the Modulation Transfer Function (MTF) at 100 cycles per degree with a 3.00 mm aperture pupil was measured, and images of the 1951 USAF target through the artificial eye were taken.

#### 2.6. Statistical analysis

Descriptive statistics were used for all objective measurements with the mean and standard deviation (SD) for the *in vitro* and *in silico* results. An ANOVA analysis for all groups was performed. All *in vitro* and *in silico* pairs were also analysed. All the analysis was performed using Matlab v2020a (MathWorks, USA). A  $p_{value} \leq 0.05$  was considered as statistically significant.

### 3. Results

#### 3.1. Material characterisation

After analysing the nominal stress–strain curves obtained in the uniaxial tests, a phenomenological behaviour which describes the experimental response at a macroscopic level was necessary to define. A hyperelastic model was used to reproduce the large deformations. A study was carried out to select the hyperelastic model that best fitted to the experimental data. From this study, the hydrophobic acrylate IOLs material was adjusted by the Ogden strain energy function with  $N=4$ :

$$\Psi = \sum_{i=1}^N \frac{2\mu_i}{\alpha_i} (\lambda_1^{-\alpha_i} + \lambda_2^{-\alpha_i} + \lambda_3^{-\alpha_i} - 3) + \frac{1}{D_1} (J^{el} - 1)^2 \quad (1)$$

with  $\lambda_{1,3}$ , being the deviatoric principal stretches.  $\mu$ ,  $\alpha$ , and  $D_1$  are the material constants and their corresponding values are:  $\mu_1 = -61.87$  MPa,  $\mu_2 = 30.25$  MPa,  $\mu_3 = 61.67$  MPa,  $\mu_4 = -29.42$  MPa,  $\alpha_1 = 10.72$ ,  $\alpha_2 = 13.43$ ,  $\alpha_3 = 5.54$ ,  $\alpha_4 = 4.24$ ,  $D_1 = 0.19$  MPa $^{-1}$ . The experimental and numerical nominal stress–strain curves were represented in Fig. 5. As can be seen, the material exhibits different tensile and compression behaviour.

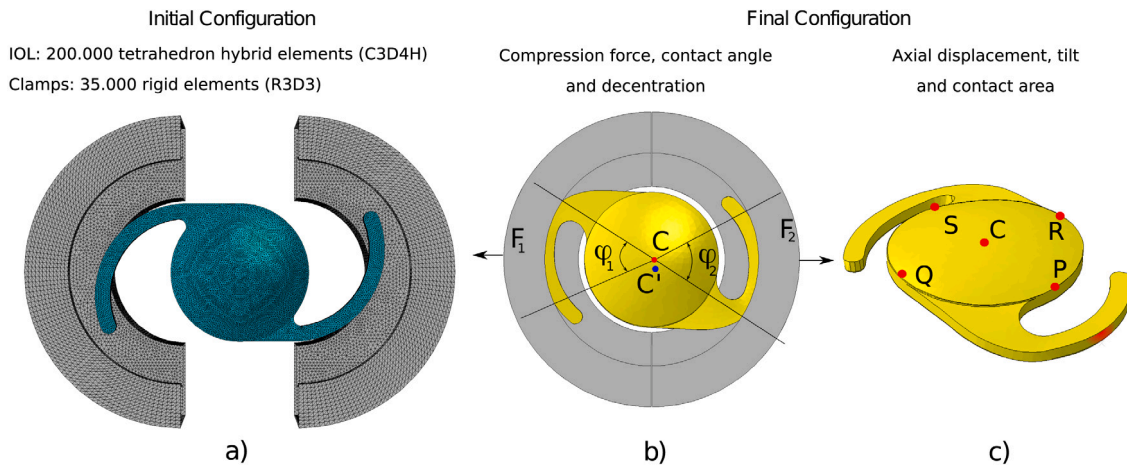


**Fig. 3.** *In silico* model of the compression test. (a) Mesh of the FE model; b) Measurement of the IOL's compression (or reaction) force, angle of contact, and decentration. Force is given by the mean force in the haptics ( $F = \frac{F_1 + F_2}{2}$ ). Angle of contact is given by the sum between ( $\gamma_1$ ) and ( $\gamma_2$ ). Decentration is the absolute distance between C and C' (red and blue point, respectively). (c) Representation of the key points (in red) used for the evaluation of the tilt (S, R, Q, P) and the axial displacement (C). The contact area is depicted in red in the front part of the haptic and is calculated internally by Abaqus v6.14.

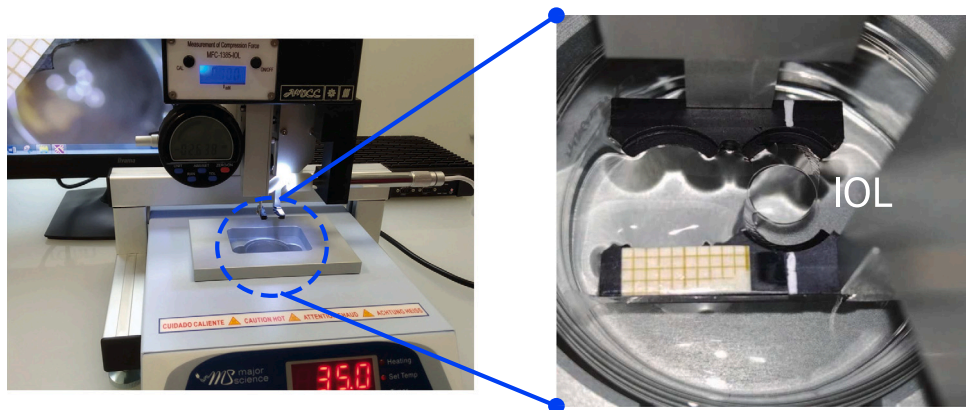


**Fig. 4.** MFC-1385-IOL device used for *in vitro* compression test.

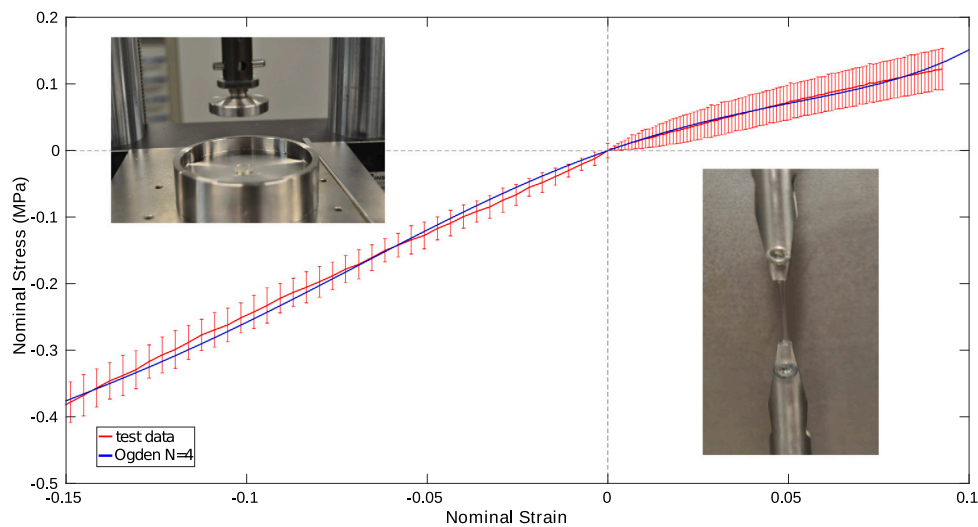


**Fig. 5.** Experimental and numerical hydrophobic acrylate material behaviour.

### 3.2. Biomechanical stability

In order to evaluate the biomechanical stability of the five C-Loop IOLs under investigation, the compression force, the axial displacement,

the tilt, the contact angle and the decentration were analysed *in vitro* and *in silico*. Fig. 6 shows the corresponding results for an IOL compression diameter of 10.00 mm. As the MFC-1385-IOL device measures the IOL response at a compression diameter of  $10.00 \pm 0.10$  mm, the mean

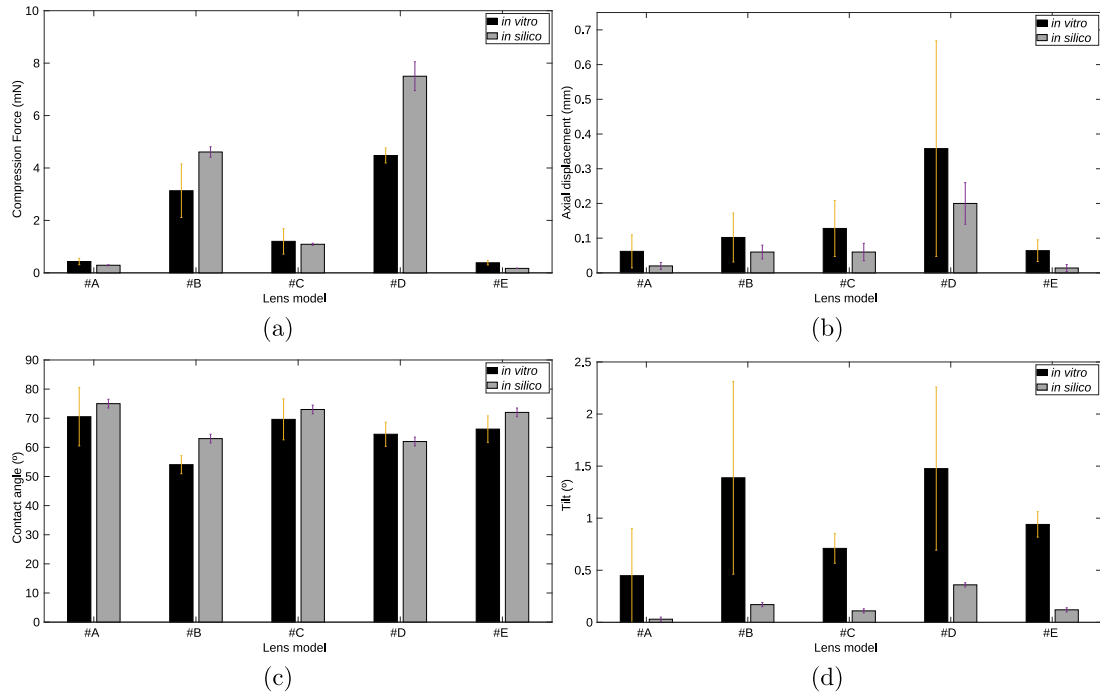


Fig. 6. Comparative values of the biomechanical stability between *in vitro* (black) and *in silico* (grey) when the clamps are closed at 10 mm: (a) Compression force; (b) Axial displacement; (c) Haptic-clamp angle of contact; (d) Tilt.

and SD *in silico* results were calculated averaging the response within the device tolerance.

Regarding the compression force, see Fig. 6a, there is a statistically significant difference ( $p_{value} < 0.05$ ) between the stiff and flexible models. Models B and D, classified as the stiff ones, present a greater *in vitro* response,  $3.13 \pm 1.02$  and  $4.47 \pm 0.28$  mN, respectively, whereas the mean compression force for the flexible models A and E was  $0.41 \pm 0.09$  mN. Model C, which has a higher width of the haptic than the other flexible models, presents a compression force of  $1.20 \pm 0.48$  mN. The *in silico* response is comparable to *in vitro* results, but providing a greater compression force of  $4.62 \pm 0.21$  and  $7.52 \pm 0.55$  mN for models B and D, respectively. Nevertheless, there is not a statistically significant difference between *in vitro* and *in silico* results ( $p_{value} > 0.05$ ), except for model D ( $p_{value} < 0.05$ ).

In terms of the axial displacement, see Fig. 6b, model D presents the highest *in vitro* value and deviation, resulting in  $0.35 \pm 0.31$  mm, opposed to  $0.19 \pm 0.05$  mm provided *in silico*. The other models (A, B, C, and E) barely presented axial displacement, neither *in vitro* nor *in silico*.

Concerning the angle of contact, see Fig. 6c, there is not statistically significant difference between *in vitro* and *in silico* results ( $p_{value} > 0.05$ ). However, there was a statistically significant difference ( $p_{value} < 0.05$ ) between the stiff models B and D, with a mean value of  $56.25 \pm 3.61^\circ$  and the flexible IOL designs (A, C, and E),  $68.45 \pm 7.86^\circ$ .

Finally, in the tilt response, see Fig. 6d, there is a statistically significant difference between *in vitro* and *in silico* results ( $p_{value} < 0.05$ ). The numerical results of the tilt are approximately zero. Moreover, for the *in vitro* results there is a statistically significant difference between the stiffest models (B and D) and the flexible ones (A, C, and E). The mean *in vitro* value of the IOL designs (B and D) is  $1.43 \pm 0.85^\circ$  whereas for the flexible IOL designs is  $0.73 \pm 0.27^\circ$ . The mean decentration is  $0.23 \pm 0.04$  mm and  $0.08$  mm for *in vitro* and *in silico*, respectively.

Fig. 7 shows the evolution of compression force, axial displacement contact area and strain energy as a function of the IOL diameter compression. Models B and D were only stable up to a compression diameter of 9.35 mm. The compression force variation, see Fig. 7a, when the haptic was compressed to 10.00 mm, ranged from 7.52 mN

for the model D to 0.30 mN for the model A. The axial displacement variation, see Fig. 7b, when the haptic was compressed to 10.00 mm, ranged from 0.19 mm for the model D to 0.01 mm for the models A, B and E. For model D, the axial displacement increases exponentially from 10.40 up to 9.85 mm and is correlated with the other responses, while model B starts to present an exponential behaviour from an IOL diameter compression of 10.00 mm. The stiff models (B and D) present a higher contact area, around  $0.55 \text{ mm}^2$  along the entire response, see Fig. 7c, whereas the flexible models present a contact area of  $0.15 \text{ mm}^2$ . Lastly, the strain energy follows the same pattern as the compression force, reaching a strain energy of  $5.27 \text{ }\mu\text{J}$  for model D at 9.85 mm.

### 3.3. *In vitro* optical performance

Fig. 8 shows the images of the USAF with a 3.00 mm diameter pupil for all IOLs under investigation. The images were taken on-axis and off-axis with a combination of misalignment and tilt (top row) and combination of misalignment, tilt and axial displacement (bottom row). As can be seen, model B presents the worst image quality when the axial displacement was set to 0. However, when the axial displacement was considered, model D had the worst image quality. Fig. 9 shows the experimental on axis and off axis MTF results. On-axis MTFs was above to 0.43 for all models (value specified at the ISO 11979-2). When the displacement parameters were considered, MTF value falls below 0.43 for all models of IOL; when the axial displacement was set to 0, MTF value falls below 0.43 for models B, C and D. The results were consistent with the USAF images.

## 4. Discussion

The ISO (11979-3:2012) specifies requirements and test methods for certain mechanical properties of IOLs intended for capsular bag placement. The mechanical properties are essential to guarantee a good stability inside the capsular bag avoiding decentration, axial displacement, tilt or rotation that affect the visual performances after cataract surgery (Garzón et al., 2015; Miháltz et al., 2018). The main goal of this study was to design an aberration-free spherical IOL and to study

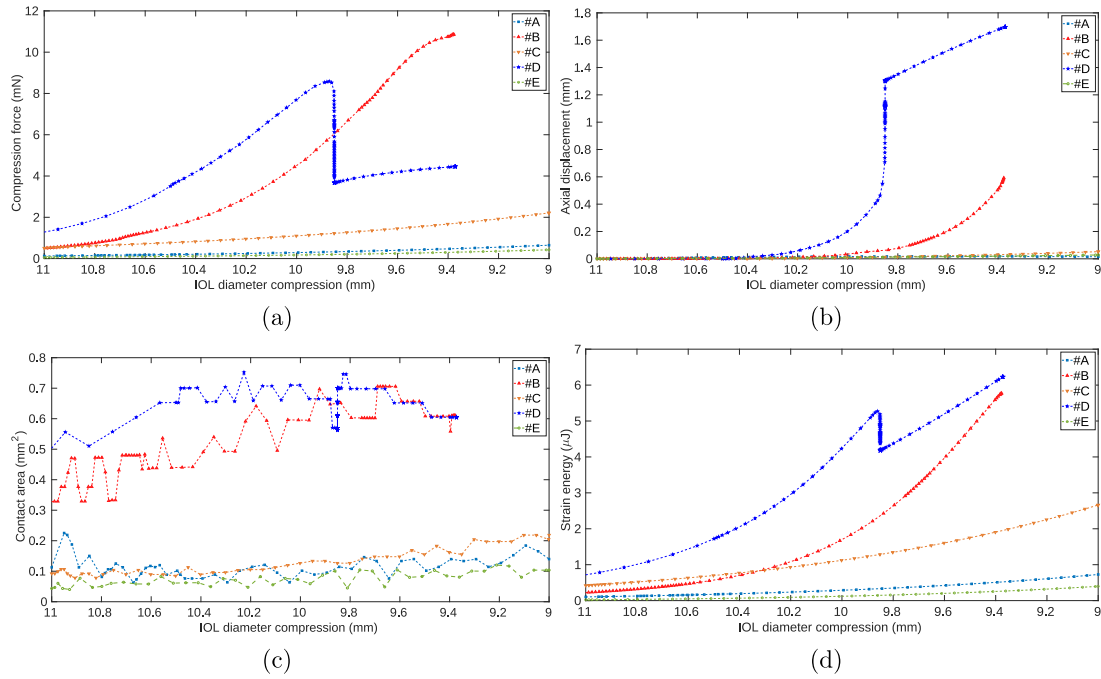


Fig. 7. *In silico* results of the compression force (a), axial displacement (b), contact area (c) and the strain energy (d) vs the IOL diameter compression (mm) for all IOLs analysed.

	Model A	Model B	Model C	Model D	Model E
On-axis					
Tilt + Decentered					
Tilt + Decentered + Axial displacement					

Fig. 8. The 1951 USAF test images of the different IOLs models for on-axis, tilt and decentered, and the worst-case scenario position for all the IOLs under investigation.

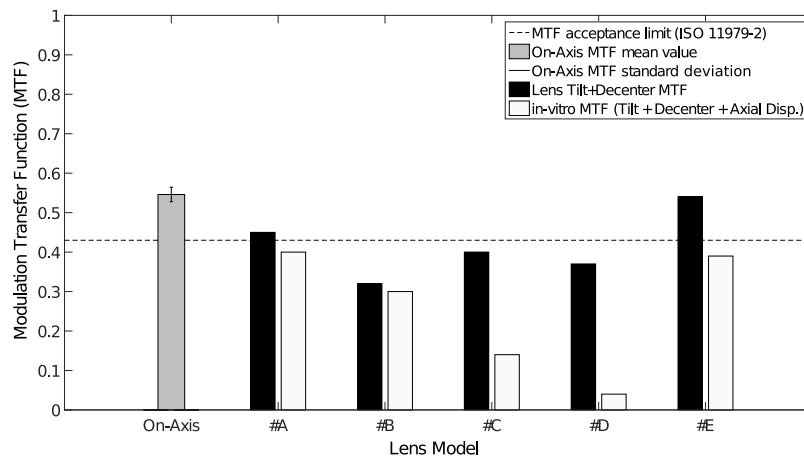


Fig. 9. MTF deviation compared to the On-axis MTF value and the MTF obtained from the results *in vitro*, measured in the PMTF instrument.

the influence of haptic geometry on the optical quality. To do this, 5 hydrophobic IOLs with different haptic design were manufactured (see Fig. 2) and the biomechanical stability was compared numerically and experimentally. The IOLs were classified as stiff (models B and D) and flexible designs (models A, C, and E) depending on their haptic geometry. Previously, we evaluated the biomechanical properties (Cabeza-Gil et al., 2019) *in silico* of these models of IOLs and we found that the stiffer IOLs designs tend to offer a worse stability than flexible ones. A comparison between *in vitro* and *in silico* results was performed.

It can be stated that these results have provided undeniable evidence of a correlation between the *in vitro* and *in silico* results, see Fig. 6. Based on the high deviation in compression force and axial displacement presented in the *in vitro* tests, to make a more accurate comparison, they were compared with the numerical results within the MFC-1385-IOL device tolerance. The deviation in the *in vitro* results can be explained by the numerical response, see Fig. 7a and Fig. 7b, which shows a high sensitivity of the responses as function of the IOL diameter compression.

The compression force showed the same trend *in vitro* and *in silico*. However the *in silico* compression force for the models B and D were slightly higher than those measured *in vitro*. Models B and D were stable up to 9.35 mm, what suggests that a lower IOL diameter compression could compromise the stability of these IOLs. Moreover, the strain energy was directly correlated with the compression force, see Fig. 7a and Fig. 7d. Bozukova et al. (2015) also found that the *in silico* radial compression forces were generally higher than those measured *in vitro*.

Experimentally, the *in vitro* axial displacement showed higher values than *in silico* results. Model D presents the greatest axial displacement, resulting in  $0.35 \pm 0.31$  mm *in vitro* conditions. Their high deviation can be explained observing Fig. 7a and Fig. 7b, which shows that the critical compression diameter of this IOL is close to 10.00 mm, where the *in vitro* and *in silico* results were compared. Recently, Lane et al. (2019) found an axial displacement at 10.00 mm ranging from  $-0.01$  mm for the Acrysof SN60WF to 0.68 mm for the enVista MX60.

Concerning the haptic-clamp angle of contact, the *in vitro* results were quite similar to the *in silico* results. The stiffest models seem to have a lower angle of contact. The actual contact area was measured numerically, which cannot be measured experimentally, and the results showed that the stiffest models presented a higher contact area, which seems to be correlated with the compression force. This inconsistency shows that the angle of contact may not be the right measurement since it is a subjective measurement and provides not so accurate results.

*In silico* optic tilt was generally lower than those measured *in vitro*. Models B and D present a mean optic tilt of  $1.43 \pm 0.85^\circ$  *in vitro* conditions and in the other models the mean optic tilt was  $0.73 \pm 0.27^\circ$  in the same conditions. Lane et al. (2019) found experimentally an optic tilt between  $0.5^\circ$  to  $1.2^\circ$  for all evaluated IOLs. From an operator's perspective, those experimental values are practically  $0^\circ$ , so it could be said that also the *in vitro* and *in silico* tilt is correlated. These results suggests that flexible IOL designs offer a better biomechanical stability than stiffer models, which is consistent with the findings in previous studies (Bozukova et al., 2013; Lane et al., 2019). Last but not least, the optical performance, evaluated experimentally, showed small changes in the MTF and image quality (USAF) when the magnitudes of displacement parameters (only tilt and decentered) are considered. However, with axial displacement, there is a considerable loss of optical quality. It allowed us to verify that the mechanical biomarkers can predict the optical performance.

The large deviation measured *in vitro* for the different main responses, particularly, for the axial displacement and optic tilt, can be also explained by some noisy factors such as temperature; IOL placement, which could affect the contact areas; or even the subjective measures taken by the operator. Previously, Lane et al. (2004, 2019), found also a great variability in their experimental work, which suggests the need of a standardised biomechanical testing procedure to compare different IOL designs.

One of the limitations of the *in vitro* measurements is that only one IOL diameter compression (10.00 mm) can be tested while the clinical outcomes might depend on the capsular bag size (Garzón et al., 2015). In this study, the biomechanical responses were evaluated numerically for different IOL diameters compression simulating different capsular bag sizes, see Fig. 7. As can be seen, a lower simulated capsular bag size induced higher compression force and axial displacement, being the highest value for the models B and D. In conclusion, the FE model proposed can reproduce faithfully the compression test, ISO (11979-3:2012). Moreover, it can be useful in the design phase to the manufacturers, reducing costs and time by exploring a feasible space of solutions during the product design process and before manufacturing. Further studies should be carried out to analyse how the compression test can predict the behaviour of the lens in the capsule.

## CRedit authorship contribution statement

**I. Cabeza-Gil:** Methodology, Software, Formal analysis, Writing - original draft. **J. Pérez-Gracia:** Investigation, Resources, Writing - original draft. **L. Remón:** Conceptualization, Supervision, Writing - reviewing & editing. **B. Calvo:** Conceptualization, Supervision, Writing - reviewing & editing.

## Declaration of competing interest

The authors declare that they have no known competing financial interests or personal relationships that could have appeared to influence the work reported in this paper.

## Acknowledgements

The authors gratefully acknowledge research support from the Spanish Ministerio de ciencia, innovación y universidades (Grant DPI2017-84047-R) and the Department of Industry and Innovation (Government of Aragon), Spain through the research group Grant T24-20R (cofinanciado con Feder 2014–2020: Construyendo Europa desde Aragon). Part of the work was performed by the ICTS 'NANBIOSIS' specifically by the High-Performance Computing Unit (U27) of the CIBER in Bioengineering, Biomaterials & Nanomedicine (CIBER-BBN at the University of Zaragoza). Moreover, authors acknowledge AJL Ophthalmic S.A. for manufacturing the proofs of concept of IOLs in this study. I. Cabeza-Gil and J. Pérez-Gracia were supported by the Spanish Ministry of Economy and Competitiveness, PRE2018-084021 and DI-16-08888, respectively.

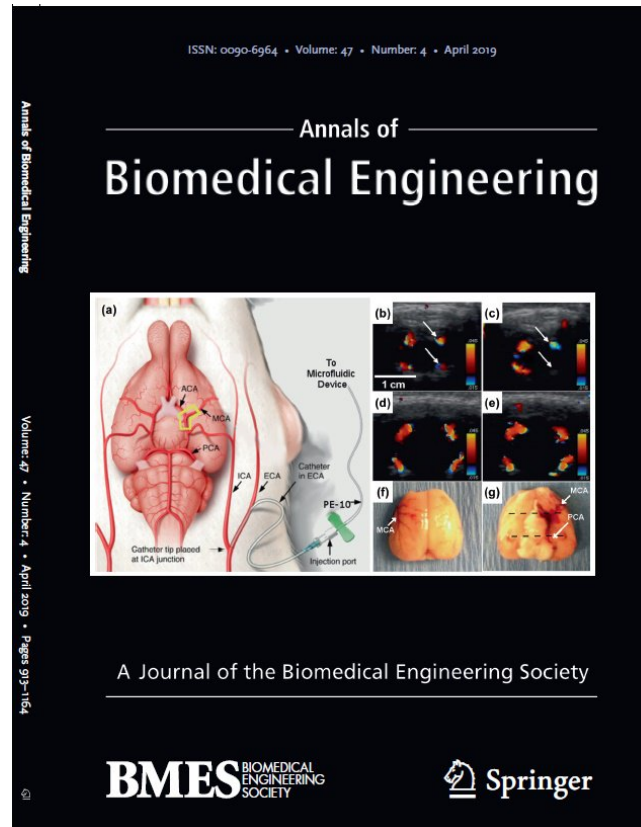
## References

- Alió, J., Plaza-Puche, A., Javaloy, J., Ayala, M., Vega-Estrada, A., 2013. Clinical and optical intraocular performance of rotationally asymmetric multifocal IOL plate-haptic design versus c-loop haptic design. *J. Refract. Surg.* 29 (4), 252–259.
- Bozukova, D., Pagnouille, C., Jérôme, C., 2013. Biomechanical and optical properties of 2 new hydrophobic platforms for intraocular lenses. *J. Cataract. Refract. Surg.* 39 (9), 1404–1414.
- Bozukova, D., Werner, L., Mamalis, N., Gobin, L., Pagnouille, C., Floyd, A., Liu, E., Stallings, S., Morris, C., 2015. Double-c loop platform in combination with hydrophobic and hydrophilic acrylic intraocular lens materials. *J. Cataract. Refract. Surg.* 41 (7), 1490–1502.
- Cabeza-Gil, I., Ariza-Gracia, M.Á., Remón, L., Calvo, B., 2019. Systematic study on the biomechanical stability of c-loop intraocular lenses: Approach to an optimal design of the haptics. *Ann. Biomed. Eng.*
- Chan, E., Mahroo, O.A.R., Spalton, D.J., 2010. Complications of cataract surgery. *Clin. Exp. Opt.* 93 (6), 379–389.
- Chang, D., 2008. Comparative rotational stability of single-piece open-loop acrylic and plate-haptic silicone toric intraocular lenses. *J. Cataract. Refract. Surg.* 34 (11), 1842–1847.
- Choi, M., Lazo, M., Kang, M., Lee, J., Joo, C., 2018. Effect of number and position of intraocular lens haptics on anterior capsule contraction: a randomized, prospective trial. *BMC Ophthalmol.* 18 (1).
- Chua, W., Yuen, L., Chua, J., Teh, G., Hill, W., 2012. Matched comparison of rotational stability of 1-piece acrylic and plate-haptic silicone toric intraocular lenses in asian eyes. *J. Cataract. Refract. Surg.* 38 (4), 620–624.

- Crnej, A., Hirschall, N., Nishi, Y., Gangwani, V., Taberner, J., Artal, P., Findl, O., 2011. Impact of intraocular lens haptic design and orientation on decentration and tilt. *J. Cataract. Refract. Surg.* 37 (10), 1768–1774.
- Garzón, N., Poyales, F., de Zárate, B.O., Ruiz-García, J., Quiroga, J., 2015. Evaluation of rotation and visual outcomes after implantation of monofocal and multifocal toric intraocular lenses. *J. Refract. Surg.* 31 (2), 90–97.
- ISO, 11979-2:2014. Ophthalmic implants. Intraocular lenses. Part 2: Optical properties and test methods. BSI Standards Limited.
- ISO, 11979-3:2012. Ophthalmic implants. Intraocular lenses. Part 3. Mechanical properties and test methods. BSI Standards Limited.
- Lane, S., Burgi, P., Milios, G., Orchowski, M., Vaughan, M., Schwarte, E., 2004. Comparison of the biomechanical behavior of foldable intraocular lenses. *J. Cataract. Refract. Surg.* 30 (11), 2397–2402.
- Lane, S., Collins, S., Das, K.K., Maass, S., Thatthamla, I., Schatz, H., Noy, S.V., Jain, R., 2019. Evaluation of intraocular lens mechanical stability. *J. Cataract. Refract. Surg.* 45 (4), 501–506.
- Miháltz, K., Lasta, M., Burgmüller, M., Vécsei-Marlovits, P., Weingessel, B., 2018. Comparison of two toric IOLs with different haptic design: Optical quality after 1 year. *J. Ophthalmol.* 2018, 1–7.
- Montgomery, D., 2001. *Design & Analysis of Experiments*, fifth ed. John Wiley, New York.
- Nagy, Z., Kránitz, K., Takacs, A., Miháltz, K., Kovács, I., Knorz, M., 2011. Comparison of intraocular lens decentration parameters after femtosecond and manual capsulotomies. *J. Refract. Surg.* 27 (8), 564–569.
- Navarro, R., Santamaria, J., Bescos, J., 1985. Accommodation-dependent model of the human eye with aspherics. *J. Opt. Soc. Amer. A* 2 (8), 1273–1281.
- Pérez-Merino, P., Marcos, S., 2018. Effect of intraocular lens decentration on image quality tested in a custom model eye. *J. Cataract. Refract. Surg.* 44 (7), 889–896.
- Prinz, A., Neumayer, T., Buehl, W., Vock, L., Menapace, R., Findl, O., Georgopoulos, M., 2011. Rotational stability and posterior capsule opacification of a plate-haptic and an open-loop-haptic intraocular lens. *J. Cataract. Refract. Surg.* 37 (2), 251–257.
- Remón, L., Siedlecki, D., Cabeza-Gil, I., Calvo, B., 2018. Influence of material and haptic design on the mechanical stability of intraocular lenses by means of finite-element modeling. *J. Biomed. Opt.* 23 (03), 1.
- Schmidbauer, J.M., Escobar-Gomez, M., Apple, D.J., Peng, Q., Arthur, S.N., Vargas, L.G., 2002. Effect of haptic angulation on posterior capsule opacification in modern foldable lenses with a square, truncated optic edge. *J. Cataract. Refract. Surg.* 28 (7), 1251–1255.
- Vock, L., Georgopoulos, M., Neumayer, T., Buehl, W., Findl, O., 2007. Effect of the hydrophilicity of acrylic intraocular lens material and haptic angulation on anterior capsule opacification. *Br. J. Ophthalmol.* 91 (4), 476–480.
- Vounotrypidis, E., Lackerbauer, C., Kook, D., Dirisamer, M., Priglinger, S., Mayer, W., 2018. Influence of total intraocular lens diameter on efficacy and safety for in the bag cataract surgery. *Oman. J. Ophthalmol.* 11 (2), 144–149.
- Wirtitsch, M., Findl, O., Menapace, R., Kriechbaum, K., Koepl, C., Buehl, W., Drexler, W., 2004. Effect of haptic design on change in axial lens position after cataract surgery. *J. Cataract. Refract. Surg.* 30 (1), 45–51.
- Zvorničanin, J., Zvorničanin, E., 2018. Premium intraocular lenses: The past, present and future. *J. Curr. Ophthalmol.* 30 (4), 287–296.



### 3.3 Work 5: Systematic Study on the Biomechanical Stability of C-loop Intraocular Lenses: Approach to an Optimal Design of the Haptics



Cabeza-Gil I., Ariza-Gracia M.Á., Remón L., Calvo B.  
Annals of Biomedical Engineering  
JIF (2020) = 3.93 (Q2: 31/89 Biomedical Engineering)  
SJR (2020) = 0.91 (Q2: 67/232 Biomedical Engineering)



Original Article

# Systematic Study on the Biomechanical Stability of C-Loop Intraocular Lenses: Approach to an Optimal Design of the Haptics

I. CABEZA-GIL <sup>1</sup>, M. Á. ARIZA-GRACIA,<sup>3</sup> L. REMÓN,<sup>2</sup> and B. CALVO<sup>1,4</sup>

<sup>1</sup>Aragón Institute of Engineering Research (i3a), University of Zaragoza, Zaragoza, Spain; <sup>2</sup>Departamento de Física Aplicada, University of Zaragoza, Zaragoza, Spain; <sup>3</sup>ARTORG Center for Biomedical Engineering Research, Universität Bern, Bern, Switzerland; and <sup>4</sup>Centro de Investigación Biomédica en Red en Bioingeniería, Biomateriales y Nanomedicina (CIBER-BBN), Zaragoza, Spain

(Received 5 September 2019; accepted 3 December 2019; published online 11 December 2019)

Associate Editor Eiji Tanaka oversaw the review of this article.

**Abstract**—To study the main design parameters that affect the mechanical stability of C-loop intraocular lenses, leading to an optimal design that minimizes the axial displacement, tilt and rotation. A total of 144 geometrical variations were studied on a 1-piece, non-angulated, C-loop hydrophobic acrylate intraocular lens. The study was performed in a finite element modeling simulation. The suitable set of variations was determined using a mixed-factorial analysis, allowing to analyse the impact of the different designs on the mechanical stability of the lens (compression force, axial displacement, tilt and rotation). The design parameters under study were: the length, width, thickness and opening angle of the haptic, the haptic–optic junction and the start of the haptic curvature. The compression (or reaction) force is affected by the haptic width, the haptic–optic junction, and the interaction between both. The axial displacement is mainly affected by the width and thickness of the haptic, and the size of the haptic–optic junction as well. The tilt is affected by the haptic thickness and the interaction between the haptic curvature and the haptic–optic junction. The rotation is affected by the start of the haptic curvature, the haptic–optic junction and the haptic width. The haptic–optic junction is one of the most influential parameters affecting the four responses studied of the C-Loop IOL. The smaller the haptic–optic junction, the better biomechanical stability.

**Keywords**—Intraocular lenses, Finite element, Haptic design, C-loop, Biomechanical stability.

Address correspondence to I. Cabeza-Gil, Aragón Institute of Engineering Research (i3a), University of Zaragoza, Zaragoza, Spain. Electronic mail: iulen@unizar.es

I. Cabeza-Gil and M. Á. Ariza-Gracia contributed equally to this work.

## INTRODUCTION

Different designs of intraocular lenses (IOLs) are available in the market to achieve an improved visual acuity and to reduce the use of spectacles after cataract refractive surgery. Premium IOLs include different options such as toric IOLs to correct pre-existing corneal astigmatism, multifocal and accommodative IOLs to provide good distance and near vision at the same time, or aspheric IOLs to provide better vision quality than traditional spherical IOLs.<sup>40</sup>

The main downside of these IOLs is that the biomechanical stability inside the capsular bag is essential to ensure a successful surgical procedure. Rotation is a crucial factor in toric<sup>24</sup> and asymmetrical multifocal<sup>3</sup> IOLs, while decentration and tilt are important in pupil-dependent multifocal and aspheric IOLs.<sup>2,27</sup> These parameters affect the optical performance and efficacy of these IOLs, resulting in significant visual disturbances.<sup>39</sup>

Rotation, decentration or tilt mainly occur in the early postoperative period, right before fusing the anterior and posterior capsule with the IOL.<sup>19</sup> Material properties,<sup>20</sup> haptic design<sup>10,12</sup> and size<sup>8</sup> of the IOL are considered to be very influential factors in the postoperative IOL stability. Incomplete viscoelastic clearance, early postoperative IOL fluctuations, capsulorhexis size and axial length are other influencing factors.<sup>23,34</sup>

After the first poly-methyl-methacrylate (PMMA) IOL was implanted by Harold Ridley in 1949,<sup>32</sup> hydrophobic and hydrophilic acrylate, and silicone<sup>36</sup> foldable materials have been developed to allow

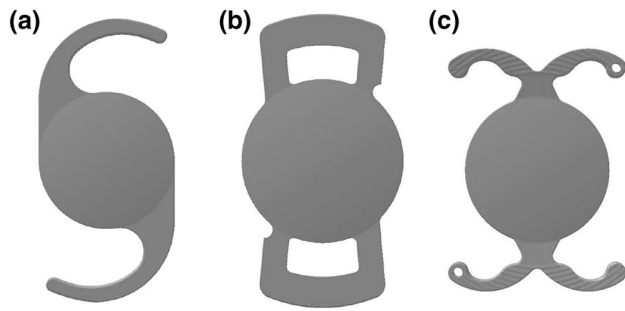


**FIGURE 1.** Different IOL designs: (a) C-loop design; (b) Plate design; (c) Double-C Loops design.

removing the cataract through smaller incisions. Moreover, a variety of IOLs with different optic size,<sup>34,35</sup> edge profiles,<sup>37</sup> haptic materials and designs<sup>10,12,38</sup> have been developed to minimize decentration, dislocations and tilt. But industry has emphasized the design of the haptics, leading to different revolutionary designs such as plate, plate-loop or open-loop (C-loop, J-loop, L-loop and Double-C Loops), see Fig. 1, style with planar and angulated haptics.<sup>5,9,21,26,30</sup>

Within this plethora of designs, loop haptics have been suggested to ensure a better stabilization and centration than IOLs with plate-like haptics.<sup>5,9,11</sup> In contrast, plate haptics showed better rotational stability.<sup>26</sup> In terms of axial stability, planar haptic designs perform better than angulated designs, reducing the impact in the final refractive errors.<sup>17,18,28,31</sup> Finally, single-piece IOLs exhibited better axial stability and more stable refractive outcomes than three-piece IOLs, presenting no difference in decentration or optic tilt.<sup>14,38</sup>

Another important factor that has been suggested to determine the biomechanical stability of the IOL is the size of the lens. For larger capsular bags, IOLs with smaller diameters had a higher risk of presenting axial displacement, decentration or tilt. Furthermore, IOLs rotated more in eyes with longer axial lengths, which often have a bigger capsular bag diameter than highly hyperopic eyes.<sup>34,35</sup> Despite the existence of several designs, all posterior chamber IOLs for cataract surgery are manufactured with a total overall diameter, neglecting either the inherent patient's variability of the capsular bag, which ranges from 9.6 to 10.2 mm, or the axial length of the eyeball.

Although there are several methods to measure decentration, tilt or rotation after implantation in a pseudophakic eye,<sup>16,29</sup> IOLs must have strict performance features to reliably predict their mechanical behavior. The International Organization for Standardization specifies guidelines and testing methods for

certain biomechanical properties of IOLs (ISO 11979-3).<sup>7</sup>

Biomechanical stability of different commercial IOLs with different materials has been studied experimentally<sup>4,5,18</sup> and numerically.<sup>31</sup> In a previous study, we used finite element modelling (FEM) to evaluate the biomechanical stability of four different hydrophobic and hydrophilic acrylate IOLs with different haptic designs following the procedure described in the ISO 11979-3.<sup>31</sup> In particular, the material and the design were found to be of importance on the postoperative behavior of an IOL.

This work presents the first systematic study based on Design of Experiments and *in silico* modeling to evaluate the effect of key design parameters on the mechanical stability of a 1-piece hydrophobic acrylate IOL with non-angulated C-loop haptics. The C-loop design was chosen as benchmark since it presents better stability and centration than other multipiece, angulated or plate designs. Likewise, an hydrophobic acrylate material was used as it presents a higher level of adhesiveness than hydrophilic acrylate or silicone, being a gold standard to prevent the posterior capsule opacification.<sup>13</sup> *In silico* analysis was performed using a finite element (FE) model, simulating the dynamic compression procedure described in the Standard ISO 11979-3.<sup>7</sup> A dataset of 144 geometrical variations was analysed to determine the lens that guarantees the best biomechanical stability (i.e., axial displacement, tilt, and rotation). The presented methodology can help manufacturers during the design phase, to know which IOLs present better stability based on the design, and represents a first step towards the customization of IOLs.

## MATERIALS AND METHODS

### *Parametrization of the Geometry and Factorial Design*

The geometry of the 1-piece, non-angulated, hydrophobic acrylate C-loop IOL was parametrized with six variables (see Fig. 2): the length ( $\lambda_{AA'}$ ), the width (WH), the thickness (T), and the opening angle ( $\varphi$ ) of the haptic, the start of the curvature haptic (HC), and the haptic–optic junction (J). The start of the haptic curvature and the opening angle of the haptic define the overall diameter of the IOL, which ranges from 11.20 to 13.70 mm.

Biomechanical stability can be evaluated through four main parameters: *compression force*—mg— (also referred to as *reaction force*), *axial displacement*—mm—, *tilt*—degrees, °—and *rotation*—degrees, °—. To study the effect of the haptic design on the biomechanical

stability, 64 and 144 geometrical variations were created according to the methodology of design of experiments.<sup>22</sup> First, a  $2^k$  full-factorial design was used to prescreen the most influential geometrical parameters of the IOL and to reduce the number of simulations. A dataset of 64 geometries was built using two levels of variation (Low and High. See Table 1) for each of the six parameters under study (i.e.,  $2^6 = 64$ ). From the prescreening analysis, the haptic–optic junction (J), the start of the haptic curvature (HC), and the thickness of the haptic (T) were considered as relevant.

Second, a mixed-level full factorial design was used to extend the prior analysis and to gain a deeper insight into the effect of the prescreened relevant variables (i.e., J, HC, T). Importantly, the haptic–optic junction (J) had to be decreased from 1.8 to 1.2 mm for two reasons: first, IOLs became unstable due to the high junction stiffness leading to unrealistic values of axial displacement and tilt; second, its prevalence biased the statistical analysis towards it, making impossible to distinguish the effect of the remaining design parameters. Hence, only an intermediate level was included for the start of the haptic curvature (HC) and the thickness of the haptic (T), resulting on a mixed-level factorial

design of 144 geometries (i.e.,  $3^2 \times 2^4 = 144$ ) that combined two parameters at three levels (HC and T), and four parameters at two levels ( $\lambda_{AA'}$ , WH,  $\varphi$ , J). For the sake of simplicity and to avoid introducing additional bias, the optic was the same for all geometries (+ 22.00 D), with an appropriate square haptic design. All the parameters were varied according to real measures of available commercial lenses (see Table 1).

After generating the dataset of geometrical combinations and associated biomechanical stability, the main effect and interactions of each parameter were studied using analysis of variance (ANOVA). The main effect plots represent the effect of either the individualised mean response for each factor level on the variance of a single outcome. Interaction plots represent how the interaction between two variables affects the variance of a single outcome. Pareto charts were used to represent the degree of influence of each design parameter on the variance of each mechanical stability outcome. Finally, the correlation between design parameters and stability outcomes was studied using the Pearson correlation coefficient (i.e., correlation matrix). All the analysis was performed using Minitab 18 (State College, Pennsylvania, USA) and Python.<sup>15,25,33</sup> A  $p$  value  $\leq 0.05$  was considered as statistically significant.

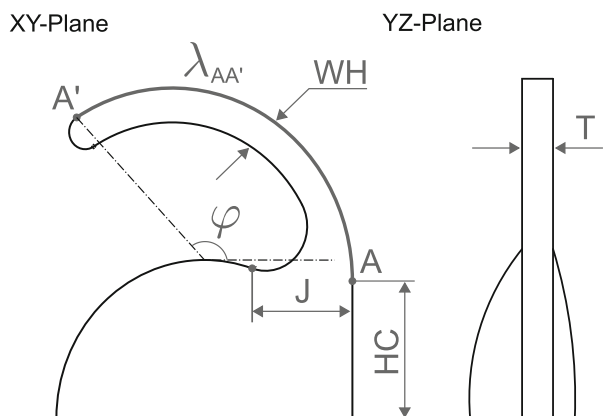


FIGURE 2. Parametrization of the C-loop IOL.

#### *In Silico Compression Test and Determination of Mechanical Stability*

The standardised compression test was performed to approximate the behaviour of the IOL in the capsular bag. Numerical simulations of the mechanical stability of the IOL during a compression test were performed using Abaqus 6.14 (Dassault Systèmes) according to the procedure described in ISO 11979-3. In this compression test, the IOL is placed between two clamps (with a curvature radius of 5 mm) and compressed to measure its mechanical stability. The clamps are initially separated a distance equal to the overall dimension of the IOL to allow its gentle positioning without introducing pretension (see Fig. 3(a)). Then,

TABLE 1. Levels of parameter's variation (Low, Medium and High) involved on the  $2^k$  and mixed-level factorial design.

Parameters	Low value	Middle value	High value
$\lambda_{AA'}$ : Haptic length (mm)	8.20	–	8.70
WH: Haptic width (mm)	0.40	–	0.65
$\varphi$ : Opening angle of the haptic ( $^\circ$ )	110	–	135
J: haptic–optic junction (mm)	0.60	–	$\{J_j, J_f\}$
HC: Start of the haptic curvature (mm)	2.00	2.30	2.50
T: Thickness haptic (mm)	0.30	0.35	0.40

$J_j$  is the junction for the prescreening analysis ( $J_j = 1.8$  mm) while  $J_f$  is the junction for the mixed-level factorial design ( $J_f = 1.2$  mm)..

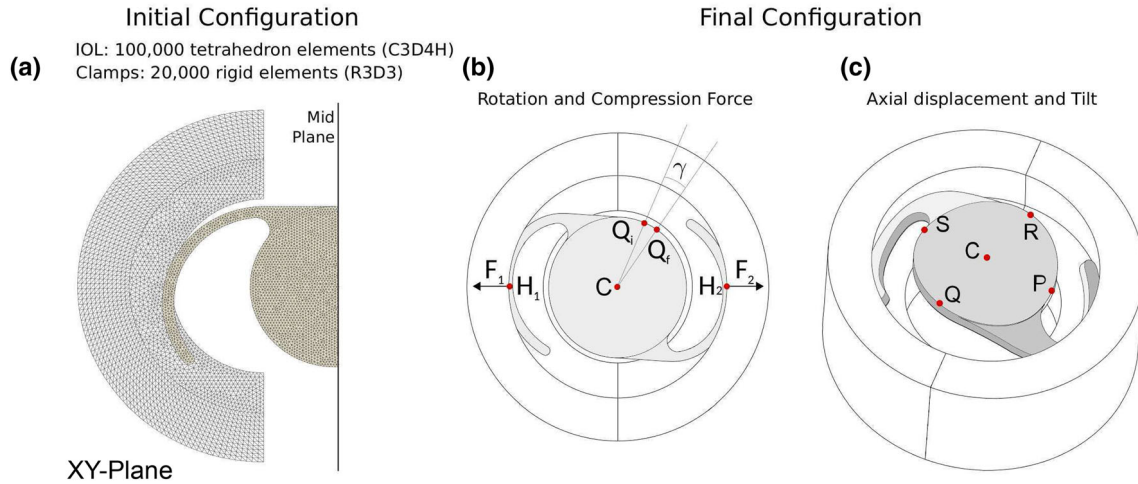


**FIGURE 3.** *In silico* model of the compression test. (a) Mesh of the *in silico* model (only half of the model is depicted); (b) Measurement of the IOL's rotation and compression (or reaction) force. Rotation is given by the relative angle ( $\gamma$ ) between the same point at the beginning ( $Q_i$ ) and the end ( $Q_f$ ) of the test. Force is given by the sum of the forces in the haptics ( $F = F_1 + F_2$ ); (c) Representation of the key points (in red) used for the evaluation of the tilt (S, R, Q, P) and the axial displacement (C).

the right clamp is displaced until a compression diameter of 10 mm while the left clamp remains fixed (see Figs. 3b and 3c).

The compression (or reaction) force at the horizontal plane was reported only at the end of the compression. The axial displacement, the tilt and the rotation were evaluated by comparing the initial and final configuration of the lens following the Standard ISO 11979-3, which establishes that four key points must be recorded in order to determine the stability of the IOL (see Figs. 3b and 3c).

The mechanical response of the hydrophobic acrylate material was adjusted from an experimental test that we previously conducted.<sup>31</sup> The numerical model used for adjusting the mechanical behavior of the hydrophobic acrylate material was the Ogden strain energy function with  $N=4$ , see Eq. 1. Their corresponding values and the data are shown in Fig. 4.

$$\Psi = \sum_{i=1}^N \frac{2\mu_i}{\alpha_i} (\lambda_1^{-\alpha_i} + \lambda_2^{-\alpha_i} + \lambda_3^{-\alpha_i} - 3) + \frac{1}{D_1} (J^{el} - 1)^2 \quad (1)$$

with  $\lambda_{1-3}$ , the principal stretches.  $\mu_i$ ,  $\alpha_i$ , and  $D_1$  are the material parameters.

## RESULTS

To evaluate the biomechanical stability of the C-Loop IOL, the compression (or reaction) force, the axial displacement, the tilt and the rotation were numerically analysed. After the prescreening analysis (see in “Parametrization of the Geometry and Factorial Design” section), the haptic–optic junction (J) was

recalibrated. High haptic junction values ( $\approx 1.8$  mm) rendered the model unstable leading to unrealistic axial displacements and rotations (see, for example, lens #129 in Table 2) which, in turn, resulted in a biased statistical analysis that was insensitive to the perturbation of any other remaining parameter. Accordingly, only results for the mixed-level factorial design (144 IOLs) are presented below. Main effect and interaction plots were analysed to confirm the consistency of the correlation analysis.

Solely based on the Pareto's analysis, the most influential parameters on the mechanical stability seemed to be related to haptic design parameters that control the inertia of the IOL and, therefore, the IOL's bending stiffness.

The compression (or reaction) force is mostly influenced by the width of the haptic (WH—59.9%) and the haptic–optic junction (J—30.5%) (see Fig. 7a). The haptic width (WH—17.7%) and the start of the haptic curvature (HC—45.6%) are the most influential parameters on the axial displacement. Overall, the 75% of the variance in the axial displacement is mostly explained by the width of the haptic, the haptic–optic junction, the start of the haptic curvature, and the thickness of the haptic (WH, J, HC, T) while the rest of the parameters represent the remaining 25% of the variance (see in Fig. 7b). Remarkably, the interaction of the haptic width with the haptic–optic junction (WH–J) and the thickness of the haptic (WH–T) represents a non-negligible 15% of the response, outlining the importance of a careful design of the haptic proportions. The tilt variance is only affected by the thickness of the haptic (T) and the interaction between the haptic–optic junction and the start of the haptic curvature (J–HC) (see Fig. 7c). The variance in the

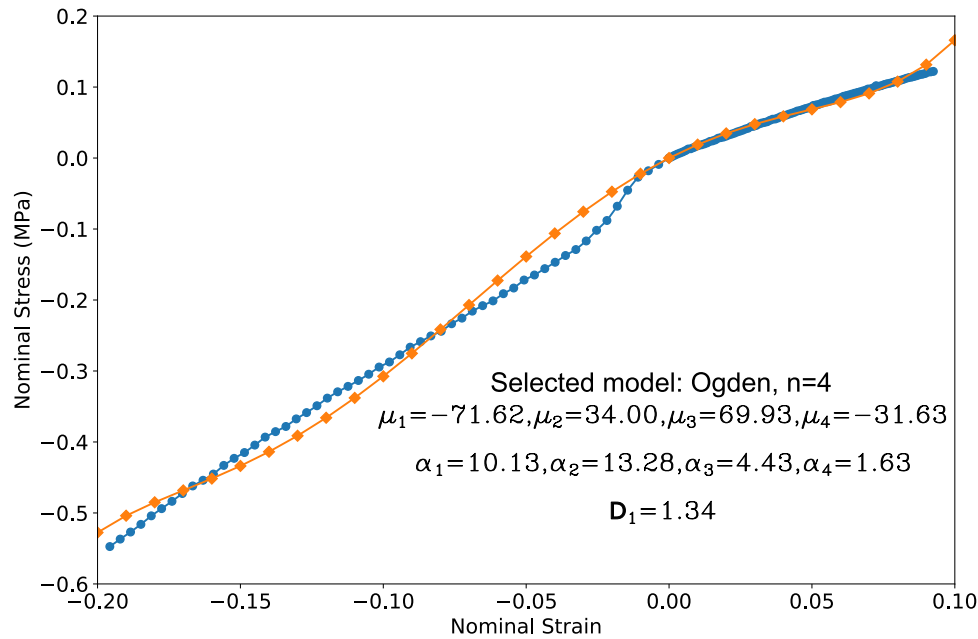


**FIGURE 4.** Adjustment of the hyperelastic model proposed, Ogden  $N = 4$ , with the experimental data obtained in our previous study<sup>31</sup>. The corresponding units of  $\mu_i$  and  $D_1$  are MPa and  $\text{MPa}^{-1}$ , respectively.  $\alpha_j$  is a dimensional

**TABLE 2.** Individualised results for representative IOLs. Design parameters are: the length ( $\lambda_{AA}$ ), width (WH) and opening angle of the haptic ( $\varphi$ ), the haptic–optic junction (J), start of the haptic curvature (HC) and the thickness (T).

IOL analysed	Factors						Total diameter (mm)	Response			
	$\lambda_{AA}$	WH	$\varphi$	J	HC	T		Compression force (mg)	Axial displacement (mm)	Tilt ( $^\circ$ )	Rotation ( $^\circ$ )
#Optimal	8.20	0.40	135	0.60	2.30	0.30	13.25	7.70	0.11	0.09	3.51
#21	8.20	0.40	135	1.80	2.30	0.40	13.25	302.11	0.21	0.10	4.95
#27	8.20	0.40	135	1.20	2.30	0.40	13.25	33.34	0.13	0.01	4.06
#35	8.20	0.40	110	0.60	2.30	0.35	13.50	13.87	0.15	0.05	4.24
#52	8.20	0.40	110	0.60	2.50	0.40	13.90	18.89	0.13	0.03	4.62
#87	8.80	0.40	135	0.60	2.30	0.35	13.25	12.57	0.12	0.05	2.96
#129	8.20	0.65	135	1.80	2.30	0.40	13.25	328.32	0.96	0.18	4.89
#139	8.80	0.65	135	0.60	2.30	0.30	13.25	36.60	0.19	0.04	4.86

rotation of the IOL is mainly explained by the start of the haptic curvature (HC—62.9%) and the width of the haptic (WH—27.6%) (see Fig. 7d). Further analysis based on the Pearson correlation matrix (see Fig. 6) supported these findings.

The compression (or reaction) force was confirmed to be strongly and directly correlated with the haptic width (WH), the haptic–optic junction (J) and the start of the haptic curvature (HC). This direct correlation would result in a moderate (J and HC) to strong (WH) increment in the reaction force if these parameters are increased. Also, a low inverse correlation was found with the haptic angle ( $\varphi$ ), likely resulting in a low reduction in force if the angle is increased.

The axial displacement presented moderate to low direct correlations with the haptic width (WH), the

haptic–optic junction (J) and the start of the haptic curvature (HC), and moderate to low inverse correlations to the haptic thickness (T) and the haptic angle ( $\varphi$ ). These correlations would suggest to decrease WH, J, or HC, or to decrease T and  $\varphi$  in order to reduce the axial displacement.

The tilt presents a low inverse correlation to the haptic length ( $\lambda_{AA}$ ) and the thickness of the haptic (T), and a low direct correlation to the haptic width (WH) and the start of the haptic curvature (HC). These correlations suggest a difficult control of the IOL's tilt just using the proposed design parameters.

The rotation of the lens presents a strong direct correlation to the start of the haptic curvature (HC), a moderate direct correlation to the haptic width (WH), and a low inverse correlation to the haptic length ( $\lambda_{AA}$ )

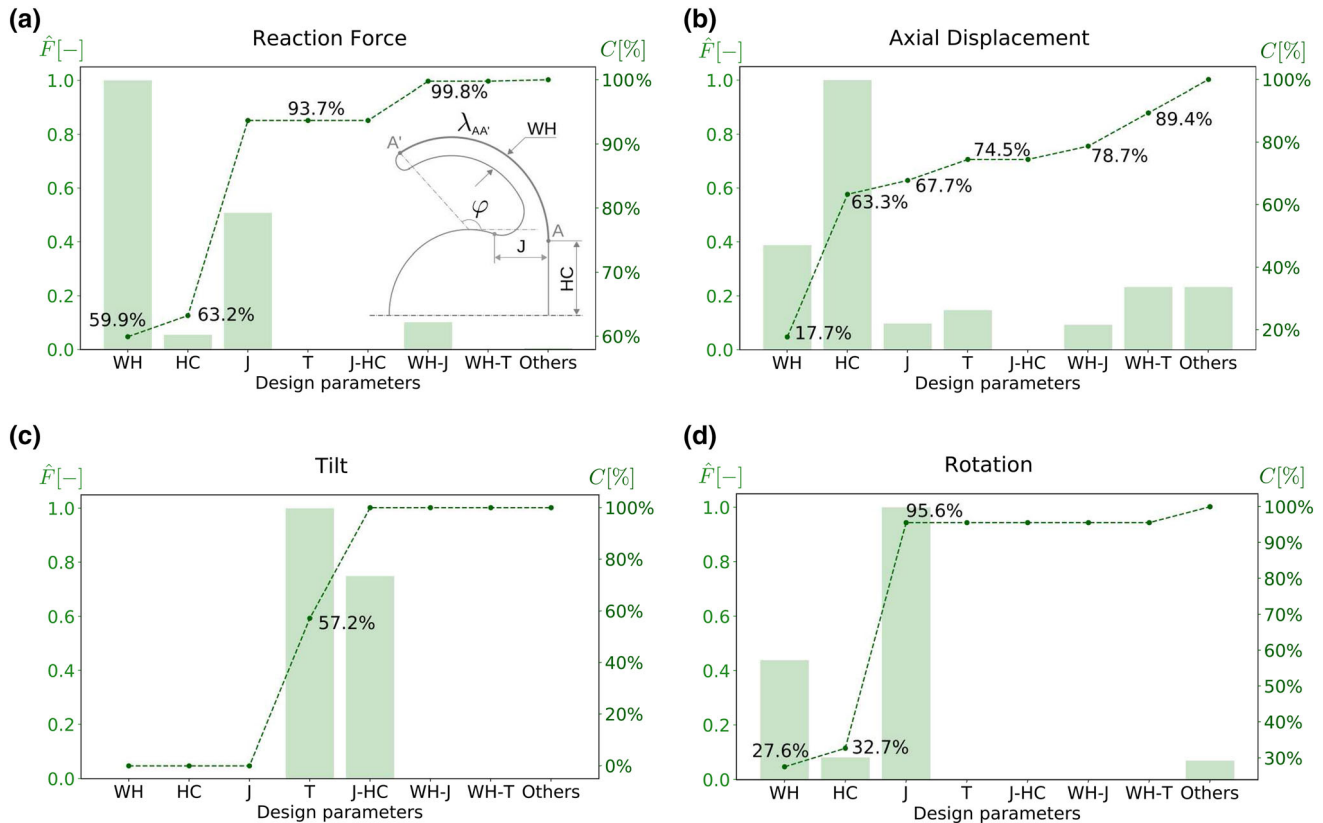


**FIGURE 5.** Pareto charts for the mixed-level ( $3^2 \times 2^4 = 144$ ) factorial design for different responses. Only statistically significant terms are depicted. Parameters with a contribution of less than a 5% were grouped in others.  $F$  is the normalized F-stat and  $C[\%]$  is the percentage of contribution. (a) Compression (or reaction) force; (b) Axial displacement; (c) Tilt; (d) Rotation; the factors and interactions shown are: the length of the haptic ( $\lambda_{AA'}$ ), the width of the haptic (WH), the opening angle of the haptic ( $\varphi$ ), the start of the haptic curvature (HC), the haptic–optic junction (J), and the thickness of the haptic (T).

and the haptic–optic junction (J). These correlations would suggest to reduce HC and WH, or to increase  $\lambda_{AA'}$  and J to obtain a lower rotation of the lens.

Finally, the compression (or reaction) force, the axial displacement and the rotation of the C-loop IOL present a moderate direct correlation between them, while the tilt loosely correlated to the other stability parameters.

Individualised biomechanical responses for representative IOLs (see Fig. 7) are presented in Table 2. Again, tilt does not seem to be highly influenced by any design parameter in particular, almost resulting in a design-independent factor with a maximum variation up to  $1^\circ$ .

## DISCUSSION

In the present work, we have introduced the first systematic study that analyses the biomechanical stability of 1-piece, non-angulated, hydrophobicacrylate C-loop IOLs with respect to different design factors. To save costs in experiments, a previous *in silico* platform<sup>31</sup> has been used to simulate the mechanical

compression test described in the Standard ISO 11972-3.<sup>7</sup> This test is the companies' gold standard for testing the mechanical stability of commercial lenses. The *in silico* platform allowed for testing 144 geometrical variations that were known to behave mechanically sound. The use of *in silico* models along with advanced statistical tools (i.e., mixed-level factorial analysis) allowed for studying the impact of design factors (length, width, thickness and opening angle of the haptic, the start of the haptic curvature, and the haptic–optic junction (see Fig. 2), on the biomechanical stability of the lens [compression force—mg, axial displacement—mm, tilt—degrees ( $^\circ$ ) and rotation—degrees ( $^\circ$ )]. Although only a 1-piece hydrophobic acrylate IOL with non-angulated C-loop haptics and a dioptric power (+ 22.00D) was considered, the proposed methodology allows for a straightforward implementation of different IOL features such as the style of the plate haptic, multipiece IOLs, different dioptric powers, or different capsular bags.

Based on the present results, the width (WH) and thickness (T) of the haptic, the start of the haptic

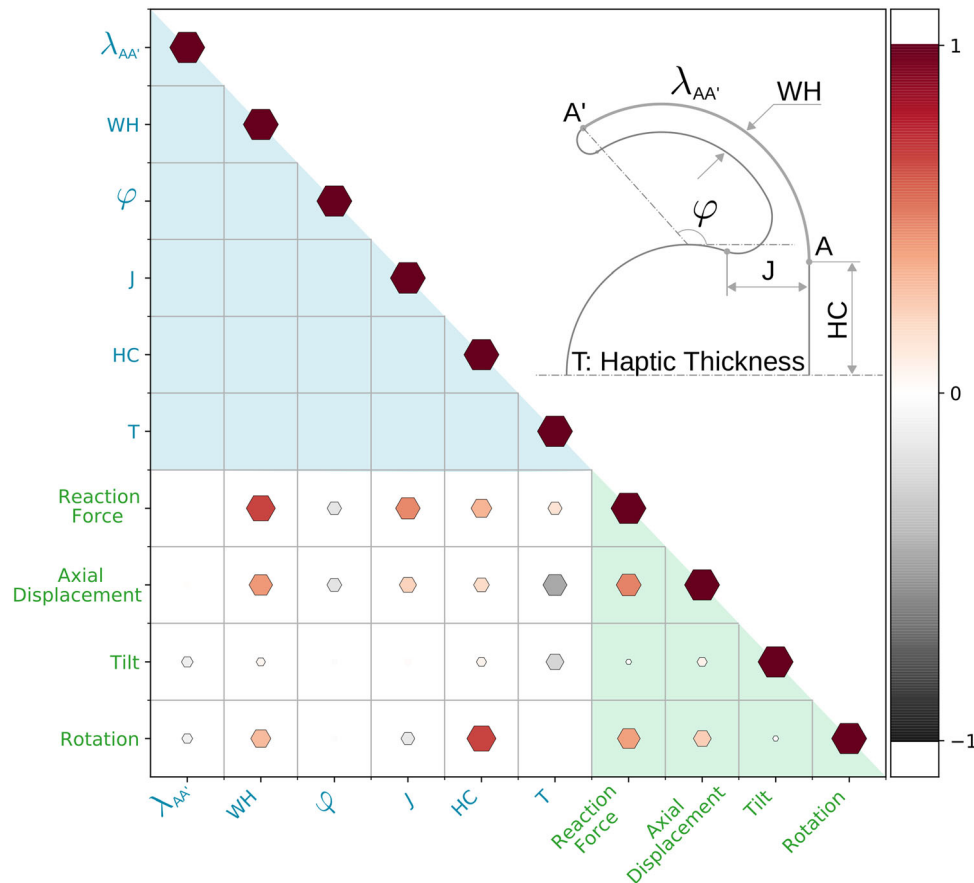


**FIGURE 6.** Pearson correlation matrix (mixed-level factorial design,  $3^2 \times 2^4 = 144$ ). Design parameters (in blue): the length ( $\lambda_{AA'}$ ), width (WH), thickness (T) and opening angle of the haptic ( $\varphi$ ), the haptic–optic junction (J), and the start of the haptic curvature (HC) and the thickness (T). Biomechanical stability outcomes (in green): rotation, compression (or reaction) force, axial displacement and tilt. Size of the hexagons depicts the degree of linear correlation: the bigger the size, the greater the linear correlation. Color of the hexagons depicts whether the linear correlation is direct (positive) or inverse (negative) (reddish palette—direct; grayish palette—inverse).

curvature (HC), and the haptic–optic junction (J) are suggested to be important factors determining the biomechanical stability of the lens (see Figs. 5 and 6). When the cross-section of the haptic increases (i.e., increased haptic width and/or thickness) and the haptic–optic junction is larger, the energy accumulated by the IOL is higher and will result on higher rotations, axial displacements and reaction forces (see, for example, IOLs 21 and 129 in Table 2). Therefore, a delicate trade-off between the length ( $\lambda_{AA'}$ ) and the cross-section of the haptic must be achieved to minimize undesired postsurgical shifts.

Individually, different stability outcomes are influenced by different design parameters (see Fig. 5): the compression (or reaction) force by the width of the haptic (WH), the haptic curvature start (HC) and the haptic–optic union (J); the axial displacement by the width (WH) and thickness (T) of the haptic, and the haptic–optic union (HC); the tilt by the thickness of

the haptic (T); and the rotation by the haptic width (WH) and the haptic curvature start (HC).

In particular, the trend in the results (see Fig. 6) suggests that the haptic–optic junction (J), the start of the haptic curvature (HC) and the haptic width (WH) are the most influential factors for all responses except for the tilt. Reducing the haptic–optic junction (J—0.6 mm) and the haptic width (WH—0.40 mm) lead to designs with better biomechanical stability (Fig. 7).

In this vein, Lane *et al.*<sup>18</sup> compared the mechanical characteristics and stability of 5 currently marketed monofocal IOLs finding that designs with flexible hinges, as the present in the Clareon CNA0T0 or AcrySof SN60WF (Alcon Laboratories, Inc.), improved the axial stability. This finding aligns well with our results in which the more flexible the haptic–optic junction, the better is the stability in terms of compression force and axial displacement. On the other hand, the least influential factor on the biomechanical



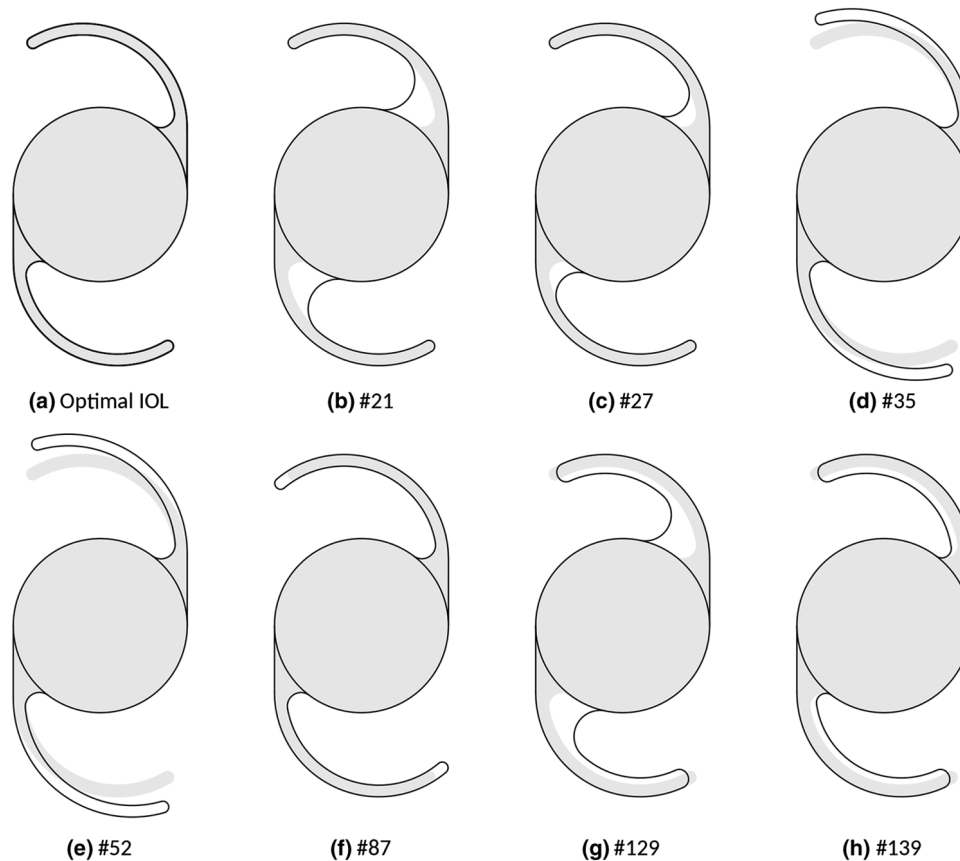


**FIGURE 7.** Geometric design of IOLs analysed in the Table 2. The optimal geometry (a) is superposed in gray upon the different select geometrical variations.

stability is the haptic length ( $\lambda_{AA'}$ ), as it had a low effect in the rotation, axial displacement or reaction force.

Unfortunately, in order to minimize the rotation of the lens, the optimal configuration would require of a larger haptic–optic junction (J) which is incompatible with minimizing, for example, the axial displacement. In the same vein, reducing the haptic thickness (T) would lead to an increased tilt and axial displacement, but a lower compression force. Due to this inverse coupling between design parameters, different design strategies are mandatory depending on the stability factor that is aimed at being minimized.

If the compression (or reaction) force, the axial displacement and the tilt aim at being minimised, then IOLs should tend to reduce their haptic width (WH) and the start of the haptic curvature (HC), while increasing the opening angle ( $\varphi$ ) and the haptic thickness (T). Providing that this design restriction is complied with, the diameter of the lens should not affect and could be individually designed to fit in the capsular bag of each patient.

Remarkably, our *in silico* platform behaved within the experimental reported ranges and com-

plied with the current manufacturing norms. Lane *et al.*<sup>17</sup> reported that the multipiece AcrySof MA30BA IOL (Alcon Laboratories, Inc.) presented the greatest axial displacement when compared to four single-piece IOLs (1.98 mm vs.  $0.15 \pm 0.40$  mm, respectively). Later on, same authors reported that, under dynamic compression up to 10 mm, the range of axial displacement varied from  $-0.01$  mm (model AcrySof SN60WF, Alcon Laboratories, Inc.) to 0.68 mm (model MX60, Bausch C Lomb, Inc.). Bozukava *et al.*<sup>4</sup> reported a range of axial displacement from 0.00 to 1.032 mm when the IOLs were compressed up to 10.0 mm. Similar range of axial displacement (0.11 to 0.96 mm) was obtained for #129 IOL variations in the present study (see extract in Table 2).

Lane *et al.*<sup>18</sup> also reported a range of optic tilt from  $0.5^\circ$  (models AcrySof SN60WF and Clareon CNA0T0) to  $1.2^\circ$  (models MX60). Bozukava *et al.*<sup>4</sup> reported higher tilt values ranging from  $0^\circ$  to  $20.12^\circ$ . Ale *et al.*<sup>1</sup> reported that, in average,  $3^\circ$  of tilt would result in 0.12 D of defocus, without affecting visual performance. In the present study, optic tilt was found to vary between  $0^\circ$  and  $0.18^\circ$  (see extract in Table 2).

The International Standards ISO 11979-2:2014<sup>6</sup> specifies that, for manufacturing toric IOLs, the angle difference between the physical axis indicator and the meridian with the lowest dioptic power must be less and equal than 5. In the present study, the range of rotation varied from 2.96° to 4.95°, being 3.51° the value for the optimal design (see extract in Table 2).

The future use of these *in silico* models along with clinical data can be used to increase the predictability of the stability of the IOLs in the capsular bag after a cataract refractive surgery. This will lead to reduced costs by exploring a feasible space of solutions during the product design process and before manufacturing. In sum, this methodology allow to compare the mechanical stability of different IOL designs, being a first step towards the customization of IOLs (i.e., choosing the optimal size of the IOL depending on the eyeball's axial length of a patient, or the diameter of the capsular bag).

#### ACKNOWLEDGMENTS

The authors gratefully acknowledge research support from the Spanish Ministerio de ciencia, innovacion y universidades (Grant DPI2017-84047-R ) and the Department of Industry and Innovation (Government of Aragon) through the research group Grant T24-17R (cofinanciado con Feder 2014–2020: Construyendo Europa desde Aragon). The authors also acknowledge the support of the Tissue Characterization Platform of CIBER-BBN, an initiative funded by the VI National R & D & i Plan 2008–2011, Iniciativa Ingenio 2010, Consolider Program, CIBER Actions and financed by the Instituto de Salud Carlos III with assistance from the European Regional Development Fund. I. Cabeza-Gil was supported by PRE2018-084021.

#### CONFLICT OF INTEREST

No author has a financial or proprietary interest in any material or method mentioned.

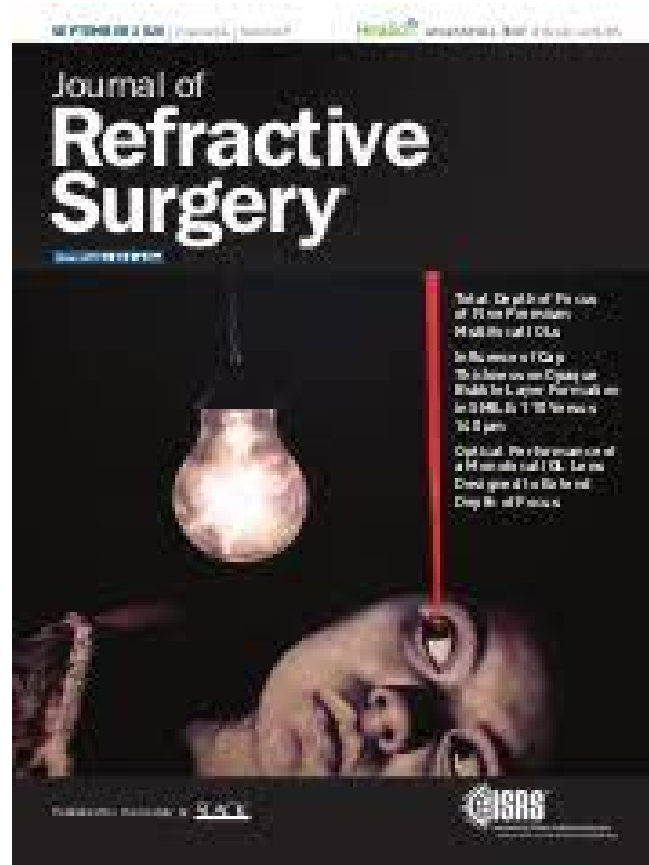
#### REFERENCES

- <sup>1</sup>Ale, J. B. Intraocular lens tilt and decentration: a concern for contemporary IOL designs. *Nepal. J. Ophthalmol.* 3:68–77, 2011.
- <sup>2</sup>Alio, J. L., A. B. Plaza-Puche, R. Fernández-Buenaga, J. Píkkel, and M. Maldonado. Multifocal intraocular lenses: an overview. *Surv. Ophthalmol.* 62:611–634, 2017.
- <sup>3</sup>Alió, J. L., A. B. Plaza-Puche, J. Javaloy, M. J., Ayala, and A. Vega-Estrada. Clinical and optical intraocular performance of rotationally asymmetric multifocal IOL plate-haptic design versus C-loop haptic design. *J. Refract. Surg.* 29:252–259, 2013.
- <sup>4</sup>Bozukova, D., C. Pagnouille, and C. Jérôme. Biomechanical and optical properties of 2 new hydrophobic platforms for intraocular lenses. *J. Cataract. Refract. Surg.* 39:1404–1414, 2013.
- <sup>5</sup>Bozukova, D., L. Werner, N. Mamalis, et al. Double-C loop platform in combination with hydrophobic and hydrophilic acrylic intraocular lens materials. *J. Cataract. Refract. Surg.* 41:1490–1502, 2015.
- <sup>6</sup>BS EN ISO 11979-2:2014 Ophthalmic implants - Intraocular lenses. Part 2: Optical properties and test methods. BSI Standards Limited, 2014.
- <sup>7</sup>BS EN ISO 11979-3:2012 Ophthalmic implants. Intraocular lenses. Mechanical properties and test methods. BSI Standards Limited, 2012.
- <sup>8</sup>Chang, D. F. Early rotational stability of the longer Staar toric intraocular lens. *J. Cataract. Refract. Surg.* 29:935–940, 2003.
- <sup>9</sup>Chang, D. F. Comparative rotational stability of single-piece open-loop acrylic and plate-haptic silicone toric intraocular lenses. *J. Cataract. Refract. Surg.* ;34:1842–1847, 2008.
- <sup>10</sup>Choi, M., M. Z. Lazo, M. Kang, M., J. Lee, and C. K. Joo. Effect of number and position of intraocular lens haptics on anterior capsule contraction: a randomized, prospective trial. *BMC Ophthalmol.* 18:78, 2018.
- <sup>11</sup>Chua, W. H., L. H. Yuen, J. Chua, G. Teh, and W. E. Hill. Matched comparison of rotational stability of 1-piece acrylic and plate-haptic silicone toric intraocular lenses in Asian eyes. *J. Cataract. Refract. Surg.* 38:620–624, 2012.
- <sup>12</sup>Crnej, A., N. Hirschall, Y. Nishi, et al. Impact of intraocular lens haptic design and orientation on decentration and tilt. *J. Cataract. Refract. Surg.* 37:1768–1774, 2011.
- <sup>13</sup>Draschl, P., N. Hirschall, N. Luft, et al. Rotational stability of 2 intraocular lenses with an identical design and different materials. *J. Cataract. Refract. Surg.* 43:234–238, 2017.
- <sup>14</sup>Hayashi, K. and H. Hayash. Comparison of the stability of 1-piece and 3-piece acrylic intraocular lenses in the lens capsule. *J. Cataract. Refract. Surg.* 31:337–342, 2005.
- <sup>15</sup>Hunter, J. D. Matplotlib: a 2D graphics environment *Comput. Sci. Eng.* 9:90-95, 2007.
- <sup>16</sup>Kumar, D. A., A. Amar, G. Prakash, S. Jacob, Y. Saravanan, and A. Agarwal. Evaluation of intraocular lens tilt with anterior segment optical coherence tomography. *Am J Ophthalmol.* 151:406–412.e2, 2011.
- <sup>17</sup>Lane, S. S., P. Burgi, G. S. Milios, M. W. Orchowski, M. Vaughan, and E. Schwarte. Comparison of the biomechanical behavior of foldable intraocular lenses. *J. Cataract. Refract. Surg.* 30:2397–2402, 2004.
- <sup>18</sup>Lane, S., S. Collins, K. K. Das, et al. Evaluation of intraocular lens stability. *J. Cataract. Refract. Surg.* 45(4):501–506, 2018.
- <sup>19</sup>Linnola, R. J., M. Sund, R. Ylönen, and T. Pihlajaniemi. Adhesion of soluble fibronectin, laminin, and collagen type IV to intraocular lens materials. *J. Cataract. Refract. Surg.* 25:1486–1491, 1999.
- <sup>20</sup>Lombardo, M., G. Carbone, G. Lombardo, M. P. De-Santo, and R. Barberi. Alysis of intraocular lens surface

- adhesiveness by atomic force microscopy. *J. Cataract. Refract. Surg.* 35:1266–1272, 2009.
- <sup>21</sup>Miháltz, K., M. Lasta, M. Burgmüller, P. V. Vécsei-Marlovits, and B. Weingessel. Comparison of two toric IOLs with different haptic design: optical aquality after 1 year. *J. Ophthalmol.* 2018:1–7, 2018.
- <sup>22</sup>Montgomery, D. *Design & Analysis of Experiments*. 5ed. New York: Wiley, 2001.
- <sup>23</sup>Nagy, Z. Z., K. Kránitz, A. I. Takacs, K. Miháltz, I. Kovács, and M. C. Knorz. Comparison of intraocular lens decentration parameters after femtosecond and manual capsulotomies. *J. Refract. Surg.* 27:564–569, 2011.
- <sup>24</sup>Garzón, N., F. Poyales, Z. B. Ortíz, J. L. Ruiz-García, and J. A. Quiroga. Evaluation of rotation and visual outcomes after implantation of monofocal and multifocal toric intraocular lenses. *J. Refract. Surg.* 31:90–97, 2015.
- <sup>25</sup>Oliphant Travis, E. *A Guide to NumPy*. New York: Trelgol Publishing, 2006.
- <sup>26</sup>Patel, C. K., S. Ormonde, P. H. Rosen, and A. J. Bron. Postoperative intraocular lens rotation. *Ophthalmology*. 106:2190–2196, 1999.
- <sup>27</sup>Pérez-Merino, P., and S. Marcos. Effect of intraocular lens decentration on image quality tested in a custom model eye. *J. Cataract. Refract. Surg.* 44:889–896, 2018.
- <sup>28</sup>Petternel, V., R. Menapace, O. Findl, et al. Effect of optic edge design and haptic angulation on postoperative intraocular lens position change. *J. Cataract. Refract. Surg.* 30:52–57, 2004.
- <sup>29</sup>Poyales, F., Garzón, N., Pizarro, D., Cobreces, S., and A. Hernández. Stability and visual outcomes yielded by three intraocular trifocal lenses with same optical zone design but differing material or toricity. *Eur. J. Ophthalmol.* 29(4):417–425, 2018.
- <sup>30</sup>Prinz, A., T. Neumayer, W. Buehl, et al. Rotational stability and posterior capsule opacification of a plate-haptic and an open-loop-haptic intraocular lens. *J. Cataract. Refract. Surg.* 37:251–257, 2011.
- <sup>31</sup>Remón, L., Siedlecki, D., Cabeza-Gil, I., and B. Calvo. Influence of material and haptic design on the mechanical stability of intraocular lenses by means of finite-element modeling. *J. Biomed. Opt.* 23:1, 2018.
- <sup>32</sup>Ridley, H. Intra-ocular acrylic lenses after cataract extraction. *Lancet* 259:118–121, 1952.
- <sup>33</sup>Rossum Guido, V., and F. L. Drake. *Python 3 Reference Manual*. Paramount, CA: CreateSpace, 2009.
- <sup>34</sup>Shah, G. D., M. R. Praveen, A. R. Vasavada, V. A. Vasavada VA, G. Rampal, and L. R. Shastri. Rotational stability of a toric intraocular lens: influence of axial length and alignment in the capsular bag. *J. Cataract. Refract. Surg.* 38:54–59, 2012.
- <sup>35</sup>Vounotrypidis, E., C. Lackerbauer, D. Kook, M. Dirisamer, S. Priglinger, and W. Mayer. Influence of total intraocular lens diameter on efficacy and safety for in the bag cataract surgery. *Oman J. Ophthalmol.* 11:144–149, 2018.
- <sup>36</sup>Werner L. Biocompatibility of intraocular lens materials. *Curr. Opin. Ophthalmol.* 19:41–49, 2008.
- <sup>37</sup>Werner, L., M. Tetz, I. Feldmann, and M. Bücken. Evaluating and defining the sharpness of intraocular lenses: microedge structure of commercially available square-edged hydrophilic intraocular lenses. *J. Cataract. Refract. Surg.* ;35:556–566, 2009.
- <sup>38</sup>Wirtitsch, M. G., O. Findl, R. Menapace, et al. Effect of haptic design on change in axial lens position after cataract surgery. *J. Cataract. Refract. Surg.* 2004;30:45–51.
- <sup>39</sup>Woodward, M. A., J. B. Randleman, R., Stulting, and Doyle. Dissatisfaction after multifocal intraocular lens implantation. *J. Cataract. Refract. Surg.* 35:992–997, 2009.
- <sup>40</sup>Zvorničanin, J., and E. Zvorničanin. Premium intraocular lenses: the past, present and future. *J. Curr. Ophthalmol.* 30:287–296, 2018.

**Publisher's Note** Springer Nature remains neutral with regard to jurisdictional claims in published maps and institutional affiliations.

### 3.4 Work 6: Biomechanical Stability of Three Intraocular Lenses With Different Haptic Designs: In Silico and In Vivo Evaluation



Remón L. Cabeza-Gil I., Calvo B., Poyales F., Garzón N.  
Journal of Refractive Surgery  
JIF (2020) = 3.57 (Q1: 15/62 Ophthalmology)  
SJR (2020) = 1.44 (Q2: 18/120 Ophthalmology)

# Biomechanical Stability of Three Intraocular Lenses With Different Haptic Designs: In Silico and In Vivo Evaluation

Laura Remón, PhD; Iulen Cabeza-Gil, MSc; Begoña Calvo, PhD; Francisco Poyales, MD; Nuria Garzón, PhD

## ABSTRACT

**PURPOSE:** To assess the biomechanical stability of three different marketed intraocular lenses (IOLs) with different haptic designs (four-loop IOL [Micro F FineVision model] and double C-loop IOL [POD F and POD FT models], all manufactured by PhysIOL), in silico (computer simulation) and in vivo (in the context of lens surgery).

**METHODS:** An in silico simulation investigation was performed using finite element modeling (FEM) software to reproduce the compression test defined by the International Organization for Standardization and in vivo implantation in patients in the context of lens surgery was evaluated 1 day and 3 months postoperatively. IOL decentration and rotation were tested. In addition, the stress and strains were analyzed with the finite element method.

**RESULTS:** In the in silico evaluation, the compression force for the POD F IOL was slightly lower than for the POD FT IOL

and Micro F IOL for all compression diameters. The axial displacement was maximum for the POD FT IOL and the tilt, rotation, and lateral decentration were substantially lower than the acceptable tolerance limits established in ISO 11979-2. In the in vivo evaluation, a total of 45 eyes from 45 patients were selected, 15 eyes for each IOL model under assessment. Statistically significant differences were found between the Micro F and POD F IOLs for lateral decentration in x-direction (in absolute value) at 3 months postoperatively ( $P = .03$ ).

**CONCLUSIONS:** Although statistically significant differences have been found when comparing the displacement, tilt, and rotation between the different lenses, these differences cannot be considered clinically relevant, which would suggest that all three IOL models yield excellent stability in those terms. FEM appears to be a powerful tool for numerical studies of the biomechanical properties of IOLs.

[*J Refract Surg.* 2020;36(9):617-624.]

In recent years, lens surgery has become a surgical procedure that seeks to not only replace the cataractous lens, but also to correct any refractive error and presbyopia. Intraocular lenses (IOLs) are no longer limited to monofocal models; on the contrary, they include refractive, diffractive, and extended range design lenses, among others.<sup>1-3</sup> These lenses are either toric or have rotational symmetry optimum centration and stability within the capsular bag is required to provide the best possible visual outcomes.<sup>4-6</sup>

The instability of implanted IOLs has been associated with several factors, including the capsulorhexis size,<sup>7</sup> incomplete viscoelastic clearance, IOL diameter versus capsular bag diameter,<sup>8,9</sup> IOL material properties,<sup>10,11</sup> and haptic designs.<sup>12-14</sup>

Some studies<sup>15-17</sup> have demonstrated that IOLs with C-loop haptics ensure better stability and centration than IOLs with plate haptics. Poyales et al<sup>18</sup> compared the rotational stability and centration of two different IOLs, the four-loop IOL (Micro F FineVision model)

From Universidad de Zaragoza, Departamento de Física Aplicada, Zaragoza, Spain (LR); Universidad de Zaragoza, Escuela de Ingeniería y Arquitectura, Aragón Institute of Engineering Research (I3A), Zaragoza, Spain (IC-G, BC); Centro de Investigación Biomédica en Red en Bioingeniería, Biomateriales y Nanomedicina (CIBER-BBN), Spain (BC); Miranza IOA, Madrid, Spain (FP, NG); and Universidad Complutense de Madrid. Departamento de Optometría y Visión, Madrid, Spain (NG).

Submitted: September 18, 2019; Accepted: June 16, 2020

Supported by Carlos III Health Institute (ISCIII) through the CIBER initiative and the Ministerio de Economía y Competitividad, Project: DPI2017-84047-R (MINICO-FEDER).

The authors have no financial or proprietary interest in the materials presented herein.

Correspondence: Nuria Garzón, PhD, Miranza IOA, c/ Galileo 104, Madrid 28003, Spain. Email: nuria.garzon@miranza.es

doi:10.3928/1081597X-20200713-02

and the double C-loop IOL (POD model), finding a good rotational stability in both lenses. However, it is not only haptic design that influences stability. Tolerance to compressive forces—to which both the haptics and the optics may be subject, once they have been implanted in the capsular bag—also seem to have an impact on IOL stability.<sup>13-15</sup> Several clinical studies<sup>19-21</sup> have measured the decentration, tilt, or rotation of IOLs after cataract surgery using different measuring systems, such as Scheimpflug imaging,<sup>20</sup> measurements using Purkinje reflections,<sup>22</sup> and slit-lamp assessment.<sup>21</sup> However, the heterogeneous methods, the accurate marking of the reference axis, and the accurate measurements of preoperative parameters makes comparisons difficult. For this reason, some numerical<sup>10</sup> and experimental<sup>12,13,15,23</sup> studies have evaluated the biomechanical stability of IOL designs before inserting the lenses in the eye, according to the requirements specified by the International Organization for Standardization (ISO 11979-3).<sup>24</sup> In a previous study, Remón et al<sup>10</sup> used finite element modeling (FEM) to evaluate the biomechanical stability of four different hydrophobic and hydrophilic IOLs with different haptic designs. The results suggest that FEM can be a powerful tool for increasing the predictability of the biomechanical stability of IOLs before their implantation in the capsular bag.

The goal of the current study was to assess the biomechanical stability of three different marketed IOLs with different haptic designs (four-loop IOL [Micro F FineVision model] and double C-loop IOL [POD F and POD FT models] manufactured by PhysIOL), using FEM to reproduce the compression test defined in ISO 11979-3.<sup>24</sup> In addition, the stability of these lenses was evaluated in vivo once they had been surgically implanted in a patient to obtain the maximum possible information on the stability of the evaluated lenses. Both studies are complementary.

## MATERIALS AND METHODS

### IOL DESCRIPTION

All IOLs evaluated in this study are aspheric trifocal diffractive lenses manufactured by PhysIOL. The optics of all three models are similar, combining two diffractive structures that fit together to offer a +3.50 diopters (D) addition for near vision and a +1.75 D addition for intermediate vision.

More specifically, the Micro F FineVision model is a four-loop IOL with 5° angulation made of 25% hydrophilic material. The optic body diameter is 6.15 mm and the overall diameter is 10.75 mm. The POD F and POD FT models are double C-loop IOLs with 5° angulation made of 26% hydrophilic material. The optic body

diameter is 6 mm and the overall diameter is 11.40 mm. The POD FT IOL, aside from its toric design, differs from its non-toric counterpart (POD F) in the hinge section at the haptic–optic junction because the POD FT IOL has been slightly widened.

The differentiating factor between these three models is the haptic design, which is a key element to ensure IOL stability.

### IN SILICO EVALUATION

A numerical simulation of the biomechanical behavior of the three IOLs during a compression test was performed by FEM using Abaqus 6.14 software (Abaqus, Inc) following the procedure described in ISO 11979-3,<sup>24</sup> which establishes a compression of the IOL haptics up to 10 mm for IOLs intended for capsular bag placement. In this compression test, the IOL is placed between two clamps (with a curvature radius of 5 mm) and compressed to measure its mechanical stability. Initially, the clamps are separated by a distance equal to the overall dimension of the IOL. Then, the right clamp is displaced to different compression diameters: 11, 10.5, and 10 mm (the value specified by the ISO standard) and 9.5 mm while the left clamp remains fixed. In the final or deformed configuration (**Figure A**, available in the online version of this article), the following variables were measured: the compression force measured at the horizontal plane, the axial shift measured at the vertical plane (ie, axial displacement), the tilt in both x- and y-directions, and the rotation, following the procedure described in a previous article.<sup>25</sup> The rotation is the resulting angle between an initial vector, with origin in the center and an extreme point on an edge of the optic, and that vector in a determined time. These variables were evaluated in the reference and the final configurations, as well as in the intermediate positions throughout the test. The axial displacement, the tilt, and the rotation were evaluated by comparing the reference and final configuration of the lens. Additionally, the optic decentration was estimated as a distance between the optic center of the IOL and the geometrical center of the two clamps at the final configuration.

The properties of the material and the geometry of the IOLs were introduced as key parameters in the software. A detailed description of the numerical model used for the mechanical characterization of the material of the IOLs can be found in a previous article.<sup>10</sup>

### IN VIVO STUDY

The second part of this study was an in vivo randomized controlled trial comparing the lateral decentration and rotation of the three diffractive trifocal lens

models evaluated, two of which were spherical and one of which was a toric lens.

A total of 45 eyes from 45 patients were selected, 15 eyes for each IOL model under assessment. The study was conducted in accordance with the tenets of the Declaration of Helsinki. The study was approved by the Ethical Committee of Hospital Clínico San Carlos, Madrid, Spain, and all participants signed the informed consent.

The eyes included in the study had an axial length within the normal range, to try to exclude potential rotations due to the capsular bag being too big or a slight IOL tilt due to a small capsular bag size. Inclusion criteria were no prior eye surgery and no history of eye trauma. In addition, corneal astigmatism had to be less than 1.00 D for those patients receiving implanted spherical IOLs. Regarding IOL assignment methodology, patients who had corneal astigmatism below 1.00 D were randomly assigned one of the two spherical models (POD F or Micro F) under study, whereas patients with higher astigmatism were always implanted with the toric model (POD FT). The selected patients underwent crystalline lens surgery involving IOL implantation in the capsular bag. In all cases, the IOL power calculation method used was the Barrett or the Toric Barrett formula. The formula's constants were customized: A-constant was set to be 118.78 for the Micro F model and 119.02 for the POD F and POD FT models.

All patients had follow-up visits 1 day, 1 week, 1 month, and 3 months postoperatively.

Lateral decentration along the x- and y-directions and rotation were quantified by the Piolet software.<sup>21</sup> Immediately after surgery, photographs were taken with a slit lamp using retroillumination and additional external lighting so both the lens marks and the conjunctival vessels could be seen clearly and sharply (day 0). During the 1-day and 3-month follow-up visits, the pupil was dilated and the same procedure was repeated.

To be able to quantify IOL decentration, the images recorded immediately after IOL implantation were used as baseline (reference) data.

## SURGICAL PROCEDURE

All surgeries were performed by the same experienced surgeon (FP) under topical anesthesia. For the cataract procedure, a continuous curvilinear capsulorhexis measuring 5.5 mm in diameter and lens fragmentation were performed with the Catalys laser (Johnson & Johnson Vision Care, Inc). A 2.2-mm, 45° angled, bevel-up surgical knife (Xstar Safety Slit Knife; Beaver-Visitec International) was used to create a self-sealing clear corneal incision. The selected IOL was then implanted in the capsular bag with a single-

use injection system (Accujet; Medice AG) and subsequently positioned guided by a computer-assisted cataract surgery system (Callisto Eye, Zeiss Cataract Suite Markerless; Carl Zeiss Meditec AG). In all cases, once the IOL insertion was completed, all traces of ophthalmic viscosurgical devices were removed.

## STATISTICAL ANALYSIS

For all quantitative variables, summary tables were created containing mean and standard deviation and maximum and minimum values. The R code (R Project) was used to determine differences between groups and between preoperative and postoperative evaluations. Due to the small sample size, the robust non-parametric Wilcoxon ranked-sum test was employed. For all tests, the threshold for statistical significance was assumed to be a *P* value of less than .05.

## RESULTS

### IN SILICO EVALUATION OF COMPRESSION TEST

**Figure B** (available in the online version of this article) shows the evolution of the different variables (compression force, axial shift measured at the vertical plane [ie, axial displacement], tilt, and rotation as a function of the clamp displacement). **Table 1** shows the results at the final configuration (compression diameter of 11, 10.5, 10, and 9.5 mm) for each IOL model. For the Micro F IOL, the maximum compression diameter was 9.8 mm; from this value, this lens loses stability. As can be observed in the figure, the compression force has an almost linear behavior for all models. The compression force for the POD F IOL was slightly lower than for the POD FT and Micro F IOLs for all compression diameters. The compression force variation, when the haptic was compressed to 10 mm, ranged from 30.009 mg for the POD F IOL to 120.230 mg for the Micro F IOL. This double C-loop design has a moderate haptic compression force, which contributes to the anteroposterior stability of the lens. The axial displacement was maximum for the POD FT IOL, obtaining a value of 0.703 mm for a compression diameter of 10 mm. For the other models, the axial displacement was insignificant for all compression diameters. The tilt, rotation, and lateral decentration were substantially lower than the tolerance limits considered acceptable in the ISO 11979-2 (**Table 1**).<sup>26</sup> The Micro F IOL had the highest value of optic tilt at 9.8 mm compression (0.785°). In terms of rotation, all models were rotationally stable. The POD F IOL had the maximum magnitude of rotation at all compression diameters, varying from 0.375° to 0.256°. The mean optic decentration for all models at the different compression diameters was 0.084 ± 0.004

TABLE 1  
**Compression Force, Axial Displacement, Tilt, Rotation, and Lateral Decentration at Different Compression Diameters for All IOLs Measured at In Silico Condition**

Variable	Micro F	POD F	POD FT
Compression force (mg)			
9.5 mm	190.324	43.123	109.234
10 mm	120.230	30.009	99.997
10.5 mm	47.676	21.342	162.253
11 mm	-	18.923	78.239
Axial displacement (mm)			
9.5 mm	0.212	0.032	0.954
10 mm	0.158	0.025	0.703
10.5 mm	0.000	0.000	0.352
11 mm	-	0.000	0.000
Tilt (°)			
9.5 mm	0.785	0.085	0.087
10 mm	0.048	0.074	0.075
10.5 mm	0.032	0.055	0.234
11 mm	-	0.049	0.085
Rotation (degrees)			
9.5 mm	0.204	0.375	0.295
10 mm	0.157	0.348	0.255
10.5 mm	0.050	0.325	0.054
11 mm	0.000	0.256	0.014
Lateral decentration (mm)			
9.5 mm	0.082	0.083	0.093
10 mm	0.083	0.083	0.091
10.5 mm	0.080	0.083	0.087
11 mm	-	0.080	0.080

IOL = intraocular lens  
 All IOLs are manufactured by PhysIOL.

mm. In general, the values obtained for all variables for each model at the lowest test diameter of 9.5 mm were slightly higher than those obtained with the largest test diameter. The finite element analysis provides other variables of interest, such as stress, strains, and strain energy.

Figure 1 shows the internal energy of the lens, mostly due to the stored strain energy. The smaller this magnitude, the better the biomechanical stability of the lens. As can be observed in the figure, the internal energy has an almost linear behavior for the POD F and POD FT IOLs, being higher for the latter. However, the internal energy for the Micro F IOL increases exponentially, which is why this lens has substantial instability.

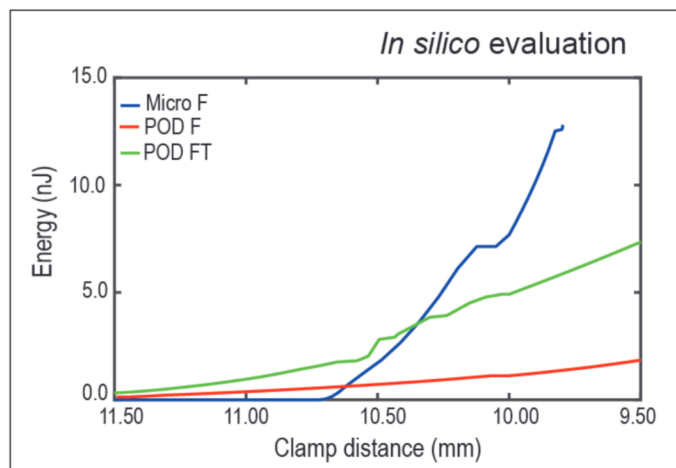


Figure 1. Evolution of the strain energy (nJ) as a function of the clamp diameter measured at in silico condition. All intraocular lenses are manufactured by PhysIOL.

Figure 2 shows the maximum principal stress for each IOL model at 10 mm compression diameter. The POD FT model showed higher values of stress in the haptic-optic junction than the other models.

#### IN VIVO STUDY

The mean axial length values were  $23.34 \pm 0.97$  mm (range: 21.19 to 25.57 mm) for the Micro F IOL group,  $23.36 \pm 0.90$  mm (range: 21.32 to 25.31 mm) for the POD F IOL group, and  $24.07 \pm 0.72$  mm (range: 22.11 to 27.54 mm) for the POD FT IOL group. The mean power of the implanted IOLs was  $21.46 \pm 2.94$  D (range: 16.50 to 27.00 D),  $21.46 \pm 3.19$  D (range: 15.00 to 25.50 D), and  $20.91 \pm 3.07$  D (range: 12.50 to 27.00 D) for the Micro F, POD F, and POD FT IOL groups, respectively.

Table 2 shows the mean lateral decentration in the x- and y-directions and the rotation outcomes measured 1 day and 3 months after surgery for each IOL group. The table includes both actual and absolute values. Actual values represent the directly measured values, whereas in absolute values the measurement's plus or minus sign has not been taken into account.

Table A (available in the online version of this article) summarizes the significance values between the different lenses. When comparing lenses to each other, statistically significant differences were found between the Micro F and POD F IOLs for absolute rotation at 1 day ( $P = .01$ ) and for displacement along the x-axis (in absolute value) at 3 months ( $P = .03$ ). When comparing the Micro F and POD FT IOLs, differences were found for displacement along the x-axis ( $P = .03$ ) and actual rotation ( $P = .01$ ) at 1 day, whereas no statistically significant differences emerged for any of the variables at the 3-month follow-up visit. Finally, the POD F versus POD FT comparison revealed statis-



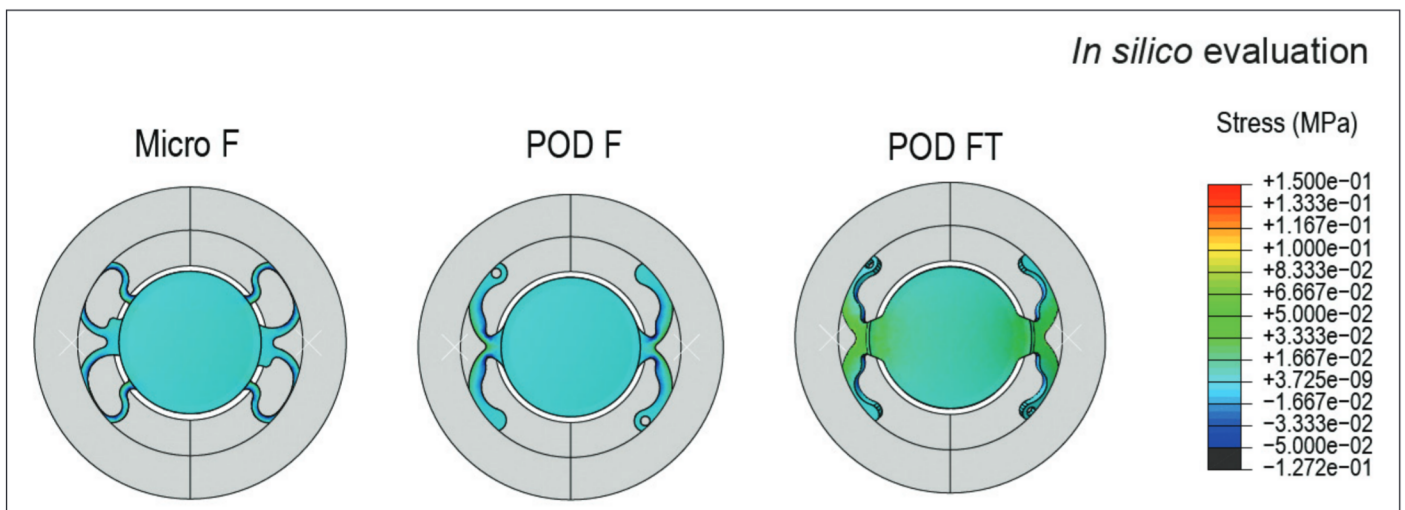


**Figure 2.** Maximum principal stress (MPa) at 10-mm compression diameter measured at in silico condition. All intraocular lenses are manufactured by PhysIOL.

**TABLE 2**  
**Lateral Decentration and Rotation Measured at In Vivo Condition 1 Day and 3 Months Postoperatively<sup>a,b</sup>**

Follow-up Visit	Micro F	POD F	POD FT
1 day			
Dx (a), mm	0.065 ± 0.168 [-0.182 to 0.329]	0.084 ± 0.191 [-0.281 to 0.454]	-0.101 ± 0.163 [-0.272 to 0.213]
Dx (abs), mm	0.141 ± 0.107 [0.000 to 0.329]	0.167 ± 0.118 [0.010 to 0.454]	0.170 ± 0.081 [0.044 to 0.272]
Dy (a), mm	0.068 ± 0.077 [-0.032 to 0.211]	0.373 ± 0.435 [-0.388 to 1.641]	0.097 ± 0.137 [-0.135 to 0.287]
Dy (abs), mm	0.081 ± 0.062 [0.011 to 0.211]	0.3251 ± 0.394 [0.004 to 1.641]	0.145 ± 0.079 [0.010 to 0.287]
Rotation (a), degrees	0.680 ± 1.755 [-1.578 to 3.864]	0.160 ± 3.490 [-4.631 to 4.634]	-0.973 ± 1.087 [-3.314 to 0.354]
Rotation (abs), degrees	1.567 ± 1.007 [0.560 to 3.864]	3.084 ± 1.419 [0.165 to 4.634]	1.129 ± 0.911 [0.213 to 3.314]
3 months			
Dx (a), mm	-0.058 ± 0.259 [-0.490 to 0.320]	-0.285 ± 0.139 [-0.434 to 0.129]	0.037 ± 0.140 [-0.225 to 0.191]
Dx (abs), mm	0.220 ± 0.137 [0.005 to 0.490]	0.098 ± 0.107 [0.001 to 0.434]	0.124 ± 0.066 [0.003 to 0.225]
Dy (a), mm	0.015 ± 0.159 [-0.465 to 0.216]	-0.018 ± 0.453 [-1.182 to 0.865]	0.115 ± 0.209 [-0.156 to 0.503]
Dy (abs), mm	0.111 ± 0.111 [0.001 to 0.465]	0.299 ± 0.331 [0.004 to 1.182]	0.175 ± 0.159 [0.011 to 0.503]
Rotation (a), degrees	0.744 ± 2.701 [-3.684 to 3.864]	1.186 ± 2.719 [-3.465 to 6.501]	0.261 ± 1.685 [-2.245 to 2.049]
Rotation (abs), degrees	2.393 ± 1.323 [0.764 to 3.864]	2.482 ± 1.516 [0.761 to 6.501]	1.590 ± 0.451 [0.845 to 2.245]

*Dx = lateral decentration in x-direction; Dy = lateral decentration in y-direction*

<sup>a</sup>Values are presented as mean ± standard deviation [range].

<sup>b</sup>Actual values (a) represent the directly measured values, whereas in absolute values (abs) the measurement's plus or minus sign has not been taken into account.

All intraocular lenses are manufactured by PhysIOL.

tically significant differences for displacement along the x-axis ( $P = .02$ ) and absolute rotation ( $P < .001$ ) at 1 day, whereas no differences were observed for any of these variables at 3 months.

### DISCUSSION

Under in silico conditions, a rigid and lower simulated bag size (ie, clamps in this model) generally induced higher values of all evaluated variables because

there is no deformation equilibrium between the capsular bag and the IOL material. Furthermore, the biomechanical response of the IOLs as a function of the clamp diameters is not a monotonic function due to the contact. This contact between the clamps and the IOL provides nonlinear behavior to the model.

The internal energy was a key output for providing essential information about the haptic design because it objectively determines the stability of the model. For

the Micro F model, the internal energy increased exponentially from a diameter of 9.7 mm, presenting an internal energy of 13.06 nJ and provoking instability for lower closure diameters. Related to the internal energy, this IOL model had the highest values of compression force whatever the compression diameter, with a range of compression force between 47.676 mg (10.5 mm compression) and 190.324 mg (9.5 mm compression). High forces could cause damage or breakage of the capsule, which will depend on the mechanical properties of the capsule. The ultimate load of the posterior capsule for people between 16 and 98 years old decreases with age in the range of 1.590 to 119 mg force in the posterior capsule and 5.240 to 560 mg in the anterior capsule.<sup>27</sup> For the other models, the energy and the compression force had an almost linear behavior whatever the compression diameter. For the POD FT IOL, the compression force when the haptic was compressed to 10 mm was 99.99 mg, and the lowest value was for the POD F IOL with 30.009 mg. Similar results were found in previous studies.<sup>13,15</sup> The internal energy deformation is related to the haptic deformation capacity. The lower the internal energy deformation, the higher the haptic deformation capacity. Therefore, the haptics of IOLs with lower internal energy will adapt to all capsule sizes, with low stress in the capsule and prevention of capsular bag damage.

Another important factor is that the optical part of the lens (**Figure 2**) did not suffer any stress or deformation for any of the IOL models at 10-mm compression diameter. As a consequence, the optical quality of the patient would not be affected.

In terms of the axial displacement, the POD FT IOL presented the maximum value, 0.703 mm for a compression diameter of 10 mm. Bozukova et al<sup>15</sup> found a smaller displacement value than in our study, 0.073 and 0.016 mm at *in silico* and *in vitro* conditions, respectively. However, in our study, the other two IOLs (Micro F and POD F) showed an insignificant axial displacement whatever the compression diameters. Axial displacement produces a change in the effective lens position that is associated with a refractive error; however, this problem is usually corrected by spectacle correction. This variable could not be measured *in vivo*.

In terms of tilt, the Micro F IOL presented the highest value, 0.785° at 9.80 mm of compression diameter. Tilt could not be measured *in vivo* with the software used for the other variables. Theoretical simulations performed by Holladay et al<sup>28</sup> demonstrated that aspherical lenses can undergo a decentration of up to 0.4 mm and a tilt of up to 7° before they start to show a lower performance than their spherical counterparts. A study by Piers et al<sup>29</sup> revealed a higher tolerance to

malposition, the resulting threshold (critical) values being at 0.8 mm of decentration and 10° of tilt. The results achieved with the lenses assessed in our study are much better than the limits proposed by Holladay et al.<sup>28</sup>

In terms of rotation, all IOL models were rotationally stable. The POD F IOL had the maximum magnitude of rotation at all compression diameters, varying from 0.375° to 0.256°. These values would not affect clinically observable visual acuity. When the rotation was evaluated *in vivo*, the three lenses showed good results. The lowest rotation was obtained for the POD FT IOL (the toric lens), although the average mean was shown to be less than 3° for all lenses during the 1-day and 3-month postoperative follow-up visits. These values demonstrate high stability, even following potential capsular contractions.

The mean total lateral decentration for all models at different compression diameters was 0.084 ± 0.004 mm, although Bozukova et al<sup>15</sup> found higher displacement values for the POD FT IOL. The three lenses showed minimal displacement 1 day after implantation, but also 3 months after surgery, when in many cases capsular contractions had already occurred that can increase the forces supported by the lenses. The greatest lateral decentration in x-direction occurred, at 1 day, with the POD FT IOL, with an average value of 0.10 mm. After 3 months, the POD F IOL showed the largest decentration in the same direction (0.285 mm), although this was not clinically significant and there were no statistically significant differences between the three lenses. The average values for the lateral decentration in y-direction were close to 0 for the three lenses and no statistically significant differences were found between them. Although statistically significant differences were found when comparing the displacement, tilt, and rotation between the different lenses, in some cases, these differences cannot be considered clinically relevant.

The results obtained with the *in silico* simulation and *in vivo* indicate that the POD FT IOL, which has the highest haptic–optic junction, has higher values of stress in the haptic–optic junction than the other models. This suggests that the haptic–optic junction is essential for the mechanical stability of the IOL in the capsular bag. We found that the POD FT IOL, which has a slightly wider haptic–optic junction than the POD F IOL, showed better stability in terms of rotation than the POD F and Micro F IOLs. It would be interesting to perform similar studies, under both *in vivo* and *in silico* conditions, with different platforms to evaluate how the haptic design affects the stability of the lenses.

The two methods used in this study have limitations, so some of the parameters cannot be measured with both systems. Numerical tests have not been done because it is not possible to measure in vivo, with any of the devices currently on the market, either the size of the capsular bag or the force compression inside the bag. More in vivo studies including very short-sighted and long-sighted patients should be performed to evaluate the behavior of the lenses in these extreme conditions.

In this study, we found several limitations of the ISO 11979-3.<sup>24</sup> It establishes that the compression force shall be measured for IOLs intended for capsular bag placement, with the haptics compressed to a diameter of 10 mm. This is a limitation because the actual clinical outcomes might differ based on a patient's capsule size. In our study, the IOL mechanics were evaluated for different compression diameters simulating different capsular bag sizes. Another limitation of the ISO standard is that the axial rotation (as a parameter) is not the subject of the ISO 11979-3 standard,<sup>24</sup> and it is a major issue of designs that are not rotationally symmetric. In our study, we performed the additional analysis of the axial rotation for each IOL model. Finally, there are no guide values of compression force in the ISO 11979-3, so we compared with the ultimate load provided by the study of Krag and Andreassen.<sup>27</sup>

Although the in silico evaluation does not reproduce the same conditions as those experienced by the lens in the capsular bag, it can nevertheless be considered an appropriate choice for analyzing the biomechanical stability of IOLs, fundamentally at the design stage. Although statistically significant differences have been found when comparing the displacement, tilt, and rotation between the different lenses, these differences cannot be considered clinically relevant, which would suggest that all three IOL models yield excellent stability in those terms.

#### AUTHOR CONTRIBUTIONS

Study concept and design (LR, IC-G, BC, FP, NG); data collection (LR, BC, FP, NG); analysis and interpretation of data (LR, IC-G, BC, FP, NG); writing the manuscript (LR, NG); critical revision of the manuscript (LR, IC-G, BC, FP); statistical expertise (LR, IC-G, BC, FP, NG); supervision (LR, IC-G, BC, FP, NG)

#### REFERENCES

1. Remón L, García-Delpech S, Udaondo P, Ferrando V, Monso-riu JA, Furlan WD. Fractal-structured multifocal intraocular lens. *PLoS One*. 2018;13(7):e0200197. doi:10.1371/journal.pone.0200197
2. Gatinel D, Houbrechts Y. Comparison of bifocal and trifocal diffractive and refractive intraocular lenses using an opti-

- cal bench. *J Cataract Refract Surg*. 2013;39(7):1093-1099. doi:10.1016/j.jcrs.2013.01.048
3. Zvornicanin J, Zvornicanin E. Premium intraocular lenses: the past, present and future. *J Curr Ophthalmol*. 2018;30(4):287-296. doi:10.1016/j.joco.2018.04.003
4. Alió JL, Plaza-Puche AB, Javaloy J, Ayala MJ, Vega-Estrada A. Clinical and optical intraocular performance of rotationally asymmetric multifocal IOL plate-haptic design versus C-loop haptic design. *J Refract Surg*. 2013;29(4):252-259. doi:10.3928/1081597X-20130318-04
5. Pérez-Merino P, Marcos S. Effect of intraocular lens decentration on image quality tested in a custom model eye. *J Cataract Refract Surg*. 2018;44(7):889-896. doi:10.1016/j.jcrs.2018.02.025
6. Woodward MA, Randleman JB, Stulting RD. Dissatisfaction after multifocal intraocular lens implantation. *J Cataract Refract Surg*. 2009;35(6):992-997. doi:10.1016/j.jcrs.2009.01.031
7. Gimbel HV, Neuhann T. Continuous curvilinear capsulorhexis. *J Cataract Refract Surg*. 1991;17(1):110-111. doi:10.1016/S0886-3350(13)81001-2
8. Shah GD, Praveen MR, Vasavada AR, Vasavada VA, Rampal G, Shastry LR. Rotational stability of a toric intraocular lens: influence of axial length and alignment in the capsular bag. *J Cataract Refract Surg*. 2012;38(1):54-59. doi:10.1016/j.jcrs.2011.08.028
9. Vounotrypidis E, Lackerbauer C, Kook D, Dirisamer M, Priglinger S, Mayer WJ. Influence of total intraocular lens diameter on efficacy and safety for in the bag cataract surgery. *Oman J Ophthalmol*. 2018;11(2):144-149.
10. Remón L, Siedlecki D, Cabeza-Gil I, Calvo B. Influence of material and haptic design on the mechanical stability of intraocular lenses by means of finite-element modeling. *J Biomed Opt*. 2018;23(3):1-10.
11. Lombardo M, Carbone G, Lombardo G, De Santo MP, Barberi R. Analysis of intraocular lens surface adhesiveness by atomic force microscopy. *J Cataract Refract Surg*. 2009;35(7):1266-1272. doi:10.1016/j.jcrs.2009.02.029
12. Lane SS, Burgi P, Milios GS, Orchowski MW, Vaughan M, Schwarte E. Comparison of the biomechanical behavior of foldable intraocular lenses. *J Cataract Refract Surg*. 2004;30(11):2397-2402. doi:10.1016/j.jcrs.2004.03.041
13. Bozukova D, Pagnouille C, Jérôme C. Biomechanical and optical properties of 2 new hydrophobic platforms for intraocular lenses. *J Cataract Refract Surg*. 2013;39(9):1404-1414. doi:10.1016/j.jcrs.2013.01.050
14. Patel CK, Ormonde S, Rosen PH, Bron AJ. Postoperative intraocular lens rotation: a randomized comparison of plate and loop haptic implants. *Ophthalmology*. 1999;106(11):2190-2195. doi:10.1016/S0161-6420(99)90504-3
15. Bozukova D, Werner L, Mamalis N, et al. Double-C loop platform in combination with hydrophobic and hydrophilic acrylic intraocular lens materials. *J Cataract Refract Surg*. 2015;41(7):1490-1502. doi:10.1016/j.jcrs.2014.10.042
16. Chang DF. Comparative rotational stability of single-piece open-loop acrylic and plate-haptic silicone toric intraocular lenses. *J Cataract Refract Surg*. 2008;34(11):1842-1847. doi:10.1016/j.jcrs.2008.07.012
17. Chua WH, Yuen LH, Chua J, Teh G, Hill WE. Matched comparison of rotational stability of 1-piece acrylic and plate-haptic silicone toric intraocular lenses in Asian eyes. *J Cataract Refract Surg*. 2012;38(4):620-624. doi:10.1016/j.jcrs.2011.10.037
18. Poyales F, Garzón N, Rozema JJ, Romero C, de Zárate BO. Stability of a novel intraocular lens design: comparison of two tri-

- focal lenses. *J Refract Surg.* 2016;32(6):394-402. doi:10.3928/1081597X-20160428-04
19. Simo IFR, Remon L. Toric intraocular lens for correction of high corneal astigmatism in cataract patients. *International Eye Science.* 2018;18(2):213-218.
  20. Zhong X, Long E, Chen W, et al. Comparisons of the in-the-bag stabilities of single-piece and three-piece intraocular lenses for age-related cataract patients: a randomized controlled trial. *BMC Ophthalmol.* 2016;16(1):100. doi:10.1186/s12886-016-0283-4
  21. Poyales F, Garzón N, Pizarro D, Cobreces S, Hernández A. Stability and visual outcomes yielded by three intraocular trifocal lenses with same optical zone design but differing material or toricity. *Eur J Ophthalmol.* 2019;29(4):417-425. doi:10.1177/1120672118795065
  22. de Castro A, Rosales P, Marcos S. Tilt and decentration of intraocular lenses in vivo from Purkinje and Scheimpflug imaging: validation study. *J Cataract Refract Surg.* 2007;33(3):418-429. doi:10.1016/j.jcrs.2006.10.054
  23. Lane S, Collins S, Das KK, et al. Evaluation of intraocular lens mechanical stability. *J Cataract Refract Surg.* 2019;45(4):501-506. doi:10.1016/j.jcrs.2018.10.043
  24. International Organization for Standardization. 11979-3: IF. Ophthalmic implants-Intraocular lenses. Part 3: Mechanical properties and test methods. 2012.
  25. Cabeza-Gil I, Ariza-Gracia MA, Remón L, Calvo B. Systematic study on the biomechanical stability of C-loop intraocular lenses: approach to an optimal design of the haptics. *Ann Biomed Eng.* 2020;48(4):1127-1136. doi:10.1007/s10439-019-02432-9
  26. International Organization for Standardization. 11979-2 IF. Ophthalmic implants-Intraocular lenses. Part 2: Optical properties and test methods. 2014.
  27. Krag S, Andreassen TT. Mechanical properties of the human posterior lens capsule. *Invest Ophthalmol Vis Sci.* 2003;44(2):691-696. doi:10.1167/iovs.02-0096
  28. Holladay JT, Piers PA, Koranyi G, van der Mooren M, Norrby NE. A new intraocular lens design to reduce spherical aberration of pseudophakic eyes. *J Refract Surg.* 2002;18(6):683-691.
  29. Piers PA, Weeber HA, Artal P, Norrby S. Theoretical comparison of aberration-correcting customized and aspheric intraocular lenses. *J Refract Surg.* 2007;23(4):374-384. doi:10.3928/1081-597X-20070401-10

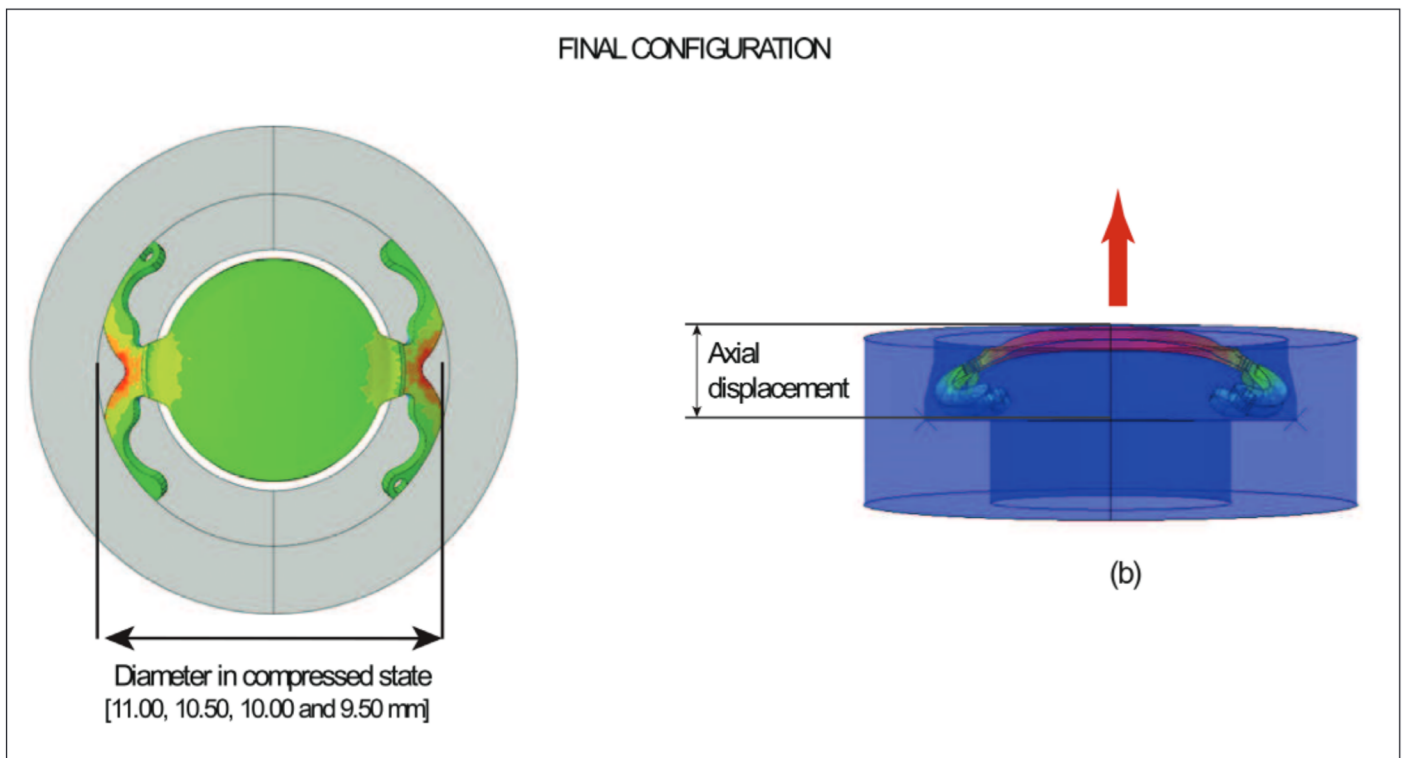


**Figure A.** Final configuration for the in silico compression test: (A) Distance between clamps equal to 10 mm, following the procedure described in International Organization for Standardization (ISO) 11979-3 and for diameters of 11, 10.5, and 9.5 mm, and (B) representation for measurement of axial displacement in compression.

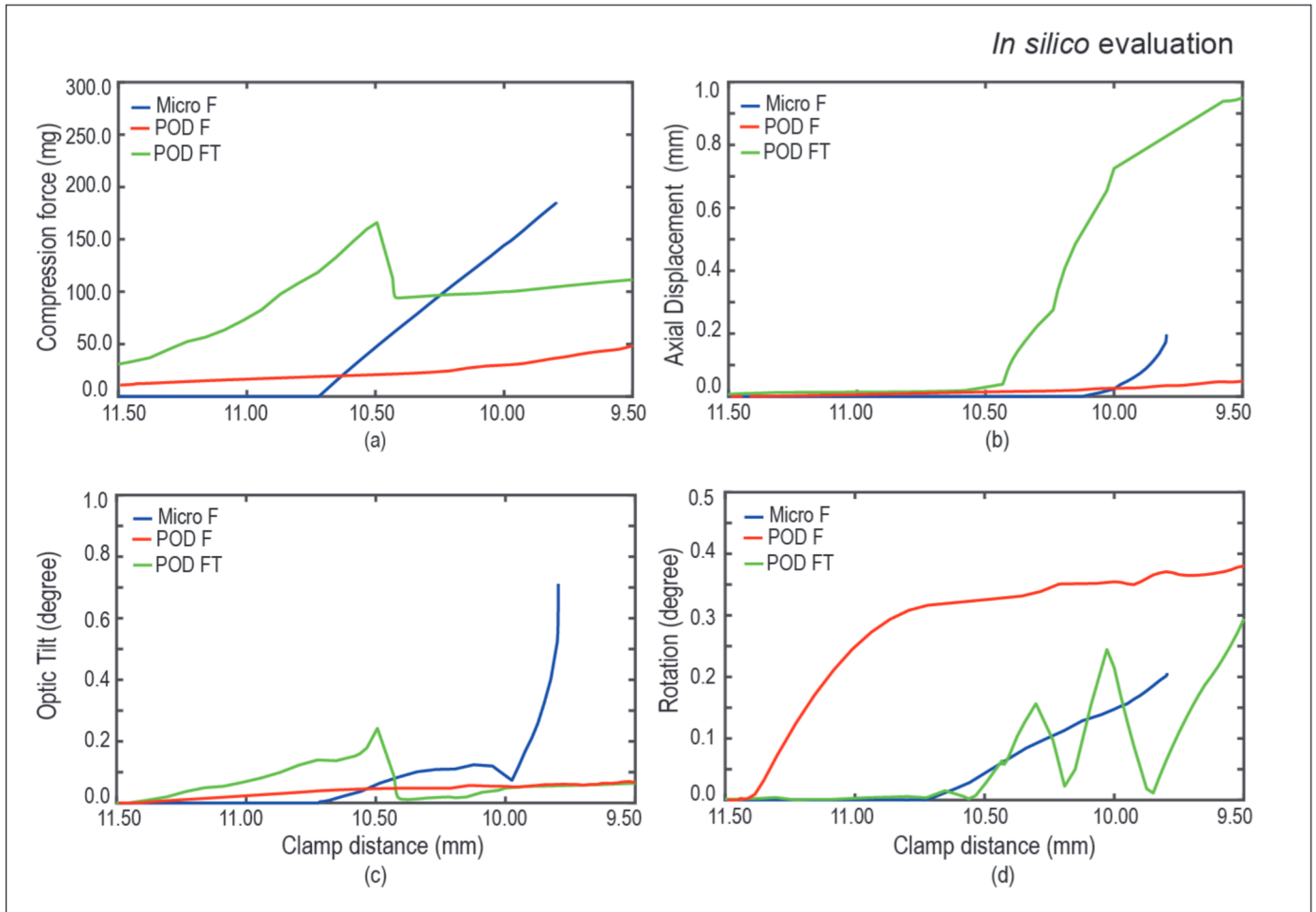


**Figure B.** Evolution of the different variables analyzed as a function of the clamp diameter measured at *in silico* condition: (A) compression force, (B) axial displacement, (C) optic tilt, and (D) rotation. The different variables were measured until the haptics compressed to a diameter of 9.5 mm, following the procedure described in International Organization for Standardization (ISO) 11979-3. All intraocular lenses are manufactured by PhysiOL.

TABLE A  
**Statistical Significance Values for All  
Variables Evaluated for the 3 IOLs  
Measured at In Vivo Condition<sup>a</sup>**

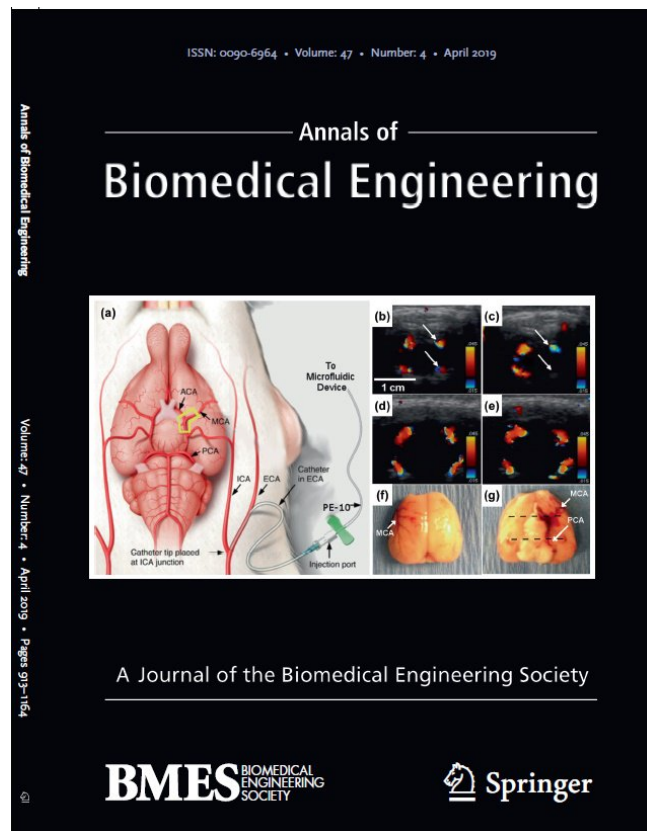
Follow-up Visit	Micro F- POD F	Micro F- POD FT	POD F- POD FT
1 day			
Dx (a), mm	.95	.03	.02
Dx (abs), mm	.80	.68	.99
Dy (a), mm	.20	.75	.32
Dy (abs), mm	.08	.06	.23
Rotation (a), degrees	.86	.01	.47
Rotation (abs), degrees	.01	.43	< .001
3 months			
Dx (a), mm	.98	.42	.23
Dx (abs), mm	.03	.06	.69
Dy (a), mm	.96	.32	.56
Dy (abs), mm	.12	.42	.41
Rotation (a), degrees	.89	.838	.51
Rotation (abs), degrees	.98	.09	.10

*IOL = intraocular lens; Dx = lateral decentration in x-direction; Dy = lateral decentration in y-direction*

<sup>a</sup>*Actual values (a) represent the directly measured values, whereas in absolute values (abs) the measurement's plus or minus sign has not been taken into account*

*All IOLs are manufactured by PhysiOL.*

### 3.5 Work 7: Customised Selection of the Haptic Design in C-Loop Intraocular Lenses Based on Deep Learning



Cabeza-Gil I., Ríos-Ruiz I., Calvo B.  
Annals of Biomedical Engineering  
JIF (2020) = 3.93 (Q2: 31/89 Biomedical Engineering)  
SJR (2020) = 0.91 (Q2: 67/232 Biomedical Engineering)





Original Article

# Customised Selection of the Haptic Design in C-Loop Intraocular Lenses Based on Deep Learning

I. CABEZA-GIL <sup>1</sup>, I. RÍOS-RUIZ,<sup>1</sup> and B. CALVO<sup>1,2</sup>

<sup>1</sup>Aragón Institute of Engineering Research (i3A), University of Zaragoza, Zaragoza, Spain; and <sup>2</sup>Centro de Investigación Biomédica en Red en Bioingeniería, Biomateriales y Nanomedicina (CIBER-BBN), Zaragoza, Spain

(Received 29 May 2020; accepted 22 September 2020; published online 9 October 2020)

Associate Editor Eiji Tanaka oversaw the review of this article.

**Abstract**—In order to increase the probability of having a successful cataract post-surgery, the customisation of the haptic design of the intraocular lens (IOL) according to the characteristics of the patient is recommended. In this study, we present two prediction models based on deep neural networks (DNNs). One is capable of predicting the biomechanical stability of any C-loop IOL, whereas the other can predict the haptic design that fits a desired biomechanical response, enabling the selection of the optimal IOL as a function of the IOL diameter compression. The data used to feed the networks has been obtained from a validated finite element model in which multitude of geometries are tested according to the ISO 11979-3 compression test, a standard for the mechanical properties of the IOLs. The biomechanical response model provides a very high accurate response (Pearson's  $r = 0.995$ ), whilst the IOL haptic design model shows that several IOL designs can provide the same biomechanical response (Pearson's  $r = 0.992$ ). This study might help manufacturers and ophthalmologists both analyse any IOL design and select the best IOL for each patient. In order to facilitate its application, a graphical user interface (GUI) was created to show the potential of deep learning methods in cataract surgery.

**Keywords**—Deep neural networks, IOLs, Biomechanical stability, Haptic design.

## INTRODUCTION

Ophthalmology is one of the medical fields with the biggest application of artificial intelligence (AI),<sup>13,36</sup> and it still leads its development for the detection, diagnosis and treatment of ocular diseases.<sup>1,34</sup>

This study presents a new possible application of AI, with the eventual aim of assisting the ophthalmologist in the planning of cataract surgery. In cataract surgery, the lens that has become cloudy is removed and replaced with an intraocular lens (IOL) to restore clear vision. At the same time, any refractive errors of the patient can be corrected with the optical part of the IOL implanted. So far, the applications of AI in cataracts have focused on detecting and classifying the grade of the cataract by using convolutional neural networks (CNNs) to analyse slit-lamp images<sup>14</sup> and on calculating the lens focal power, focusing on the optics of the lens.<sup>16,32</sup> In our case, our approach is to help the planning of cataract surgery in terms of biomechanics, as the surgeon chooses the IOL to implant considering the desired positioning of the lens in the capsular bag. For this reason, it is crucial to assure the biomechanical stability of the IOL inside this capsular bag.

The biomechanical stability of the lens has been mainly associated with the proper alignment of the IOL by the ophthalmologist, the haptic design and the mechanical properties of the IOL, as well as the dimension and mechanical properties of the capsular bag of the patient.<sup>11,31,37</sup> The mechanical properties of the capsular bag have been predicted as a function of age.<sup>19</sup> However, the dimensions of the human lens capsule, specifically the equatorial diameter, have not yet been accepted as function of age, considering the difficulty of acquiring those dimensions *in vivo*. Nevertheless, we consider it a matter of time until new ophthalmology devices are developed to easily measure the capsule. Recently, Barbé *et al.*<sup>2</sup> proposed a 35-MHz ultrasound biomicroscopy to determine the lens equatorial length in dogs with cataracts.

Address correspondence to I. Cabeza-Gil, Aragón Institute of Engineering Research (i3A), University of Zaragoza, Zaragoza, Spain. Electronic mail: iulen@unizar.es

The aim of this work is to propose an AI methodology based on deep neural networks (DNNs)<sup>5,21</sup> in particular, to determine both the biomechanical response of a C-loop IOL and to provide the optimal haptic design for the lens regarding the dimension of the capsular bag of the patient, all as estimated through an ISO compression test. The advantages that DNNs provide lie in real-time performance and high accuracy. Specially in clinical applications, these two factors are highly valuable, as fast interventions based on reliable predictions can entail an improvement in the well-being of the patient. Currently, the way to evaluate haptic design is through the standardised compression test according to ISO 11979-3:2012.<sup>6</sup> In this test, the lens is compressed by two rigid clamps, resembling the compression of the lens in the capsule. The influence of the size of the capsule is obtained in the response of the IOL to different diameter compressions.<sup>30</sup> Several authors have measured numerically and experimentally the biomechanical stability of IOLs.<sup>3,4,7,30</sup> IOLs with the greatest stability are most likely to give optimum refractive and visual outcomes after implantation.<sup>22,23</sup>

DNNs need to be fed with big amounts of data. Due to the difficulty of conducting such number of experimental tests, we built a validated finite element (FE) model in order to save costs and time.<sup>7</sup> We will make use of a C-loop IOL design, the geometry of which has been parametrised to include all the design possibilities in the current market.<sup>7</sup>

By computing a big battery of cases, we will create our dataset of different IOL designs and their corresponding mechanical response according to the compression test. This dataset will be used to train two models of DNNs, see Fig. 1. For the IOL biomechanical response model, we will create five DNNs that will predict the biomechanical response of the IOL chosen to be implanted in the patient, in terms of five different biomarkers. This model will be fed with the most relevant dimensions of a C-loop IOL, as well as the estimation of the diameter of the capsular bag of the patient. With these data, the model will provide the information of the biomechanical markers that account for the stability of the IOL and that, ultimately, indicate whether the lens would have a good or bad optical performance in that patient.

As for the IOL haptic design model, the sequence is reversed. We will create one single DNN. Its inputs are the biomechanical parameters expected for the IOL to assure stability, as well as the estimation of the diameter of the capsular bag of the patient. With this information, the model will predict the design param-

eters of the best IOL to fit those requirements. This structure might be more interesting from an ophthalmologist point of view as the customised IOL before performing the surgery is chosen. The study here proposed could be implemented for specific situations where there is certainty of different sizes of capsule, i.e. cataracts in children or adults or different breeds of dogs.<sup>24</sup>

A graphical user interface (GUI) is available for the readers as supplementary material. This application helps in the understanding and application of the methodology here implemented.

The paper is organised as follows. Firstly, Materials and Methods gathers the data acquisition and the design of each deep neural network *via* a sensitivity analysis. Then, the results for the IOL biomechanical response and IOL haptic design models are presented to be finally discussed in the last section.

## MATERIALS AND METHODS

### *Dataset Acquisition*

For the dataset acquisition, we used a computational FE model using the software Abaqus 6.14 v, experimentally validated, of a 1-piece, non-angulated, hydrophobic acrylate C-loop IOL.<sup>7</sup> This model reproduces a standardised compression test that approximates the contraction of the lens in the capsular bag. For the model, the geometry of the IOL was parametrised using six parameters, see Fig. 2a. These are the length ( $\lambda_{AA'}$ ), the width (WH), the thickness (T), and the opening angle ( $\varphi$ ) of the haptic, the start of the curvature haptic (HC) and the haptic-optic junction (J). Among these, we determined in our previous study<sup>7</sup> that the length and the opening angle of the haptics were the least relevant to the lens response. Therefore, the battery of cases was generated by randomly ranging the other four geometric parameters in a balanced way, as detailed in Fig. 2a. Following this method, we obtained a total of 1000 balanced geometries to be numerically analysed, with the overall diameter of the IOLs ranging from 11.00 to 13.00 mm.

In order to include the diameter of the capsule of the patient in the model, we quantified the biomechanical response as a function of the clamps close, or the IOL diameter compression. In the compression test, the clamps are assured to be contacting every IOL when they are 10.50 mm apart, and they keep closing until they are separated 9.00 mm. This parameter, ranging from 9.00 up to 10.50 mm, is also added as an input of

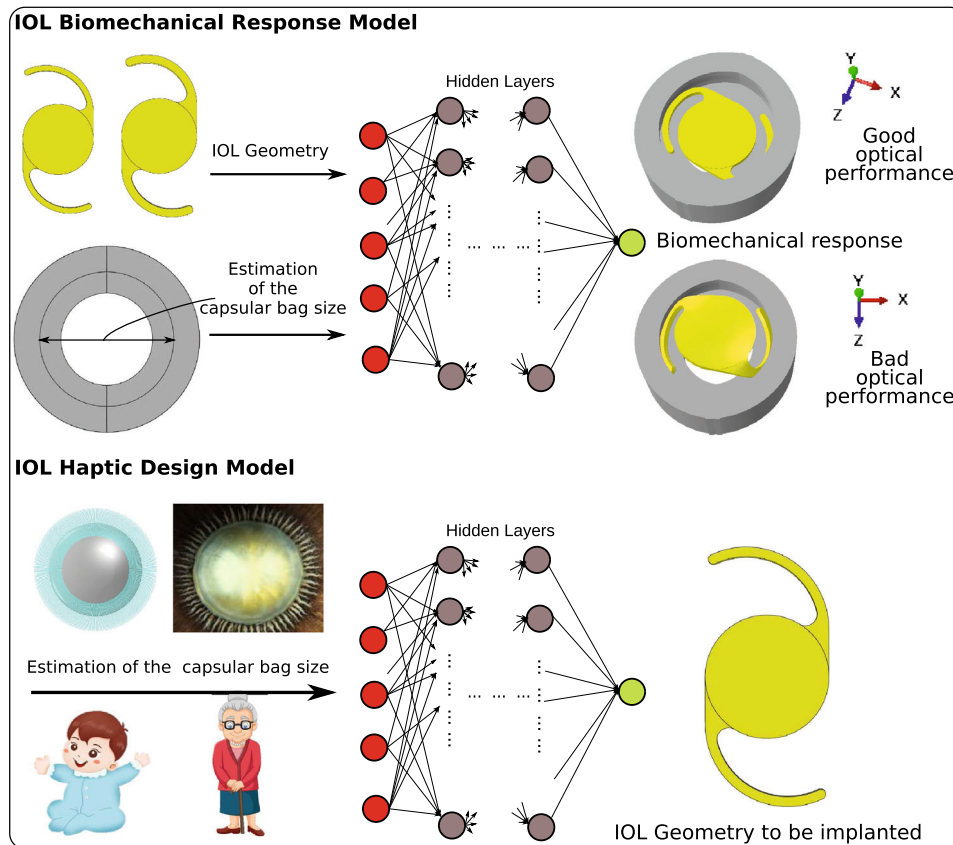


**FIGURE 1.** Outline of the two models of DNNs developed in this study. The IOL biomechanical response model predicts the biomechanical response, that is, the optical performance of an IOL when indicating its geometry and an estimation of the capsular bag of the patient. The IOL haptic design model, on the other hand, predicts the geometry of the IOL that will provide a good optical performance for a specific patient, according to the diameter of their capsular bag.

the model. By doing this, we are able to augment the 1000 simulations up to 37,171 datasets.

The outputs of the simulation that account for the biomechanical stability of the lens are represented in Fig. 2b. The results were automatically obtained *via* a URDFIL Abaqus subroutine. Then, the files were pre-processed in Matlab R2020a to obtain the analysed variables according to the ISO 11979-3 compression test. These are the compression force (mN), also referred to as reaction force, the axial displacement (mm), the tilt ( $^{\circ}$ ), the rotation ( $^{\circ}$ ) and the strain energy (nJ). The distribution of the output data is shown in Fig. 3 and Table 1. There appears to be no clear correlations among the output parameters, perhaps with the exception of the reaction force and the strain energy. Regarding the scatter of each output parameter, it can be noted how they differ from a normal distribution. Also, the outputs range in different orders of magnitude, e.g. the mean of the strain energy is around 450 nJ, that of the reaction force is 0.8 mN and the average of the tilt values is practically  $0^{\circ}$ . This diversity

in the outputs is the main cause that led us to define five independent DNNs to predict each variable separately in the IOL biomechanical response model. Finally, all geometries were carried out from a pre-screening analysis [7] that excluded potentially bad designs. Therefore, several outputs of the model, especially the tilt, take values close to zero, as these represent biomechanically stable IOLs.

For every neural network, we split the total of 37,161 cases into 80% for training (29,729) and 20% for prediction (7432). 20% of the training data (5946) was used as a validation set while the DNNs were trained. All inputs of the DNNs are normalised in advance.

### *Deep Neural Networks*

In this study, we use DNNs as deep learning method to predict the IOL behaviour because of many advantages compared to other machine learning methods: their good performance in properly describ-

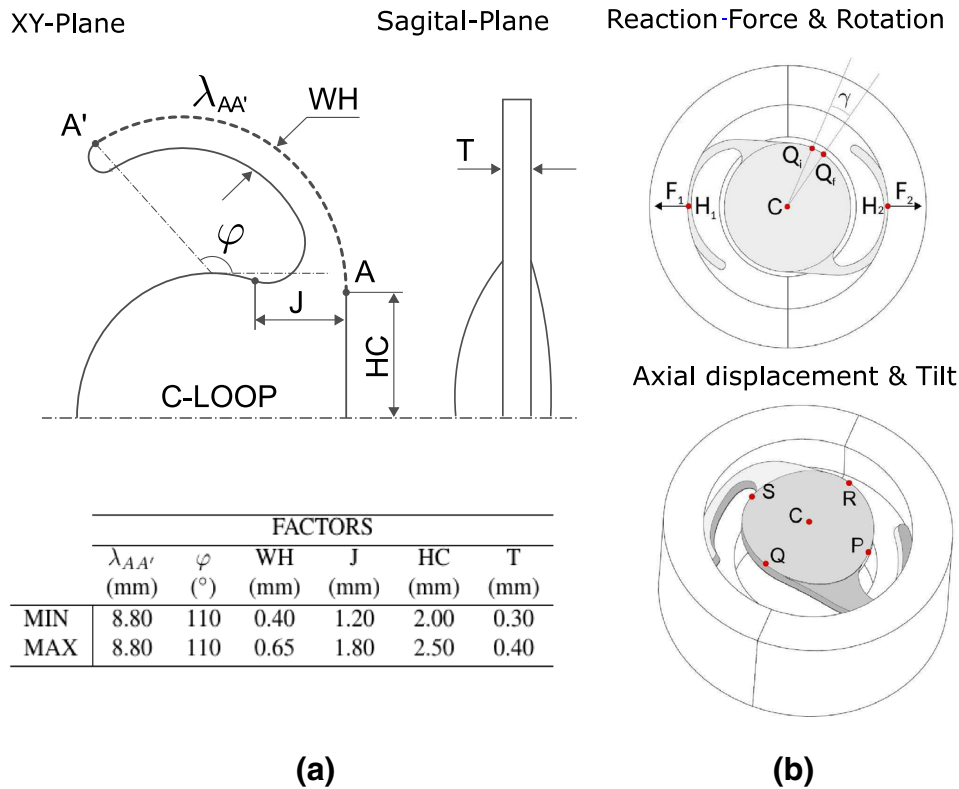


**FIGURE 2.** Geometry of the IOL and biomarkers of its mechanical stability. (a) Parametrisation of the IOL and range of values of each factor covered in the FE simulations. (b) Mechanical Biomarkers: reaction force is given by the sum of the forces in the haptics ( $F = F_1 + F_2$ ); rotation is given by the relative angle ( $\gamma$ ) between the same point at the beginning ( $Q_i$ ) and the end ( $Q_r$ ) of the test. Representation of the key points (in red) used for the evaluation of the tilt (S, R, Q, P) and the axial displacement (C). The strain energy is defined as the energy stored in the IOL due to deformation. Adapted from Cabeza-Gil *et al.*<sup>7</sup>

ing non-linear correlations between multiple inputs and outputs,<sup>35</sup> the capacity to use GPU (GeForce GTX 2060 SUPER), increasing the computer speed for such amount of datasets; the highly flexible architectures; and a similar or higher performance than other machine learning methods.<sup>12,17,21,26</sup> They are also a good substitute for complex FE models with high computation costs,<sup>15</sup> as trained DNNs can give new predictions in real-time. Every DNN in this study was designed with the same functions and following the same process. Therefore, we now explain the overall established methodology.

To design the DNNs, several functions need to be assigned.<sup>25</sup> In the first place, we chose the widely-used rectified linear unit (ReLU) as activation function.<sup>28</sup> The activation function is responsible for transforming the summed weighted input from the neuron into the activation of the neuron or output for that input. The ReLU function overcomes the vanishing gradient problem, allowing models to learn faster and perform better.<sup>25</sup> The choice of an appropriate activation function is then one of the main keys of the performance of the network.

In the second place, the optimisation method we chose was the Adam function,<sup>20</sup> as it has shown good performance in the training of DNNs. Subsequently, the loss function is what will guide the neural network in its training. In this study, we used the mean squared error (MSE) as loss function, see Eq. 1. We also obtained the mean absolute error (MAE) as supporting information, see Eq. 2. MSE is an interesting metric as it overexposes the presence of outliers in the predictions and is recommended when the error distribution is expected to be Gaussian.<sup>9</sup> The MSE and MAE equations are presented below:

$$MSE = \frac{1}{n} \sum_{i=1}^n (y - \hat{y})^2 \quad (1)$$

$$MAE = \frac{1}{n} \sum_{i=1}^n \|y - \hat{y}\| \quad (2)$$

where  $n$  is the number of samples,  $y$  is the response and  $\hat{y}$  is the predicted response.

Finally, we included two additional functions to improve the performance of the networks. First, we added a function that reduces the learning rate if there

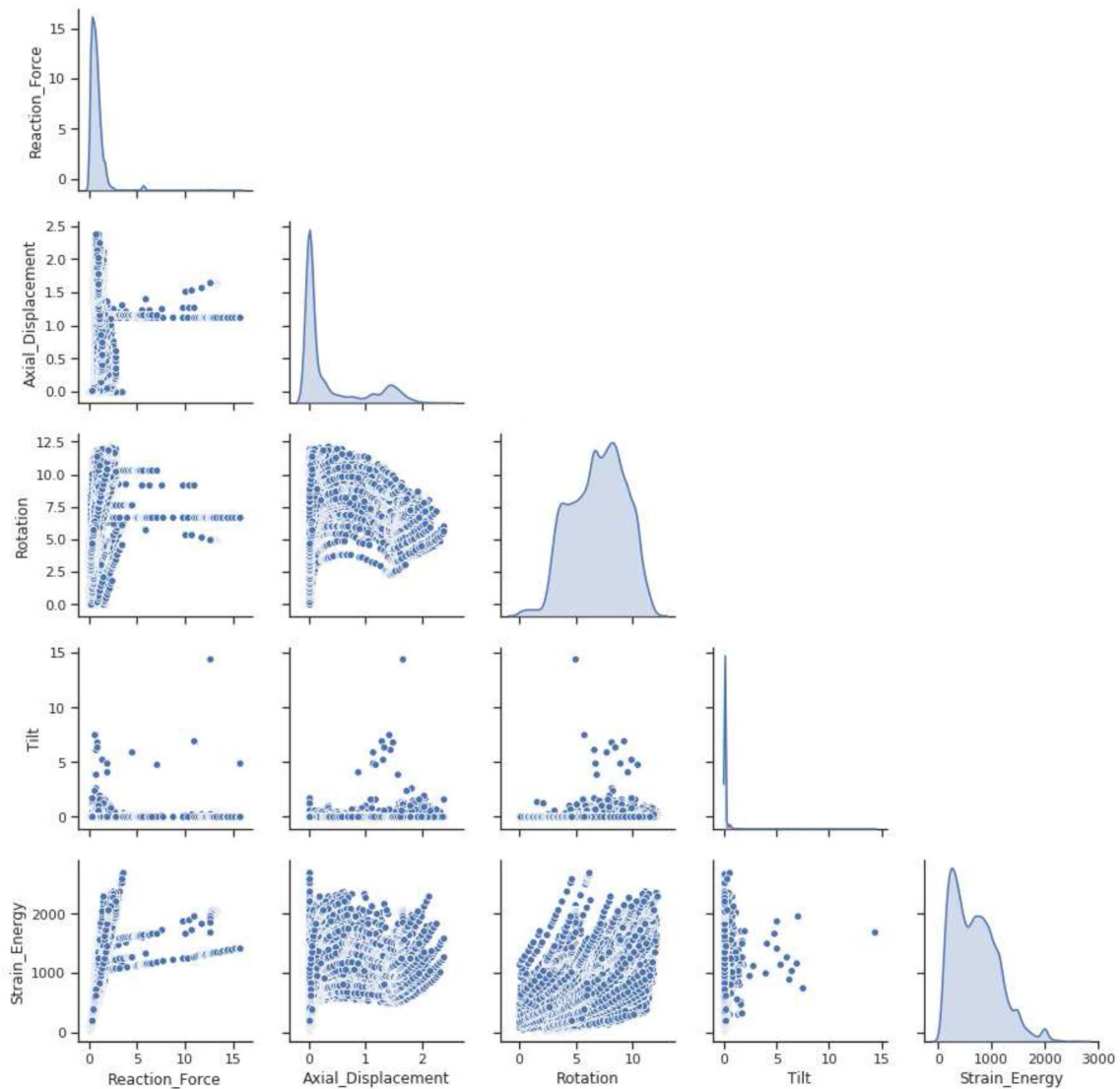


**FIGURE 3.** Scatter plots and histograms of the output variables of the FE model. No significant correlations are found between variables, with the exception of reaction force and strain energy. All variables follow a noticeably different distribution. As a consequence, it is difficult to combine them efficiently as outputs for one single DNN.

**TABLE 1.** Distribution of all the data involved in the design of the DNNs.

		Mean	Std	Min	25%	50%	75%	Max
IOL design	Width of the haptic (mm)	0.53	0.07	0.40	0.48	0.55	0.60	0.65
	Start of the haptic curvature (mm)	2.26	0.14	2.00	2.14	2.27	2.39	2.50
	Junction (mm)	1.47	0.17	1.20	1.30	1.43	1.61	1.80
	Thickness (mm)	0.35	0.03	0.30	0.32	0.34	0.37	0.40
Clamps closure/ IOL diameter compression (mm)	9.60	0.44	9.00	9.22	9.50	9.93	10.50	
Variables analysed	Reaction force (mN)	0.83	0.89	0.05	0.39	0.68	1.02	15.75
	Axial displacement (mm)	0.36	0.56	0.00	0.00	0.03	0.48	2.38
	Rotation (°)	6.97	2.31	0.00	5.17	7.12	8.76	12.16
	Tilt (°)	0.01	0.11	0.00	0.00	0.00	0.00	14.38
	Strain_Energy (nJ)	455.52	700.20	426.13	43.44	651.54	976.41	2,701.00

For each variable, the table shows the mean and standard deviation, the minimum and maximum values, as well as the 25, 50 and 75 percentiles. There were 37,161 datasets for each variable..

has not been a decrease in the loss function (MSE) in 10 epochs. Second, we defined an early stopping of 70 epochs, meaning that if the loss function does not decrease for these amount of epochs, the fitting of the network must stop without reaching the total number of epochs initially determined. This last criterion is important in terms of computational cost.

With all these functions established, we then pursued a sensitivity analysis. The objective of this analysis was to define the simplest neural network possible to best predict the results. To achieve this, we pursued the following procedure for every DNN: we started with a DNN with only two hidden layers of 256 neurons each. For every iteration, we doubled the number of neurons per layer, until the MSE did not decrease. When this happened, we increased the number of layers and started the iteration again. Apart from this, we also tried both, dropout layers and regularizers in order to avoid overfitting.<sup>5,25</sup> However, they have not performed well in our networks. All the iterations carried out for the DNN predicting reaction force are detailed in Table 2.

Once established the architecture of the DNN, and in order to validate the methodology, an analysis was performed on the activation function, optimiser and loss function, see Table 3. Firstly, the two most common loss functions were analysed, MAE and MSE, observing that when the MAE is chosen, the number of outliers, observed by the MSE, is significantly higher. For this study, the MSE as loss function is more beneficial than the MAE as Chai and Draxler stated,<sup>9</sup> since big clinical errors must be avoided. Secondly,

three optimisers were analysed: Adam, stochastic gradient descent (SGD) and RMSprop. The best performance obtained was using the Adam optimiser as Kingma and Ba.<sup>20</sup> Finally, the ReLU, hyperbolic tangent (tanh) and sigmoid activation functions were analysed. The best performance was obtained with the ReLU activation function.<sup>28</sup> Therefore, the functions initially selected were validated and were subsequently used for every DNN. After both analyses, the selected DNNs (including number of hidden layers and neurons) that predict the five mechanical biomarkers are represented in Fig. 4a.

As well as these five DNNs that constitute the IOL biomechanical response model that predicts the IOL behaviour, we developed one more neural network to predict the geometrical parameters as function of the biomechanical response, that is, the IOL haptic design model. For this DNN, the same activation, optimisation and loss functions were used. This DNN is more complex as it has five continuous variables as outputs. This higher complexity can be perceived in the design of this network (Fig. 4b), as it needed a higher number of neurons per each of the five hidden layers.

Within each epoch, the training dataset is run through the network for its fitting. These data are fed to the network in batches, where for each batch the DNN is updated. The batch size considered in our case was 64. Once the whole training set has been evaluated and the DNN fit accordingly, the network is validated. In this process, the validation set is tested in the adjusted DNN. The MSE of the validation set is used as loss function and the network is upgraded. Once the

TABLE 2. Sensitivity analysis of the design of the DNN that predicts the reaction force.

DNN		Output [reaction force]							Time (min)
		Training		Validation		Prediction		Epochs	
No of neurons in the corresponding layer (neurons in L1 + neurons in Li + ... + Ln)		MSE	MAE	MSE	MAE	MSE	MAE		
#1	256 + 256	6.05·10 <sup>-03</sup>	3.60·10 <sup>-02</sup>	9.79·10 <sup>-02</sup>	4.49·10 <sup>-02</sup>	7.30·10 <sup>-02</sup>	4.09·10 <sup>-02</sup>	1945	42
#2	512 + 512	5.15·10 <sup>-03</sup>	3.24·10 <sup>-02</sup>	1.14·10 <sup>-02</sup>	3.85·10 <sup>-02</sup>	6.04·10 <sup>-03</sup>	3.37·10 <sup>-02</sup>	2883	78
#3	1024 + 1024	5.04·10 <sup>-03</sup>	3.12·10 <sup>-02</sup>	1.15·10 <sup>-02</sup>	3.83·10 <sup>-02</sup>	6.83·10 <sup>-03</sup>	3.68·10 <sup>-02</sup>	3000	114
#4	512 + 512 + 512	3.89·10 <sup>-03</sup>	2.70·10 <sup>-02</sup>	8.19·10 <sup>-03</sup>	3.40·10 <sup>-02</sup>	5.82·10 <sup>-03</sup>	3.37·10 <sup>-02</sup>	3000	88
#5	512 D + 512 D + 512	1.62·10 <sup>-02</sup>	6.80·10 <sup>-02</sup>	1.85·10 <sup>-02</sup>	8.48·10 <sup>-02</sup>	1.13·10 <sup>-02</sup>	8.00·10 <sup>-02</sup>	327	13
#6	512 R + 512 R + 512	3.82·10 <sup>-02</sup>	7.97·10 <sup>-02</sup>	4.89·10 <sup>-02</sup>	8.10·10 <sup>-02</sup>	3.88·10 <sup>-02</sup>	7.73·10 <sup>-02</sup>	707	17
#7	256 + 256 + 256 + 256	4.80·10 <sup>-03</sup>	2.87·10 <sup>-02</sup>	1.04·10 <sup>-02</sup>	3.42·10 <sup>-03</sup>	5.81·10 <sup>-03</sup>	3.18·10 <sup>-02</sup>	612	12
#8	512 + 512 + 512 + 512	5.20·10 <sup>-03</sup>	3.07·10 <sup>-02</sup>	1.07·10 <sup>-02</sup>	3.76·10 <sup>-02</sup>	6.11·10 <sup>-03</sup>	3.42·10 <sup>-02</sup>	494	16
#9	512 D + 512 D + 512 + 512	1.18·10 <sup>-02</sup>	6.13·10 <sup>-02</sup>	1.49·10 <sup>-02</sup>	5.71·10 <sup>-02</sup>	1.05·10 <sup>-02</sup>	5.72·10 <sup>-02</sup>	1368	17
#10	1024 + 1024 + 1024 + 1024	3.81·10 <sup>-03</sup>	2.94·10 <sup>-02</sup>	9.50·10 <sup>-03</sup>	3.66·10 <sup>-02</sup>	5.62·10 <sup>-03</sup>	3.58·10 <sup>-02</sup>	3000	47
#11	512 + 512 + 512 + 512 + 512	3.69·10 <sup>-03</sup>	2.54·10 <sup>-02</sup>	6.04·10 <sup>-03</sup>	3.00·10 <sup>-02</sup>	5.31·10 <sup>-03</sup>	2.98·10 <sup>-02</sup>	1946	65
#12	1024 + 1024 + 1024 + 1024 + 1024	4.05·10 <sup>-03</sup>	2.70·10 <sup>-02</sup>	9.28·10 <sup>-03</sup>	3.25·10 <sup>-02</sup>	5.51·10 <sup>-03</sup>	3.17·10 <sup>-02</sup>	1773	29
#13	512 + 512 + 512 + 512 + 512 + 512	3.90·10 <sup>-03</sup>	2.82·10 <sup>-02</sup>	6.58·10 <sup>-03</sup>	3.33·10 <sup>-02</sup>	8.21·10 <sup>-03</sup>	3.32·10 <sup>-02</sup>	1339	16

The same methodology is followed for all the DNNs proposed in this paper. In each step, the number of neurons per layer was increased. If the error did not decrease in respect of the previous design, then the number of hidden layers was increased. The effect of regularizers (*R*) and dropout layers (*D*) was also evaluated. MSE has dimensions of mN<sup>2</sup> and MAE of mN.

**TABLE 3. Assessment of the inner functions of the DNNs.**

DNN [512 (x5)]			Output [reaction force]							
Activation function	Optimiser	Loss function	Training		Validation		Prediction		Epochs	Time (min)
			MSE	MAE	MSE	MAE	MSE	MAE		
#1	ReLU	Adam	$3.69 \cdot 10^{-03}$	$2.54 \cdot 10^{-02}$	$6.04 \cdot 10^{-03}$	$3.00 \cdot 10^{-02}$	$5.31 \cdot 10^{-03}$	$2.98 \cdot 10^{-02}$	1946	65
#2	ReLU	Adam	$4.61 \cdot 10^{-03}$	$1.66 \cdot 10^{-02}$	$1.26 \cdot 10^{-02}$	$2.43 \cdot 10^{-02}$	$6.93 \cdot 10^{-03}$	$2.31 \cdot 10^{-02}$	1919	22
#3	ReLU	SGD	$1.70 \cdot 10^{-02}$	$6.72 \cdot 10^{-02}$	$2.19 \cdot 10^{-02}$	$6.87 \cdot 10^{-02}$	$1.79 \cdot 10^{-02}$	$6.72 \cdot 10^{-02}$	3000	27
#4	ReLU	RMSprop	$4.65 \cdot 10^{-03}$	$3.16 \cdot 10^{-02}$	$1.27 \cdot 10^{-02}$	$4.06 \cdot 10^{-02}$	$7.31 \cdot 10^{-03}$	$3.84 \cdot 10^{-02}$	1388	15
#5	Sigmoid	Adam	$3.16 \cdot 10^{-02}$	$3.16 \cdot 10^{-02}$	$3.16 \cdot 10^{-02}$	$3.16 \cdot 10^{-02}$	$3.16 \cdot 10^{-02}$	$3.16 \cdot 10^{-02}$	932	10
#6	tanh	Adam	$3.43 \cdot 10^{-02}$	$9.09 \cdot 10^{-02}$	$3.57 \cdot 10^{-02}$	$9.12 \cdot 10^{-02}$	$3.91 \cdot 10^{-02}$	$9.31 \cdot 10^{-02}$	1709	52

The network predicting reaction force, on which this analysis was performed, consists of 5 hidden layers of 512 neurons each. The best performance is given when the ReLU activation function, Adam optimiser and MSE as loss function are used (#1)..

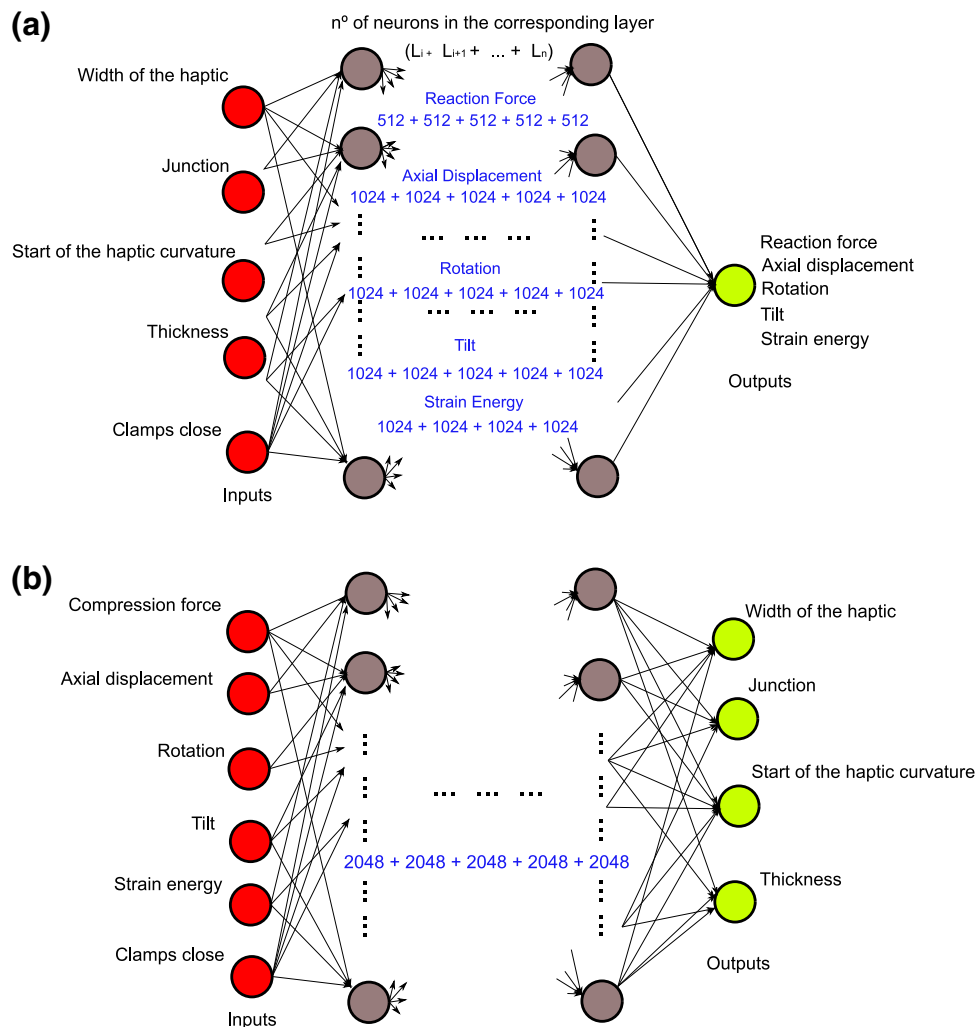


**FIGURE 4. Outline of the DNNs structure for the regression problem. (a) IOL biomechanical response model: Description of the five DNNs, one for each output variable represented. The inputs for each DNN are four geometrical parameters of the IOL and the clamps close. The number of hidden layers and neurons per layer is shown in the centre. (b) IOL haptic design model: Representation of the DNN that predicts the geometrical parameters of the IOL when introducing the biomarkers of the stability of the IOL. Number of layers and neurons also represented in the centre.**

fitting of the DNN has finished as further training implies no improvement in the loss function, the potential of the DNN is evaluated with the prediction set, a set of parameters that were not included in any way in the fitting of the network. All the analyses and the DNNs were performed using the library of Keras in Python.<sup>5,10,18,33</sup>

Finally, as an estimator of complexity, the training time of every case studied is shown in Tables 2 and 3. This measure is dependent on the hardware (GeForce GTX 2060 SUPER). However, as it increases, it gives a notion of the higher complexity of the networks. It is to be noted that, once the networks are trained, they are able to give real time predictions.

## RESULTS

In this section, we will comment separately the results obtained for the IOL biomechanical response model, that includes the five DNNs that predict the mechanical response, and the IOL haptic design

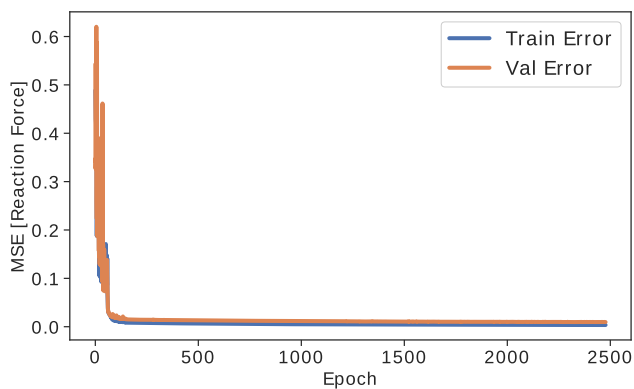


**FIGURE 5.** Learning curve for the DNN predicting the reaction force. Representation of the loss function of the model, MSE, in function of the epochs of training.

model, which predicts, with one DNN, the best geometry that presents the requested mechanical biomarkers for a good optical performance.

### *IOL Biomechanical Response Model*

This model is composed of 5 neural networks, one for each marker of the biomechanical stability of the IOL. With this decision, the prediction of each parameter is more accurate than an aggregate prediction, since there are big differences in the distribution of all output variables.

Regarding the training of the model, Fig. 5 represents the learning curve for an example variable, the reaction force. It shows how the MSE for both, the training and the validation set, diminishes quickly in the first epochs, while it keeps decreasing further until it converges to the established criterion. It is also interesting to perceive how the training error is somewhat below the validation error throughout the entire training. This small difference in favour of the training set implies that the model shows no significant overfitting.

Table 4 shows the training, validation and predicting capacity of the network in terms of error, as well as the number of epochs needed to train each independent network. The root mean square error (RMSE) is represented instead of the MSE as it permits a physical interpretation of its values. For all outputs, due to the non-existence of algorithms that prevent overfitting, the prediction error is slightly higher than the training. For the reaction force, a MAE of around  $3 \cdot 10^{-02}$  mN is obtained for all tests, whereas the RMSE for the prediction is similar to the values of training, around  $7 \cdot 10^{-02}$  mN. The fitting of this network required 2472 epochs of training and validation. The axial displacement shows very small errors, with a MAE of  $1.27 \cdot 10^{-02}$  mm and a RMSE of  $5.09 \cdot 10^{-02}$  mm in the

**TABLE 4.** DNN results.

		Outputs				
		Reaction force (mN)	Axial displacement (mm)	Rotation (°)	Tilt* (°)	Strain energy (nJ)
Training	RMSE	$6.07 \cdot 10^{-02}$	$3.16 \cdot 10^{-02}$	$1.85 \cdot 10^{-01}$	$1.07 \cdot 10^{-01}$	18.21
	MAE	$2.81 \cdot 10^{-02}$	$9.07 \cdot 10^{-03}$	$6.97 \cdot 10^{-02}$	$1.01 \cdot 10^{-02}$	5.57
Validation	RMSE	$7.77 \cdot 10^{-02}$	$4.35 \cdot 10^{-02}$	$2.16 \cdot 10^{-01}$	$5.29 \cdot 10^{-02}$	19.33
	MAE	$3.51 \cdot 10^{-02}$	$1.27 \cdot 10^{-02}$	$8.67 \cdot 10^{-02}$	$0.91 \cdot 10^{-02}$	6.41
Prediction	RMSE	$7.28 \cdot 10^{-02}$	$5.09 \cdot 10^{-02}$	$2.14 \cdot 10^{-01}$	$1.34 \cdot 10^{-01}$	20.34
	MAE	$3.40 \cdot 10^{-02}$	$1.27 \cdot 10^{-02}$	$8.47 \cdot 10^{-02}$	$1.24 \cdot 10^{-02}$	6.26
Epochs		2,472	1,061	977	134	3,125
Time (min)		29	26	19	8	106

The training, the validation and the prediction errors are shown for each response. The loss function was the MSE. In order to allow a physical interpretation of this error, its root (RMSE) is represented. The metric MAE is also reflected. Table also shows the number of epochs needed for each network to accomplish the loss function..



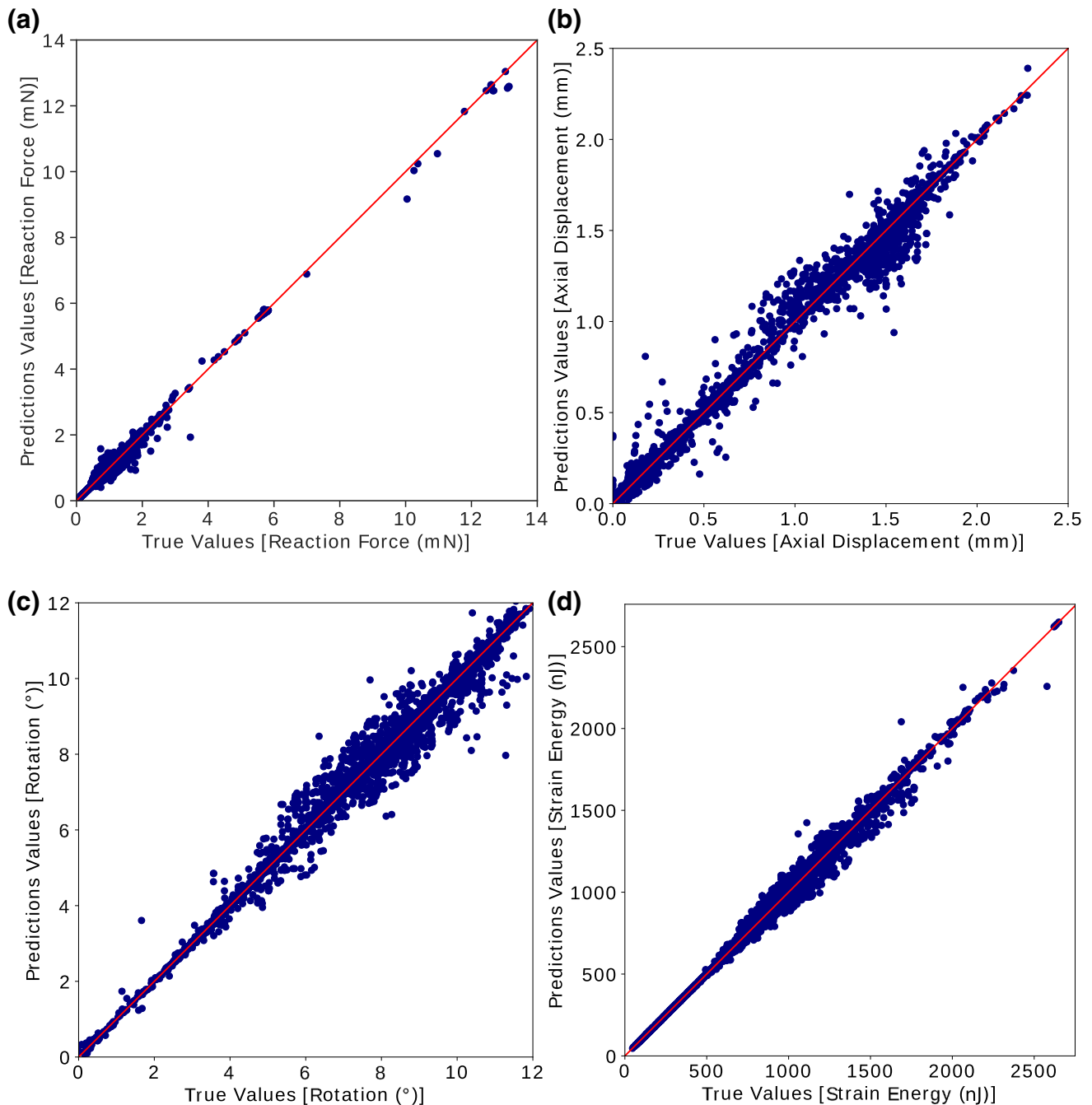


**FIGURE 6.** Model predictability. 7432 predicted values are compared to the ground truth for the different responses, except for the tilt: (a) Reaction force; (b) Axial displacement; (c) Rotation; (d) Strain energy.

prediction test, with a network trained for 1061 epochs. The MAE in the prediction of the rotation is  $8.47 \cdot 10^{-02} \text{ }^\circ$  and a RMSE of  $2.14 \cdot 10^{-01} \text{ }^\circ$  in the prediction test. This network required 977 epochs. The MAE and RMSE of the tilt are  $1.24 \cdot 10^{-02} \text{ }^\circ$  and  $1.34 \cdot 10^{-01} \text{ }^\circ$ , respectively, in the prediction test. The number of epochs needed to train the DNN that predicted the tilt were 134, the least of all networks. Finally, a MAE and a RMSE of 6.26 and 20.34 nJ are

obtained for the predictions of the strain energy, respectively, and it took 3125 epochs to train this DNN.

Figure 6 represents the values predicted by the DNN versus the ground truth of the prediction set. Note that the tilt is not represented as practically all its values are zero (more than 75%), see Table 1. Values in the red line are data predicted with no error. It is interesting how, in the reaction force, shown in Fig. 6a,

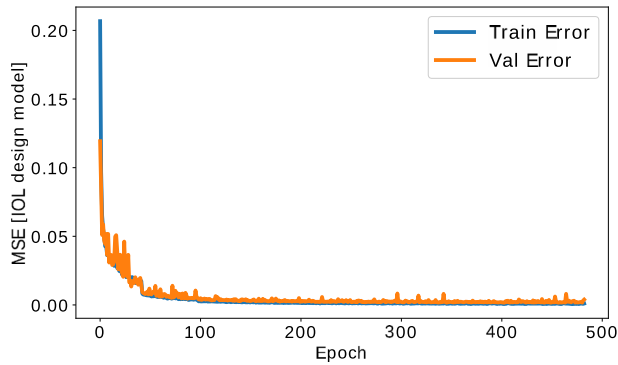


**FIGURE 7.** Learning curve for the DNN that predicts the IOL geometry. Representation of the loss function of the model, MSE, in function of the epochs of training.

even the more outlying values (reaction forces over 8 mN) can be accurately predicted by our network. To compare the prediction capacity, all predictions and actual values were evaluated using Pearson's correlation coefficient (Pearson's  $r$ ). The corresponding Pearson's  $r$  for the reaction force, axial displacement, rotation and strain energy were 0.996, 0.995, 0.992 and 0.998, respectively. Therefore, the IOL biomechanical response model had an average Pearson correlation coefficient of 0.995.

#### *IOL Haptic Design Model*

This model consists of one DNN that predicts the geometrical parameters of the IOL when introducing its desired mechanical response. Note that the clamps close, representing the diameter of the capsular bag of the patient, is again an input parameter of the network. Also, the complexity of prediction is increased by the fact that the outputs were actually the inputs of the FE model, and so the values they take are not continuous but discrete.

The learning curve for this new model is shown in Fig. 7. In this case, the model converges with less epochs of training than the networks of the first model, but the general trend of the curve is the same. The training error remains always below the validation error, which suffers some spikes throughout the training. The spikes can be better explained in the prediction results detailed below.

Table 5 shows the results in terms of error of this model. It includes the normalised mean square error (NMSE) and normalised mean absolute error (NMAE) obtained for each output. Both metrics of error are normalised in order to be able to compare them among all output variables. Considering this scaling, it is easier to evaluate the relevance of these errors in respect of the outputs. The orders of magnitude of the errors are at least two times smaller than

the actual values, indicating fairly accurate predictions. The DNN presents similar results for the prediction of the width of the haptic and the start of haptic curvature, with a NMAE of  $4.49 \cdot 10^{-3}$  and  $4.60 \cdot 10^{-3}$  and a NMSE of  $1.79 \cdot 10^{-4}$  and  $1.58 \cdot 10^{-4}$ , respectively. The junction has a higher NMAE and NMSE,  $6.20 \cdot 10^{-3}$  and  $3.08 \cdot 10^{-4}$ , respectively. The thickness, which presents the least accurate predictions, shows errors of  $8.01 \cdot 10^{-3}$  and  $7.95 \cdot 10^{-4}$  for the NMAE and NMSE, respectively. Overall, the DNN presented a NMAE of  $5.83 \cdot 10^{-3}$  and a NMSE of  $3.25 \cdot 10^{-4}$ . 589 epochs were needed to train this DNN.

These results are also reflected in Fig. 8, which displays the predicted geometrical values versus the real geometric parameters. The fact that these were the inputs of the computational model can be perceived by how the true values take specific values and not fulfill the whole spectrum (data are distributed in vertical lines). This characteristic makes the prediction seem more disperse and is what caused the spikes in the learning curve of the model. However, the diagonal tendency of the graphs is still noticeable. The corresponding Pearson correlation coefficient for the width of the haptic, junction, start of the haptic curvature and thickness were 0.995, 0.992, 0.994 and 0.991, respectively. Therefore, the IOL Design model had a average Pearson correlation coefficient of 0.992. The variations are considered acceptable as there is more than one combination of geometrical parameters of the IOL that can provide the same mechanical response.

#### *Graphical User Interface*

In order to show the potential applicability of this work, we have developed a simple interactive program based on the methodology of this study. With this GUI, we intend to show in a user-friendly way the information that our deep learning systems can provide to clinicians or manufacturers, as well as to make both models available for the readers.

In the interface, the user can choose whether they want to obtain the biomechanical response of a certain C-loop IOL, by introducing its geometrical parameters, or the IOL geometry that fits a certain response. For this second case, it is important to point out that, for a future clinical application, the program should not need the biomechanical markers as inputs. The clinician would only need to introduce the diameter of the lens of the patient and, internally, the system would make sure that the IOL chosen provides the most stable design. Figure 9 shows the main interface of the program, as well as the results windows for both

TABLE 5. DNN Results.

		Outputs				
		Width of the haptic	Junction	Start of the haptic curvature	Thickness	Average model
Training	NMSE	$5.12 \cdot 10^{-05}$	$1.07 \cdot 10^{-04}$	$6.00 \cdot 10^{-03}$	$3.01 \cdot 10^{-04}$	$1.29 \cdot 10^{-04}$
	NMAE	$4.69 \cdot 10^{-03}$	$5.25 \cdot 10^{-03}$	$4.67 \cdot 10^{-03}$	$6.55 \cdot 10^{-03}$	$5.29 \cdot 10^{-03}$
Validation	NMSE	$1.55 \cdot 10^{-04}$	$2.40 \cdot 10^{-04}$	$1.44 \cdot 10^{-04}$	$7.17 \cdot 10^{-04}$	$3.02 \cdot 10^{-04}$
	NMAE	$4.88 \cdot 10^{-03}$	$6.59 \cdot 10^{-03}$	$5.46 \cdot 10^{-03}$	$8.35 \cdot 10^{-03}$	$6.32 \cdot 10^{-03}$
Prediction	NMSE	$1.79 \cdot 10^{-04}$	$3.08 \cdot 10^{-04}$	$1.58 \cdot 10^{-04}$	$7.95 \cdot 10^{-04}$	$3.25 \cdot 10^{-04}$
	NMAE	$4.49 \cdot 10^{-03}$	$6.20 \cdot 10^{-03}$	$4.60 \cdot 10^{-03}$	$8.01 \cdot 10^{-03}$	$5.83 \cdot 10^{-03}$
Epochs		–	–	–	–	482
Time (min)		–	–	–	–	23

The training, the validation and the prediction errors are shown for each response. The loss function was the NMSE. The metric NMAE is also reflected. NMSE and NMAE for the whole model are also shown, as well as the number of epochs needed to accomplish the loss function..

models. This program is available for readers as supplementary information.

## DISCUSSION

In this study, we have presented a new methodology to predict the stability of the implanted IOLs in the capsular bag. Nowadays, experimental tests are the most common technique to assure the mechanical stability of the IOL, by performing the standardised compression test ISO 11979-3.<sup>6</sup> However, these experiments are costly considering the manufacturing of the specific IOL and hours of human work, hampering the possibility of measuring differences in behaviour for slight variations in the lens design. As an improvement, we developed in a previous study a validated finite element model of the compression test.<sup>7</sup> This technique allows a faster and more affordable analysis of the behaviour of the IOLs, which enables to identify the most stable designs. As a last step of this process, we considered the possibility of bringing these techniques closer to the clinicians and manufacturers, for whom shorter times and more applicability are needed. To do so, we decided to benefit from the advantages that AI and neural networks in particular provide. Hence, we have developed a deep learning system based on a wide battery of numerical simulations to analyse the haptic design of C-loop IOLs of the ISO 11979-3 compression test.<sup>6</sup>

This system is presented in two different models, depending on the information they will predict. The IOL biomechanical response model predicts five mechanical biomarkers that provide information of the stability of the IOL. The results obtained are promising as the model can predict these biomarkers with great accuracy. In terms of the prediction capacity, a MAE of 0.03 mN in the reaction force was achieved, with a low RMSE of 0.07 mN. Considering that the mean value of this variable is 0.83 mN and that the minimum

value of all the 37,161 datasets was of 0.05 mN, these errors in the prediction can be accepted. Moreover, the main importance of the reaction force that the IOL exerts is that it could provoke damage or breakage of the capsule. According to Krag and Andreassen,<sup>19</sup> the ultimate load resistance of the posterior capsule for people between 16 years old and 98 years old decreases with age from 15.90 to 1.19 mN in the posterior capsule and from 52.40 to 5.60 mN in the anterior capsule. All these values are two and more orders of magnitude higher than the errors of our DNN, confirming its good predictability. As commented, this error is neither clinically nor numerically relevant, and the same tendency occurs for the other variables analysed.

Regarding the axial displacement, a MAE of 0.01 mm and a RMSE of 0.05 mm is achieved. The prediction response is not as good for this response as the others and there are more outliers, see Fig. 6. However, such small variations in the axial displacement do not affect the refractive power of the IOLs.

Regarding the tilt, it shows a MAE of  $0.01^\circ$  and a RMSE of  $0.1^\circ$ . This is a particular variable, as more than 75% of its values are zero, and it has a standard deviation of  $0.11^\circ$ . Therefore, these possible deviations are considered acceptable for the prediction of this variable, considering they are below its standard deviation. As for the other outputs, the rotation and the strain energy presented an error less than 2% their mean value.

We find this model interesting for two different scenarios. Firstly, for IOL designing and manufacturing companies, as they would be able to check the stability of their lenses within milliseconds, instead of the experimental costs and time, and the computational cost of FE models. Secondly, for the case an ophthalmologist wants to check whether the IOL of their stock will suit their patient according to the diameter of their capsule.

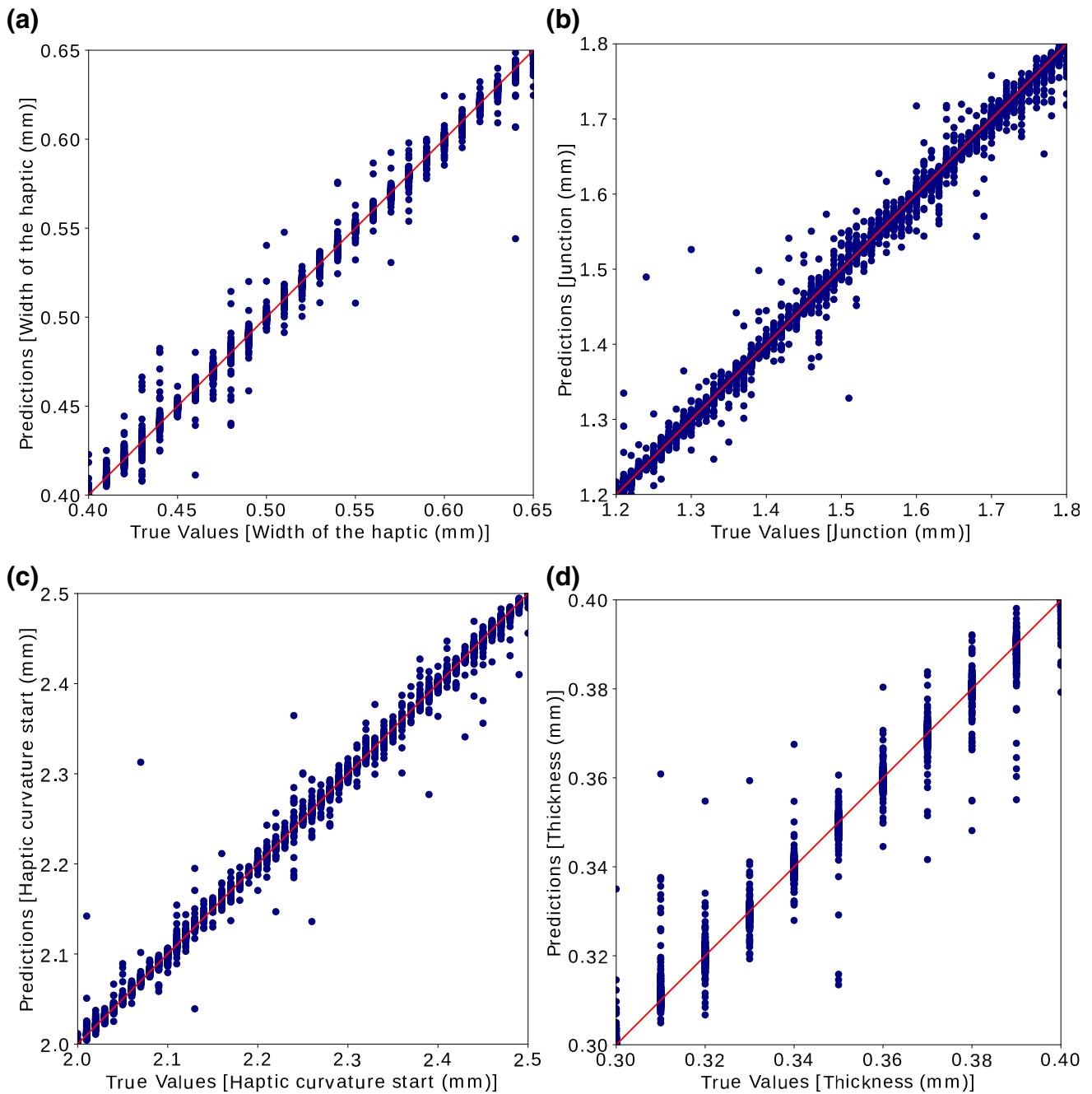


**FIGURE 8. Model predictability.** 7432 predicted values are compared to the ground truth for the different responses: (a) Width of the haptic; (b) Junction; (c) Start of the haptic curvature; (d) Thickness.

The IOL haptic design model, on the other hand, predicts the geometrical parameters of the haptics for the best IOL to fit a particular capsular size, assuring that it provides the mechanical biomarkers requested for a good optical performance. In this model, we achieve a promising NMSE of  $3.25 \cdot 10^{-04}$ , which suggests a very good prediction capability. Nevertheless, we obtained very interesting results as the NMSE values for the width of the haptic, the junction and the

start of the haptic curvature were lower than for the thickness. We had observed previously that those geometrical parameters are the most influential, and we did obtain that the thickness was not so relevant.<sup>7</sup> For this reason, the possible range of the thickness is wider for an established biomechanical response, that is, a similar biomechanical output can be obtained with different values of thickness.

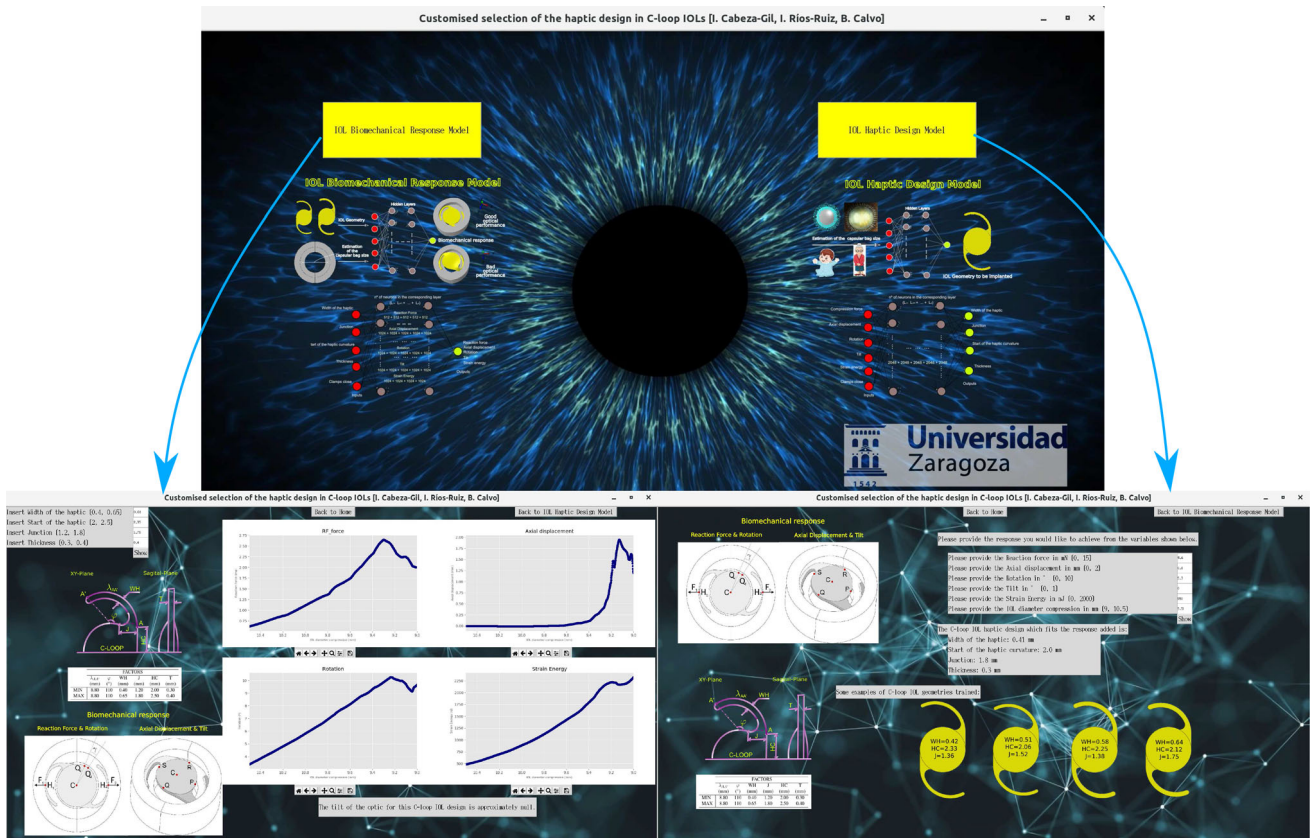


**FIGURE 9.** Main menu of the GUI designed. The corresponding button takes you to the IOL biomechanical response model or to the IOL haptic design model.

Both models provided a higher accurate prediction, with a Pearson's  $r$  of 0.995 and 0.992 for the IOL biomechanical response and IOL haptic design models, respectively, compared to other AI applications in the field of bioengineering.<sup>8,29</sup> However, it is true that the use of numerical data favours a higher accuracy because of the high variability that is presented in experimental data.

One of the weaknesses of the study is that the influence of each factor cannot be analysed with neural networks. Other deep learning models, like XGBoost,<sup>34</sup> provide information of the relevance of each parameter in the output, or the interactions that take place within variables. This was not performed as in our previous work,<sup>7</sup> we had already studied the different correlations among factors and the influence of each geometric parameter in the output mechanical biomarkers. Another one is the maybe insufficient ISO 11979-3 compression test, which can provoke inaccurate predictions of the behaviour of IOLs inside the capsule. Further complex models with the interaction of the IOL with the capsule should be designed.<sup>27</sup>

Moreover, a big set of data was needed to feed the DNNs, and the handling of big arrays of data implies

high computational costs. However, once the DNNs are trained, they are able to give real time predictions for new variables. This immediacy is what allowed us to design and display an executable file that includes all the trained networks. With this program, the user will be able to obtain the predictions of the networks with little computational cost.

The application of this model is directly targeted to clinicians. In particular, ophthalmologists can find this very useful as the diameter of the capsular bag changes with the age of a person (child or adult). Also in the case of veterinary ophthalmology, as different animals and even breeds have significantly different eye sizes. Therefore, a system that could provide them with the information on which IOL to use on each patient could lead to better results in cataract surgery.

With this study, we would like to show the first step and the boost that could be achieved with this application of artificial intelligence in cataract surgery. This novel methodology could also be implemented for other IOL designs in humans and in animals. For futures studies, simulating and validating the IOL in the capsular bag would make the study more realistic.

## ELECTRONIC SUPPLEMENTARY MATERIAL

The online version of this article (<https://doi.org/10.1007/s10439-020-02636-4>) contains supplementary material, which is available to authorized users.

## ACKNOWLEDGMENTS

The authors gratefully acknowledge research support from the Spanish Ministerio de ciencia, innovacion y universidades (Grant DPI2017-84047-R) and the Department of Industry and Innovation (Government of Aragon) through the research group Grant T24-20R (cofinanciado con Feder 2014-2020: Construyendo Europa desde Aragon). The authors also acknowledge the support of the Tissue Characterization Platform of CIBER-BBN, an initiative funded by the VI National R & D & i Plan 2008-2011, Iniciativa Ingenio 2010, Consolider Program, CIBER Actions and financed by the Instituto de Salud Carlos III with assistance from the European Regional Development Fund. I. Cabeza-Gil and I. Ríos-Ruiz were supported by PRE2018-084021 and Government of Aragon, order IIU/1408/2018, respectively.

## DISCLOSURE

No author has a financial or proprietary interest in any material or method mentioned.

## REFERENCES

- <sup>1</sup>Ariza-Gracia, M. Á., J. Zurita, D. P. Piñero, B. Calvo, and J. F. Rodríguez-Matas. Automated patient-specific methodology for numerical determination of biomechanical corneal response. *Ann. Biomed. Eng.* 44:1753–1772, 2015.
- <sup>2</sup>Barbé, C., N. Harran, and F. Goulle. Intra- and interobserver reliability of lens equatorial length measurement using 35-MHz ultrasound biomicroscopy in dogs with cataract. *Vet. Ophthalmol.* 20:329–334, 2016.
- <sup>3</sup>Bozukova, D., C. Pagnouille, and C. Jérôme. Biomechanical and optical properties of 2 new hydrophobic platforms for intraocular lenses. *J. Cataract. Refract. Surg.* 39:1404–1414, 2013.
- <sup>4</sup>Bozukova, L., D. Werner, N. Mamalis, L. Gobin, C. Pagnouille, A. Floyd, E. Liu, S. Stallings, and C. Morris. Double-C loop platform in combination with hydrophobic and hydrophilic acrylic intraocular lens materials. *J. Cataract. Refract. Surg.* 41:1490–1502, 2015.
- <sup>5</sup>Brownlee, J. Deep Learning with Python: Develop Deep Learning Models on Theano and TensorFlow Using Keras. Vermont: Machine Learning Mastery, 2016.
- <sup>6</sup>BS EN ISO 11979-3:2012 Ophthalmic implants. Intraocular lenses. Mechanical properties and test methods. BSI Standards Limited, 2012.
- <sup>7</sup>Cabeza-Gil, I., M. Á. Ariza-Gracia, L. Remón, and B. Calvo. Systematic study on the biomechanical stability of C-loop intraocular lenses: Approach to an optimal design of the haptics. *Ann. Biomed. Eng.* 48:1127–1136, 2019.
- <sup>8</sup>Cano-Espinosa, C., G. Gonzalez, G. R. Washko, M. Cazorla, and R. S. J. Estepar. Biomarker localization from deep learning regression networks. *IEEE Trans. Med. Imaging* 39:2121–2132, 2020.
- <sup>9</sup>Chai, T., and R. R. Draxler. Root mean square error (RMSE) or mean absolute error (MAE)? Arguments against avoiding RMSE in the literature *Geosci. Model Dev.* 7:1247–1250, 2014.
- <sup>10</sup>Chollet, F. Keras. 2015. <https://github.com/fchollet/keras>.
- <sup>11</sup>Crnej, A., N. Hirnschall, Y. Nishi, V. Gangwani, J. Taberner, P. Artal, and O. Findl. Impact of intraocular lens haptic design and orientation on decentration and tilt. *J. Cataract. Refract. Surg.* 37:1768–1774, 2011.
- <sup>12</sup>Delfa, N. J. L., and J. R. Potvin. Predicting manual arm strength: A direct comparison between artificial neural network and multiple regression approaches. *J. Biomech.* 49:602–605, 2016.
- <sup>13</sup>Du, X. L., W. B. Li, and B. J. Hu. Application of artificial intelligence in ophthalmology. *Int. Ophthalmol.* 11(9):1555, 2018.
- <sup>14</sup>Gao, X., S. Lin, and T. Y. Wong. Automatic feature learning to grade nuclear cataracts based on deep learning. *IEEE Trans. Biomed.* 62:2693–2701, 2015.
- <sup>15</sup>Ghaboussi, J., T.-H. Kwon, D. A. Pecknold, and Y. M. Hashash. Accurate intraocular pressure prediction from applanation response data using genetic algorithm and neural networks. *J. Biomech.* 42:2301–2306, 2009.
- <sup>16</sup>González, D. C., and C. P. Bautista. Accuracy of a new intraocular lens power calculation method based on artificial intelligence. *Eye* 2020. <https://doi.org/10.1038/s41433-020-0883-3>.
- <sup>17</sup>Hung, C.-Y., W.-C. Chen, P.-T. Lai, C.-H. Lin. and C.-C. Lee. Comparing deep neural network and other machine learning algorithms for stroke prediction in a large-scale population-based electronic medical claims database. 39th Annual International Conference of the IEEE Eng Med Biol Soc, 2017.
- <sup>18</sup>Hunter, J. D. Matplotlib: A 2D graphics environment. *Comput. Sci. Eng.* 9:90–95, 2007.
- <sup>19</sup>Krag, S., and T. T. Andreassen. Mechanical properties of the human posterior lens capsule. *Invest. Ophthalmol. Vis. Sci.* 44:691, 2003.
- <sup>20</sup>Kingma, D. P., and J. A. Ba. A Method for Stochastic Optimization, 2014.
- <sup>21</sup>Kriegeskorte, N., and T. Golan. Neural network models and deep learning. *Curr. Biol.* 29:R231–R236, 2019.
- <sup>22</sup>Lane, S., P. Burgi, G. Milios, M. Orchowski, M. Vaughan, and E. Schwarte. Comparison of the biomechanical behavior of foldable intraocular lenses. *J. Cataract. Refract. Surg.* 30:2397–2402, 2004.
- <sup>23</sup>Lane, S., S. Collins, K. Das, S. Maass, I. Thatthamla, H. Schatz, S. V. Noy, and R. Jain. Evaluation of intraocular lens stability. *J. Cataract. Refract. Surg.* 45(4):501–506, 2018.
- <sup>24</sup>McMullen, R. J. and B. C. Gilger. Keratometry, biometry and prediction of intraocular lens power in the equine eye. *Vet. Ophthalmol.* 9:357–360, 2006.

- <sup>25</sup>Moolayil, J. Learn keras for deep neural networks—a fast-track approach to modern deep learning with python, 2nd ed. New York: Springer, 2019.
- <sup>26</sup>Ngarambe, J., A. Irakoze, G. Y. Yun, and G. Kim. Comparative performance of machine learning algorithms in the prediction of indoor daylight illuminances. *Sustainability* 12:4471, 2020.
- <sup>27</sup>Pedrigi, R. M. and J. D. Humphrey. Computational model of evolving lens capsule biomechanics following cataract-like surgery. *Ann. Biomed. Eng.* 39:537–548, 2010.
- <sup>28</sup>Ramachandran, P., B. Zoph, and Q. V. Le. Searching for Activation Functions. 2018.
- <sup>29</sup>Rane, L., Z. Ding, A. H. McGregor, and A. M. J. Bull. Deep learning for musculoskeletal force prediction. *Ann. Biomed. Eng.* 47:778–789, 2018.
- <sup>30</sup>Remón, L., D. Siedlecki, I. Cabeza-Gil, and B. Calvo. Influence of material and haptic design on the mechanical stability of intraocular lenses by means of finite-element modeling. *J. Biomed. Opt.* 23:1, 2018.
- <sup>31</sup>Shah, G., M. Praveen, A. Vasavada, V. Vasavada, G. Rampal, and L. Shastry. Rotational stability of a toric intraocular lens: Influence of axial length and alignment in the capsular bag. *J. Cataract. Refract. Surg.* 38:54–59, 2012.
- <sup>32</sup>Tan Q.-Q., J. Lin, J. Tian, X. Liao, C.-J. Lan. Objective optical quality in eyes with customized selection of aspheric intraocular lens implantation. *BMC Ophthalmol.* 19:152, 2019.
- <sup>33</sup>Van Rossum, G., and F. Drake. Python 3 Reference Manual. Scotts Valley, CA.: CreateSpace, 2009.
- <sup>34</sup>Yoo, T. K., I. H. Ryu, H. Choi, J. K. Kim, I. S. Lee, J. S. Kim, G. Lee, and T. H. Rim. Explainable machine learning approach as a tool to understand factors used to select the refractive surgery technique on the expert level. *Transl. Vis. Sci. Technol.* 9:8, 2020.
- <sup>35</sup>Yu, D., Y. Qing, Z. Jianxun, and D. Jun. An artificial neural network approach to the predictive modeling of tensile force during renal suturing. *Ann. Biomed. Eng.* 41:786–794, 2012.
- <sup>36</sup>Zarbin, M. A. Artificial intelligence: Quo vadis? *Transl. Vis. Sci| Technol.* 9:1, 2020.
- <sup>37</sup>Zeng, L. and F. Fang. Advances and challenges of intraocular lens design [invited]. *Appl. Opt.* 57:7363, 2018.

**Publisher's Note** Springer Nature remains neutral with regard to jurisdictional claims in published maps and institutional affiliations.

**3.6 Work 8: Predicting the biomechanical stability of IOLs inside the post-cataract capsular bag with a finite element model.**

Cabeza-Gil I., Calvo B.  
Under Review



# Predicting the biomechanical stability of IOLs inside the postcataract capsular bag with a finite element model

I. Cabeza-Gil<sup>a,\*</sup>, B. Calvo<sup>a,b</sup>

<sup>a</sup>Aragón Institute of Engineering Research (i3A), University of Zaragoza, Spain.

<sup>b</sup>Centro de Investigación Biomédica en Red en Bioingeniería, Biomateriales y Nanomedicina (CIBER-BBN), Spain.

---

## Abstract

**Background and Objectives:** Although cataract surgery is a safe operation in developed countries, there is still room for improvement in terms of patient satisfaction. One of the key issues is assessing the biomechanical stability of the IOL within the capsular bag to avoid refractive errors that lead to a second surgery. For that purpose, a numerical model was developed to predict IOL biomechanical stability in the short- and long-term.

**Methods:** A finite element model containing the implanted IOL, the postcataract capsular bag, the zonules, and a portion of the ciliary body was designed. The C-loop hydrophobic LUCIA IOL was used to validate the model and two more worldwide IOL designs were tested: the double C-loop hydrophobic POD FT IOL and the plate hydrophilic AT LISA IOL. To analyse the biomechanical stability in the long-term, the effect of the fusion footprint, which occurs days following cataract surgery, was simulated. Moreover, several scenarios were analysed: the size and location of the capsulorexhis, the capsular bag diameter, the initial geometry of the capsular bag, and the material properties of the bag.

**Results:** The biomechanical stability of the LUCIA IOL was simulated and compared successfully with the in vitro results. The plate AT LISA design deformed the capsular bag diameter up to 11.0 mm against 10.5 mm for the other designs. This design presented a higher axial displacement and lower rotation, 0.19 mm and 0.2°, than the C-loop design, 0.09 mm and 0.9°.

**Conclusions:** All optomechanical biomarkers were optimal, assuring good optical performance of the three IOLs under investigation. Our findings showed that the capsulorexhis size influences the stiffness of the capsular bag; however, the shape in the anterior and posterior curvature surfaces of the bag barely affect. The results also suggested that the IOL is prone to mechanical perturbations with the fusion footprint, but they were not high enough to produce a significant refractive error. The proposed model could be a breakthrough in the selection of haptic design according to patient criteria.

**Keywords:** intraocular lens; cataract surgery; effective lens position;

---

## 1. Introduction

A cataract is a cloudy area in the lens of the eye that leads to decreased vision. Sight can be restored by cataract surgery, which consists of replacing the opacified crystalline lens with an artificial intraocular lens (IOL). The importance of performing increasingly successful surgeries is paramount as cataract surgery is currently the most frequently performed surgical procedure, with approximately 28 million cataract procedures performed annually worldwide.<sup>1</sup>

---

\*Corresponding author

Email address: iulen@unizar.es -- +34 658403556 (I. Cabeza-Gil)

<sup>1</sup>Financial Disclosure: No author has a financial or proprietary interest in any material or method mentioned.

<sup>2</sup>Address: Edificio Betancourt, Universidad de Zaragoza, Calle María de Luna, 3, 50018 Zaragoza.

The IOL implanted in the eye is formed by the optics, which substitute the optical power of the crystalline lens, and the haptic design, see the IOLs in Fig. 1.a. The haptic design contributes to offering proper positional stability inside the capsular bag, avoiding axial displacement, decentration, tilt, or rotation of the optics that might result in residual refractive errors and other complications, which could require explantation or repositioning of the IOL in certain cases.<sup>2,3</sup>

To date, the main requirement in the preoperative phase is to calculate the IOL power of the patient, which depends on corneal power, the axial length, and the effective lens position (ELP)<sup>4,5</sup> (i.e. the distance from the cornea to the IOL, which is also influenced by the IOL axial displacement<sup>6</sup>). However, the ophthalmic instruments and the methods used in the information gathered preoperatively to select the optimal IOL have not yet reached high standards,<sup>7</sup> leading to only 70% of eyes predicted within  $\pm 0.5$  D of accuracy.<sup>8</sup>

On the other hand, there is a trend to use stiff designs (plates) for toric IOLs to avoid rotation, while the C-loop design is commonly used for monofocal IOLs. Nevertheless, there is no objective tool to help clinicians make their decision<sup>7</sup> since it is not known which haptic design is better than others in the long-term (in terms of biomechanical stability, posterior capsule opacification (PCO) and other complications postsurgery). This implies that the choice of the most appropriate design for a patient continues to be a challenge.<sup>9</sup>

Prior to commercialisation, the IOL biomechanical stability was analysed according to the standard ISO 11979-3 compression test.<sup>10,11,12</sup> In these tests, the IOL is compressed between two rigid clamps, whereas IOL mechanical biomarkers related to the IOL optical performance are registered. Nevertheless, the predictability of IOL biomechanical stability with the standard ISO 11979-3 is limited as it does not consider capsular bag deformation, which can lead to other complications postsurgery.<sup>13,14</sup> The possible causes of IOL biomechanical instability after surgery are unclear. Some assumptions support that it could be produced by the accommodation process that results in a slight contraction of the capsular bag<sup>15</sup> or by the fusion footprint associated with connection between the anterior and posterior capsules days after cataract surgery.<sup>16</sup>

Studies on the biomechanical stability of the ensemble formed by the IOL and the postcataract capsular bag can be divided into three groups: *in vivo*, *in vitro*, and *in silico*. To the best of our knowledge, there are several studies measuring IOL biomechanical stability *in vivo*.<sup>17,18,19,20,21,22</sup> However, the measures provided in these studies are of limited quality. Few mechanical biomarkers are often reported due to limitations in ophthalmic instrumentation, which does not allow a whole 3D reconstruction of the model. Therefore, new sophisticated 3D quantitative imaging data are needed to further understand the postsurgery behaviour of the IOL and the capsular bag. On the other hand, there are some significant *in vitro* studies analysing the IOL biomechanical stability and the appearance of PCO.<sup>23,24,16</sup> The relevance of developing increasingly realistic *in vitro* models is enormous, as all outcomes can be

more easily monitored, allowing 3D reconstruction and favouring further understanding of the problem. Last, few numerical studies have been developed in the field. Cornaggia et al.<sup>14</sup> performed finite element (FE) simulations without explicitly modelling the IOL to observe how the IOL forces affect the mechanical stability of the postcataract capsular bag; Berggren et al.<sup>25</sup> analysed the stress field of the postcataract capsular bag, whereas other finite element analyses were focused on modelling the lens capsule tearing after capsulorexhis and studying accommodation under cataract surgery.<sup>26,27,28</sup>

On the road to IOL customisation, some studies have proposed computational models, which could be used as digital twins to select the optimal IOL optics and haptic design.<sup>29,30,31,32</sup> In this trend, we would like to present an FE model that simulates the biomechanical stability of the ensemble formed by the IOL and the postcataract capsular bag. The model tries to explore and predict IOL biomechanical stability with the aim of assuring excellent visual quality of the patient.

Specifically, the goals of this work are to: (I) Perform an initial validation of the FE model by comparison with the available experimental data in the short-term<sup>16</sup> prior to suffering any possible postsurgery perturbation. II) Compare the results obtained by compressing the IOL between two rigid clamps, in the compression standard test,<sup>10,33,6</sup> and in the capsular bag; (III) Analyse the effects of the fusion footprint on IOL biomechanical stability (long-term).<sup>16</sup> The relevance of analysing the post-surgery effect of the fusion footprint is huge, as it could produce biomechanical instability in the IOL as a consequence of the contraction and deformation of the postcataract capsular bag; (IV) Compare three worldwide IOLs designs; (V) and test different scenarios in the biomechanical stability of the ensemble: the capsulorexhis size and location, the capsular bag diameter, and different mechanical properties of the capsular bag according to age.<sup>34,35</sup>

## **2. Materials & Methods**

In this section, the FE model designed to reproduce the in vitro tests by Wormstone et al.<sup>16</sup> with the LUCIA IOL is explained. For that purpose, the analysis of short- and long-term biomechanical stability is described. Finally, a sensitivity analysis performed to understand the effect of some key parameters of the FE model is presented.

### *2.1. FE model*

The FE model consists of the postcataract capsular bag, the zonules, a portion of the ciliary body, where the zonules are attached, and the artificial IOL implanted. Since there are no experimental measures of the geometry of the postcataract capsular bag that make 3D reconstruction possible, a collapsed capsular bag was considered;<sup>36,37</sup> see Fig. 1.a and see Fig. 1.b.

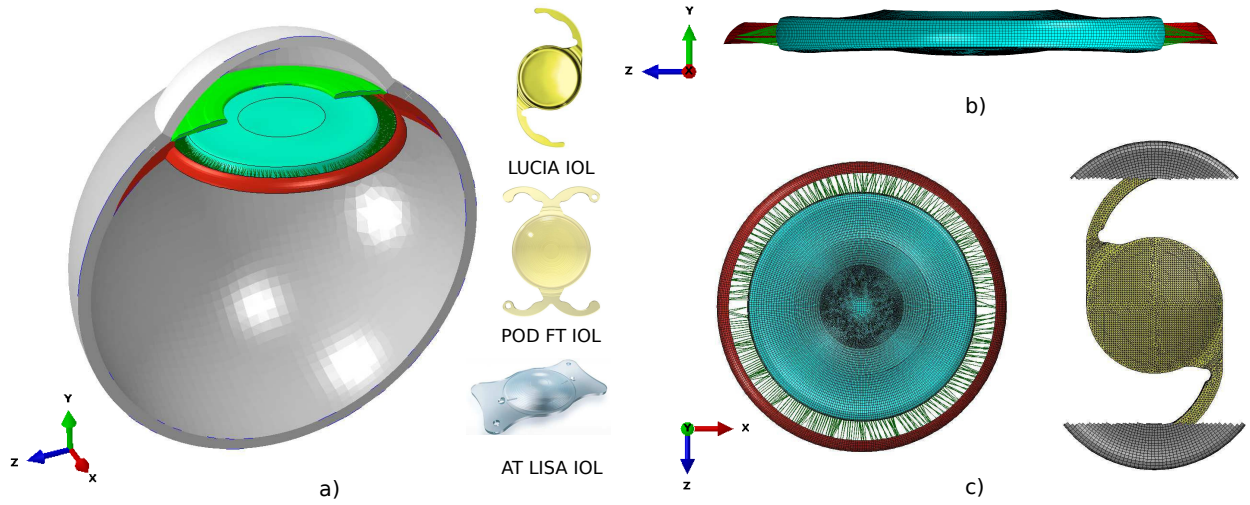


Figure 1: a) Elements considered for the biomechanical stability of the IOL inside the eye (postcataract capsular bag, zonules, a portion of the ciliary body and the implanted IOL). The eyeball is depicted only for visual purposes. The three IOLs under investigation are shown: LUCIA IOL, POD FT IOL and AT LISA IOL. Profile (b) and plant (c) view of the FE mesh structure of the capsular bag and the LUCIA IOL. In an initial step, two rigid clamps (grey) are used to introduce the IOL, bending the haptics, inside the capsular bag.

The capsular bag equatorial diameter and the capsulorexhis diameter were 10.1 mm (short axis) and 4.5 mm, respectively, based on the measurements reported by Wormstone et al.<sup>16</sup> The thickness distribution of the capsular bag was reported for a 65 y/o subject.<sup>38</sup> Last, the capsular bag material was modelled with an incompressible Ogden (n=1) model using stress-strain curves:<sup>34,35</sup>

$$\Psi = \sum_{i=1}^N \frac{2\mu_i}{\alpha_i} (\lambda_1^{-\alpha_i} + \lambda_2^{-\alpha_i} + \lambda_3^{-\alpha_i} - 3), \quad (1)$$

being  $\mu_1 = 0.42$  MPa and  $\alpha_1 = 10.49$  [-].

The zonules were modelled with linear connector elements, assuming that the zonules might not be stretched due to the increase in the equatorial diameter after postcataract capsular bag buckling. These elements were characterised by means of a force-displacement equation, and no compression was considered:

$$F(u) = ku, \quad (2)$$

being  $k = 5 \cdot 10^{-06}$  N/mm.

Three worldwide IOLs with different haptic designs were tested. The C-loop hydrophobic LUCIA IOL (Carl Zeiss Meditec AG, Germany) was used in in vitro tests; the double C-loop hydrophobic POD FT IOL (PhysIOL, 40 Beaver-Visitec International, USA); and the plate hydrophilic AT LISA IOL (Carl Zeiss Meditec AG, Germany), see Fig. 1.a. The LUCIA IOL has an overall diameter of 13.00 mm, while the POD FT and AT LISA IOLs have overall

diameters of 11.40 and 11.00 mm, respectively. All IOLs have an optic diameter of 6.00 mm and an optical power of +22.0 D.

The hydrophobic and hydrophilic IOL acrylic materials used were characterised in previous studies<sup>6</sup> and modelled with an incompressible Ogden ( $n=1$ ) material model (see Eq. 1, where  $\mu_1 = 0.60$  MPa and  $\alpha_1 = 0.86$  [-] for the hydrophilic acrylate and  $\mu_1 = 0.15$  MPa and  $\alpha_1 = 5.86$  [-] for the hydrophobic acrylate). The engineering stress-strain relationship curves of all materials under investigation are reflected in the Supplemental Data.

The general-purpose finite element code Abaqus v.14.1 was used to build the FE model; see Fig. 1.b and Fig. 1.c. A mesh sensitivity analysis was performed to establish the final mesh size; The IOLs were meshed with approximately 150,000 linear tetrahedron (C3D4) elements; the capsular bag was meshed with 62,354 4-node general-purpose shell elements with reduced integration (S4R) ; and 2,000 zonules were modelled. The ciliary body ring was considered a fixed rigid body as the boundary condition of the model.

## 2.2. Analysis of short-term biomechanical stability

Due to the highly nonlinear nature of the problem, i.e. interaction between the IOL and the postcataract capsular bag and the wrinklins formed in the capsular bag after the mechanical perturbation of the IOL, an explicit analysis was performed. The simulation was divided into three steps. First, the IOL was placed inside the capsular bag with the aid of two rigid clamps to fit the IOL overall diameter to the capsular bag diameter (see Fig. 1.c). These clamps were removed in the posterior steps. Second, the interaction between the IOL and capsular bag was initialised and stabilised. For that purpose, a ‘hard’ contact was considered to minimise penetration. Third, a quasi-static analysis is performed through 3 s of virtual time. With this analysis, the biomechanical response in the short-term (i.e. 24 h after cataract surgery) can be reproduced.

To validate the FE model with the LUCIA IOL, the same in vitro biomarkers<sup>16</sup> were registered: the long axis –mm–, which is the maximum capsular bag diameter due to the IOL stiffness, see Fig. 2; the short axis –mm–, which is the smallest bag diameter; the Tip-to-Tip and the Notch-to-Notch, –mm–, specific measures for each IOL; and the capsulorexis and the total bag area, –mm<sup>2</sup>–. Moreover, the optomechanical biomarkers of the IOL optics, which are related to the IOL optical performance (axial displacement –mm–, decentration –mm–, tilt and rotation –°–), were also measured.<sup>6,33</sup>

## 2.3. Analysis of the long-term biomechanical stability: fusion footprint

The fusion footprint occurs progressively days after cataract surgery and is the connection between the anterior and posterior surfaces of the capsule. This fusion footprint is formed in the nonhaptic regions of the capsular bag,

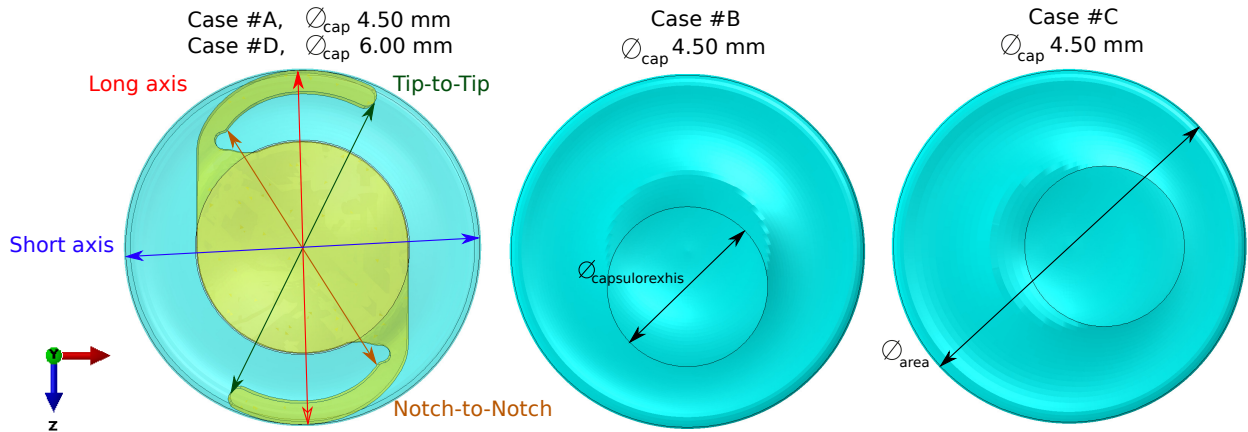


Figure 2: Location and size of capsulorexhis under investigation: capsulorexhis of 4.50 (case #A) and 6.00 mm (case #D) centered; and capsulorexhis of 4.50 mm decentered in the -Z and -X axes (case #B and #C, respectively). The IOL orientation is shown in the -Z axis.

while the haptic and optic IOL parts maintain separation of the anterior and posterior surfaces, preventing fusion at these sites.<sup>16</sup>

This biological process was simulated after stabilising the IOL in the capsular bag in two additional steps. First, pressure is applied in some portion of the anterior surface, while the posterior surface is fixed in the Y axis, simulating the progression of the fusion footprint. This pressure was calculated iteratively with the aim of barely affecting the ensemble formed by the IOL and the capsular bag. Finally, pressure was applied in the remaining parts of the anterior capsule to produce the total fusion footprint of both surfaces.

#### 2.4. Sensitive Analyses

The FE model addresses high complexity and can be helpful for evaluating different aspects. Therefore, several scenarios were simulated to analyse several key parameters of the FE model. All simulations were performed for the LUCIA IOL.

First, the effect of the initial geometry of the capsular bag was studied. A precataract geometry, without having been collapsed, was analysed (i.e. with the hypothesis that the capsular bag does not collapse immediately after capsulorexhis and the phacoemulsification technique). The radii of curvature of the precataract capsular bag were based on Chang et al.<sup>39</sup> measures, with anterior and posterior radii of curvature of 7.85 and 5.75 mm, respectively. For comparative purposes, the same capsular bag equatorial diameter was designed, 10.1 mm, as the flattened/collapsed capsular bag geometry under investigation. See Supplemental Data to see the geometries under investigation.

Second, the stiffness of the zonules should be obtained iteratively for each FE model because depending on the number of zonules modelled, the force applied is different. Therefore, ten simulations were performed varying the  $k$  constant; see Eq. 2, from  $10^{-03}$  to  $10^{-07}$  N/mm, to observe the effect of this parameter.

Third, the influence of the mechanical properties of the capsular bag on the biomechanical stability of the ensemble formed by the IOL and the capsular bag was studied. Ten simulations were performed, mimicking the aging of the capsular bag.<sup>34,35</sup> For that purpose, as there is not enough characterisation of the capsular bag in the literature to propose different hyperelastic models, the Young modulus reported by Krag and Andreassen,<sup>34,35</sup> which ranges from 0.5 to 2.5 MPa, were used. The elastic modulus was converted to a Neo-Hookean hyperelastic model with the following relationship considered for isotropic incompressible materials:

$$E = 3\mu, \quad \mu = 2C_{10} \quad (3)$$

where  $C_{10}$  is the Neo-Hookean constant of the hyperelastic material model:

$$\Psi = C_{10}(I_1 - 3) \quad (4)$$

and  $I_1$  is the first invariant of the right Cauchy-Green deformation tensor.

Fourth, the influence of the capsular bag equatorial diameter was studied. Two additional analyses were performed for a postcataract capsular bag with a lower and higher diameter, 9.70 and 10.40 mm, respectively.

Finally, the influence of the size and location of the capsulorexhis on the biomechanical stability of the ensemble was analysed. To do so, four cases were designed: the reference case with a capsulorexhis diameter of 4.50 mm in the centre, see case #A in Fig. 2; the same case but with a capsulorexhis diameter of 6.00 mm, see case #D; and two capsulorexhis of 4.50 mm decentered in both the -Z and -X axes, case #B and case #C, respectively, see Fig. 2.

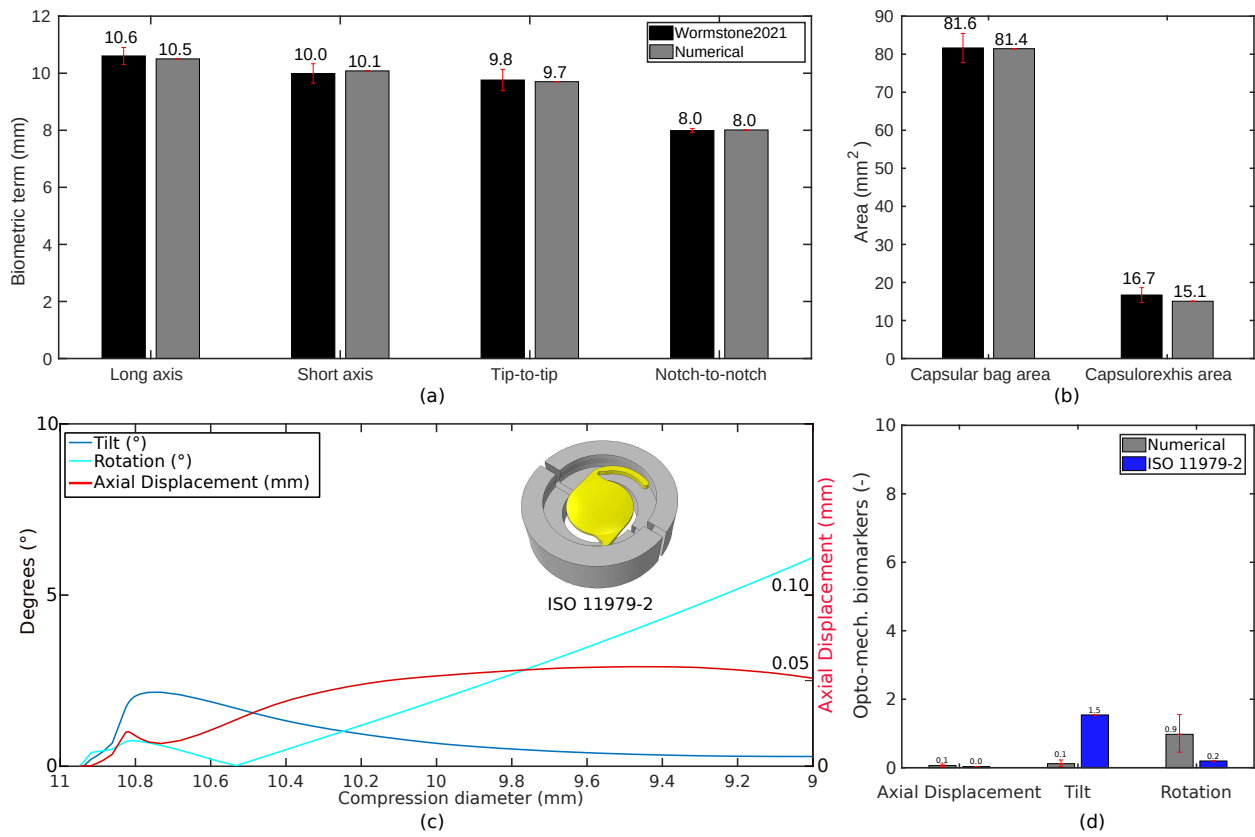


Figure 3: Biomechanical stability of the LUCIA IOL in the short-term. (a) and (b) In silico vs in vitro results. (a) Biometric terms. (b) Capsular bag and capsulorexhis areas. (c) Mechanical behaviour in the ISO 11979-3 compression test. (d) IOL mechanical biomarkers between the rigid clamps vs the deformable capsular bag. The results were compared for a compression diameter of 10.5 mm as the result of the mechanical biomarker, the long axis, in the LUCIA IOL simulation.

### 3. Results

#### 3.1. Short term biomechanical stability

Fig. 3.a and Fig. 3.b show a comparison between the numerical and in vitro results.<sup>16</sup> All numerical results lie within the deviation reported. The LUCIA IOL enlarges the capsular bag diameter from 10.1 to 10.5 mm.

Fig. 3.c shows the main optical outcomes (axial displacement (right-axis, -mm-), tilt and rotation (left-axis, -°-)) of the IOL following compression test ISO 11989-3<sup>10</sup> for compression diameters ranging from 11.0 to 9.0 mm. Fig. 3.d shows the comparison between the mechanical biomarkers for the IOL compression test and the IOL inside the capsular bag; see Fig. 3.a. The rotation and tilt values are of little relevance in clinical practice, and thus, both tests seem to be correlated. The IOL does not present decentration. Ale<sup>40</sup> reported that less than 3° of tilt and 0.3 mm of decentration are clinically unnoticed for any IOL design.

Fig. 4.a shows a cutting view of the eyeball when the IOL has been implanted. Fig. 4.b depicts the wrinkling in both anterior and posterior capsular bag surfaces. Wrinkling is a null energy state due to compression strengths



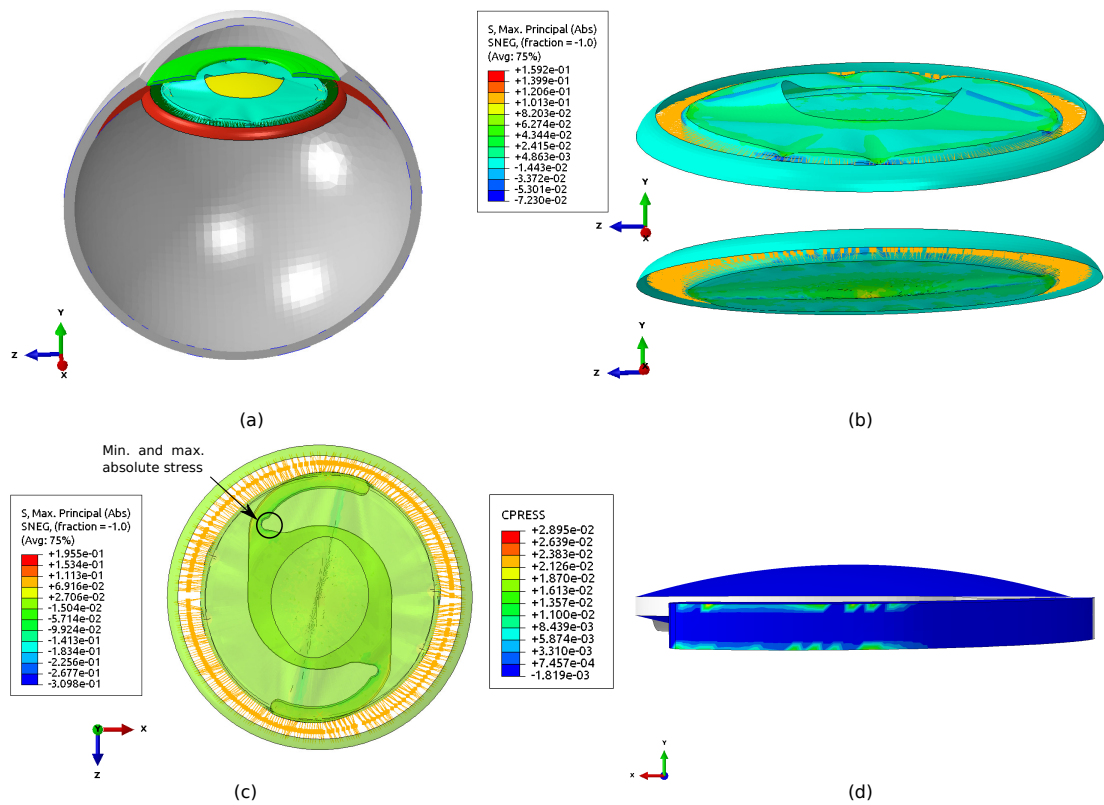


Figure 4: Visualization of the LUCIA IOL inside the capsular bag. (a) A cutting view of the FE model presented. (b) Images of the anterior and posterior capsular bag surfaces. (c) A plant view of the IOL inside the capsular bag at the final configuration. (d) contact pressure (MPa) of the haptic region.

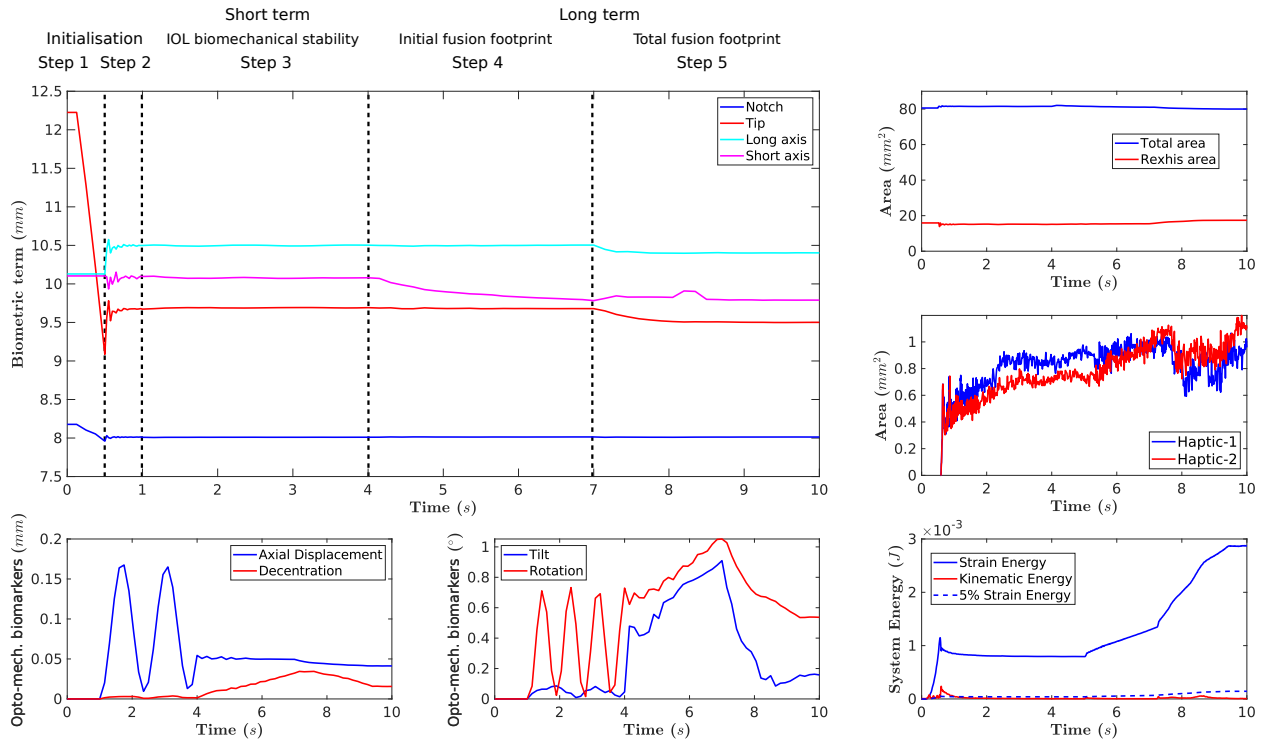


Figure 5: Biometric measures of the LUCIA IOL and the capsular bag analysed throughout the simulation: the Notch-to-Notch and Tip-to-Tip (mm); the long and short axis of the capsular bag (mm); the area of the total capsular bag and the capsulorexhis ( $\text{mm}^2$ ); the contact area between the IOL haptics and the capsular bag; the optical contribution terms, axial displacement and decentration (mm) and the rotation and tilt ( $^\circ$ ); and the strain and kinematic energy of the system. The fusion footprint is added with two extra steps.

in membranes. The wrinkling is formed in the axis direction where the IOL haptics are compressed. The use of numerical methods allows variable quantification that are not physically measurable. For instance, Fig. 4.c displays a plant view of the maximum principal stresses of the final configuration of the LUCIA IOL inside the capsular bag, which is similar to what Wormstone et al.<sup>16</sup> reported. Finally, Fig. 4.d shows the contact pressure applied in the haptic region of the LUCIA IOL.

### 3.2. Long-term biomechanical stability: fusion footprint

All results data of the LUCIA IOL throughout the simulation are shown in Fig. 5. As commented in Sect. 2.3, an initial fusion footprint of the anterior and posterior surface of the capsular bag is simulated in Step 4 to finally simulate the total fusion footprint of the capsule in the last step.

The capsular bag contracts slightly with the fusion footprint, as can be observed in the long- and short-axis measures. The long axis is reduced from 10.5 mm in the IOL biomechanical step to 10.4 mm in the last step (see Fig. 5), while the short axis is shortened by 0.29 mm (from 10.07 to 9.78 mm)

The total capsular bag area is reduced slightly from  $81.76 \text{ mm}^2$  to  $79.98 \text{ mm}^2$ , while the capsulorexhis area

increases from 15.15 to 17.36 mm<sup>2</sup>. Moreover, the contact area between the IOL haptic and the capsular bag increases slightly with the progression of the fusion footprint.

Regarding the IOL optomechanical biomarkers, the optics of the IOL have small vibrations in the biomechanical stability step due to the explicit analysis performed. It is hardly noticeable visually, but it has been considered deviations in the numerical results obtained. All optomechanical biomarkers are of scarce relevance in clinical practice,<sup>40</sup> although the fusion footprint seems to slightly affect the tilt and rotation of the LUCIA IOL. Finally, the validity of the quasi-static analysis was checked through the strain and kinematic energies of the system. The kinematic energy is under 5% of the total strain energy of the system throughout the simulation. Fig. 6.a and 6.b. reflect a partial and a total fusion footprint, respectively.

### *3.3. Short-term biomechanical stability of three worldwide IOLs*

The final configurations of the POD FT and AT LISA IOLs are depicted in Fig. 6.c and 6.d, respectively. The results of the three IOLs under investigation are shown in Fig. 7. LUCIA and POD FT IOLs present the same long axis, 10.5 mm, against 11.00 mm that presents the LISA IOL, indicating that the IOL has barely compressed. The short axis shows consistency with the long axis (i.e., it is smaller when the long axis is larger). As expected, the LISA IOL presents the smallest short axis, while the POD FT IOL presents a higher short axis than the LUCIA IOL, probably due to its double C-loop design (see Fig. 7).

Regarding optomechanical biomarker values, the LUCIA IOL barely presents axial displacement,  $0.09 \pm 0.07$  mm, while the POD FT and LISA present axial displacements of  $0.16 \pm 0.13$  mm and  $0.19 \pm 0.22$  mm, respectively. The values of tilt, rotation, and decentration for all IOLs are of scarce relevance in clinical practice.

As expected, the final total capsular bag area of the AT LISA IOL was higher than that of the LUCIA and POD FT IOLs. Surprisingly, the capsulorexhis area of the POD FT was higher than that of the LUCIA and AT LISA IOLs.

### *3.4. Sensitivity analyses of key parameters of the model*

The effect of the main parameters of the FE model evaluated via sensitivity analysis are shown in Fig. 8: the initial geometry of the capsular bag; the force stretched by the zonules, see Fig. 8.a; the stiffness of the capsular bag, see Fig. 8.b; the capsular bag diameter, see Fig. 8.c; and the capsulorexhis size and location, see Fig. 8.d. For graphical purposes, only three simulations are shown, although the consistency of the results and the robustness of the FE model were verified. In all simulations, the LUCIA IOL optomechanical biomarkers were optimal and thus presented a quality optical performance.

The initial geometric configuration of the capsular bag shows little influence (see Supplemental Data). The anterior and posterior surfaces do not influence the deformation of the equatorial diameter of the capsular bag. This

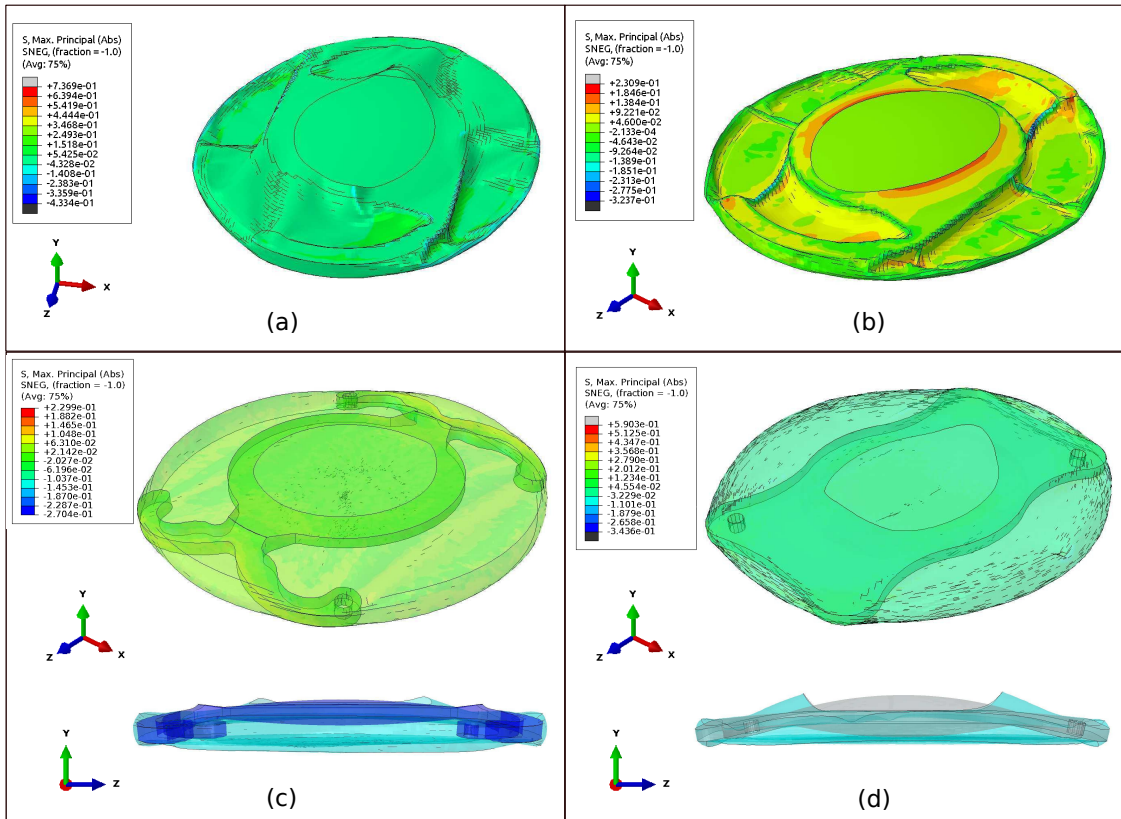


Figure 6: (a) Maximum absolute stresses of the ensemble formed by the IOL and the capsular bag when the fusion footprint between both capsules is progressively forming. (b) Maximum absolute stresses of the ensemble formed by the IOL and the capsular bag when the fusion footprint is totally formed. Isometric view of the maximum absolute stresses in the ensemble formed by the IOL and the postcataract capsular bag for the POD FT (c) and AT LISA IOLs (d), respectively. A profile view showing the axial displacement of the IOL is also depicted.

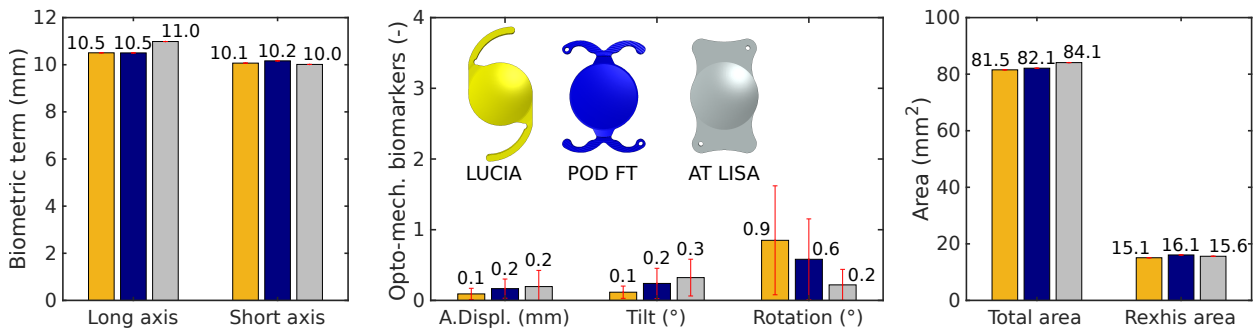


Figure 7: The biomechanical stability of the ensemble formed by the IOL and the capsular bag is shown for the three IOLs under investigation.

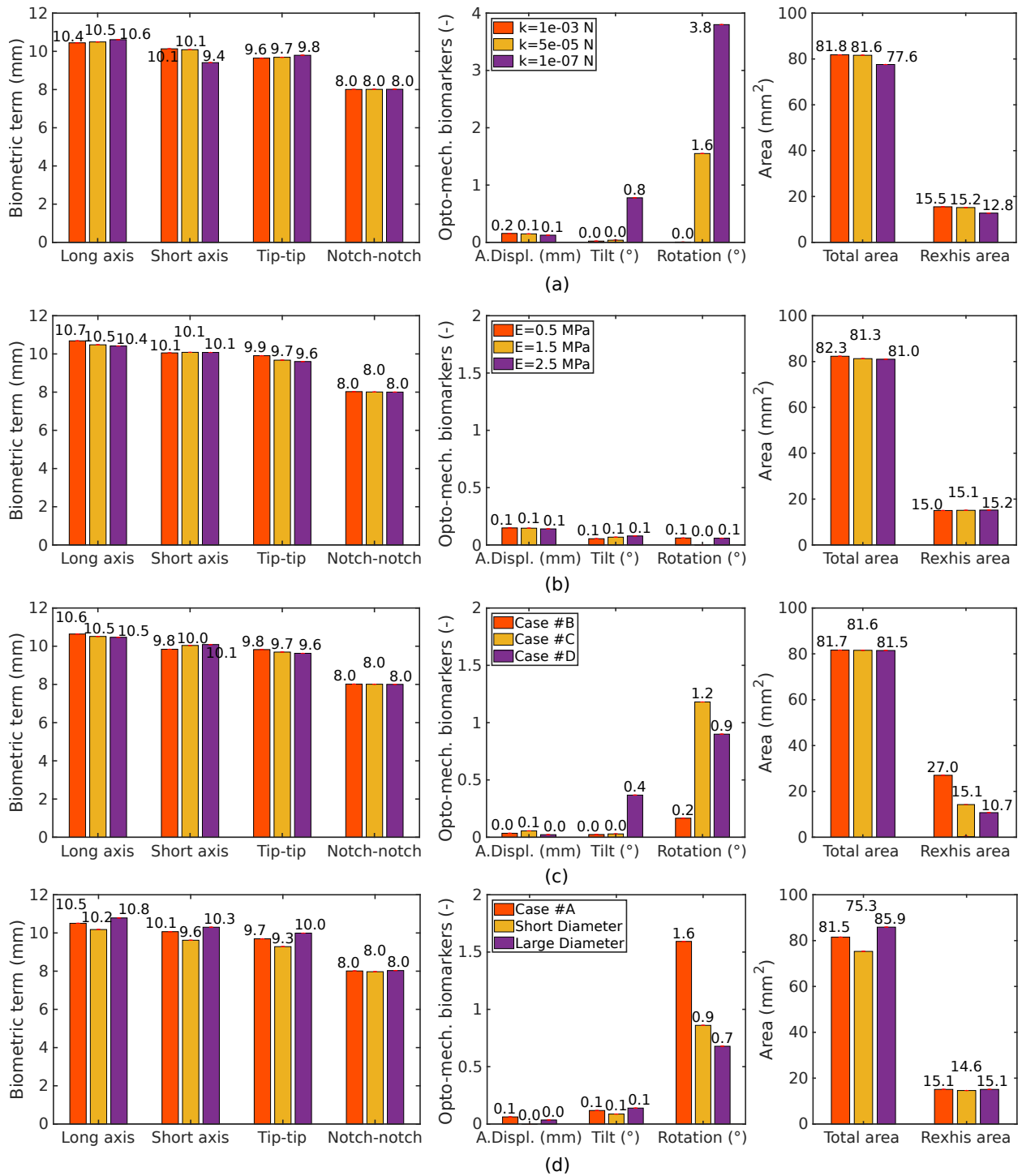


Figure 8: The biomechanical stability of the ensemble formed by the IOL and the capsular bag was analysed for several hypotheses: the effect of the zonule stiffness (a); the mechanical properties of the capsular bag (b); the capsular bag diameter (c); and the location and size of the capsulorexhis (d).

behaviour is confirmed with the appearance of wrinkling, a state of minimum local strain energy,<sup>41</sup> and the immediate buckling of the pre-cataract capsular bag once the IOL interacts with it (see Supplemental Data).

The stiffness of the capsular bag is directly correlated with the stiffening of the zonules (a higher  $k$ ), as shown in Fig. 8.a. The long axis, which is the stretching the IOL produces to the bag, and the short axis measurements of the capsular bag were 10.4 and 10.1 mm, respectively, for a  $k = 10^{-03}$  N/mm against 10.6 and 9.4 mm for a  $k = 10^{-07}$  N/mm. The rotation is higher and the total and rexis area is lower than the mean average values when the stiffening of the zonules is lower ( $k < 5 \cdot 10^{-07}$  N/mm), which indicates that the boundary conditions of the capsular bag might not be correct under these values.

As expected, the long axis is lower when the capsular bag is stiffer (see Fig8.b) and when the capsular bag diameter is lower (see Fig8.c). The IOL exerts more resistance for higher compression diameters, and thus, the change in the long axis versus the initial capsular bag diameter is higher, 0.5 mm (10.2 - 9.7 mm) for the short diameter against 0.4 mm for the large diameter (10.8 - 10.4 mm).

The size of the capsulorexis influences the stiffness of the capsular bag, as reflected in the long axis for case #A (with a capsulorexis diameter of 4.5 mm) and 10.5 mm and for case #B and 10.6 mm (a capsulorexis diameter of 6.0 mm). The capsulorexis location has a slight effect on the short axis and the Tip-to-Tip measure of the IOL; however, it does not seem to have an effect on the long axis, which is the most important outcome of biomechanical stability of the postcataract capsular bag.

#### 4. Discussion

The power of FE models is unlimited, as it can deepen our understanding in complex biological processes. In this vein, this study aimed to develop a numerical tool that predicted the IOL biomechanical stability inside the postcataract capsular bag, which is directly related through optomechanical biomarkers to the visual quality of the patient.<sup>6</sup>

The accuracy of the proposed FE model was demonstrated by comparing the results obtained with those in vitro<sup>16</sup> in the short-term prior to suffering any possible postsurgery perturbations (i.e. fusion footprint). To validate the FE model, the following responses were analysed: the long axis and short axis of the capsular bag, which are the stretching diameter due to the IOL stiffness and the contraction of the capsular bag perpendicular to the haptics, respectively; the Tip-to-Tip and Notch-to-Notch distances of the LUCIA IOL, as Wormstone et al.<sup>16</sup> measured; and the total area of the capsular bag and capsulorexis. Our results lied within the experimental deviation.<sup>16</sup> Furthermore, the IOL optical performance was evaluated through optomechanical biomarkers: the axial displacement, the decentration, the tilt and the rotation of the IOL optics. The IOL optical performance was adequate for all IOLs under investigation.

These optomechanical biomarkers also presented a good correlation between the presented FE model and the

standard compression tests for the same compression diameter.<sup>6</sup> POD FT and AT LISA were also correlated with the compression standard tests (see Supplemental Data).

The fusion footprint does not seem to affect the biomechanical stability of the LUCIA IOL. While not all results were significant, the overall direction of the results *in vitro*<sup>16</sup> and *in silico* showed good correlation: the short axis decreased  $3.92 \pm 0.50$  % against 2.92% *in silico*; the total capsular bag reduced in area by  $4.26 \pm 0.45$ % versus 2.33 % numerically; the capsulorexhis reduced in size by  $2.45 \pm 0.50$ %, while it increased 8.02 % *in silico*. This could be both the proliferation of cells that was not considered in the FE model and the view of the capsulorexhis. In the FE model, the capsulorexhis size is constant throughout the simulation. However, as this size is measured in a horizontal plane, the measurement can be different as a function of the anterior surface shape of the capsular bag; Finally, as the angle of contact is a subjective measurement, we obtained the contact area, provided objectively by the FE software. A higher angle of contact was reported *in vitro*, as occurs numerically with the contact area. The haptic designs suffered mechanical perturbations, but these were not noticeable enough to produce significant changes in biomechanical stability. More experimental evidence and other IOL designs are needed to state that the fusion footprint barely affects biomechanical stability.

Once the FE model was developed, three worldwide IOL designs, LUCIA IOL, POD FT IOL and AT LISA IOL, were analysed. Although the capsular bag is stiffer than the hydrophilic acrylate (see Supplemental Data), the stiff design AT LISA was barely compressed, largely deforming the bag. The LUCIA IOL was completely adapted to the capsular bag, while the POD FT seems to be a mixed design between both designs. The axial displacement presented for the POD FT and AT LISA IOLs seems to occur *in vivo* for stiff designs, in particular for the AR40e IOL (Johnson & Johnson, USA), which has PMMA haptics.<sup>18</sup> The values of tilt, rotation, or decentration for all IOLs were of little relevance in clinical practice, but it could be particularly observed that the LUCIA IOL is more prone to rotate than the other designs. This trend was confirmed *in vivo*.<sup>17,20,21</sup> Greater rotational stability is reported for plate designs over C-loop designs,<sup>17,22</sup> while Remon et al.<sup>20</sup> showed that POD FT IOL barely presents rotation one day and three months after cataract surgery, as *in silico*.

This study also aimed to analyse the influence of several aspects on the biomechanical stability of the IOL inside the capsular bag: the initial geometry of the postcataract capsular bag; the stiffness of the zonules; the mechanical properties of the capsular bag; the capsular bag diameter; and the size and location of the capsulorexhis. Similar to Cornaggia et al.,<sup>14</sup> we observed that the size and location of capsulorhexis has little effect on IOL decentration and tilt following standard cataract surgery. Nevertheless, analysing other responses, such as the long and short axes produced by the IOL in the capsular bag, we provided compelling evidence that the capsulorexhis size influences the stiffness of the capsular bag and thus the final configuration of the IOL and the visual quality of the patient. We also observed that

the capsular bag diameter presents a higher relevance in the postcataract capsular bag stiffness. For numerical models, it is not necessary to know the exact shape of the anterior and posterior capsular bag surface, as their influence in the capsular bag deformation is limited.

The main limitation of the study is that the FE model could only be accurately compared with an in vitro model. More experimental measures and innovative pre- and post-operative methods are needed to polish the proposed FE model (i.e. adding the aqueous and vitreous humour). Overall, there is a lack of data on when and why patients are not satisfied with surgery, especially in developing countries, and which sex is more prone to suffer postsurgery complications.

Another limitation is that the proposed FE model only considers biomechanical changes, which are related to the visual quality of the patient.<sup>6</sup> Further sophisticated developments could be performed in the proposed FE model to explore other relevant factors in cataract surgery, such as PCO, as some authors conducted recently in vitro<sup>16,24</sup> or late spontaneous in-the-bag intraocular lens dislocation.<sup>42</sup>

There are a wide variety of applications for the proposed FE model. Initially, it could help both manufacturers and clinicians design and select the most appropriate IOL design in the pre-design stage. In the long run, with the introduction of quality 3D quantitative imaging data,<sup>43</sup> a digital twin with customised eye models could be developed in clinical practice, helping ophthalmologists to make IOL selections according to patient criteria and thus significantly reducing the error in ELP prediction.<sup>7</sup> Finally, with further improvements that carry the simulation to a more realistic level, the proposed FE model could be an effective tool in testing new designs, such as accommodative IOLs.

## **5. Conclusion**

An exploration of the biomechanical stability of the ensemble formed by the postcataract capsular bag and the IOL was performed with the FE method. Thanks to the numerical tool, some findings were revealed: a larger capsulorexis makes the postcataract capsular bag more flexible; the shape of the anterior and posterior surface curvature of the capsular bag barely affects the stiffness of the bag, which could be a help for designing new numerical models; and regarding IOL designs, C-loop designs are intended to adjust their haptics to the equatorial capsular diameter against as plate designs, stiffer ones, which are prone to deform largely the bag.

## **6. Acknowledgements**

The authors gratefully acknowledge research support from the Spanish Ministerio de ciencia, innovacion y universidades (Grant DPI2017-84047-R) and the Department of Industry and Innovation (Government of Aragon) through the research group Grant T24-20R (cofinanciado con Feder 2014-2020: Construyendo Europa desde Aragon). Part



of the work was performed by the ICTS “NANBIOSIS” specifically by the Tissue & Scaffold Characterization Unit (U13) and High Performance Computing Unit (U27), of the CIBER in Bioengineering, Biomaterials & Nanomedicine (CIBER-BBN at the University of Zaragoza). I. Cabeza-Gil was supported by PRE2018-084021.

## 7. Declaration of Competing Interest

No author has a financial or proprietary interest in any material or method mentioned.

## References

- [1] I. G., Cataract surgical devices market: Global industry trends, share, size, growth, opportunity and forecast 2020–2025., Press Release.
- [2] R. J. Olson, Cataract surgery from 1918 to the present and future—just imagine!, *American Journal of Ophthalmology* 185 (2018) 10–13. doi:10.1016/j.ajo.2017.08.020.
- [3] K. Miháltz, M. Lasta, M. Burgmüller, P. V. Vécsei-Marlovits, B. Weingessel, Comparison of two toric IOLs with different haptic design: Optical quality after 1 year, *Journal of Ophthalmology* 2018 (2018) 1–7. doi:10.1155/2018/4064369.
- [4] S. Norrby, Sources of error in intraocular lens power calculation, *Journal of Cataract and Refractive Surgery* 34 (3) (2008) 368–376. doi:10.1016/j.jcrs.2007.10.031.
- [5] S. Norrby, R. Bergman, N. Hirschall, Y. Nishi, O. Findl, Prediction of the true IOL position, *British Journal of Ophthalmology* 101 (10) (2017) 1440–1446. doi:10.1136/bjophthalmol-2016-309543.
- [6] I. Cabeza-Gil, J. Pérez-Gracia, L. Remón, B. Calvo, Effect of haptic geometry in c-loop intraocular lenses on optical quality, *Journal of the Mechanical Behavior of Biomedical Materials* 114 (2021) 104165. doi:10.1016/j.jmbbm.2020.104165.
- [7] S. Marcos, E. Martínez-Enriquez, M. Vinas, A. de Castro, C. Dorronsoro, S. P. Bang, G. Yoon, P. Artal, Simulating outcomes of cataract surgery: Important advances in ophthalmology, *Annual Review of Biomedical Engineering* 23 (1). doi:10.1146/annurev-bioeng-082420-035827.
- [8] K. B. Darcy, D. Gunn, S. Tavassoli, J. Sparrow, J. X. Kane, Assessment of the accuracy of new and updated intraocular lens power calculation formulas in 10930 eyes from the UK national health service, *Journal of Cataract & Refractive Surgery* 46:1 (2020) 2–7.
- [9] H. Fukumitsu, V. J. Camps, S. Miraflores, D. P. Piñero, Could anatomical changes occurring with cataract surgery have a clinically significant effect on effective intraocular lens position?, *International Ophthalmology* doi:10.1007/s10792-021-01751-y.
- [10] BS EN ISO 11979-3:2012, Ophthalmic implants. Intraocular lenses. Mechanical properties and test methods., BSI Standards Limited, 2012.
- [11] D. Bozukova, C. Pagnouille, C. Jérôme, Biomechanical and optical properties of 2 new hydrophobic platforms for intraocular lenses., *Journal of Cataract & Refractive Surgery* 39 (9) (2013) 1404–1414. doi:10.1016/j.jcrs.2013.01.050.
- [12] S. Lane, S. Collins, K. K. Das, S. Maass, I. Thatthamla, H. Schatz, S. V. Noy, R. Jain, Evaluation of intraocular lens mechanical stability, *Journal of Cataract and Refractive Surgery* 45 (4) (2019) 501–506. doi:10.1016/j.jcrs.2018.10.043.
- [13] I. Wormstone, Y. Wormstone, A. Smith, J. Eldred, Posterior capsule opacification: What's in the bag?, *Progress in Retinal and Eye Research* (2020) 100905 doi:10.1016/j.preteyeres.2020.100905.
- [14] A. Cornaggia, L. M. Clerici, M. Felizietti, T. Rossi, A. Pandolfi, A numerical model of capsulorhexis to assess the relevance of size and position of the rhexis on the IOL decentering and tilt, *Journal of the Mechanical Behavior of Biomedical Materials* 114 (2021) 104170. doi:10.1016/j.jmbbm.2020.104170.

- [15] G. Marchini, E. Pedrotti, M. Modesti, S. Visentin, R. Tosi, Anterior segment changes during accommodation in eyes with a monofocal intraocular lens: High-frequency ultrasound study, *Journal of Cataract and Refractive Surgery* 34 (6) (2008) 949–956. doi:10.1016/j.jcrs.2008.02.018.
- [16] I. M. Wormstone, N. B. Damm, M. Kelp, J. A. Eldred, Assessment of intraocular lens/capsular bag biomechanical interactions following cataract surgery in a human in vitro graded culture capsular bag model, *Experimental Eye Research* 205 (2021) 108487. doi:10.1016/j.exer.2021.108487.
- [17] C. Patel, S. Ormonde, P. H. Rosen, A. J. Bron, Postoperative intraocular lens rotation, *Ophthalmology* 106 (11) (1999) 2190–2196. doi:10.1016/s0161-6420(99)90504-3.
- [18] C. Koepl, O. Findl, K. Kriechbaum, S. Sacu, W. Drexler, Change in IOL position and capsular bag size with an angulated intraocular lens early after cataract surgery, *Journal of Cataract and Refractive Surgery* 31 (2) (2005) 348–353. doi:10.1016/j.jcrs.2004.04.063.
- [19] J. F. Alfonso, L. Fernández-Vega, A. Señaris, R. Montés-Micó, Prospective study of the acri.LISA bifocal intraocular lens, *Journal of Cataract and Refractive Surgery* 33 (11) (2007) 1930–1935. doi:10.1016/j.jcrs.2007.06.067.
- [20] L. Remón, I. Cabeza-Gil, B. Calvo, F. Poyales, N. Garzón, Biomechanical stability of three intraocular lenses with different haptic designs: In silico and in vivo evaluation, *Journal of Refractive Surgery* 36 (9) (2020) 617–624. doi:10.3928/1081597x-20200713-02.
- [21] D. Schartmüller, L. Schwarzenbacher, E. L. Meyer, S. Schriefl, C. Leydolt, R. Menapace, Comparison of long-term rotational stability of three commonly implanted intraocular lenses, *American Journal of Ophthalmology* 220 (2020) 72–81. doi:10.1016/j.ajo.2020.07.019.
- [22] X. Zhu, J. Meng, W. He, X. Rong, Y. Lu, Comparison of the rotational stability between plate-haptic toric and c-loop haptic toric IOLs in myopic eyes, *Journal of Cataract and Refractive Surgery* 46 (10) (2020) 1353–1359. doi:10.1097/j.jcrs.0000000000000259.
- [23] J. A. Eldred, D. J. Spalton, I. M. Wormstone, An in vitro evaluation of the anew zephyr open-bag IOL in the prevention of posterior capsule opacification using a human capsular bag model, *Investigative Ophthalmology & Visual Science* 55 (11) (2014) 7057. doi:10.1167/iovs.14-15302.
- [24] A. Hillenmayer, C. M. Wertheimer, S. Kassumeh, A. von Studnitz, N. Luft, A. Ohlmann, S. Priglinger, W. J. Mayer, Evaluation of posterior capsule opacification of the alcon clareon IOL vs the alcon acrysof IOL using a human capsular bag model, *BMC Ophthalmology* 20 (1). doi:10.1186/s12886-020-01349-5.
- [25] C. C. Berggren, K. A. Ameku, R. M. Pedrigi, Altered stress field of the human lens capsule after cataract surgery, *Journal of Biomechanics* 115 (2021) 110127. doi:10.1016/j.jbiomech.2020.110127.
- [26] M. T. Cardoso, B. Feijóo, A. P. G. Castro, F. J. Ribeiro, P. R. Fernandes, Axisymmetric finite element modelling of the human lens complex under cataract surgery, *Symmetry* 13 (4) (2021) 696. doi:10.3390/sym13040696.
- [27] S. Han, C. He, K. Ma, Y. Yang, A study for lens capsule tearing during capsulotomy by finite element simulation, *Computer Methods and Programs in Biomedicine* 203 (2021) 106025. doi:10.1016/j.cmpb.2021.106025.
- [28] S. F. Han, Y. Yang, Numerical modelling to assess the tear force of human capsulotomy margin, *Computer Methods in Biomechanics and Biomedical Engineering* (2021) 1–7doi:10.1080/10255842.2021.1881495.
- [29] P. Rosales, S. Marcos, Customized computer models of eyes with intraocular lenses, *Optics Express* 15 (5) (2007) 2204. doi:10.1364/oe.15.002204.
- [30] I. Cabeza-Gil, I. Ríos-Ruiz, B. Calvo, Customised selection of the haptic design in c-loop intraocular lenses based on deep learning, *Annals of Biomedical Engineering*doi:10.1007/s10439-020-02636-4.
- [31] D. C. González, C. P. Bautista, Accuracy of a new intraocular lens power calculation method based on artificial intelligence, *Eye* 35 (2) (2020) 517–522. doi:10.1038/s41433-020-0883-3.
- [32] M. I. Mohd Tamrin, M. Z. Che Azemin, N. F. Md Noor Rudin, M. H. Mohd Salleh, M. R. Hilmi, A. A. Alwan, A. Shah, Predicting spatial

- displacement based on intraocular image design using convolution neural network – preliminary findings, *Journal of Information Systems and Digital Technologies* 3(1), 74–82.
- [33] I. Cabeza-Gil, M. Á. Ariza-Gracia, L. Remón, B. Calvo, Systematic study on the biomechanical stability of c-loop intraocular lenses: Approach to an optimal design of the haptics, *Annals of Biomedical Engineering* 48 (4) (2019) 1127–1136. doi:10.1007/s10439-019-02432-9.
- [34] S. Krag, T. T. Andreassen, Mechanical properties of the human lens capsule, *Progress in Retinal and Eye Research* 22 (6) (2003) 749–767. doi:10.1016/s1350-9462(03)00063-6.
- [35] S. Krag, T. T. Andreassen, Mechanical properties of the human posterior lens capsule, *Investig Ophthalmol Vis Sci* 44 (2) (2003) 691. doi:10.1167/iovs.02-0096.
- [36] A. Vasavada, R. Singh, Relationship between lens and capsular bag size, *Journal of Cataract and Refractive Surgery* 24 (4) (1998) 547–551. doi:10.1016/s0886-3350(98)80300-3.
- [37] S. K. Pandey, L. Werner, E. M. Wilson, A. M. Izak, D. J. Apple, Capsulorhexis ovaling and capsular bag stretch after rigid and foldable intraocular lens implantation, *Journal of Cataract and Refractive Surgery* 30 (10) (2004) 2183–2191. doi:10.1016/j.jcrs.2004.02.079.
- [38] R. I. Barraquer, R. Michael, R. Abreu, J. Lamarca, F. Tresserra, Human lens capsule thickness as a function of age and location along the sagittal lens perimeter, *Investig Ophthalmol Vis Sci* 47 (5) (2006) 2053. doi:10.1167/iovs.05-1002.
- [39] Y.-C. Chang, G. M. Mesquita, S. Williams, G. Gregori, F. Cabot, A. Ho, M. Ruggeri, S. H. Yoo, J.-M. Parel, F. Manns, In vivo measurement of the human crystalline lens equivalent refractive index using extended-depth OCT, *Biomedical Optics Express* 10 (2) (2019) 411. doi:10.1364/boe.10.000411.
- [40] J. B. Ale, Intraocular lens tilt and decentration: A concern for contemporary IOL designs, *Nepalese Journal of Ophthalmology* 3 (1) (2011) 68–77. doi:10.3126/nepjoph.v3i1.4281.
- [41] X. F. Wang, Q. S. Yang, S. seong Law, Wrinkled membrane element based on the wrinkling potential, *International Journal of Solids and Structures* 51 (21-22) (2014) 3532–3548. doi:10.1016/j.ijsolstr.2014.06.004.
- [42] J. Bisevac, N. S. Anisimova, R. Nagymihály, O. Kristianslund, K. Katta, A. Noer, I. H. Sharafetdinov, L. Drolsum, M. C. Moe, B. E. Malyugin, G. Petrovski, Long-term myofibroblast persistence in the capsular bag contributes to the late spontaneous in-the-bag intraocular lens dislocation, *Scientific Reports* 10 (1). doi:10.1038/s41598-020-77207-7.
- [43] S. Ortiz, P. Pérez-Merino, S. Durán, M. Velasco-Ocana, J. Birkenfeld, A. de Castro, I. Jiménez-Alfaro, S. Marcos, Full OCT anterior segment biometry: an application in cataract surgery, *Biomedical Optics Express* 4 (3) (2013) 387. doi:10.1364/boe.4.000387.



## Chapter 4

# Evaluation of IOL delivery during Cataract Surgery

This chapter contains only this work **Cabeza-Gil et al. Experimental evaluation of the injection force exerted in intraocular lens delivery with syringe-type injectors [8]**, which evaluates experimentally the influence of the IOL haptic design, the IOL thickest area and the IOL material in the force exerted during IOL delivery.

### 4.1 Work 9: Experimental evaluation of the injection force exerted in intraocular lens delivery with syringe-type injectors



Cabeza-Gil I., Ríos-Ruiz I., Calvo B.  
Journal of the Mechanical Behavior of Biomedical Materials  
JIF (2020) = 3.90 (Q2: 32/89 Biomedical Engineering)  
SJR (2020) = 0.86 (Q2: 69/232 Biomedical Engineering)



Contents lists available at ScienceDirect

Journal of the Mechanical Behavior of Biomedical Materials

journal homepage: [www.elsevier.com/locate/jmbbm](http://www.elsevier.com/locate/jmbbm)

Research paper

## Experimental evaluation of the injection force exerted in intraocular lens delivery with syringe-type injectors

I. Cabeza-Gil<sup>a</sup>, I. Ríos-Ruiz<sup>a,\*</sup>, B. Calvo<sup>a,b</sup><sup>a</sup> Aragón Institute of Engineering Research (I3A), University of Zaragoza, Spain<sup>b</sup> Centro de Investigación Biomédica en Red en Bioingeniería, Biomateriales y Nanomedicina (CIBER-BBN), Spain

## ARTICLE INFO

## Keywords:

Cataract surgery  
Hydrophobic and hydrophilic acrylate  
IOL material  
IOL haptic design

## ABSTRACT

The process of intraocular lens (IOL) delivery within the capsular bag during cataract surgery is crucial, as the integrity of the IOL, the injector and the ocular structures should be preserved at all times. This study aims to obtain the main parameters that affect the injection force exerted in the ejection of an intraocular lens (IOL) through syringe-type injectors. For that purpose, ejection tests were carried out in vitro, measuring the resistance force throughout the entire delivery process. The effect of IOL material, haptic design, IOL thickest area and ophthalmic viscosurgical device (OVD) was studied by ejecting seven IOLs with four syringe-type injectors of different sizes, 3.0, 2.2 and 1.8 mm. In all injectors, plate hydrophilic IOLs present the lowest resistance forces; hydrated C-loop hydrophobic IOLs present higher forces and the C-loop hydrophobic IOL in dry conditions presents the highest resistance forces. All IOLs could be properly delivered with an injector size of 2.2 mm, making injector sizes of 3.0 mm outdated. The injector size of 1.8 mm damaged several IOLs. IOL material and cartridge nozzle size were the most influential parameters in IOL delivery. IOL thickest area was also relevant but in a lesser extent whereas IOL haptic design was not as relevant.

## 1. Introduction

Since the implantation of the first intraocular lens (IOL) by Ridley (1952), the field of cataract surgery has been developing substantially. From the use of flexible materials with different haptic designs in the IOLs to the development of less invasive implantation devices, important advances have improved the outcome of the surgery (Rahimy et al., 2013; Cabeza-Gil et al., 2019; Remón et al., 2020; Ang et al., 2020). Nowadays, one of the main goals of cataract surgery is focused on the incisions, their size and location (Beltrame et al., 2002; Elkady et al., 2009), in order to reduce the risk of suffering post-surgery complications, like an infection from contamination (Nagaki et al., 2003), and assure a faster recovery (Dewey et al., 2014). This aim has promoted the development of new soft materials for the IOL, such as hydrophobic and hydrophilic acrylate, together with the availability of innovative surgical instruments as injectors and new foldable IOL designs (Kodjikian et al., 2006).

Incision damage has been studied to depend on injection speed and type (Ouchi, 2012; Allen et al., 2012). Currently, the most common injector types are syringe and screw. The latter allows a constant insertion speed, avoiding abrupt alterations in the delivery. However, its mechanism requires the use of both hands. In contrast, syringe-type injectors can be operated using only one hand, allowing surgeons to

use the other hand to secure and stabilize the eye. The main limitation of this design is that the force applied by the IOL delivery system needs to be manually controlled and carefully balanced in order to minimize possible complications in the cornea of the patient, by damaging the IOL or the injection system in the delivery.

The main findings in literature focus on how the geometry of the injector affects the corneal incision (Kohnen and Klaproth, 2008; Nanavaty and Kubrak-Kisza, 2017; Arboleda et al., 2019; Haldipurkar et al., 2020). In terms of surgical outcomes, the insertion of the IOLs causes enlargement of all corneal incision wounds (Kohnen and Klaproth, 2008; Arboleda et al., 2019; Haldipurkar et al., 2020). Nevertheless, fast-speed IOL insertion, newer motorized injectors and new injector designs have been shown to decrease the amount of wound enlargement caused by IOL insertion (Ouchi, 2012; Allen et al., 2012; Khokhar et al., 2014; Tataru et al., 2015; Wang et al., 2016; Yamakawa et al., 2017). Their most significant differences are the size of the nozzle, the shape of the silicone cushion and the design of the lens cartridge, which has shown to influence IOL ejection (Kleinmann, 2005; Marcovich, 2006). Furthermore, Kleinmann and Kleinmann (2014) designed a finite element (FE) model for comparing stress induced on corneal incisions during IOL implantation. However, to the best of our knowledge, only two studies have evaluated the resistance force exerted

\* Correspondence to: Edificio Betancourt, Universidad de Zaragoza, Calle María de Luna, 3, 50018 Zaragoza, Spain.  
E-mail address: [itziar@unizar.es](mailto:itziar@unizar.es) (I. Ríos-Ruiz).

<https://doi.org/10.1016/j.jmbbm.2021.104793>

Received 23 April 2021; Received in revised form 20 August 2021; Accepted 22 August 2021

Available online 30 August 2021

1751-6161/© 2021 The Authors.

Published by Elsevier Ltd.

This is an open access article under the CC BY-NC-ND license

(<http://creativecommons.org/licenses/by-nc-nd/4.0/>).

by the IOL delivery system (Bozukova et al., 2013; Usui and Tanaka, 2015). Bozukova et al. (2013) reported the maximum force needed to inject 13 different IOLs in the ACCUJECT™ 2.2-1P syringe-type injector, whereas Usui and Tanaka (2015) evaluated several IOL deliveries using 5 different syringe-type injectors. This resistance force is an interesting in vitro marker, as high or unbalanced forces can lead to damage in the IOL and poor surgery outcome.

This study was aimed to analyze the effect of IOL material, haptic design and IOL thickest area, as well as the dimensions and shape of the syringe-type injection system, in the resistance force exerted in IOL delivery for cataract surgery. The influence of the ophthalmic viscosurgical device (OVD) (Bissen-Miyajima, 2008) was also studied by conducting tests with three different viscoelastic solutions.

## 2. Material & methods

### 2.1. Materials

The injection devices chosen for all the experiments of this study were the ACCUJECT™ 3.0-1P, 2.2-1P, VISCOJECT™-BIO 2.2 (Medicel, Switzerland) and BLUEMIXS®180 (Carl Zeiss Meditec AG, Germany), four syringe-type injectors shown in Fig. 1. Seven different IOLs were ejected in these injectors, see Fig. 2, and the resistance force exerted by the system was measured.

Three hydrophilic IOL plate designs were tested, AT LISA (Carl Zeiss Meditec AG, Germany), Y60 and LIOCAN (AJL Ophthalmic, Spain). The AT LISA and Y60 models are quite similar in many ways: their haptic design, overall diameter and thickest area, see Fig. 2. The LIOCAN model shares the same shape as Y60 but with a bigger overall diameter, 14.25 mm. Four hydrophobic IOLs were analyzed: a hydrophobic double C-loop POD F GT (PhysIOL, Beaver-Visitec International, USA), which has an overall diameter of 11.40 mm and has the lowest thickest area of all IOLs under investigation, 0.65 mm; and three different hydrophobic C-loop IOLs, two IOL prototypes that were designed in a previous work (Cabeza-Gil et al., 2020), hereinafter referred to as model #C and #D, and the AIALA model (AJL Ophthalmic, Spain), see Fig. 2. All three C-loop IOLs have different designs of the haptics, but they share the same overall diameter of 13.00 mm. Moreover, the AIALA model has a lower thickest area than models #C and #D, 0.83 mm against 1.13 mm. A priori, model #C is considered a flexible C-loop design whilst the other two are considered stiffer designs, according to their behavior in the standardized compression test ISO 11979-3 (Cabeza-Gil et al., 2019, 2020).

The optical power of all human IOLs tested was +22.0 diopters (D) while the LIOCAN, a dog-intended IOL, was +41.0 D. The optic thickness of the IOLs or its thickest area was measured with CellScale MicroTester, see Supplemental Data file for further knowledge on the technique used. All IOLs were kept submerged in a saline solution for at least 72 h before the experiments to assure they were tested in a hydrated state. Additionally, model #D was analyzed in a dry state, i.e., not having been kept submerged before the tests, as a comparison of the material behavior with and without water content. This was performed as several ophthalmology companies offer the IOL preloaded in the injector and not submerged in a saline solution.

The thickest area of the IOL is expected to have a large influence on the force exerted by the injector due to the high compression stress to which the IOL is subjected to when passing through the lens cartridge and the nozzle. For this reason, seven different AT LISA models with an optical power between 0.0 and 27.0 D, which implies a range of thickest areas from 0.29 mm to 1.23 mm, were analyzed in the BLUEMIXS®180 injector, see Table 1, the one recommended for this IOL.

In all tests, the injector was filled with an OVD, as in clinical interventions. In order to observe the influence of this viscoelastic solution, three different OVDs, AJL VISC 1.4%, AJL VISC 2.0% and AJL VISC 3.0% (AJL Ophthalmic, Spain)—percentages referring to the amount of sodium hyaluronate they contain—were tested with model #D IOL in the ACCUJECT™ 2.2-1P injector in dry conditions.

### 2.2. Experimental procedure

The tests consisted in a controlled displacement of the loading pusher of the injector, replicating the IOL injection by the ophthalmologist, while the force needed in the ejection was recorded. The loading pusher was displaced the total length of the loading pusher to assure the ejection of the IOL, i.e., 42.5 mm for injectors ACCUJECT™ 2.2-1P, 3.0-1P and BLUEMIXS®180 and 52.5 mm for injector VISCOJECT™-BIO 2.2, at a constant velocity of 4 mm/s, as supposed for clinical values (Allen et al., 2012). The IOLs were placed into their reference configuration, without bending the IOL haptics as shown in Fig. 3. A video of an IOL delivery in each injector is uploaded as Supplemental Data to help the reader understand the process of the experiments.

The resistance force exerted by the IOL delivery system was measured and recorded using an Instron 5548 Electroplus Microtester with a 50 N full-scale load cell, see Fig. 3, for all injectors under investigation. In the specific cases where 50 N were not enough to push the IOL through the nozzle, which happened only with BLUEMIXS®180 injector, a 250 N full-scale load cell was used. Finally, IOL resistance force to injection along the length of the injector was processed with MATLAB 2020a (MathWorks, USA). To compare all results, an ANOVA analysis, considering a  $p_{value} < 0.05$  as significant, was performed.

All experiments were conducted at a temperature of  $23.5 \pm 1$  °C and a relative humidity of 28%. This setting is based on the conditions in the operating room. A minimum of three tests were conducted for each testing condition.

### 2.3. Study design

The stages followed in this study are here described. Firstly, the effect on the resistance force in IOL delivery of the composition of the OVD was evaluated testing three different OVDs, AJL VISC 1.4%, AJL VISC 2.0% and AJL VISC 3.0%, with injector ACCUJECT™ 2.2-1P and model #D in dry conditions.

Secondly, the effect of the IOL and the size of the injector was analyzed. To do so, every IOL under investigation was ejected in all four injectors and the resistance force of the delivery was recorded. Fig. 2 shows all the IOLs that were ejected and Fig. 1 shows all the injectors used in the study. All tests were carried out using AJL VISC 1.4%. In order to isolate the effect of the IOL, control cases of all injectors were previously performed. These tests consisted in the ejection of the system without any IOL, allowing to observe the forces exerted intrinsically by the injectors. These tests were conducted for 2.50 mm more than the ejection tests, at the same constant speed of 4 mm/s, to monitor the force exerted by the injector itself, which is that of the silicone cushion passing through the cartridge.

Thirdly, in order to compare the effect of the material exclusively, hydrophobic and hydrophilic acrylate, two lenses without the haptics (only the spherical optic part) with the same optical power, +22.0 D, and therefore thickest area, but different materials were analyzed in the ACCUJECT™ 2.2-1P injector. In this test, the effect of the haptic geometry of the IOL is subtracted. Thus, it can also serve as control test for the effect of the haptics in the delivery system.

Finally, the effect of the thickest area of the IOL, which is highly correlated with IOL optical power, was analyzed. For that purpose, all AT LISA IOLs described in Table 1 were tested in the BLUEMIXS®180 injector.

## 3. Results

For a better understanding of the IOL delivery process, Fig. 4 shows an example curve of the force exerted by the IOL delivery system to describe the most important regions throughout the delivery process. As example, the resistance force of the Y60 IOL ejected by the ACCUJECT™ 2.2-1P syringe-type injector is shown. The shape of this graph has been assured throughout the research to be representative of any IOL ejected







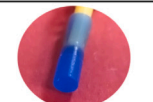


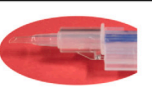
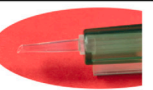
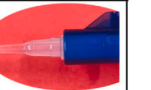
Injector model				
	ACCUJECT™	ACCUJECT™	VISCOJECT™	BLUEMIXS®
Incision size (mm)	3.0	2.2	2.2	1.8
Silicone cushion				
Lens cartridge				

Fig. 1. The syringe-type injectors ACCUJECT™ 3.0-1P, ACCUJECT™ 2.2-1P, VISCOJECT™-BIO 2.2 and BLUEMIXS®180 and their main characteristics are shown. All injectors share the same silicone cushion, except for that of VISCOJECT™-BIO 2.2, which has a rounder shape. The shape of the silicone cushion is the same as the shape of the nozzle.








IOL model							
	AT LISA	Y60	LIOCAN	POD F GF	AIALA	Model #C	Model #D
Acrylate Material	Hydrophilic	Hydrophilic	Hydrophilic	Hydrophobic	Hydrophobic	Hydrophobic	Hydrophobic
IOL type	Plate	Plate	Plate	Double C-loop	C-loop	C-loop	C-loop
Thickest area (mm)	1.16 ± 0.02	1.02 ± 0.03	1.30 ± 0.03	0.65 ± 0.01	0.83 ± 0.05	1.13 ± 0.11	1.13 ± 0.11
Overall diameter (mm)	11.00	10.75	14.25	11.40	13.00	13.00	13.00

Fig. 2. All the IOL models analyzed in the study. The material, the haptic design and the overall diameter of each IOL are shown. Moreover, the thickest area, which is the maximum optic thickness, was measured since it is expected to be a relevant factor in the resistance force in the IOL delivery system. The optic diameter of all IOLs under investigation is 6.00 mm, except for the LIOCAN model, which is 6.50 mm.

Table 1

Diopters and thickest area (mm) of the different AT LISA IOLs tested in the BLUEMIXS®180 injector to evaluate the influence of the thickest area in ejection force.

AT LISA Power (D)	+0.0	+3.5	+8.0	+12.5	+18.0	+22.0	+27.0
Thickest area (mm)	0.29 ± 0.02	0.48 ± 0.02	0.61 ± 0.02	0.74 ± 0.02	0.98 ± 0.02	1.16 ± 0.02	1.27 ± 0.02

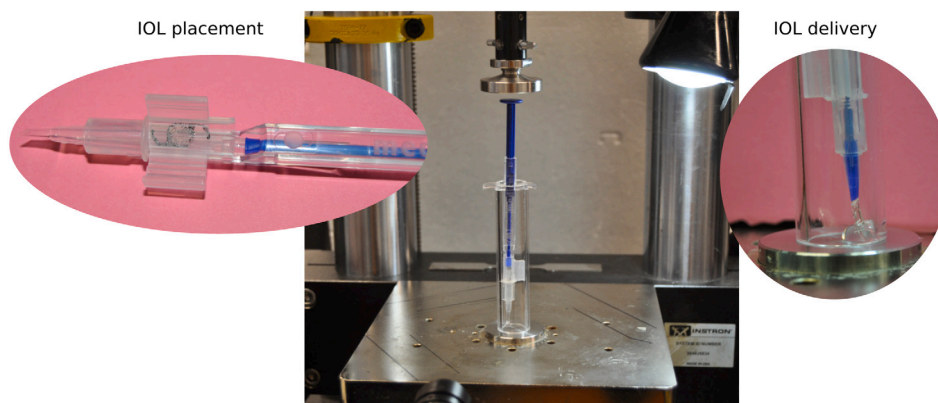


Fig. 3. IOL delivery system using an Instron 5548 Electropuls Microtester. A methacrylate tube was designed to place and fix the injector during IOL delivery. Figure shows the placement of the IOL on the left and the process of delivery on the right.

in a syringe-type injector. Four key regions can be highlighted in the graph. Firstly, a peak force that appears approximately 9 mm after starting to push the injector corresponds to the initial contact of the loading pusher with the IOL. Subsequently, the IOL starts being dragged and the applied force increases as the IOL and silicone cushion are inserted into the lens cartridge. This occurs while the displacement of the loading pusher is between 15 and 30 mm. Once they are in, the force applied decreases gradually, as there are no abrupt changes in

the cross-sectional area of the nozzle. At around 30 mm of displacement of the loading pusher, the IOL reaches the tip of the injector, the narrowest part of the nozzle, and for the next 8 mm the force significantly increases as the IOL is driven out. This is the part of the IOL delivery where the resistance force is the highest (not counting the subsequent silicone cushion delivery) and thus, this is the force that will be compared among all cases. It is also the most important part of the delivery, as it is mostly at this moment when the IOL can be



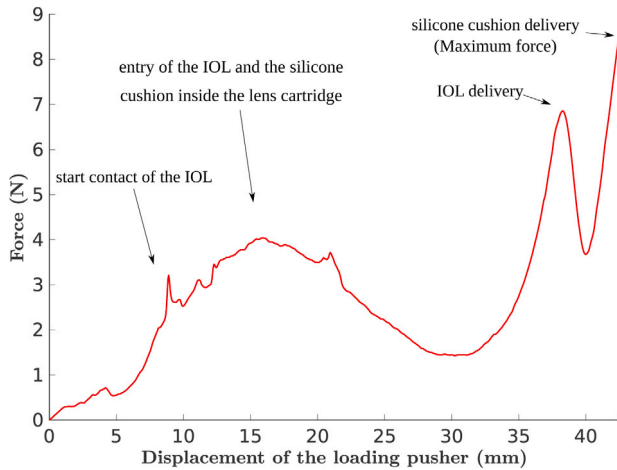


Fig. 4. Description of the IOL delivery process. Resistance force of the Y60 IOL through the ACCUJECT™ 2.2-1P injector. All syringe-type injectors under investigation follow the same pattern in the resistance force exerted.

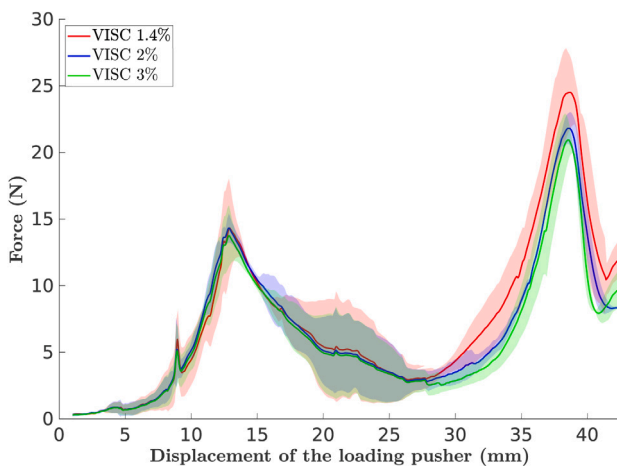


Fig. 5. Study of the effect of OVD composition in IOL delivery (model #D in dry conditions) by means of the resistance force using three different sodium hyaluronate concentrations, AJL visc 1.4% (red), AJL visc 2% (blue) and AJL visc 3% (green). All cases were reproduced three times ( $n = 3$ ).

damaged or erratically delivered. The process of IOL delivery would already be finished by this point. However, for this example graph, the following displacement of the silicone cushion through the tip and its eventual ejection are shown. It can be noted that the ejection force rises considerably, even more than for the IOL delivery, as the cushion is wider and less lubricated. In the following graphs, except for the control cases, the delivery of the cushion has been removed as it has no clinical interest.

### 3.1. Effect of OVD

The three different OVDs object of this study were compared by means of ejecting model #D in dry conditions with ACCUJECT™ 2.2-1P injector, see Fig. 5. It seems that the higher the sodium hyaluronate concentration, the lower the force exerted by the IOL delivery system. However, there is no statistically significant difference in the maximum resistance force ( $p_{value} > 0.05$ ) among the different viscoelastic solutions. From these results, the remaining tests were decided to be carried out with the AJL VISC 1.4%.

### 3.2. Effect of IOL delivery and injector size

Before testing the lenses on both injectors, a control assay, i.e., without any IOL, was performed to evaluate the resistance force exerted by each injector itself, see Fig. 6A. The maximum force obtained at the end of the pusher displacement and the resistance force when the IOL would be driven out – at around 30 mm as commented above – are shown in Table 2.

The comparison between the forces exerted by the different IOLs under investigation for the ACCUJECT™ 3.0-1P is presented in Fig. 6B and Table 3. All cases can be differentiated into 4 groups, regarding the force exerted by the ejection of the IOL, that match the differences in IOL material and IOL thickest area: model #D (dry), which unsurprisingly presented the highest force exerted,  $15.78 \pm 2.00$  N; models #D (submerged) and #C, two C-loop hydrophobic designs, presented an average of force 7.19 and 7.76 N; the models AIALA and POD F GF, hydrophobic designs with a lower thickest area, presented a slightly lower average force than models #D (submerged) and #C, 4.82 and 4.84 N; and the hydrophilic plate designs, AT LISA, Y60 and LIOCAN, presented the lowest average force of 3.51, 3.71 and 2.68 N, respectively. For graphical purposes and due to their similar behavior with models #D and AT LISA, respectively, models #C and Y60 are not plotted in Fig. 6. Their graphs can be observed in the Supplemental Data file.

Fig. 6C and D show the force exerted by the IOLs under investigation when ejected by the injector ACCUJECT™ 2.2-1P and VISCOJECT™-BIO 2.2. Again, the same trend referring to the difference in behavior according to IOL material and IOL thickest area was observed. The maximum forces and their corresponding deviations for each IOL are gathered in Table 3.

Fig. 6E shows the force exerted by model #D (submerged), POD F GF and AT LISA when ejected by the BLUEMIXS®180. The other IOLs are not included as they were macroscopically damaged in the delivery process. The same trend as in the other injectors is obtained. However, the average forces are notably higher. Model #D (submerged) presented the highest force,  $78.29 \pm 14.67$  N, followed by the POD F GF IOL, with  $36.78 \pm 1.96$  N and finally by the AT LISA IOL,  $25.88 \pm 2.02$  N. The resistance force in the IOL delivery process for the damaged IOLs is presented in the Supplemental Data file.

### 3.3. Effect of IOL material: delivery of the optic part

In order to verify the influence of the material, the hydrophobic and hydrophilic acrylic material under in vivo conditions (hydrated) were compared in the ACCUJECT™ 2.2-1P injector. The haptics were carefully removed from the IOLs to test only the optic of +22.0 diopters and same diameter (6 mm), subtracting the effect of the geometry. Fig. 7A shows the resistance force for the two optics with different materials. The maximum resistance force for the hydrophobic acrylate is considerably higher,  $14.29 \pm 2.47$  N, compared to the maximum resistance force for the hydrophilic acrylate (HEMA),  $5.83 \pm 1.83$  N.

### 3.4. Effect of IOL thickest area

Lastly, the influence of the thickest area of the IOLs was analyzed by means of testing AT LISA IOLs with an optical power range between 0.0 and 27.0 D in the BLUEMIXS®180 injector, see Fig. 7B. For graphical purposes, some IOLs have not been plotted, see Supplemental Data file. The IOL barely exerted resistance force up to an IOL optical power of 8.0 D, which corresponds to a thickest area of 0.61 mm, see Table 1. With this IOL, the maximum force was  $17.83 \pm 2.93$  N. A similar resistance force was obtained for the IOL with an optical power of 12.5 D and 0.74 mm of thickest area. The following significant change is for the IOL of 18.0 D, 0.98 mm of thickest area, with a maximum force of  $22.74 \pm 1.93$  N. Finally, a similar resistance force was obtained for the IOLs with 22.0 and 27.0 D, 1.16 and 1.27 mm in thickest area respectively, of  $25.82 \pm 3.14$  N.

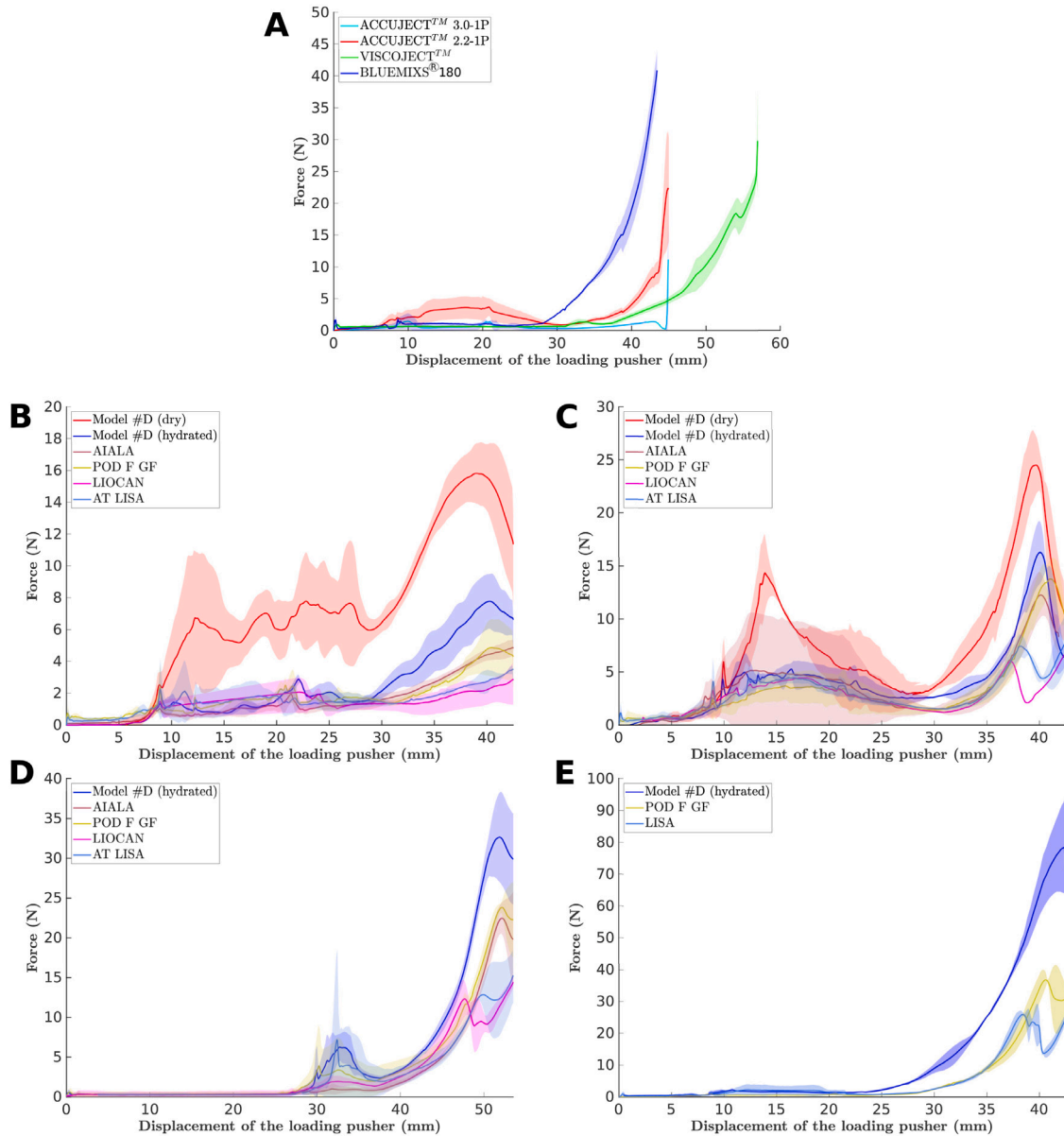


**Fig. 6.** A. Resistance force (N) of the four syringe-type injectors under investigation, the ACCUJECT™ 3.0-1P and 2.2-1P, the VISCOJECT™ and the BLUEMIXS®180, without the ejection of an IOL (n = 5 for all cases). IOLs delivery in the ACCUJECT™ 3.0-1P injector B., in the ACCUJECT™ 2.2-1P injector, C. in the VISCOJECT™ 2.2 injector, D., and in the BLUEMIXS®180, E., for the different IOLs analyzed: model #D dry (n = 6) and hydrated (n = 5), model #C (n = 5), AIALA (n = 5), AT LISA (n = 5), Y60 (n = 5) and LIOCAN (n = 6). Some videos of the IOL delivery process for each injector under investigation are uploaded as Supplemental Data.

**Table 2**

Maximum force (N) exerted by the injector itself and the resistance force of each injector when the IOL would be driven out for the four syringe-type injectors under investigation.

	ACCUJECT™ 3.0-1P	ACCUJECT™ 2.2-1P	VISCOJECT™	BLUEMIXS®180
Maximum force	11.16 ± 7.16	22.24 ± 8.18	29.24 ± 7.45	40.49 ± 3.62
Contributed force in IOL delivery	0.85 ± 0.11	2.95 ± 0.58	9.20 ± 2.63	14.71 ± 1.86

**4. Discussion**

The resistance force exerted by an IOL injection system is an interesting in vitro marker for comparing the mechanical effect of material, geometry and injection device in the delivery of the IOL. It can give an insight in the adequacy of certain conditions, considering that high resistance forces are undesirable as they can damage the IOL or the delivery system during implantation, as well as complicate a controlled and balanced ejection. Therefore, in this study, the force needed to deliver IOLs with different conditions and in different injectors was

obtained and compared, in order to evaluate the effect of geometry, optical power (related to the IOL thickest area) and material of the IOL, as well as injector size, in the delivery.

This study has obtained clear evidence of the influence of IOL material, nozzle diameter of the injector and IOL thickest area in the IOL delivery process. The importance of a proper hydration of the IOLs has also been proven by testing the same C-loop hydrophobic IOL, model #D, being or not hydrated before the tests. When the IOL was tested dry, the force needed to eject it was notably higher and thus, the chances of IOL damaging increased significantly, see Fig. 6,

**Table 3**

Maximum force (N) applied for each IOL and injector under investigation. The force expressed in the Table is the peak force when the IOL is driven out.

	ACCUJECT™ 3.0-1P	ACCUJECT™ 2.2-1P	VISCOJECT™-BIO 2.2	BLUEMIXS®180
Model #D (dry)	15.78 ± 2.00	24.48 ± 3.19	Damaged	–
Model #D (submerged)	7.76 ± 1.74	16.26 ± 3.01	32.89 ± 5.49	78.29 ± 14.67
Model #C	7.19 ± 1.44	15.55 ± 1.55	34.38 ± 3.02	–
AIALA	4.82 ± 0.53	12.25 ± 2.05	22.45 ± 1.97	Damaged
POD F GF	4.84 ± 1.76	13.79 ± 1.81	23.82 ± 1.01	36.78 ± 1.96
AT LISA	3.51 ± 0.27	7.42 ± 1.00	12.78 ± 0.96	25.88 ± 2.02
Y60	3.71 ± 1.25	6.52 ± 0.95	14.03 ± 4.14	Damaged
LIOCAN	2.68 ± 1.22	6.00 ± 0.91	12.26 ± 2.46	Damaged

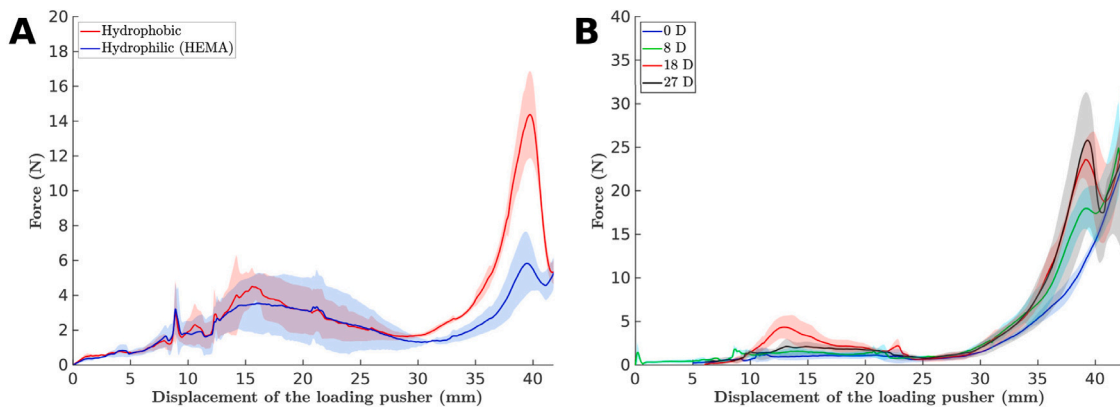


**Fig. 7.** A. Comparative between the delivery of the optic part of the IOL (+22.0 D, without the haptics) for hydrophobic and hydrophilic acrylate. All cases were reproduced three times ( $n = 3$ ). B. Resistance force for several AT LISA IOLs with a different optical power range [0.0 – 27.0 D], which is related to IOL thickest area ( $n = 5$  for all tests conducted).

which in fact happened with some injectors, see [Table 3](#). The resistance forces obtained could be differentiated into 4 groups, depending on the state or type of material of the IOLs and the IOL thickest area: model #D, hydrophobic acrylate in dry state, which presented the highest resistance force; models #D and #C; POD F GF and AIALA IOLs, all hydrophobic acrylate in hydrated state; and AT LISA, Y60 and LIOCAN, all hydrophilic acrylate plate designs in hydrated state, which presented the lowest resistance forces. The same trend was confirmed for all injectors under investigation, ACCUJECT™ 2.2-1P, 3.0-1P, VISCOJECT™-BIO 2.2 and BLUEMIXS®180, see [Fig. 6](#). These behaviors lead to the conclusion that the hydrophobic acrylate has different mechanical properties in the dry and hydrated state. Further material tests can be carried out to confirm this conclusion. Additionally, the effect of IOL material was verified testing the same optics, one made of hydrophobic and the other of hydrophilic acrylate. These tests confirmed the high effect of the material in the resistance force, as the hydrophobic optic produced a force of 14.29 N, more than twice as much as the hydrophilic one, which resulted in 5.83 N. These results were similar to the forces obtained in the tests of the IOLs with the same material and optics, models #C and #D submerged and Y60, respectively.

Therefore, it could be said that haptic design barely influences the force exerted, see [Fig. 6](#), and [Fig. 7A](#). This can be explained considering that the force required to push the IOL through the cartridge depends on the relationship between the diameter of the cartridge nozzle and the volume of the IOL in its thickest area. Since the haptics are not a part of the thickest area of the IOL, this explains why the IOL haptic has no relevant importance in the determination of the force required to push the IOL. This trend was also confirmed in the similarity of the resistance force exerted by models #D and #C, two different C-loop hydrophobic models, and the different plate hydrophilic designs, AT LISA and Y60, see Supplemental Data file.

As a clear verification of the influence of the thickest area of the IOLs, model AT LISA with different optical powers, and thus different thickest area measurements, was tested in injector BLUEMIXS®180.

With these tests, the high correlation between the thickest area and the resistance force was verified, see [Fig. 7B](#).

In this study, few IOLs were damaged in the tests, all happening in injector BLUEMIXS®180, which has the lowest nozzle size, 1.8 mm, and model #D (dry) in injector VISCOJECT™-BIO 2.2. Only models #D (hydrated), POD F GF and AT LISA were suitable to be tested correctly in the BLUEMIXS®180 injector, see [Table 3](#). The rest of the IOLs were damaged in the delivery process with this injector. Surprisingly, the Y60 IOL, similar to AT LISA, was damaged in this injector whilst AT LISA was not. It is likely that the hydrophilic material of both lenses was not completely the same. In screening tests, which were not included in the study, some IOLs were damaged when they were misplaced in the lens cartridge. IOLs with no apparent breakage were checked in an optical microscope to observe any internal damage. It was not observed in any case.

The present study has also shown that the injector size of 3.0 mm is outdated and that even IOLs such as LIOCAN, a dog-purpose IOL, could be implanted in injectors of 2.2 mm. Moreover, observing the resistance force exerted by model #D in dry state, it is recommended for IOL manufacturers to preload the IOL in a saline solution.

The importance of the injector in the resistance force of the system can be checked when comparing the different results in [Fig. 6](#) and [Table 3](#). For injector BLUEMIXS®180, the resistance forces are higher as the diameter of the tip is smaller, resulting in a higher force to push the IOL through the nozzle. This is less desirable. However, a smaller nozzle implies a smaller incision size in the cornea ([Arboleda et al., 2019](#); [Haldipurkar et al., 2020](#); [Oshika and Wolfe, 2019](#)). Therefore, a compromise should be reached between the incision size and the proper IOL delivery. The relevance of the injector was also shown in the study of [Usui and Tanaka \(2015\)](#). In their case, the values of force range from 2 to 20 N for injector with a nozzle diameter higher than 2.2 mm, similar to the results obtained in our tests.

In this study, the same syringe-type injector as [Bozukova et al. \(2013\)](#), ACCUJECT™ 2.2-1P, was used. The resistance forces obtained for IOL ejection in this study are similar to what [Bozukova et al.](#)

obtained. However, the test method was different, as they used a loading–unloading cycle. The maximum resistance force in the control assay – the injection without any IOL – of Bozukova et al. was of 13 N against the 22.24 N obtained in this study for a displacement of the pusher of 45 mm. If the pusher in this study had been displaced only 1 mm less, the maximum resistance force would be of around 13 N. Therefore, the results can be assumed comparable.

One of the limitations of the study was that the tests were conducted in an air filled chamber instead of a fluid filled chamber that would mimic natural environment. Usui and Tanaka (2015) performed these tests in a porcine eye and in a plastic dish and they obtained that the forces in the plastic dish were slightly lower. Another limitation might be the few trials conducted per sample that could have influenced the OVD conclusion. Moreover, further investigations could study the effect of injector material, as more flexible nozzles are expected to enlarge with IOL ejection and therefore require less injection force.

This study has added some light to the effect of IOL characteristics in the delivery. The importance of a well preserved and hydrated IOL prior to use has been demonstrated. Furthermore, the minor effect of the composition of the viscoelastic solution was shown. Finally, the material of the IOL, the injector size and the IOL thickest area were key factors in the resistance force exerted by the system. When comparing to literature, the importance of the delivery device was made clear. Nevertheless, a compromise between the resistance force and the incision size must be met when selecting the adequate injector.

## 5. Conclusions

The shape of the resistance force curves throughout the entire ejection process of an IOL with a syringe-type injector is explained in this work. The IOL material is key in the IOL delivery, being the hydrophilic acrylate the one that produces smaller forces. Moreover, hydrophobic IOLs are recommended to be hydrated before implantation as dry IOLs present higher resistance forces and thus higher probability of damage. Injector sizes of 3.0 mm are outdated. No hydrated IOL was apparently damaged with an injector size of 2.2 mm.

## CRediT authorship contribution statement

**I. Cabeza-Gil:** Conceptualization, Methodology, Resources, Formal analysis, Investigation, Writing – original draft. **I. Ríos-Ruiz:** Methodology, Validation, Formal analysis, Investigation, Writing – review & editing. **B. Calvo:** Conceptualization, Validation, Resources, Supervision, Project administration, Writing – review & editing.

## Declaration of competing interest

The authors declare that they have no known competing financial interests or personal relationships that could have appeared to influence the work reported in this paper.

## Acknowledgments

The authors gratefully acknowledge research support from the Spanish Ministerio de Ciencia, Innovación y Universidades (Grant DPI2017-84047-R) and the Department of Industry and Innovation (Government of Aragon) through the research group Grant T24-20R (cofinanciado con Feder 2014-2020: Construyendo Europa desde Aragon). Part of the work was performed by the ICTS “NANBIOSIS” specifically by the Tissue & Scaffold Characterization Unit (U13), of the CIBER in Bioengineering, Biomaterials & Nanomedicine (CIBER-BBN at the University of Zaragoza). CIBER Actions are financed by the Instituto de Salud Carlos III with assistance from the European Regional Development Fund. I. Cabeza-Gil and I. Ríos-Ruiz were supported by Spanish Ministerio de Ciencia, Innovación y Universidades, through grant PRE2018-084021, and Government of Aragon, order IIU/1408/2018, respectively.

## Appendix A. Supplementary data

Supplementary material related to this article can be found online at <https://doi.org/10.1016/j.jmbbm.2021.104793>.

## References

- Allen, D., Habib, M., Steel, D., 2012. Final incision size after implantation of a hydrophobic acrylic aspheric intraocular lens: New motorized injector versus standard manual injector. *J. Cataract. Refract. Surg.* 38 (2), 249–255. <http://dx.doi.org/10.1016/j.jcrs.2011.08.038>.
- Ang, M., Gatinel, D., Reinstein, D.Z., Mertens, E., del Barrio, J.L.A., Alió, J.L., 2020. Refractive surgery beyond 2020. *Eye* <http://dx.doi.org/10.1038/s41433-020-1096-5>.
- Arboleda, A., Arrieta, E., Aguilar, M., Sotolongo, K., Nankivil, D., Parel, J., 2019. Variations in intraocular lens injector dimensions and corneal incision architecture after cataract surgery. *J. Cataract. Refract. Surg.* 45 (5), 656–661. <http://dx.doi.org/10.1016/j.jcrs.2018.10.047>.
- Beltrame, G., Salvat, M., Driussi, G., Chizzolini, M., 2002. Effect of incision size and site on corneal endothelial changes in cataract surgery. *J. Cataract. Refract. Surg.* 28 (1), 118–125. [http://dx.doi.org/10.1016/s0886-3350\(01\)00983-x](http://dx.doi.org/10.1016/s0886-3350(01)00983-x).
- Bissen-Miyajima, H., 2008. Ophthalmic viscosurgical devices. *Curr. Opin. Ophthalmol.* 19 (1), 50–54. <http://dx.doi.org/10.1097/icu.0b013e3282f14db0>.
- Bozukova, D., Pagnouille, C., Jérôme, C., 2013. Biomechanical and optical properties of 2 new hydrophobic platforms for intraocular lenses. *J. Cataract. Refract. Surg.* 39 (9), 1404–1414. <http://dx.doi.org/10.1016/j.jcrs.2013.01.050>.
- Cabeza-Gil, I., Ariza-Gracia, M.A., Remón, L., Calvo, B., 2019. Systematic study on the biomechanical stability of c-loop intraocular lenses: Approach to an optimal design of the haptics. *Ann. Biomed. Eng.* 48 (4), 1127–1136. <http://dx.doi.org/10.1007/s10439-019-02432-9>.
- Cabeza-Gil, I., Pérez-Gracia, J., Remón, L., Calvo, B., 2020. Effect of haptic geometry in C-loop intraocular lenses on optical quality. *J. Mech. Behav. Biomed. Mater.* 104165. <http://dx.doi.org/10.1016/j.jmbbm.2020.104165>.
- Dewey, S., Beiko, G., Braga-Mele, R., Nixon, D., Raviv, T., Rosenthal, K., 2014. Microincisions in cataract surgery. *J. Cataract. Refract. Surg.* 40 (9), 1549–1557. <http://dx.doi.org/10.1016/j.jcrs.2014.07.006>.
- Elkady, B., Nero, D.P., Alió, J., 2009. Corneal incision quality: Microincision cataract surgery versus microcoaxial phacoemulsification. *J. Cataract. Refract. Surg.* 35 (3), 466–474. <http://dx.doi.org/10.1016/j.jcrs.2008.11.047>.
- Haldipurkar, S., Shetty, V., Haldipurkar, T., Dhamankar, R., Sehdev, N., Khatib, Z., Nagvekar, P., Mhatre, P., Setia, M., 2020. Incision size changes after cataract surgery with intraocular lens implantation. *J. Cataract. Refract. Surg.* 46 (2), 222–227. <http://dx.doi.org/10.1097/j.jcrs.0000000000000014>.
- Khokhar, S., Sharma, R., Patil, B., Aron, N., Gupta, S., 2014. Comparison of new motorized injector vs manual injector for implantation of foldable intraocular lenses on wound integrity: an ASOCT study. *Eye* 28 (10), 1174–1178. <http://dx.doi.org/10.1038/eye.2014.162>.
- Kleinmann, G., 2005. Linear deposits on the surfaces of intraocular lenses implanted through a hexagonal cartridge which mimic scratches/cracks on the lenses. *Br. J. Ophthalmol.* 89 (11), 1474–1477. <http://dx.doi.org/10.1136/bjo.2005.071738>.
- Kleinmann, G., Kleinmann, I., 2014. Intraocular lens injector–induced stress on the corneal incisions during lens implantation. *Am. J. Ophthalmol.* 158 (1), 185–191.e1. <http://dx.doi.org/10.1016/j.ajo.2014.03.001>.
- Kodjikian, L., Beby, F., Rabilloud, M., Bruslea, D., Halphen, I., Fleury, J., Grange, J.-D., Garweg, J.G., 2006. Influence of intraocular lens material on the development of acute endophthalmitis after cataract surgery? *Eye* 22 (2), 184–193. <http://dx.doi.org/10.1038/sj.eye.6702544>.
- Kohnen, T., Klaproth, O., 2008. Incision sizes before and after implantation of SN60wf intraocular lenses using the monarch injector system with c and d cartridges. *J. Cataract. Refract. Surg.* 34 (10), 1748–1753. <http://dx.doi.org/10.1016/j.jcrs.2008.06.031>.
- Marcovich, A.L., 2006. The course of surface deposits on a hydrophilic acrylic intraocular lens after implantation through a hexagonal cartridge. *Br. J. Ophthalmol.* 90 (10), 1249–1251. <http://dx.doi.org/10.1136/bjo.2006.097857>.
- Nagaki, Y., Hayasaka, S., Kadoi, C., Matsumoto, M., Yanagisawa, S., Watanabe, K., Watanabe, K., Hayasaka, Y., Ikeda, N., Sato, S., Kataoka, Y., Togashi, M., Abe, T., 2003. Bacterial endophthalmitis after small-incision cataract surgery. *J. Cataract. Refract. Surg.* 29 (1), 20–26. [http://dx.doi.org/10.1016/s0886-3350\(02\)01483-9](http://dx.doi.org/10.1016/s0886-3350(02)01483-9).
- Nanavaty, M., Kubrak-Kisza, M., 2017. Evaluation of preloaded intraocular lens injection systems: Ex vivo study. *J. Cataract. Refract. Surg.* 43 (4), 558–563. <http://dx.doi.org/10.1016/j.jcrs.2017.02.019>.
- Oshika, T., Wolfe, P., 2019. In vitro comparison of delivery performance of 4 preloaded intraocular lens injector systems for corneal and sclerocorneal incisions. *J. Cataract. Refract. Surg.* 45 (6), 840–846. <http://dx.doi.org/10.1016/j.jcrs.2018.10.050>.
- Ouchi, M., 2012. Effect of intraocular lens insertion speed on surgical wound structure. *J. Cataract. Refract. Surg.* 38 (10), 1771–1776. <http://dx.doi.org/10.1016/j.jcrs.2012.06.031>.

- Rahimy, E., Wilson, J., Tsao, T.-C., Schwartz, S., Hubschman, J.-P., 2013. Robot-assisted intraocular surgery: development of the IRISS and feasibility studies in an animal model. *Eye* 27 (8), 972–978. <http://dx.doi.org/10.1038/eye.2013.105>.
- Remón, L., Cabeza-Gil, I., Calvo, B., Poyales, F., Garzón, N., 2020. Biomechanical stability of three intraocular lenses with different haptic designs: In silico and in vivo evaluation. *J. Refract. Surg.* 36 (9), 617–624. <http://dx.doi.org/10.3928/1081597x-20200713-02>.
- Ridley, H., 1952. Intra-ocular acrylic lenses : A recent development in the surgery of cataract. *Br. J. Ophthalmol.* 36 (3), 113–122. <http://dx.doi.org/10.1136/bjo.36.3.113>.
- Tataru, C.P., Dogaroiu, A.C., Mihai, C., 2015. Modified injector for optimal insertion of standard ctrs in lax zonules. *Eur. J. Ophthalmol.* 26 (1), 98–100. <http://dx.doi.org/10.5301/ejo.5000613>.
- Usui, M., Tanaka, T., 2015. Resistance force for intraocular lens insertion through lens cartridges and syringe-type injectors. *J. Cataract. Refract. Surg.* 41 (8), 1745–1751. <http://dx.doi.org/10.1016/j.jcrs.2015.03.018>.
- Wang, L., Wolfe, P., Chernosky, A., Paliwal, S., Tjia, K., Lane, S., 2016. In vitro delivery performance assessment of a new preloaded intraocular lens delivery system. *J. Cataract. Refract. Surg.* 42 (12), 1814–1820. <http://dx.doi.org/10.1016/j.jcrs.2016.10.014>.
- Yamakawa, M., Kusaka, M., Yamada, S., Akimoto, M., 2017. Remnant extraction by using an intraocular lens injector with essential flow. *Eur. J. Ophthalmol.* 27 (4), 509–511. <http://dx.doi.org/10.5301/ejo.5000962>.



## Chapter 5

# Discussion

This thesis is focused on the aging of the crystalline lens, from biomechanically analysing the mechanism of accommodation, lens mechanics and the mechanical causes of presbyopia up to developing some numerical methodologies to test IOL haptic design and experimentally evaluate IOL delivery. As it is presented as a compendium of articles, each publication contains a thorough discussion and comparison with literature. Therefore, this chapter only reflects the main achievements, conclusions and the future questions arising from this work.

This thesis highlights through the developing of several high-fidelity simulations that numerical methodologies can support certain regulations. They can be an additional barrier to demonstrate the proper functioning of the device/drug, and even in certain standards, they can facilitate the company's compliance with regulations.

### 5.1 Achievements

- A high-fidelity simulation of the mechanism of accommodation [1] was developed. The simulation reproduces the Helmholtz's theory of accommodation, which states that the dynamic optical change of the lens is produced by the contraction of the ciliary muscle, which releases the resting zonular tension. After releasing this tension, the lens becomes rounded by the stress field in the lens capsule in the unaccommodated state. The main biometric parameters of the lens (anterior and posterior radii of curvature, the anterior and posterior lens movement, and the lens cortex and lens nucleus thicknesses) and the accommodative change was accurately compared with experimental data [15]. The morphological changes of the ciliary muscle contraction were also accurately compared with experimental data [102].
- The change in lens shape (anterior and posterior radii of curvature, lens thickness and diameter and the change in lens nucleus) according to the range of mechanical properties of the lens and lens capsule published in literature [48, 49] was analysed. For this purpose, a high-fidelity simulation of ex-vivo stretching lens tests was developed (from the accommodated lens geometry) [2].

- Mechanical characterisation of the viscoelastic properties of the hydrophobic and hydrophilic acrylate used in IOLs (Benz HF-1.2 Universal Blank (Benz Research and Development, USA) and hydrophilic acrylic material Benz IOL 25 (Benz Research & Development, USA) (Benz Research & Development)) through depth sensing indentation and inverse finite element modelling [3].
- Mechanical characterisation of the hyperelastic properties of the acrylates used in IOLs through uniaxial tests [4, 5].
- A high-fidelity simulation of the IOL compression standard test following ISO 11979-3:2012 [4, 84] was developed. Five IOLs were manufactured according to our previous study to validate the simulations [4, 5].
- To relate the mechanical biomarkers (axial displacement, tilt, decentration and rotation) of IOLs with visual performance [4].
- Numerical methodology to analyse the effect of IOL geometric parameters (Optic-Haptic junction, IOL haptic thickness, IOL haptic length, IOL haptic angle) in the biomechanical stability [5].
- Three IOLs (POD F, POD FT and Micro F Fine Vision Model, all manufactured by Physiol) were clinically evaluated and compared with in-silico values [6].
- Specific-patient methodology of the IOL haptic design during cataract surgery [7]. A deep neural network was trained to predict the best IOL haptic design depending on the patient characteristics (age and equatorial capsular bag diameter). With a more design approach, the DNN could also provide the mechanical response for a determined compression diameter of a wide variety of C-loops IOL.
- A high-fidelity simulation of the mechanical behaviour of the IOL inside the capsular bag in the short- and long-term was developed. The IOL position was simulated just after cataract surgery and the fusion footprint between the anterior and posterior capsule which produces a shrinkage of the bag was reproduced. This simulation could be a breakthrough to investigate other AIOLs.
- Methodology to test the force exerted in IOL delivery using a universal test machine (Instron 5548 Electroplus Microtester) [8].



## 5.2 Conclusions

- The lens mechanical properties govern the lens mechanics during accommodation. The stiffness of the posterior capsule and the stiffness ratio between the lens nucleus and cortex are key on how the lens changes its shape. The geometry has little influence; the lens capsule thickness is directly related to the stiffness of the capsule; and the lens stiffness gradient attempts to maximise the stiffness ratio between the nucleus and cortex. These results were confirmed with the simulation of the mechanism of accommodation, which showed that the main cause of presbyopia is the stiffening of the lens nucleus, contrary to what was thought that the stiffening of the capsule or the loss of the capsule elasticity was the main cause of presbyopia [1, 2].
- Micro- and nano-methodologies can be used in combination with inverse finite element modelling to characterise the IOL material properties. We observed a stiffer and a more pronounced time-dependent behaviour of the hydrophobic acrylic material used in IOLs than the hydrophilic one [8]. The same trend was macroscopically confirmed [4, 5].
- The numerical work presented in this thesis supports the inclusion of numerical models to assist certain regulations. A compelling evidence of the reliability of the numerical simulations in the IOL standards tests [83, 84] was shown. The numerical methodology could be used to avoid time and costs for the manufacturers. Apart from the accurate comparative with the experimental values and the correlation of the IOL mechanical biomarkers with the optical performance, the results obtained in the IOL compression tests were related to clinical values [4, 6].
- The main factor of the C-loop haptic design in the mechanical stability of the IOL is the junction size between the optics and the haptic [5]. Deep learning can be used for patient-specific approaches in cataract surgery, specifically for IOL design [7]. A customised FE model predicting the IOL position inside the capsular bag could be previously performed in the pre-operative phase to minimise post-cataract complications.
- IOL position inside capsular bag highly depends on IOL selection (material and design) and surgeon placement. The stiffness of the capsular bag and the post-cataract diameter also have a high influence on IOL position. The stiffness of the capsular bag is inversely correlated with the size of the capsulorexhis.
- The factors that limit the injection diameter in syringe-type injectors were evaluated. The material is the governing factor in the IOL delivery, followed by the IOL thickest area. Although the haptic design does not seem to have a high influence on the force exerted during IOL delivery, it must be not damaged during IOL delivery. [8].

### 5.3 Future Lines

- With the conclusions obtained in this thesis, the first question that arises regarding presbyopia is how the increase in the lens nucleus stiffness can be prevented. Other lines that can benefit from the conclusions of this thesis are advanced AIOLs, that try to mimic the crystalline lens. A high stiffness ratio between two different gels causes the radii of curvature to change greatly upon deformation.
- The following logical step in the mechanism of accommodation is the inclusion of complex elements that are in the eye cavity and could have an effect on accommodation. For instance, the effect of some vitreous structures could be studied [103].
- We proposed different FE models to test the IOL haptic design, the IOL compression standard test [4, 5, 84] and the prediction of the IOL position in the capsular bag. There is a high potential of the numerical model of the IOL inside the capsular bag, but more data is needed to make it more accurate. That model could be used for different potential scenarios, i.e. from trying new ophthalmic solutions, i.e. novel AIOLs, up to giving a probability of the IOL position inside the capsular bag for every patient, making a revolutionary breakthrough in cataract surgery.
- We evaluated the force exerted by different IOL designs but further tests are needed to understand which parameters limit the injection size and how much it could be minimised without compromising IOL structure and the surgeon or robot manoeuvrability.

## Chapter 6

# Discusión

Esta tesis se centra en el estudio del envejecimiento del cristalino, desde el análisis biomecánico del mecanismo de acomodación, la mecánica del cristalino y las causas mecánicas de la presbicia hasta el desarrollo de algunas metodologías numéricas para testear el diseño háptico de la lente intraocular (IOL) y evaluar experimentalmente la inyección de la misma. Como se presenta por compendio de artículos, cada publicación contiene una discusión exhaustiva y una comparación con la literatura. Por lo tanto, este capítulo sólo refleja los principales logros, las conclusiones y las cuestiones futuras que surgen de este trabajo.

Esta tesis pone de manifiesto, mediante el desarrollo de varias simulaciones validadas, que las metodologías numéricas pueden dar soporte a determinadas normativas o regulaciones. Pueden servir como barrera adicional para demostrar el buen funcionamiento del dispositivo/fármaco, e incluso en ciertas normas, pueden facilitar el cumplimiento de la normativa por parte de la empresa.

### 6.1 Logros

- Se ha logrado una simulación del mecanismo de acomodación [1]. El cálculo reproduce la teoría de acomodación de Helmholtz, que afirma que el cambio dinámico del cristalino se produce por la contracción del músculo ciliar, que a su vez, libera la tensión en las zónulas, permitiendo al cristalino acomodarse. El cristalino acomoda ya que la capsula del mismo está tensionada en el estado no acomodado. Tanto los parámetros biométricos del cristalino (radios de curvatura posterior y anterior, movimiento anterior y posterior del cristalino, diámetro ecuatorial del cristalino, y espesores del cristalino) como el cambio acomodativo se correlacionaron con los valores experimentales [15]. Los cambios morfológicos del músculo ciliar fueron también correlacionados con valores experimentales [102].
- Se ha analizado el cambio de forma de la lente (radio anterior y posterior de curvatura, el espesor y el diámetro del cristalino, y el cambio del espesor del núcleo del cristalino) conforme a las propiedades mecánicas del cristalino. Para ello, se ha desarrollado una simulación altamente fiable de los tests de estiramiento ex-vivo de la lente (a partir de la geometría acomodada) [1, 2].

- Se ha realizado una caracterización mecánica de las propiedades viscoelásticas del acrilato hidrofóbico e hidrofílico utilizado en las IOLs (Benz HF-1.2 Universal Blank (Benz Research and Development, USA) and hydrophilic acrylic material Benz IOL 25 (Benz Research & Development, USA) (Benz Research & Development)) a través de micro-indentación y la modelización inversa por elementos finitos [3].
- Se ha realizado también la caracterización mecánica las propiedades hiperelásticas de los acrilatos utilizados en las IOLs a través de ensayos uniaxiales [4, 5].
- Se ha desarrollado una simulación del ensayo estándar de compresión de las IOLs [4]. Además, se fabricaron cinco IOLs según un estudio previo para validar las simulaciones [4, 5].
- Se ha desarrollado una metodología para relacionar los biomarcadores mecánicos de las IOLs en los ensayos de compresión (desplazamiento axial, inclinación, decentración y rotación) con el rendimiento visual [4].
- Metodología numérica para analizar el efecto de los parámetros geométricos de la IOL (entronque o unión háptico-óptica, espesor del háptico de la IOL, longitud del háptico, ángulo del háptico de la IOL) en la estabilidad biomecánica [5].
- Tres IOLs (los modelos POD F, POD FT y Micro F Fine Vision, todas fabricadas por Physiol) fueron evaluadas clínicamente y comparadas con los valores in-silico [6].
- Metodología específica-paciente del diseño háptico de la IOL durante la cirugía de cataratas [7]. Se entrenó una red neuronal para predecir el mejor diseño háptico en función de las características del paciente (edad y diámetro del saco capsular). Con un enfoque más de diseño, la red también predecía la respuesta biomecánica para cualquier diámetro de compresión de cualquier tipo de C-loop introducida.
- Se ha desarrollado una simulación validada de la IOL dentro del saco capsular reproduciendo su comportamiento a corto y largo plazo. La posición de la IOL fue simulada justo después de la cirugía de cataratas y tras la huella de fusión que se produce entre la capsula anterior y posterior.
- Metodología para comprobar la fuerza ejercida en la inyección de las IOLs con una máquina de testeo universal (Instron 5548 Electropus Microtester) [8].

## 6.2 Conclusiones

- Las propiedades mecánicas del cristalino gobiernan la mecánica del mismo durante la acomodación. La rigidez de la cápsula posterior y la relación de rigidez entre el núcleo y el córtex del cristalino son fundamentales en cómo el cristalino cambia de forma. La geometría tiene poca influencia; el grosor de la cápsula del cristalino está directamente relacionado con la rigidez de la cápsula; y el gradiente de rigidez del cristalino intenta maximizar la relación de rigidez entre el núcleo y el córtex. Estos resultados se confirmaron con la simulación del mecanismo de acomodación, que demostró que la principal causa de la presbicia es la rigidización del núcleo del cristalino, al contrario de lo que se pensaba que la rigidización de la cápsula o la pérdida de la elasticidad de la cápsula era la principal causa de la presbicia [1, 2]
- Las micro- y nano-metodologías pueden combinarse con la modelización inversa mediante elementos finitos para caracterizar las propiedades de materiales oftalmológicos. Observamos un comportamiento más rígido y más pronunciado en función del tiempo del material acrílico hidrofóbico utilizado en las IOLs que el hidrofílico [8]. La misma tendencia se confirmó en ensayos uniaxiales [4, 5].
- Los trabajos numéricos presentados en esta tesis apoyan la inclusión de modelos numéricos para ayudar a ciertas regulaciones. Se ha mostrado una evidencia contundente de la fiabilidad de las simulaciones numéricas en los ensayos de compresión de las normas de lentes intraoculares [83, 84]. La metodología numérica podría utilizarse para ahorrar tiempo y costes a los fabricantes. Además de la comparación precisa con los valores experimentales y la correlación de los biomarcadores mecánicos de la IOL con el rendimiento óptico, los resultados obtenidos en los ensayos de compresión de la IOL se relacionaron con los valores clínicos [4, 6].
- El principal factor del diseño háptico de lazo C de las IOLs es el entronque, la unión entre la óptica y el háptico [5]. Deep learning puede utilizarse para enfoques personalizados en la cirugía de cataratas, específicamente para el diseño de IOLs [7]. Un modelo de elementos finitos personalizado que prediga la posición de la IOL dentro del saco capsular podría realizarse previamente en la fase preoperatoria para evitar cualquier complicación post-cirúrgica.
- La posición de la IOL dentro del saco capsular depende en gran medida de la selección de la IOL (material y diseño) y de la colocación por parte del cirujano. La rigidez del saco capsular y el diámetro del saco después de la cirugía también tienen una gran influencia en la posición final de la IOL. La rigidez del saco capsular está inversamente correlacionada con el tamaño de la capsulorexis.
- Se evaluaron los factores que limitan el diámetro de inyección en los inyectores de tipo syringe. El material es el factor que rige la inyección de la IOL, seguido del espesor central de la IOL. El diseño háptico apenas

tiene influencia en la fuerza ejercida durante la inyección, sin embargo, ha de considerarse para no dañar los hápticos durante la inyección [8].

### 6.3 Líneas Futuras

- Con las conclusiones obtenidas en esta tesis, la primera pregunta que surge respecto a la presbicia es cómo se puede prevenir el aumento de rigidez del núcleo del cristalino. Otras líneas que pueden beneficiarse de las conclusiones de esta tesis son las IOL acomodativas (AIOL), que tratan de imitar el funcionamiento dinámico del cristalino. Una alta relación de rigidez entre dos geles diferentes provoca una alta deformación en los radios de curvatura.
- El siguiente paso lógico en el mecanismo de acomodación es la inclusión de elementos más complejos que están en el ojo y que podrían tener un efecto en la acomodación. Por ejemplo, se podría estudiar el efecto de algunas estructuras vitreas [103].
- Proponemos diferentes modelos de elementos finitos para probar el diseño háptico de la IOL, tanto el modelo de compresión de la IOL siguiendo la norma ISO 11979-3:2012 [4, 5, 84], como el modelo para predecir la posición de la IOL dentro del saco capsular. El modelo numérico de la IOL dentro del saco tiene un gran potencial, pero se necesitan más datos para realizar una validación más precisa. Este modelo podría utilizarse en diferentes escenarios, desde probar nuevas soluciones oftálmicas, es decir, nuevas AIOLs, hasta dar una probabilidad de la posición de la IOL dentro del saco capsular para cada paciente, lo que supondría un avance revolucionario en la cirugía de cataratas.
- Evaluamos la fuerza ejercida por diferentes diseños de IOL, pero se necesitan más pruebas para comprender qué parámetros limitan el tamaño de la inyección y cuánto podría minimizarse sin comprometer la estructura de la IOL y la maniobrabilidad del cirujano o del robot.

## Chapter 7

# Other Activities during the Ph.D. Period 2019-2022

### 7.1 Diffusion of the Results

This chapter includes other activities related to the dissemination of the project, the research stay carried out, previous work related to this thesis and the supervision of different works during the thesis.

#### 7.1.1 Contributions by Iulen Cabeza Gil

1. **2022 Annual Meeting. Association for Research in Vision and Ophthalmology (ARVO). Denver (US).** Quantification of ciliary muscle movement during accommodation from transscleral OCT images. I. Cabeza-Gil, M. Ruggeri, Y.C. Chang, B. Calvo, F. Manns. 2021
2. **26<sup>th</sup> Congress of the European Society of Biomechanics (ESB). Milan (Italy).** Ocular accommodation: exploring presbyopia causes with a validated numerical model. I. Cabeza-Gil, J. Grasa, B. Calvo. 2022
3. **IX Workshop for Young Researchers in Aragon Institute of Engineering Research. Zaragoza (Spain).** Numerical Approach of the Ciliary Muscle Contraction. A preliminary Step to Reproduce Human Accommodation. I. Cabeza-Gil, J. Grasa, A. Glasser, B. Calvo. 2020
4. **37<sup>th</sup> Congress on the European Society of Cataract & Refractive Surgeons (ESCRS). Paris (France).** Understanding the main mechanical parameters of C-loop intraocular lenses. I. Cabeza-Gil, L. Remón, M. A. Ariza-Gracia, B. Calvo. 2019
5. **25<sup>th</sup> Congress of the European Society of Biomechanics (ESB). Wien (Austria).** Effects of design parameters on the stability of the C-loop Intraocular lenses by a full factorial design. I. Cabeza-Gil, L. Remón, M. A. Ariza-Gracia, B. Calvo. 2019

#### 7.1.2 Contributions by Collaborators

1. **2022 Annual Meeting. Association for Research in Vision and Ophthalmology (ARVO). Denver (US).** Longitudinal changes in thickness of the aging human lens measured with OCT. M. Ruggeri, Y.C. Chang,

- I. Cabeza-Gil, L. Rohman, B. Maceo Heilman ; F. Cabot, S.H. Yoo, A. Ho, Arthur, J.M. Parel, F. Manns. 2022
2. **Mechanistic Machine Learning and Digital Twins for Computational Science, Engineering & Technology (MMLDT-CSET). San Diego (US).** Deep learning approach to determine the biomechanics of intraocular lenses. One step closer to patient customization.. I. Ríos-Ruiz, I. Cabeza-Gil, B. Calvo. 2021
  3. **26<sup>th</sup> Congress of the European Society of Biomechanics (ESB). Milan (Italy).** Intraocular lens insertion during cataract surgery. I. Cabeza-Gil, I. Ríos-Ruiz, J. Frechilla, B. Calvo. 2021
  4. **2019 Edition. Congress of Numerical Methods in Engineering (CNM). Guimaraes (Portugal).** Effect of haptic geometry on the mechanical stability of intraocular lenses using finite element analysis. I. Cabeza-Gil, L. Remón, M. A. Ariza-Gracia, B. Calvo. 2019
  5. **IX Reunión del Capítulo Español de la Sociedad Europea de Biomecánica (ESB).** Mechanical stability of the C-loop intraocular lenses by a in-silico study. I. Cabeza-Gil, L. Remón, M. A. Ariza-Gracia, B. Calvo. 2019

## 7.2 Stays in Research Institutions

Ophthalmic Bascom Center (Bascom Palmer Eye Institute, University of Miami) Miami, US. Under the supervision of Marco Ruggeri and Fabrice Manns [August-December, 2021] .

The following publication has resulted from this research stay:

Automated Segmentation of the Ciliary Muscle in OCT Images using Fully Convolutional Networks. I. Cabeza-Gil, M. Ruggeri, Y-C. Chang, B. Calvo and F. Manns. Biomedical Optics Express. Accepted. [104]

## 7.3 Previous Works related to this Thesis

Remón, L, Siedlecki, D, Cabeza-Gil, I & Calvo, B. Influence of material and haptic design on the mechanical stability of intraocular lenses by means of finite- element modeling. J Biomed Opt 23, 1 (2018) [82].

## 7.4 Projects with Multinational Corporations

Project: IOL FE Analysis. CARL ZEISS MEDITEC AG



## 7.5 Supervisor of B.S. and M.Sc. Thesis

This section gathers the bachelor and master thesis where I have helped as supervisor. All thesis were presented in the University of Zaragoza.

1. **S. Rivero.** In silico analysis of the biomechanical stability of Double C-Loop lenses in the capsular bag. Directors: B. Calvo and I. Cabeza-Gil. 2020 – 2021.
2. **P. Fernández.** Biomechanical analysis of the stability of intraocular lenses after cataract surgery. Directors: B. Calvo and I. Cabeza-Gil. 2020 – 2021.
3. **J. Frechilla.** Finite element analysis of intraocular lens injection for cataract surgery. Directors: B. Calvo and I. Cabeza-Gil. 2020 – 2021.
4. **B. Bonet.** Influence of the composition and thermal parameters in the heating of recipients in the cooking with induction cookers. Directors: M.A. Martínez and I.Cabeza-Gil. 2019 – 2020.
5. **M.P. Cabello.** Numerical simulation of intraocular lens insertion during cataract surgery. Directors: B. Calvo and I. Cabeza-Gil. 2019 – 2020.
6. **J. Puyuelo.** Statistical analysis of the haptic design of Plate Loop intraocular lenses. Directors: B. Calvo and I. Cabeza-Gil. 2019 – 2020.
7. **M. Bienzobas.** Numerical simulation of soft contact lenses. Directors: E. Lanchares and I. Cabeza-Gil. 2018 – 2019.
8. **S. Rivero.** Optimization of the biomechanical stability of Double C-Loop intraocular lenses to ensure the biomechanical stability. Directors: B. Calvo and I. Cabeza-Gil. 2018 – 2019.

## 7.6 Funding

This thesis and the research stay was supported by the Spanish Ministerio de Ciencia, Innovacion y Universidades (Grant DPI2017-84047-R) and the individual grant PRE2018-084021. Also supported by: an PID2020-113822RB-C12/ funded by MCIN/ AEI /10.13039/501100011033.



# Bibliography

1. Cabeza-Gil, I., Grasa, J. & Calvo, B. A validated finite element model to reproduce Helmholtz's theory of accommodation: a powerful tool to investigate presbyopia. *Ophthalmic and Physiological Optics* **41**, 1241–1253 (2021).
2. Cabeza-Gil, I., Grasa, J. & Calvo, B. A numerical investigation of changes in lens shape during accommodation. *Scientific Reports* **11** (2021).
3. Cabeza-Gil, I., Calvo, B., Rico, A., Reinhardt-Hervás, C. & Rodríguez, J. Mechanical characterisation of hydrophobic and hydrophilic acrylates used in intraocular lenses through depth sensing indentation. *Journal of the Mechanical Behavior of Biomedical Materials* **126**, 104997 (2022).
4. Cabeza-Gil, I., Pérez-Gracia, J., Remón, L. & Calvo, B. Effect of haptic geometry in C-loop intraocular lenses on optical quality. *Journal of the Mechanical Behavior of Biomedical Materials* **114**, 104165 (2021).
5. Cabeza-Gil, I., Ariza-Gracia, M. Á., Remón, L. & Calvo, B. Systematic Study on the Biomechanical Stability of C-Loop Intraocular Lenses: Approach to an Optimal Design of the Haptics. *Annals of Biomedical Engineering* **48**, 1127–1136 (2019).
6. Remón, L., Cabeza-Gil, I., Calvo, B., Poyales, F. & Garzón, N. Biomechanical Stability of Three Intraocular Lenses With Different Haptic Designs: In Silico and In Vivo Evaluation. *Journal of Refractive Surgery* **36**, 617–624 (2020).
7. Cabeza-Gil, I., Ríos-Ruiz, I. & Calvo, B. Customised Selection of the Haptic Design in C-Loop Intraocular Lenses Based on Deep Learning. *Annals of Biomedical Engineering* **48**, 2988–3002 (2020).
8. Cabeza-Gil, I., Ríos-Ruiz, I. & Calvo, B. Experimental evaluation of the injection force exerted in intraocular lens delivery with syringe-type injectors. *Journal of the Mechanical Behavior of Biomedical Materials* **124**, 104793 (2021).
9. Lavanya, R. *et al.* Comparison of anterior chamber depth measurements using the IOLMaster, scanning peripheral anterior chamber depth analyser, and anterior segment optical coherence tomography. *British Journal of Ophthalmology* **91**, 1023–1026 (2007).
10. Hove, J. V., Nilsson, S. F. E. & Wu, S. *Adler's Physiology of the Eye* 820 pp. ISBN: 0323057144 (Elsevier Health Science, Apr. 2011).
11. Helmholtz, H. Ueber die Accommodation des Auges. *Albrecht von Graefes Archiv für Ophthalmologie* **2**, 1–74 (1855).
12. Glasser, A. & Kaufman, P. L. The mechanism of accommodation in primates. *Ophthalmology* **106**, 863–872 (1999).
13. Glasser, A. & Campbell, M. C. Presbyopia and the optical changes in the human crystalline lens with age. *Vision Research* **38**, 209–229 (1998).
14. Glasser, A. & Campbell, M. C. Biometric, optical and physical changes in the isolated human crystalline lens with age in relation to presbyopia. *Vision Research* **39**, 1991–2015 (1999).

15. Ramasubramanian, V. & Glasser, A. Objective measurement of accommodative biometric changes using ultrasound biomicroscopy. *Journal of Cataract and Refractive Surgery* **41**, 511–526 (2015).
16. Brown, N. The change in shape and internal form of the lens of the eye on accommodation. *Experimental Eye Research* **15**, 441–459 (1973).
17. Croft, M. A. *et al.* Extralenticular and Lenticular Aspects of Accommodation and Presbyopia in Human Versus Monkey Eyes. *Investigative Ophthalmology & Visual Science* **54**, 5035 (July 2013).
18. DJ, C. On the hydraulic suspension theory of accommodation. *Transactions of the American Ophthalmological Society* **84**, 846–868 (1986).
19. Fisher, R. F. Is the vitreous necessary for accommodation in man? *British Journal of Ophthalmology* **67**, 206–206 (1983).
20. Manns, F. *et al.* Optomechanical Response of Human and Monkey Lenses in a Lens Stretcher. *Investigative Ophthalmology & Visual Science* **48**, 3260 (2007).
21. Woodman-Pieterse, E. C., Read, S. A., Collins, M. J. & Alonso-Caneiro, D. Anterior scleral thickness changes with accommodation in myopes and emmetropes. *Experimental Eye Research* **177**, 96–103 (2018).
22. Niyazmand, H., Read, S. A., Atchison, D. A. & Collins, M. J. Effects of accommodation and simulated convergence on anterior scleral shape. *Ophthalmic and Physiological Optics* **40**, 482–490 (2020).
23. Ioannidis, J. P. A. Why Most Published Research Findings Are False. *PLoS Medicine* **2**, e124 (2005).
24. Ruggeri, M. *et al.* Assessment of scleral shape and thickness during accommodation using OCT in ARVO Annual Meeting Abstract (2018).
25. Cabot, F. *et al.* Assessment of Scleral Thickness During Accommodation Using Dynamic OCT Imaging in *Investigative Ophthalmology & Visual Science* (ARVO Meeting) (2019).
26. Schachar, R. A. & Bax, A. J. Mechanism of human accommodation as analyzed by nonlinear finite element analysis. *Comprehensive Therapy* **27**, 122–132 (2001).
27. Schachar, R. A. The Mechanism of Accommodation and Presbyopia. *International Ophthalmology Clinics* **46**, 39–61 (2006).
28. Croft, M. A. *et al.* Accommodative Movements of the Vitreous Membrane, Choroid, and Sclera in Young and Presbyopic Human and Nonhuman Primate Eyes. *Investigative Ophthalmology & Visual Science* **54**, 5049 (July 2013).
29. Green, D. G., Powers, M. K. & Banks, M. S. Depth of focus, eye size and visual acuity. *Vision Research* **20**, 827–835 (1980).
30. Richdale, K. *et al.* Quantification of Age-Related and per Diopter Accommodative Changes of the Lens and Ciliary Muscle in the Emmetropic Human Eye. *Investigative Ophthalmology & Visual Science* **54**, 1095 (2013).
31. Tamm, E. R. & Lütjen-Drecoll, E. Ciliary body. *Microscopy Research and Technique* **33**, 390–439 (1996).
32. Winn, B., Culhane, H. M., Gilmartin, B. & Strang, N. C. Effect of beta- adrenoceptor antagonists on autonomic control of ciliary smooth muscle. *Ophthalmic and Physiological Optics* **22**, 359–365 (2002).
33. Pardue, M. T. & Sivak, J. G. Age-Related Changes in Human Ciliary Muscle. *Optometry and Vision Science* **77**, 204–210 (2000).
34. Van Alphen, G. & Graebel, W. Elasticity of tissues involved in accommodation. *Vision Research* **31**, 1417–1438 (1991).
35. Farnsworth, P. N. & Burke, P. Three-dimensional architecture of the suspensory apparatus of the lens of the Rhesus monkey. *Experimental Eye Research* **25**, 563–576 (1977).

36. Michael, R. *et al.* Elastic Properties of Human Lens Zonules as a Function of Age in Presbyopes. *Investigative Ophthalmology & Visual Science* **53**, 6109 (2012).
37. Bernal, A., Parel, J.-M. & Manns, F. Evidence for Posterior Zonular Fiber Attachment on the Anterior Hyaloid Membrane. *Investigative Ophthalmology & Visual Science* **47**, 4708 (2006).
38. Goldberg, D. B. Computer-animated model of accommodation and presbyopia. *Journal of Cataract and Refractive Surgery* **41**, 437–445 (2015).
39. *Clinical Anatomy and Physiology of the Visual System* (Elsevier, 2012).
40. Taylor, A. *et al.* Long-term intake of vitamins and carotenoids and odds of early age-related cortical and posterior subcapsular lens opacities. *The American Journal of Clinical Nutrition* **75**, 540–549 (2002).
41. Gupta, A. *et al.* In vivo SS-OCT imaging of crystalline lens sutures. *Biomedical Optics Express* **11**, 5388 (2020).
42. Appleton, B. Radiant Energy and the Eye. *Military Medicine* **146**, 105–105 (1981).
43. Hejtmancik, J. F. & Shiels, A. in *Progress in Molecular Biology and Translational Science* 119–127 (Elsevier, 2015).
44. Chang, Y.-C. *et al.* In vivo measurement of the human crystalline lens equivalent refractive index using extended-depth OCT. *Biomedical Optics Express* **10**, 411 (2019).
45. Siedlecki, D. *et al.* Distortion Correction of OCT Images of the Crystalline Lens. *Optometry and Vision Science* **89**, E709–E718 (2012).
46. Navarro, R. & López-Gil, N. Impact of internal curvature gradient on the power and accommodation of the crystalline lens. *Optica* **4**, 334 (2017).
47. Birkenfeld, J., de Castro, A. & Marcos, S. Contribution of Shape and Gradient Refractive Index to the Spherical Aberration of Isolated Human Lenses. *Investigative Ophthalmology & Visual Science* **55**, 2599 (2014).
48. Wilde, G., Burd, H. & Judge, S. Shear modulus data for the human lens determined from a spinning lens test. *Experimental Eye Research* **97**, 36–48 (2012).
49. Krag, S. & Andreassen, T. T. Mechanical properties of the human lens capsule. *Progress in Retinal and Eye Research* **22**, 749–767 (2003).
50. Krag, S. & Andreassen, T. T. Mechanical Properties of the Human Posterior Lens Capsule. *Investig Ophthalmol Vis Sci* **44**, 691 (2003).
51. Krag, S, Olsen, T & Andreassen, T. T. Biomechanical characteristics of the human anterior lens capsule in relation to age. *Investigative Ophthalmology & Visual Science* **38**, 357–363. ISSN: 1552-5783 (Feb. 1997).
52. Vilupuru, A. S., Roorda, A. & Glasser, A. Spatially variant changes in lens power during ocular accommodation in a rhesus monkey eye. *Journal of Vision* **4**, 6 (2004).
53. Anderson, H. A., Hentz, G., Glasser, A., Stuebing, K. K. & Manny, R. E. Minus-Lens–Stimulated Accommodative Amplitude Decreases Sigmoidally with Age: A Study of Objectively Measured Accommodative Amplitudes from Age 3. *Investigative Ophthalmology & Visual Science* **49**, 2919 (2008).
54. Wang, K. & Pierscionek, B. K. Biomechanics of the human lens and accommodative system: Functional relevance to physiological states. *Progress in Retinal and Eye Research* **71**, 114–131 (2019).
55. Hamasaki, D., Ong, J. & Marg, E. The Amplitude of Accommodation in Presbyopia. *Optometry and Vision Science* **33**, 3–14 (1956).
56. Koretz, J. F., Kaufman, P. L., Neider, M. W. & Goeckner, P. A. Accommodation and presbyopia in the human eye—aging of the anterior segment. *Vision Research* **29**, 1685–1692 (1989).

57. Wold, J. E., Hu, A., Chen, S. & Glasser, A. Subjective and objective measurement of human accommodative amplitude. *Journal of Cataract and Refractive Surgery* **29**, 1878–1888 (2003).
58. Ostrin, L. A. & Glasser, A. Accommodation measurements in a prepresbyopic and presbyopic population. *Journal of Cataract and Refractive Surgery* **30**, 1435–1444 (2004).
59. Fricke, T. R. *et al.* Global Prevalence of Presbyopia and Vision Impairment from Uncorrected Presbyopia. *Ophthalmology* **125**, 1492–1499 (2018).
60. Porela-Tiihonen, S., Kokki, H., Kaarniranta, K. & Kokki, M. Recovery after cataract surgery. *Acta Ophthalmologica* **94**, 1–34 (2016).
61. Usui, M. & Tanaka, T. Resistance force for intraocular lens insertion through lens cartridges and syringe-type injectors. *Journal of Cataract and Refractive Surgery* **41**, 1745–1751 (2015).
62. Dewey, S. *et al.* Microincisions in cataract surgery. *Journal of Cataract and Refractive Surgery* **40**, 1549–1557 (2014).
63. Zvorničanin, J. & Zvorničanin, E. Premium intraocular lenses: The past, present and future. *Journal of Current Ophthalmology* **30**, 287–296 (2018).
64. Shichi, H. Cataract formation and prevention. *Expert Opinion on Investigational Drugs* **13**, 691–701 (2004).
65. Liu, Y.-C., Wilkins, M., Kim, T., Malyugin, B. & Mehta, J. S. Cataracts. *The Lancet* **390**, 600–612 (2017).
66. Hiller, R., Sperduto, R. D. & Edered, F. Epidemiologic associations with nuclear, cortical and posterior subcapsular cataracts. *American Journal of Epidemiology* **124**, 916–925 (1986).
67. Donaldson, P. J., Grey, A. C., Heilman, B. M., Lim, J. C. & Vaghefi, E. The physiological optics of the lens. *Progress in Retinal and Eye Research* **56**, e1–e24 (2017).
68. Holland, E. *et al.* The AcrySof Toric Intraocular Lens in Subjects with Cataracts and Corneal Astigmatism. *Ophthalmology* **117**, 2104–2111 (2010).
69. Berdeaux, G., Cochener, B., Lafuma, A., Khoshnood, B & Courouve. Comparison of outcomes with multifocal intraocular lenses: a meta-analysis. *Clinical Ophthalmology*, 45 (2011).
70. Shajari, M. *et al.* Comparison of 9 modern intraocular lens power calculation formulas for a quadrifocal intraocular lens. *Journal of Cataract and Refractive Surgery* **44**, 942–948 (2018).
71. Melles, R. B., Holladay, J. T. & Chang, W. J. Accuracy of Intraocular Lens Calculation Formulas. *Ophthalmology* **125**, 169–178 (2018).
72. Behndig, A. *et al.* Aiming for emmetropia after cataract surgery: Swedish National Cataract Register study. *Journal of Cataract and Refractive Surgery* **38**, 1181–1186 (2012).
73. Lundström, M. *et al.* Risk factors for refractive error after cataract surgery: Analysis of 282 811 cataract extractions reported to the European Registry of Quality Outcomes for cataract and refractive surgery. *Journal of Cataract and Refractive Surgery* **44**, 447–452 (2018).
74. Tang, M., Li, Y. & Huang, D. An Intraocular Lens Power Calculation Formula Based on Optical Coherence Tomography: A Pilot Study. *Journal of Refractive Surgery* **26**, 430–437 (2010).
75. Józwick, A., Siedlecki, D. & Zając, M. Analysis of Purkinje images as an effective method for estimation of intraocular lens implant location in the eyeball. *Optik* **125**, 6021–6025 (2014).

76. Chang, Y.-C. *et al.* Pre-operative Prediction of Post-cataract Surgery IOL Position Using Anterior Chamber Depth and Lens Thickness Determined with Extended-depth OCT in *Investigative Ophthalmology & Visual Science (ARVO Meeting)* (2017).
77. Yoo, Y.-S., Whang, W.-J., Kim, H.-S., Joo, C.-K. & Yoon, G. Preoperative biometric measurements with anterior segment optical coherence tomography and prediction of postoperative intraocular lens position. *Medicine* **98**, e18026 (2019).
78. Satou, T. *et al.* Development of a new intraocular lens power calculation method based on lens position estimated with optical coherence tomography. *Scientific Reports* **10** (2020).
79. Remón, L., Arias, A., Calatayud, A., Furlan, W. D. & Monsoriu, J. A. Through-focus response of multifocal intraocular lenses evaluated with a spatial light modulator. *Applied Optics* **51**, 8594 (2012).
80. Patel, C., Ormonde, S., Rosen, P. H. & Bron, A. J. Postoperative intraocular lens rotation. *Ophthalmology* **106**, 2190–2196 (1999).
81. Zhu, X., Meng, J., He, W., Rong, X. & Lu, Y. Comparison of the rotational stability between plate-haptic toric and C-loop haptic toric IOLs in myopic eyes. *Journal of Cataract and Refractive Surgery* **46**, 1353–1359 (2020).
82. Remón, L., Siedlecki, D., Cabeza-Gil, I & Calvo, B. Influence of material and haptic design on the mechanical stability of intraocular lenses by means of finite-element modeling. *J Biomed Opt* **23**, 1 (2018).
83. ISO. *Ophthalmic implants. Intraocular lenses. Part 2: Optical properties and test methods.* (ed ) ISBN: 9780580708800 (BSI Standards Limited, 11979-2:2014).
84. ISO. *Ophthalmic implants. Intraocular lenses. Part 3. Mechanical properties and test methods.* (ed ) ISBN: 9780580708800 (BSI Standards Limited, 11979-3:2012).
85. Wormstone, I. M., Damm, N. B., Kelp, M. & Eldred, J. A. Assessment of intraocular lens/capsular bag biomechanical interactions following cataract surgery in a human in vitro graded culture capsular bag model. *Experimental Eye Research* **205**, 108487 (2021).
86. Wormstone, I., Wormstone, Y., Smith, A. & Eldred, J. Posterior capsule opacification: What's in the bag? *Progress in Retinal and Eye Research* **82**, 100905 (2021).
87. Haripriya, A. *et al.* Long-term Posterior Capsule Opacification Reduction with Square-Edge Polymethylmethacrylate Intraocular Lens. *Ophthalmology* **124**, 295–302 (2017).
88. Marchini, G., Pedrotti, E., Modesti, M., Visentin, S. & Tosi, R. Anterior segment changes during accommodation in eyes with a monofocal intraocular lens: High-frequency ultrasound study. *Journal of Cataract and Refractive Surgery* **34**, 949–956 (2008).
89. Chang, D. F. Early rotational stability of the longer Staar toric intraocular lens. *Journal of Cataract and Refractive Surgery* **29**, 935–940 (2003).
90. Zhong, X. *et al.* Comparisons of the in-the-bag stabilities of single-piece and three-piece intraocular lenses for age-related cataract patients: a randomized controlled trial. *BMC Ophthalmology* **16** (2016).
91. Wang, X., Dong, J., Wang, X. & Wu, Q. IOL Tilt and Decentration Estimation from 3 Dimensional Reconstruction of OCT Image. *PLoS ONE* **8** (ed Li, T.) e59109 (2013).
92. Maedel, S. *et al.* Comparison of intraocular lens decentration and tilt measurements using 2 Purkinje meter systems. *Journal of Cataract and Refractive Surgery* **43**, 648–655 (2017).
93. Bourne, R. R. A. *et al.* Magnitude, temporal trends, and projections of the global prevalence of blindness and distance and near vision impairment: a

- systematic review and meta-analysis. *The Lancet Global Health* **5**, e888–e897 (2017).
94. Berdahl, J. *et al.* Patient and Economic Burden of Presbyopia: A Systematic Literature Review. *Clinical Ophthalmology* **14**, 3439–3450 (2020).
  95. Wang, W. *et al.* Cataract Surgical Rate and Socioeconomics: A Global Study. *Investigative Ophthalmology & Visual Science* **57**, 5872 (2017).
  96. Rossi, T. *et al.* Primary Blast Injury to the Eye and Orbit: Finite Element Modeling. *Investigative Ophthalmology & Visual Science* **53**, 8057 (2012).
  97. Ariza-Gracia, M. Á., Flecha-Lescún, J., Büchler, P. & Calvo, B. Corneal Biomechanics After Intrastromal Ring Surgery: Optomechanical In Silico Assessment. *Translational Vision Science & Technology* **9**, 26 (2020).
  98. Wang, K., Venetsanos, D. T., Wang, J., Augousti, A. T. & Pierscionek, B. K. The importance of parameter choice in modelling dynamics of the eye lens. *Scientific Reports* **7** (2017).
  99. Wang, K., Hoshino, M., Uesugi, K., Yagi, N. & Pierscionek, B. K. Contributions of shape and stiffness to accommodative loss in the ageing human lens: a finite element model assessment. *Journal of the Optical Society of America A* **36**, B116 (2019).
  100. Hajj, H. A. *et al.* CATARACTS: Challenge on automatic tool annotation for cataRACT surgery. *Medical Image Analysis* **52**, 24–41 (2019).
  101. González, D. C. & Bautista, C. P. Accuracy of a new intraocular lens power calculation method based on artificial intelligence. *Eye* **35**, 517–522 (2020).
  102. Wagner, S., Zrenner, E. & Strasser, T. Ciliary muscle thickness profiles derived from optical coherence tomography images. *Biomedical Optics Express* **9**, 5100 (2018).
  103. Croft, M. A. *et al.* Intraocular accommodative movements in monkeys; relationship to presbyopia. *Experimental Eye Research*, 109029 (2022).
  104. Cabeza-Gil, I., Ruggeri, M., Chang, Y.-C., Calvo, B. & Manns, F. Automated Segmentation of the Ciliary Muscle in OCT Images using Fully Convolutional Networks. *Biomedical Optics Express* (**in press**) (2022).



## Appendix A

# Metrics of the Scientific Journals

According to the regulation of the University of Zaragoza regarding Doctoral Thesis presented by compendium of publications, the FI (Web of Science) and the reference for each publication is described.

1. Cabeza-Gil, I., Grasa, J. & Calvo, B. A validated finite element model to reproduce Helmholtz's theory of accommodation: a powerful tool to investigate presbyopia. *Ophthalmic and Physiological Optics* 41, 1241–1253 (2021) [1]. JIF (2020): 3.12 (Q2: 23/62 Ophthalmology).
2. Cabeza-Gil, I., Grasa, J. & Calvo, B. A numerical investigation of changes in lens shape during accommodation. *Scientific Reports* 11 (2021) [2]. JIF (2020): 4.38 (Q1: 17/72 Multidisciplinary Sciences).
3. Cabeza-Gil, I., Calvo, B., Rico, A., Reinhardt-Hervás, C. & Rodríguez, J. Mechanical characterisation of hydrophobic and hydrophilic acrylates used in intraocular lenses through depth sensing indentation. *Journal of the Mechanical Behavior of Biomedical Materials* 126, 104997 (2022) [3]. JIF (2020): 3.90 (Q2: 32/89 Biomedical Engineering).
4. Cabeza-Gil, I., Pérez-Gracia, J., Remón, L. & Calvo, B. Effect of haptic geometry in C-loop intraocular lenses on optical quality. *Journal of the Mechanical Behavior of Biomedical Materials* 114, 104165 (2021) [4]. JIF (2020): 3.90 (Q2: 32/89 Biomedical Engineering).
5. Cabeza-Gil, I., Ariza-Gracia, M. Á., Remón, L. & Calvo, B. Systematic Study on the Biomechanical Stability of C-Loop Intraocular Lenses: Approach to an Optimal Design of the Haptics. *Annals of Biomedical Engineering* 48, 1127–1136 (2019) [5]. JIF (2020): 3.93 (Q2: 31/89 Biomedical Engineering).
6. Remón, L., Cabeza-Gil, I., Calvo, B., Poyales, F. & Garzón, N. Biomechanical Stability of Three Intraocular Lenses With Different Haptic Designs: In Silico and In Vivo Evaluation. *Journal of Refractive Surgery* 36, 617–624 (2020) [6]. JIF (2020): 3.57 (Q1: 15/62 Ophthalmology).
7. Cabeza-Gil, I., Ríos-Ruiz, I. & Calvo, B. Customised Selection of the Haptic Design in C-Loop Intraocular Lenses Based on Deep Learning. *Annals of Biomedical Engineering* 48, 2988–3002 (2020) [7]. JIF (2020): 3.93 (Q2: 31/89 Biomedical Engineering).
8. Cabeza-Gil, I., Ríos-Ruiz, I. & Calvo, B. Experimental evaluation of the injection force exerted in intraocular lens delivery with syringe-type injectors. *Journal of the Mechanical Behavior of Biomedical Materials* 124, 104793 (2021) [8]. JIF (2020): 3.90 (Q2: 32/89 Biomedical Engineering).